Amine-borane dehydropolymerisation catalysed by iridium POCOP complexes

Chloe May van Beek

Doctor of Philosophy

University of York

Department of Chemistry

March 2026

Abstract

Polyaminoboranes (PABs) are isosteres of polyolefins by the isoelectronic relationship between the C—C and B—N units.[1] These polymeric materials have potential use as precursors to B,N-based pre-ceramics, *e.g.* hexagonal boron nitride (*h*-BN) an isostere of graphene.

This thesis describes the controlled synthesis of polyaminoborane with previously reported catalyst, Ir(^{t}Bu-POCOP)H_2 (POCOP = κ^3-1,3-(OP^{t}Bu$_2$)$_2$C$_6$H$_3$])[4]. Chapter 1 provides a summary of the synthesis of polyaminoboranes, with a focus on transition metal catalysed reactions, and the mechanisms that have previously been reported. The applications of polyaminoboranes were also discussed.

Chapter 2 introduces the kinetics of the dehydrogenation of $H_3B{\cdot}NH_2Me$ with Ir(^{t}Bu-POCOP)$(H)_2$, identifying an unexpected induction period, with potential causes of this induction period discussed. The speciation of the reaction was studied by NMR spectroscopy *in situ* and *in operando*. Relevant catalytic intermediates were identified and studied for the dehydrogenation of $H_3B{\cdot}NH_2Me$ independently. Equilibria between the identified catalytically relevant complexes were studied and discussed in this chapter.

Chapter 3 presents the proposed mechanistic pathways for the dehydrogenation of $H_3B{\cdot}NH_2Me$ with Ir(^{t}Bu-POCOP)$(H)_2$. This study will combine data from kinetic experiments, Eyring analysis, isotope labelling experiments, DFT calculations and kinetic modelling to propose a mechanism. The synthesis and characterisation of an anionic iridium trihydride complex is also reported.

Chapter 4 discusses the reaction conditions that have been identified that allow for the control of molecular weight of polyaminoborane, with a relationship based on $k_{obs} \propto M_n$. This chapter includes scale up of the reaction to 20 g with very low catalyst loadings (0.001 mol%). The synthesis of BN ceramics (boron nitride) from polyaminoboranes is also detailed in this chapter.

Chapter 5 investigates the use of Ir(POCOP) catalysts with different R-groups on the phosphine to dehydrogenate $H_3B{\cdot}NH_2Me$, to determine their effect on the rate of reaction and so in turn molecular weight.

Author's Declaration

I declare that this thesis is a presentation of original work and I am the sole author. This work was carried out under the supervision of Professor Andrew S. Weller and Professor Richard Douthwaite at the University of York. I declare that all work is my own, unless otherwise stated, and that this work has not previously been presented for a degree or other qualification at this University or elsewhere. All sources are acknowledged as references.

Part of this work has been disclosed in a patent: PCT/GB2025/052441, Catalytic Method.

Large portions of this work have been presented for publication:

- C. M. van Beek, M. A. Sajjad, J. C. Goodall, C. L. Lyall, J. P. Lowe, S. B. Duckett, J. S. McIndoe, C. Killeen, G. C. Lloyd-Jones, U. Hintermair, S. A. Macgregor, R. E. Douthwaite and A. S. Weller, *J. Am. Chem. Soc.*, 2026, *under review.*
- P. Y. Lee, B. M. Maciejewska, M. J. Cross, C. M. van Beek, C. N. Brodie, A. S. Bhaskaran, G. T. Tebutt, R. M. Schofield, S. J. Page, E. Darnbrough, M. Swart, A. S. Weller, N. Grobert, *Adv. Comps. Hybrid Mater.*, 2025, **8**, 392.

Acknowledgments

The first and biggest thank yous have to go to my incredibly patient and supportive supervisors. Andy and Richard, thank you for giving me this opportunity and for coming on this journey with me. I couldn't have done it without either of you. Andy, I have learnt so much being in your lab, I've grown so much in confidence and knowledge, that I don't recognise the person I was over three years ago. A large part of that has been down to you, your unwavering support, high standards and faith in me always. I also want to thank both you and Kate for welcoming us into your home for what always felt like family dinner, it makes the world of difference especially when you've just moved to a new place and it doesn't feel like home yet. Also, Kate's sticky toffee pudding is incredible! Richard, thank you for always being there when I had questions and needed advice, your support through this process means a lot.

Thank you to all the collaborators that helped to make this work possible. Stuart and Arif, thank you for all the Macgrellers. Guy, thank you for taking the time to chat kinetics with me, even if it was an excuse for a steak. Uli, Catherine and John, thank you for hosting me down in Bath to use the DreAM facility. Ping-Yuan, Basia and Nicole thank you for doing cool fiber things with polyaminoboranes. Also, a huge thank you to all the technical staff at York, all of us would be hopeless without you.

There are some post-docs that I need to thank. Matt, thank you for always sharing your experience and wisdom with us PhDs, I swear no matter what complex someone was making you'd already made it at some point and could point us in the direction of a better prep. I really miss your one liners, and have found myself quoting some of them as time went on. Kris, I really value your friendship especially at the start of my PhD. You always made yourself available for a chat and you have supported all of us PhDs when we needed it. We did eventually forgive you for all of your stories starting with 'when I was in Canada'. Alex, thank you for joining Team AB (I was definitely getting out numbered). It was nice to have someone to bounce ideas off of and pass on my AB knowledge on to. Also, I will never forget the sad frankfurters and lentils in Esslingen. Mads, we didn't cross over for very long but I hope SMOM treats you well and you enjoy your time in the UK.

To all of the Weller and Douthwaite PhDs, these last 3 and a half years wouldn't have been the same without all of you. Thank you for all of your support, and for making one of the most stressful things I have ever done also one of the most enjoyable. Hel, I feel like we clicked from the very start of my

PhD, I miss our long chats and story telling escapades, and our trips to fill our water bottles up just so that we could rant. Jooooeeeeee, thank you for always trying to run whatever scunge I gave you on the diffy, they weren't all that bad though, right? Chlo, you are one of the sunniest people I have ever met, you're incredibly kind and just an all-round good egg. Thank you for all of the support over the years and always being there when I needed a hug. Mat, it was just us in Team AB for the longest time, I always thought we balanced each other out. I could follow your thought acrobatics and you could remain calm while I was fuming in trying times. We both made it though (without boron poisoning) and that's all that matters. Rebecca, I had the pleasure of welcoming you into our lab and it has been so nice having you with us. Thank you for all of the coffees and chats, *awkward head boop*. Jack, it's been so nice to watch you grow from an MChem to the place you are in now. But you may be the most accident-prone member of the Weller group to date. Dom, you're a man of few words and many facial expressions (especially after a couple of drinks). You've taken on the mantel of Team AB, and I hope it treats you well. Ian, all the best with SMOM, even if you picked the wrong side. To Ayman, thank you for always being a friendly face and always taking the time to chat and catch up. Lukas, I feel like we bonded at that first Dalton in Warwick and then nothing ever changed. Thank you for always being there to chat and for all of the support over the years. A shout out to the rest of the PhDs and MChems: Vyom, Samira, Jack, Rola, Matt, Orry, Anna, Natalia and Tom, it was lovely having you all as part of the groups and I wish you all the best. With a special shout out for Natalia for not only doing a summer project with me but then coming back to do her MChem, it has been a pleasure and I'm still dreaming about those Brazilian desserts.

I couldn't have done this without the unwavering support from my family and friends, all of the visits, phone calls and facetimes helped to keep my spirits up when things got tough. I am looking forward to celebrating this with each and every one of you. Mum and Dad, your never-ending love, encouragement and faith in me means more than you will ever know. Finally, Kris you have been my biggest supporter and have always believed in me. These three and a half years have been some of the happiest so far and a lot of that is down to you. I can't thank you enough for your love and support throughout this process and can honestly say it wouldn't have been the same without you.

Abbreviations

$\%V_{Bur}$	% buried volume of the ligand
$[BAr^F{}_4]$	Tetrakis[3,5-bis(trifluoromethyl)phenyl]borate
[^{i}Pr-VB]	tert-Butylimino-tri(pyrrolidino)phosphorane
Ad	Adamantyl
Ad-POCOP	1,3-bis[(di-adamantylphosphino)oxy]benzene
CTB	cyclotriborazane
D.P.	Degree of polymerisation
DMAB	$H_3B{\cdot}NHMe_2$
DSC	Differential Scanning Calorimetry
EDX	Energy Dispersive X-ray Spectroscopy
EELS	Electron Energy Loss Spectroscopy
ESI-MS	Electrospray Ionisation Mass Spectrometry
EXSY	Exchange Spectroscopy
GPC	Gel Permeation Chromatography
h-BN	Hexagonal boron nitride
ICP-OES	Inductively Coupled Plasma Optical Emission Spectroscopy
^{i}Pr-PN^{H}P	κ^3-$(CH_2CH_2P^iPr_2)_2NH$
^{i}Pr-POCOP	1,3-bis[(di-*iso*-propylphosphino)oxy]benzene
IR	Infrared
KIE	Kinetic Isotope Effect
MLC	Metal-ligand cooperative
MMAB	$H_3B{\cdot}NH_2Me$
M_n	Number average molecular weight
MS	Mass Spectrometry
M_w	Weight average molecular weight
NBD	Norbornadiene
NMR	Nuclear Magnetic Resonance
PNP	bis(triphenylphosphine)iminium
ppm	parts per million
ROSEY	Rotating-frame Overhauser Effect Spectroscopy

STEM	Scanning transmission electron microscopy
^{t}Bu-PCN	1-[3-[(di-*tert*-butylphosphino)methyl]phenyl]-1*H*-pyrazole
^{t}Bu-POCOP	1,3-bis[(di-*tert*-butylphosphino)oxy]benzene
TGA	Thermogravimetric Analysis
THF	Tetrahydrofuran
XPS	X-ray Photoelectron Spectroscopy

Key Complexes

Chapter 2:

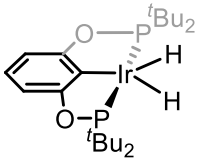

1

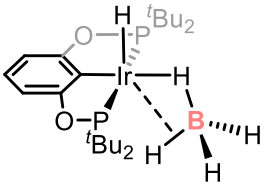

2

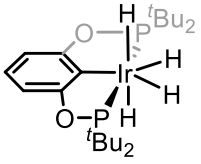

3

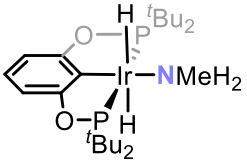

4

Chapter 3:

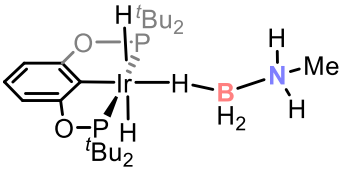

5

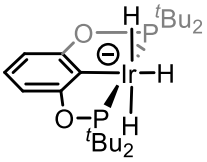

[6]$^-$

Chapter 5:

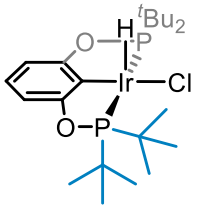

7

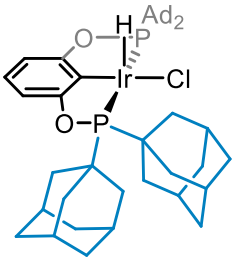

8

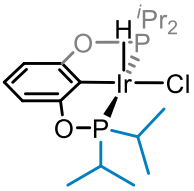

9

Table of Contents

Chapter 1: Introduction

1.1 Preamble

This doctoral thesis presents the research findings of a PhD project focussed on the dehydropolymerisation of amine-boranes using an iridium catalyst, Ir(^{t}Bu-POCOP)(H)$_2$ (^{t}Bu-POCOP = κ^3-2,6-(^{t}Bu$_2$PO)$_2$C$_6$H$_3$), to form mainchain B–N polymers 'polyaminoboranes'. After the speciation and kinetics (Chapter two) have been discussed, the mechanism (Chapter three), polymer properties (Chapter four), and other catalysts (Chapter five) will be explored. As such, this first introduction chapter will discuss the general background of amine-borane dehydropolymerisation, previous work that has been done using an iridium-based catalyst and the applications of polyaminoboranes.

1.2 Amine-boranes

Amine-boranes consist of a Lewis acid/Lewis base adduct, and the bonding in these compounds is dative where the amine donates a lone pair into the borane's vacant p-orbital (Figure 1.1) *e.g.* H$_3$B·NH$_2$Me. Amine-borane adducts have pseudo tetrahedral geometries about the B and N moieties with sp^3 hybridisation at both centres.[1, 2]

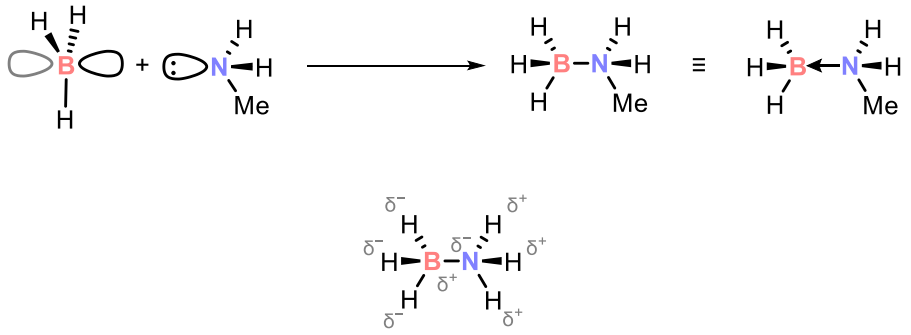

Figure 1.1. Description of bonding in an amine-borane adduct *e.g.* H$_3$B·NH$_2$Me.

The B–N bond in amine-boranes are known to undergo dissociation in solution *e.g.* THF.[3] This has been evidenced by amine exchange with an existing adduct that allows for the synthesis of new amine-boranes. This occurs as long as the new adduct forms a stronger bond, or if the freed amine is volatile and so formation of the new adduct is more favourable.[4, 5] While gas-

phase dissociation enthalpies show that addition of alkyl chains at the nitrogen centre results in a stronger dative bond due to increased electron density at nitrogen, alkyl substitution at the boron centre results in a decrease in stability.[3, 6] Haaland proposed this was not solely caused by strain from steric factors but due to a higher reorganisation energy for alkyl boranes compared with BH_3 to form diboranes.[6] Steric factors also play a role; experimental and computational findings show that increased steric bulk around the nitrogen or boron atoms results in a less stable adduct with respect to ammonia borane and therefore a weaker dative bond.[7, 8] This may lead to a higher degree of dissociation in the B–N bond.

Similarities can be drawn to the structure of alkanes, *i.e*. ethane, due to the isoelectronic relationship between B–N bonds and C–C bonds. The apparent change in electronegativity across the B–N unit (3.04 and 3.56 for boron and nitrogen, respectively)[9] is thought to cause a partial positive charge at boron and a partial negative charge at nitrogen.[6, 10] This leads to the hydrogen atoms in the B–H unit to be hydridic (δ^-) in nature and the N–H to be protic (δ^+), see Figure 1.1. This relationship causes a change in the properties when compared to the organic analogue due to the dipole caused by the B—N atoms, the protic (N—H) and hydridic (B—H) protons, and the potential for non-classical hydrogen bonds to form.[1, 11] For example, ammonia borane is a solid at room temperature while ethane is a gas at room temperature.[3]

Single B–N bonds are weaker than C–C bonds. When considered in their simplest forms ammonia borane ($H_3B{\cdot}NH_3$) and ethane, the measured dissociation enthalpy for the dative bond in ammonia borane at 25 °C is 27.2 kcal mol^{-1}.[12] Under the same conditions the covalent bond in ethane has a dissociation enthalpy of 90.1 kcal mol^{-1}.[12]

Inter/intramolecular interactions between molecules occur *via* ‘dihydrogen’ bonding between N–H···H–B.[1] These interactions facilitate H_2 loss across the B−N unit,[1] making the dehydrogenation of amine-boranes more favourable than for alkanes.

1.2.1 Uses of amine-boranes

Amine-boranes have found many uses in organic transformations *e.g.* hydroboration and reduction reactions (Figure 1.2).[13] Other examples in the literature include use of amine-boranes in borylation, transfer hydrogenation and B–H insertion reactions.[14-16] Amine-boranes provide an alternative borane reagent that is air stable and easy to handle.

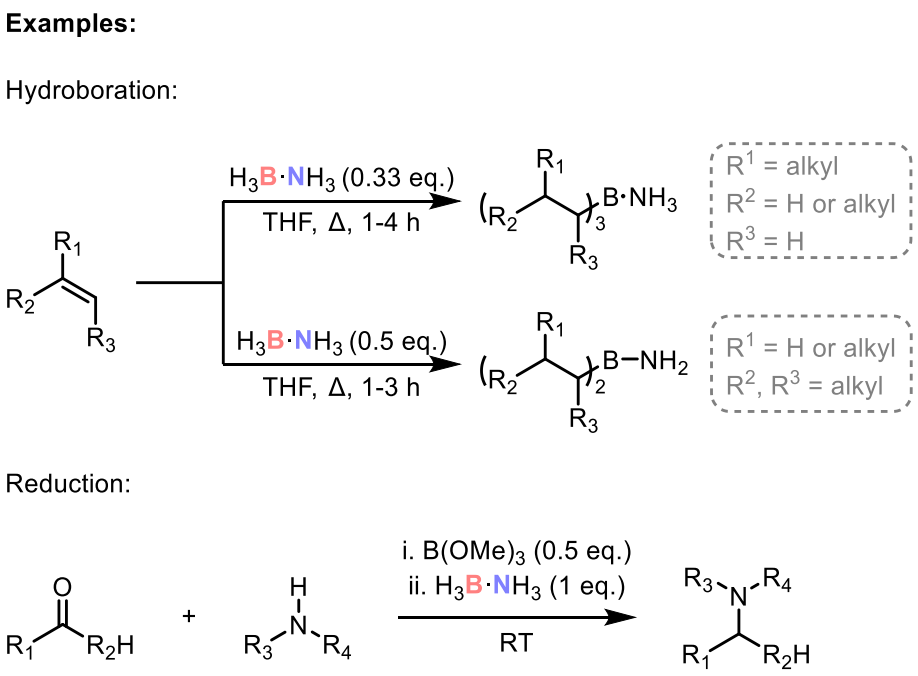

Figure 1.2. Examples of the use of ammonia borane in hydroboration and reduction reactions.[17, 18]

Interest in ammonia borane as a hydrogen storage material transpired in the early 2000s due to its relative stability and high hydrogen content (19.7 wt%).[19] However, to benefit from using this material 3 equivalents of hydrogen need to be released and there are currently no catalytic processes that allow the release of three equivalents of hydrogen from ammonia borane to form boron nitride.[20] The regeneration of the spent fuel still remains a challenge, as it lies thermodynamically uphill.[20] This means that it would be a single use hydrogen storage material as the loss of hydrogen is not reversible.

Currently amine-boranes remain an area of interest in the formation of inorganic polymers (polyaminoboranes). Polyaminoboranes are potential polymeric precursors to BN-based

ceramics such as hexagonal boron nitride.[19, 21] Hexagonal boron nitride (*h*-BN) is of interest as it has low electrical conductivity, excellent heat conductivity, superhydrophobicity and has many applications in lubricants, medical imaging and electronics.[22, 23]

1.3 Methods for the dehydropolymerisation of amine-boranes

1.3.1 Overview

Dehydrogenation of amine-boranes *e.g.* $H_3B{\cdot}NH_2Me$ may result in the formation of multiple dehydrocoupled products (Figure 1.3 A). Commonly observed products are polyaminoboranes $-(H_2B{\cdot}NHMe)_n-$, cyclotriborazane CTB $(H_2BNMeH)_3$, and borazine $(HBNMe)_3$. These are inorganic analogues of common organic molecules, Figure 1.3 B.[24] The products produced in these reactions can normally be rationalised in terms of the amount of hydrogen produced. For example, formation of polyaminoborane results in one equivalent of H_2 being released, borazine results in two equivalents released and more than two equivalents of H_2 released would indicate formation of polyborazylene (Figure 1.3 B).

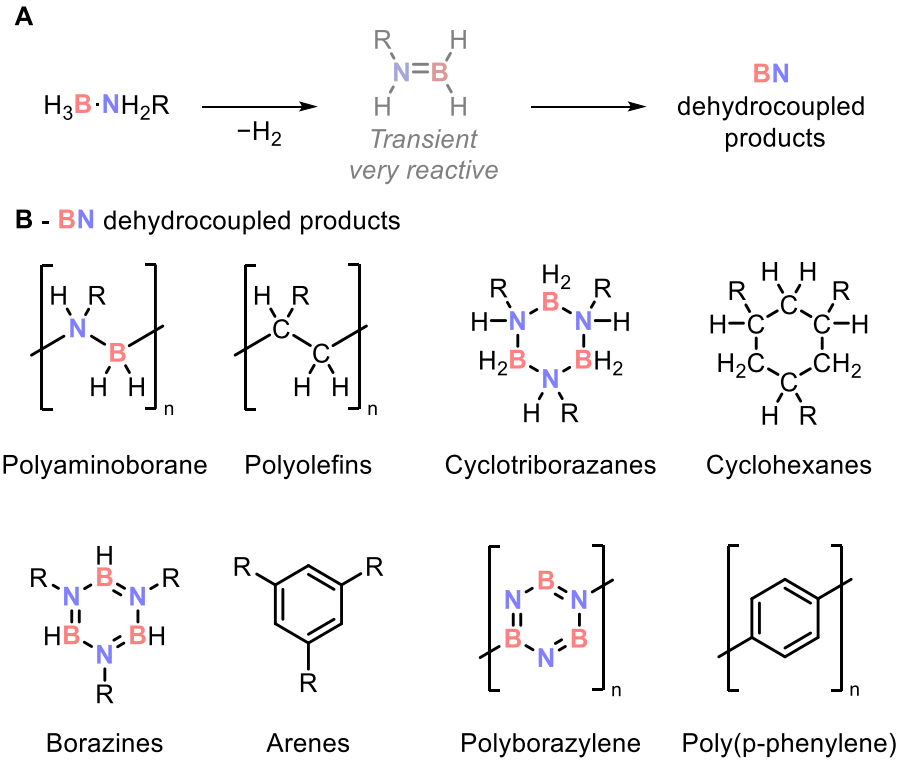

Figure 1.3. A) Dehydrogenation of amine-borane to form dehydrocoupled products. B) Examples of BN dehydrocoupled products and their organic analogues.[24]

Polymers with B−N units in their backbone have been of interest since the 1980s as a potential preceramic material to hexagon boron nitride (*h*-BN), that can be easily shaped.[3, 25, 26] This will be discussed in more detail in Section 1.7. Use of transition metal catalysts is one way that selectivity for a single product has been increased *i.e.* polyaminoboranes.[27, 28] Transition-metal-free synthetic routes will be discussed in section 1.3.3.

The challenge in the dehydropolymerisation of amine-boranes is to establish control over the two reaction processes that are intricately linked together, in a cascade-like polymerisation.[29] The first step of the reaction is the dehydrogenation of the pre-monomer amine-borane to form the short-lived, reactive amino-borane monomer by the transition metal catalyst, Figure 1.4. This is followed by the polymerisation reaction of the amino-borane units, which is thought to initiate at a transition mental centre or from an amine initiator.[30, 31] This control has yet to be achieved. This thesis will focus on the dehydropolymerisation of $H_3B{\cdot}NH_2Me$ using Ir(^{t}Bu-POCOP)$(H)_2$ (**1**), ^{t}Bu-POCOP = κ^3-2,6-(^{t}Bu$_2$PO)$_2$C$_6$H$_3$. It will aim to provide a detailed kinetics, speciation, and mechanistic study, that allows a thorough understanding of catalysis and rationalisation of the reaction behaviour and mechanism. This will ultimately lead to a fine control over the polyaminoborane, allowing for their use in the production of 1- and 2-D BN materials.

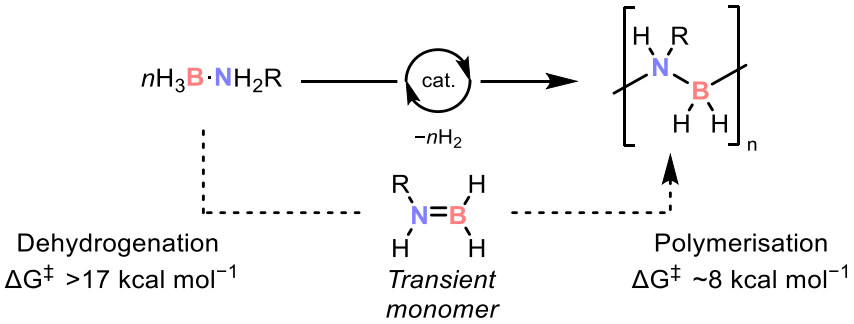

Figure 1.4. Dehydropolymerisation of amine-boranes. The values of $\Delta G^{\ddagger}$ for the dehydrogenation mechanism and polymerisation mechanism were reported for catalyst Ir(^{t}Bu-POCOP)$(H)_2$ in the literature.[30, 32]

1.3.2 General mechanisms for polymerisation

There are three overarching polymerisation mechanisms that are dependent on the polymer molecular weight over time. The three mechanisms; chain-growth, living and step-growth are shown graphically as a plot of molecular weight over time in Figure 1.5.

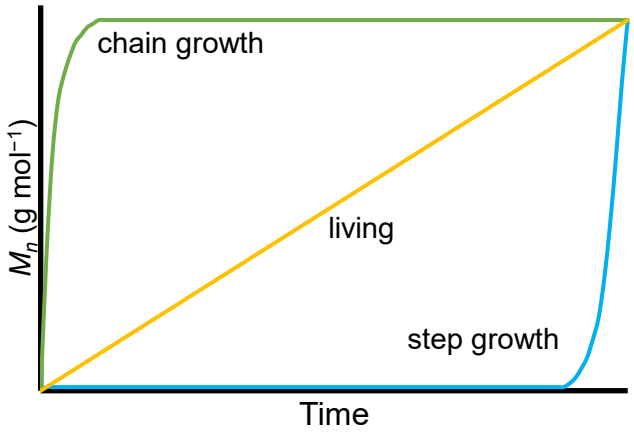

Figure 1.5. Types of polymerisation mechanism; chain growth, linear and step growth.

Chain-growth polymerisations take place from a reactive site or initiator; the monomer adds to a reactive end group of the growing chain or by a coordination-insertion mechanism at the metal (*e.g.* ethene polymerisation).[33] Chain growth polymerisations result in larger molecular weights at shorter reaction times that then remains constant throughout the reaction.[33] The monomer is also consumed slowly over time, and there is a termination step or chain transfer step that limits the molecular weight of the polymer formed. Examples of chain-growth polymerisations include polyethylene and polypropylene.[33] With step-growth polymerisation mechanisms the monomer is consumed quickly at the start of the reaction and the increase in molecular weight occurs slowly over time. Reactions occur between monomers, oligomers and polymers to grow the polymer chains resulting in larger molecular weight at longer reaction times.[33] Some examples include the formation of polyphosphinoboranes,[34, 35] polyesters and polyamides.[33] Living polymerisations are essentially chain-growth polymerisations where there is no termination event or chain transfer event, resulting in the molecular weight increasing over the course of the reaction, *e.g.* ring-opening metathesis polymerisation

(ROMP).[36] Living polymerisations mechanisms have been linked to controlled polymer formation, resulting in control over molecular weight and low polydispersities.[37] This fine control makes living polymerisations desirable.

1.3.3 Transition metal free routes to polyaminoboranes

Routes to polyaminoboranes without the use of transition metal catalysts are relatively underdeveloped. There have been reports of thermally induced dehydrocoupling of amine-boranes *i.e* $H_3B{\cdot}NH_3$ or $H_3B{\cdot}NH_2Me$, that result in mixtures of ill-defined BN products, including polyaminoborane.[19] Previously, there have been several reports of polymeric BN based material formed from different reaction conditions; the pyrolysis of ammonia-borane, reaction of diborane and lithium amide, and reaction of diborane with $K[Me_2N{\cdot}BH_3]$ in OEt_2.[38-40] However, little to no characterisation of the polymeric materials was reported.

Main-group catalysts and frustrated Lewis pair catalysts have been shown to dehydrocouple various amine-borane substrates, but their ability to form polyaminoborane is limited, with some able to form dimers $[R_2N{\cdot}BH_2]_2$ where R = Me or H,[41-43] while others report the formation of oligomers.[44, 45] There is no correlation between type of catalyst and formation of dimer or oligomer.

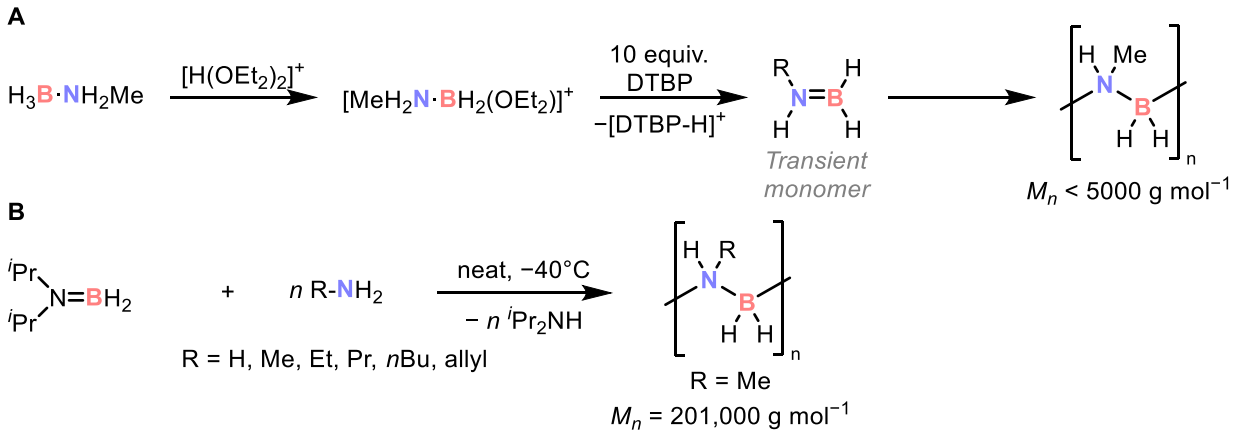

Scheme 1.1. Two examples of transition-metal-free synthesis of polyaminoborane, a) salt formation, b) amine exchange. $[(BC_6F_5)_4]^-$ removed from a) for clarity.

There are two examples in the literature of transition-metal-free catalysis routes to polyaminoboranes, Scheme 1.1. Manners and coworkers describe a route that forms a

reactive amino-borane monomer that readily polymerises by reaction of amine-borane ($H_3B{\cdot}NH_2Me$) with a Brønsted acid ($[H(OEt_2)_2][B(C_6F_5)_4]$) to form the amine-boronium cation salt.[46] Addition of 10 equivalents of 2,6-di-*tert*-butylpyridine (DTBP) to the amine-boronium cation at 25 °C in diethyl ether resulted in formation of polyaminoborane in <1 minute, Scheme 1.1a. Characterisation of the product was carried out by ^{11}B NMR spectroscopy. Gel Permeation Chromatography (GPC) did not yield peaks for polymer M_n > 5,000 g mol^{-1}, indicating polymer of low molecular weight was formed.

A stochiometric route to polyaminoboranes was put forth by Alcaraz, Scheme 1.1b.[47] Reaction of diisopropylaminoborane with various primary amines NH_2R (R = H, Me, Et, Pr, Bu, allyl) at −40 °C resulted in the formation of amino-boranes which produced polyaminoborane in all cases. The materials were characterised thoroughly and M_w varied from 170,000-5,450,000 g mol^{-1} with polydispersities ranging between 1.2-10.2. Reactions carried out at room temperature resulted in various BN products; this indicated that aminoborane was formed but does not selectively polymerise to form polyaminoboranes.

1.3.4 Transition metal catalysts

There have been many catalysts developed for the dehydropolymerisation of amine-boranes, see examples in Figure 1.6. While some early transition metal complexes are known to be active in catalysis,[48, 49] it is much more common to find examples for late transition metals, *e.g.* Rh, Ir, Ru, Fe. Some examples of the late transition metal catalysts will be discussed in more detail in this section. The catalyst is required to control two processes, starting with the dehydrogenation of pre-monomer amine-borane to form the reactive, and short-lived monomer aminoborane. The metal catalyst then plays a role in the selectivity of the dehydrocoupled products formed, with many examples of selective polyaminoborane formation.[50-59] The metal-catalysed dehydrogenation step tends to have calculated barriers of $\Delta G^{\ddagger}$ >17 kcal mol^{-1}.[32, 51] The reactive aminoborane monomer will readily polymerise with a calculated barrier of $\Delta G^{\ddagger}$ ~ 8 kcal mol^{-1}.[30] In this thesis the two processes will be discussed

separately, with a particular focus on the dehydrogenation reaction as this is the rate-limiting factor.

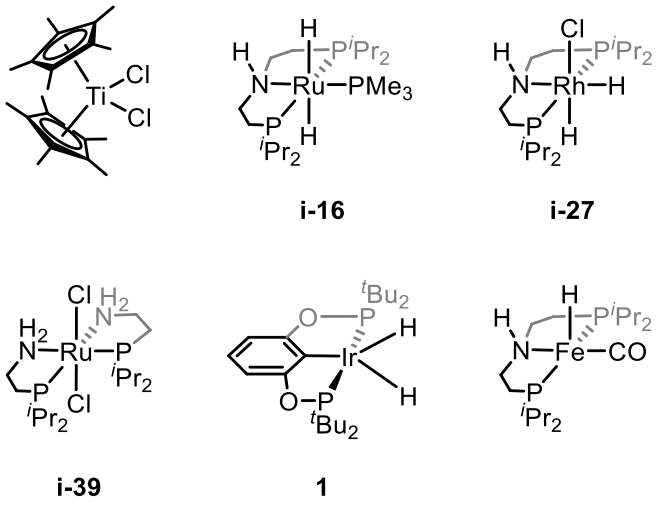

Figure 1.6. Examples of transition metal catalysts for the dehydropolymerisation of amine-boranes.[48, 51, 54-57, 59, 60]

Typically, catalysts contain or have the ability to form metal–hydride (M–H) bonds. This is important as a key feature of the dehydrogenation of amine-boranes is B–H or N–H activation. There are three suggested mechanism types for transition metal catalysed dehydropolymerisation and examples of these will be discussed in the subsequent sections.

1.3.5 Inner-sphere mechanism

Inner-sphere mechanisms in amine-borane dehydropolymerisation are generally characterised by B–H and N–H activation from an intermediate σ-amine-borane complex,[61, 62] Scheme 1.2. This can occur in either order, though it is more common for N–H activation to be the turnover limiting step.[27] Some examples will be discussed in this section.

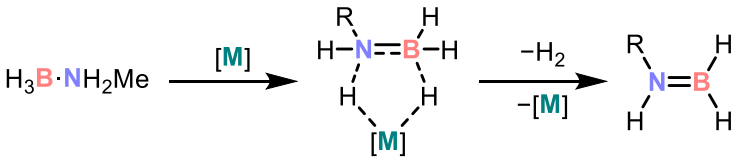

Scheme 1.2. General scheme illustrating an inner-sphere mechanism.

An example of inner-sphere coordination comes from the group of Weller, reporting an experimental and computational investigation into the formation of oligomers from $H_3B{\cdot}NH_3$ with an iridium catalyst $[Ir(PCy_3)_2(H)_2(H_2)_2][BAr^F{}_4]$ (Scheme 1.3), $[BAr^F{}_4]^-$ refers to tetrakis[3,5-bis(trifluoromethyl)phenyl]borate.[63, 64] The first step is loss of H_2 and coordination of an amine-borane unit to form $[Ir(PCy_3)_2(H)_2$ (η^2-$H_3B{\cdot}NH_3$)][$BAr^F{}_4$] (**i-1**).[63]

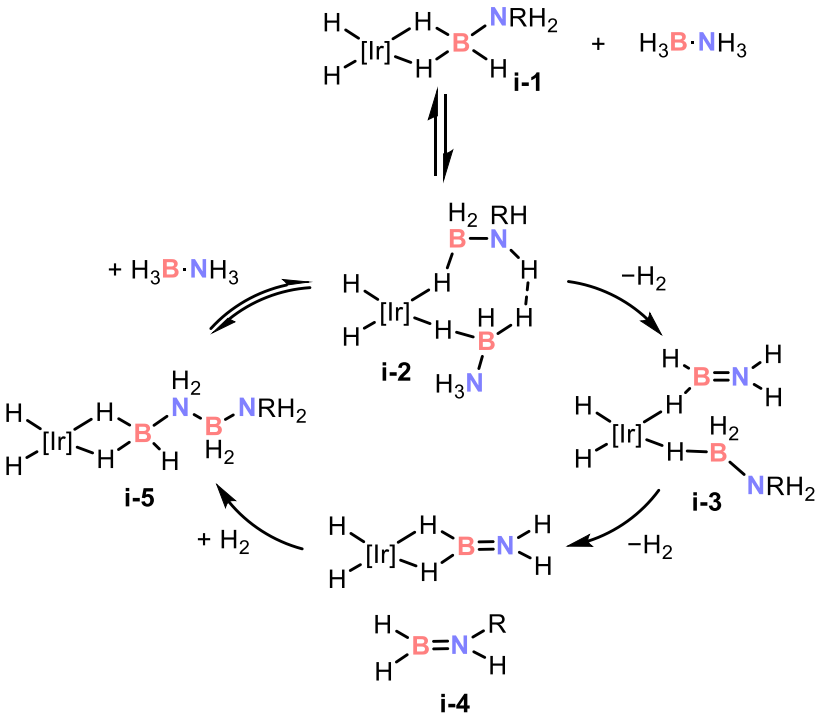

Scheme 1.3. Proposed inner-sphere mechanism for the dehydrogenation of ammonia borane with $[Ir(PCy_3)_2(H)_2$ (η^2-$H_3B{\cdot}NH_3$)][$BAr^F{}_4$].[63, 64] [Ir] = $[Ir(PCy_3)_2]^+$.[63, 64]

The proposed mechanism can be defined by sequential B–H activation, H_2 loss and rate-limiting N–H activation, Scheme 1.3. This study highlights the promoting effect additional amine-boranes units can have on the dehydrogenation reaction (**i-1**). With an additional amine-borane unit present the dehydrogenation barrier calculated by DFT is ~25 kcal mol^{-1}, while absence of this additional pre-monomer unit results in barriers >33 kcal mol^{-1}. This trend is consistent with both substrates ($H_3B{\cdot}NH_3$ and $H_3B{\cdot}NH_2Me$). However, use of $H_3B{\cdot}NH_2Me$ as a substrate resulted in a single oligomerisation event which is thought to be due to steric

effects as the terminal NH_2Me is distant from the metal centre and so less likely to lose H_2 (**i-5**).[63]

Shubina and co-workers reported an unsymmetrical iridium pincer complex Ir(^{t}Bu-PCN)HCl (^{t}Bu-PCN = 1-[3-[(di-*tert*-butylphosphino)methyl]phenyl]-1*H*-pyrazole) for amine-borane dehydrogenation focussing on ammonia borane and DMAB ($H_3B{\cdot}NHMe_2$), Scheme 1.4.[65] Studies were also carried out with deuterated analogues of ammonia borane. The isotopic substitution resulted in a kinetic isotope effect (KIE) for both B–D (1.6) and N–D (2.9) substitution. This indicated that both B–H and N–H activation was involved in or prior to, the rate determining step.

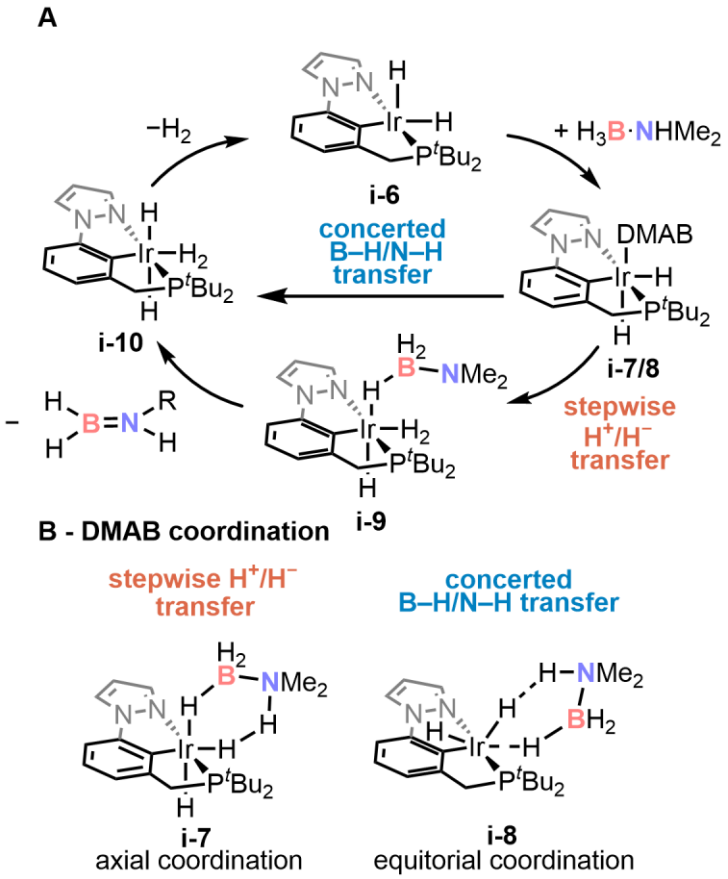

Scheme 1.4. A) The two inner-sphere mechanisms suggested for the dehydrogenation of $H_3B{\cdot}NHMe_2$ by Ir(^{t}Bu-PCN)HCl.[65] B) DMAB coordination.

The authors propose two catalytic cycles assisted by DFT calculations. Both cycles include the coordination of $H_3B{\cdot}NHMe_2$ to the catalyst, resulting in two isomers with different

dehydrogenation pathways (Scheme 1.4 A). The concerted B–H/N–H transfer mechanism results in equatorial $H_3B{\cdot}NHMe_2$ coordination (**i-8**) followed by concerted B–H/N–H transfer. The other pathway continues *via* an axial $H_3B{\cdot}NHMe_2$ coordination (**i-7**) followed by stepwise proton and hydride transfer (Scheme 1.4B). Stochiometric reactions of Ir(^{t}Bu-PCN)HCl with $H_3B{\cdot}NHMe_2$ in toluene were studied by variable-temperature IR spectroscopy. The appearance of new B–H bands in the IR spectrum were attributed to the stretching vibrations of the terminal and bridging B–H environments.[65] This suggests that co-ordination of the amine-borane to the metal centre *via* the B–H group is preferential.

More recently, Weller and co-workers reported the use of a cationic iridium catalyst with the ^{i}Pr-PN^{H}P ligand [^{i}Pr-PN^{H}P = κ^3-($CH_2CH_2P^iPr_2)_2NH$], this ligand will be discussed for other group 8 and group 9 metals in Section 1.3.6.[53]

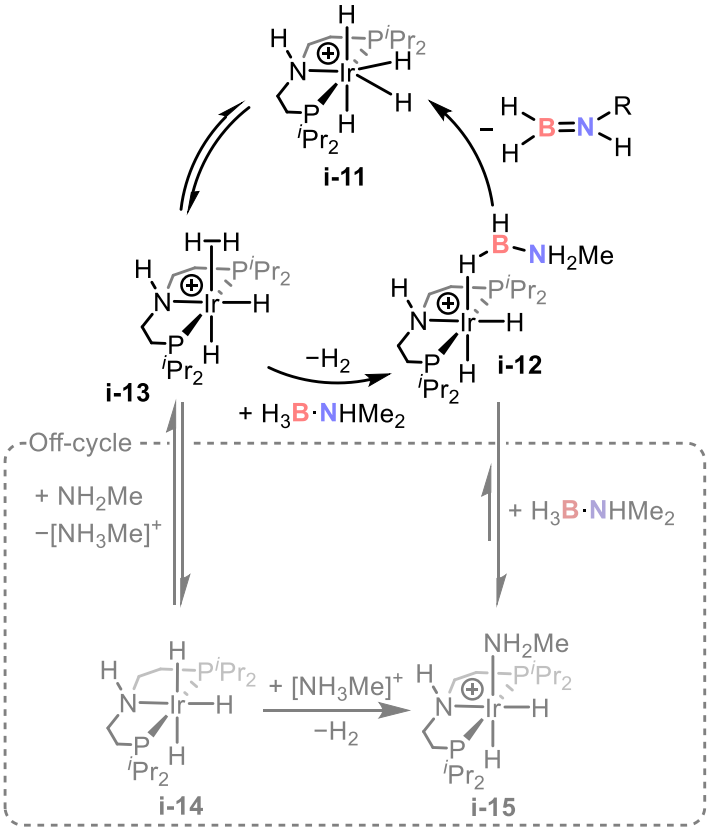

Scheme 1.5. Inner sphere mechanism for the dehydrogenation of $H_3B{\cdot}NH_2Me$ with [Ir(^{i}Pr-PN^{H}P)(H)$_2$($H_3B{\cdot}NH_2Me$)]$^+$.[53]

Neutral forms of the catalyst *i.e. cis*-Ir(^{i}Pr-PN^{H}P)H_2Cl and Ir(^{i}Pr-PN^{H}P)H_3 performed poorly as dehydrogenation catalysts, resulting in little to no activity. Cationic forms of the catalyst yielded more promising results. Use of pre-catalyst [Ir(^{i}Pr-PN^{H}P)$(H)_2(H_3B{\cdot}NMe_3)$][BAr$^{F}_4$] resulted in full dehydrogenation of $H_3B{\cdot}NH_2Me$ to selectively form polyaminoborane. Conditions of 1 mol% catalyst in 1,2-$F_2C_6H_4$ at 293 K yielded a reaction time of 6 hours, k_{obs} = 6.4(8) × 10^{-4} M s^{-1}, and polyaminoborane was formed (M_n = 39,900 g mol^{-1} Đ = 1.6). Under the same reaction conditions but with THF as a solvent, the initial rate was lower k_{obs} = 1(1) × 10^{-4} M s^{-1}, and the reaction did not go to completion. Analysis by NMR spectroscopy showed formation of inactive **i-14**. DFT calculations demonstrated that the neutral catalyst has a higher barrier than the cationic catalyst, 24.3 kcal mol^{-1} and 22.5 kcal mol^{-1}, respectively (level of theory: BP86[D3BJ,CH2Cl2]/Def2TZVP//BP86/ SDD (Ir, P, with polarization on P); 6-31G** on all other atoms).[53] Interestingly, addition of $[NH_3Me]^+$ to neutral **i-14** results in productive catalytic turnover, forming cationic **i-15** and allowing access to the cationic catalytic cycle.

In the proposed mechanism [Ir(^{i}Pr-PN^{H}P)$(H)_2(H_3B{\cdot}NMe_3)$][BAr$^{F}_4$] undergoes a substitution with $H_3B{\cdot}NH_2Me$ to form an on-cycle species, [Ir(^{i}Pr-PN^{H}P)$(H)_2(H_3B{\cdot}NH_2Me)$][BAr$^{F}_4$] (Scheme 1.5, **i-12**). Concerted B–H/N–H activation leads to formation of a tetrahydride species [Ir(^{i}Pr-PN^{H}P)$(H)_4$][BAr$^{F}_4$] (**i-11**). Interactions of an additional $H_3B{\cdot}NH_2Me$ molecule with the NH of the pincer ligand formed an outer-sphere adduct during the dehydrogenation reaction, which was observed by shifted hydride signals in the ^{1}H NMR spectrum. This was also supported by DFT calculations that found the formation of this adduct to significantly reduce the calculated barrier. This is another example of excess $H_3B{\cdot}NH_2Me$ having a promoting effect on catalysis.

Hydrogen loss and $H_3B{\cdot}NH_2Me$ coordination complete the catalytic cycle. NH_2Me was found to have an inhibitory effect on catalysis, thought to be due to the formation of the neutral trihydride species (Ir(^{i}Pr-PN^{H}P)H_3, **i-14**) by deprotonation of [Ir(^{i}Pr-PN^{H}P)$(H)_2(H_2)$][BAr$^{F}_4$] **i-13**. **i-14** was independently shown to be a poor dehydrogenation catalyst. The resting state of this catalytic cycle was found to be the cationic amine complex [Ir(^{i}Pr-PN^{H}P)$(H)_2(NH_2Me)$][BAr$^{F}_4$],

i-15 that forms *via* a proton-rebound process. Mechanisms involving proton-rebound processes will be discussed in more detail in a later section.

Evidence for this catalyst undergoing an inner-sphere mechanism came by the synthesis of [Ir(^{i}Pr-PN^{Me}P)(H)$_2$(H$_3$B·NH$_2$Me)][BAr$^F_4$]. The complex was a competent catalyst for the dehydrogenation of amine-borane with comparable initial rates to [Ir(^{i}Pr-PN^{H}P)(H)$_2$(H$_3$B·NH$_2$Me)][BAr$^F_4$], k_{obs} = 14(2) × 10^{-4} M s^{-1} and 6.4(8) × 10^{-4} M s^{-1}, respectively.[53] It is interesting to note that other examples of amine-borane dehydropolymerisation catalysts that use this ligand motif but with different metals are all thought to proceed *via* metal-ligand cooperative processes. This type of mechanism will be discussed in the next section.

1.3.6 Metal-Ligand Cooperative (MLC) processes

Metal-Ligand Cooperative (MLC) processes are defined by both the metal and the ligand being involved in the bond-breaking or bond-making process. Scheme 1.6 illustrates this in terms of amine-borane dehydropolymerisation.

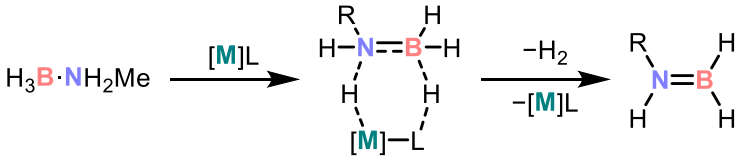

Scheme 1.6. General scheme illustrating a metal-ligand cooperative (MLC) process.

A common motif in MLC catalysts is the [M]–N bond that can undergo reversible protonation, with extensive research carried out for hydrogenation and dehydrogenation reactions.[66, 67] Outer-sphere mechanisms are common for this type of catalyst as the substrate is well suited to N–H activation at the metal centre and interactions between the B–H of the amine-borane and the acidic N–H of the ligand (Scheme 1.6).

There are multiple examples of MLC processes in amine-borane dehydropolymerisation chemistry. The four examples shown in Figure 1.7 all feature the same pincer ligand, ^{i}Pr-PN^{H}P that was discussed for an example of an inner-sphere mechanism in Section 1.3.5.

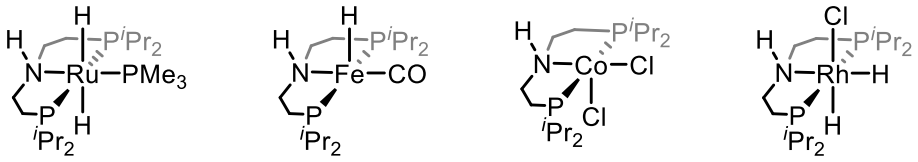

i-16 **i-22** **i-27**

Figure 1.7. Examples of catalysts that undergo metal-ligand cooperation with ^{i}Pr-PN^{H}P ligand.[51, 56, 57, 68]

In 2009, Schneider and co-workers used the Ru complex Ru(^{i}Pr-PN^{H}P)(H)$_2$(PMe$_3$) (**i-16**) to dehydropolymerise amine-boranes *i.e.* H$_3$B·NH$_3$ and H$_3$B·NH$_2$Me, with a further contribution in 2013.[57, 58] They found **i-16** to be capable of dehydrogenating the pre-monomer amine-borane and forming polyaminoborane selectively with little by-product formation. Initially, to ensure that catalysis was operating *via* an MLC process, the N–H was substituted for N–Me, blocking the coordination site of the amine. This resulted in a slowed but full dehydrogenation of the substrate. The authors propose this is due to an alternate inner-sphere mechanism that may operate when the N–H site is blocked, however this mechanism proceeds with a higher overall barrier compared with **i-16** where the N–H site is not blocked.

In order to substantiate these claims, stochiometric experiments were carried out with H$_3$N·BEt$_3$ and **i-16**. This resulted in formation of a new complex identified as an amido borane complex (**i-18**) by NMR spectroscopy. Formation of this was attributed to an exchange mechanism from a transient dihydrogen complex (Scheme 1.7). Reaction with Me$_3$N·BH$_3$ resulted in no change by NMR spectroscopy. This highlights a potential coordination mode of amine-boranes for this catalyst (**i-17**).

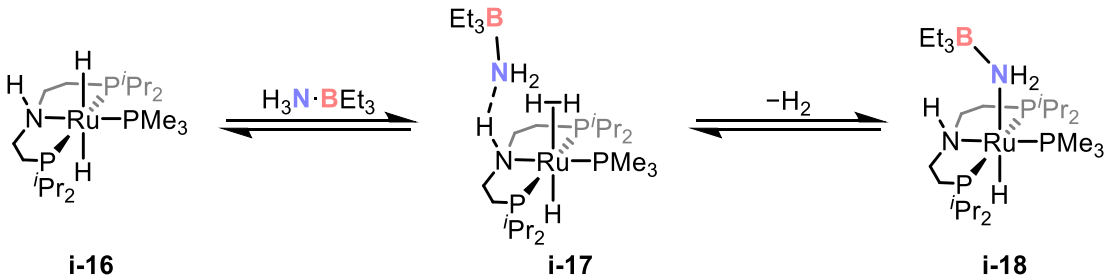

i-16 **i-17** **i-18**

Scheme 1.7. Reaction of Ru(^{i}Pr-PN^{H}P)(H)$_2$(PMe$_3$) and H$_3$N·BEt$_3$ showing likely initial coordination mode.

This binding mode was echoed in the proposed mechanism for the dehydrogenation of $H_3B{\cdot}NH_3$. Amine-borane binds reversibly to the catalyst, leading to a proton exchange to form an amine-borane bound di-hydrogen complex (**i-20**), (Scheme 1.8). H_2 is lost and B–H activation occurs at the metal centre (**i-21**), followed by the loss of aminoborane and reformation of the catalyst, Scheme 1.8 (**i-19**). This is an example where N–H activation is thought to be the initial step in the coordination of the monomer. This is different from all of the examples of inner-sphere mechanisms discussed in Section 1.3.5.

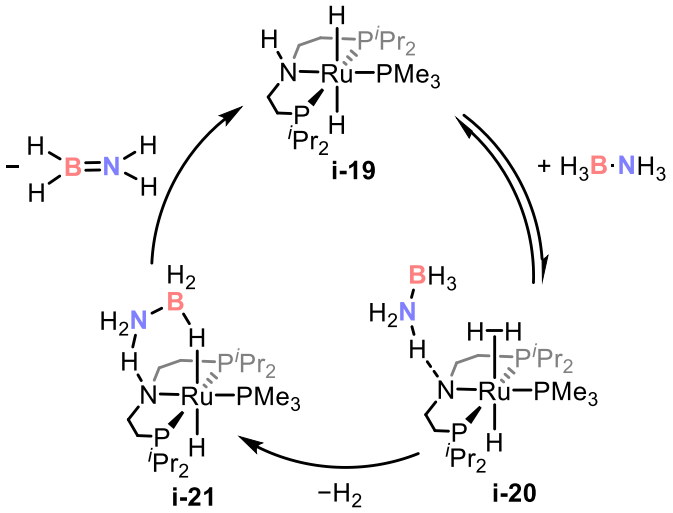

Scheme 1.8. Proposed mechanism for the dehydrogenation of $H_3B{\cdot}NH_3$ with Ru(^{i}Pr-PN^{H}P)(H)$_2$(PMe$_3$).[57]

Schneider and co-workers reported an iron catalyst with the same ligand structure, Fe(^{i}Pr-PN^{H}P)(H)$_2$(CO).[56] No induction period was observed and one equivalent of H_2 was released. Formation of polyaminoborane was reported along with small amounts of by-products observed in the ^{11}B NMR spectrum (borazine, polyborazylene, cyclotriborazane (CTB), *etc.*).

DFT calculations on the Fe system supported an MLC mechanism as some of the computed intermediates were stabilized by hydride interactions with the N–H of the pincer ligand. In this contribution the authors propose a similar, simplified version of the mechanism in shown in Scheme 1.8.[56] Binding of $H_3B{\cdot}NH_3$ and loss of H_2 occurs in one step from Fe(^{i}Pr-PN^{H}P)(H)$_2$(CO). This leads to formation of an aminoborane-bound iron complex.

Aminoborane is released which can then go on to polymerise. This is similar to the mechanism presented for the ruthenium catalyst in Scheme 1.8, if the binding of amine-borane was not reversible hence facilitating the cascade of substrate binding and H_2 loss.

Use of the PNP ligand with cobalt resulted in some differences in reactivity, when Co(^{i}Pr-PN^{H}P)(Cl)$_2$ (**i-22**) was investigated for the dehydrogenation of $H_3B{\cdot}NH_2Me$.[68] Initially, when tested in catalysis there was no H_2 evolution and no monomer consumption. Addition of two equivalents NH_2Me resulted in full conversion to polyaminoborane (M_n = 47600 g mol^{-1}, Đ = 1.5) along with one equivalent of hydrogen being produced.

The authors propose that the catalyst proceeds *via* a mechanism similar to that reported for Ru(^{i}Pr-PN^{H}P)(H)$_2$(PMe$_3$) and Fe(^{i}Pr-PN^{H}P)(H)(CO) (Scheme 1.9). The catalyst (**i-22**) is activated by NH_2Me and $H_3B{\cdot}NH_2Me$ to form Co(^{i}Pr-PN^{H}P)(H)(Cl) – **i-23**. After which an alternate pathway was discussed in which catalysis operates *via* a Co(I)/Co(III) inner-sphere dehydrogenation pathway, after abstraction of a hydride to form the square planar Co(I) complex (Scheme 1.9, **i-25**). Dehydrogenation of $H_3B{\cdot}NH_2Me$ results in the formation of an octahedral Co(II) complex (**i-26**). Comparable to previous reports, substitution of the N–H of the pincer ligand with N–Me resulted in no reaction supporting that this catalyst operates *via* an MLC process.[68]

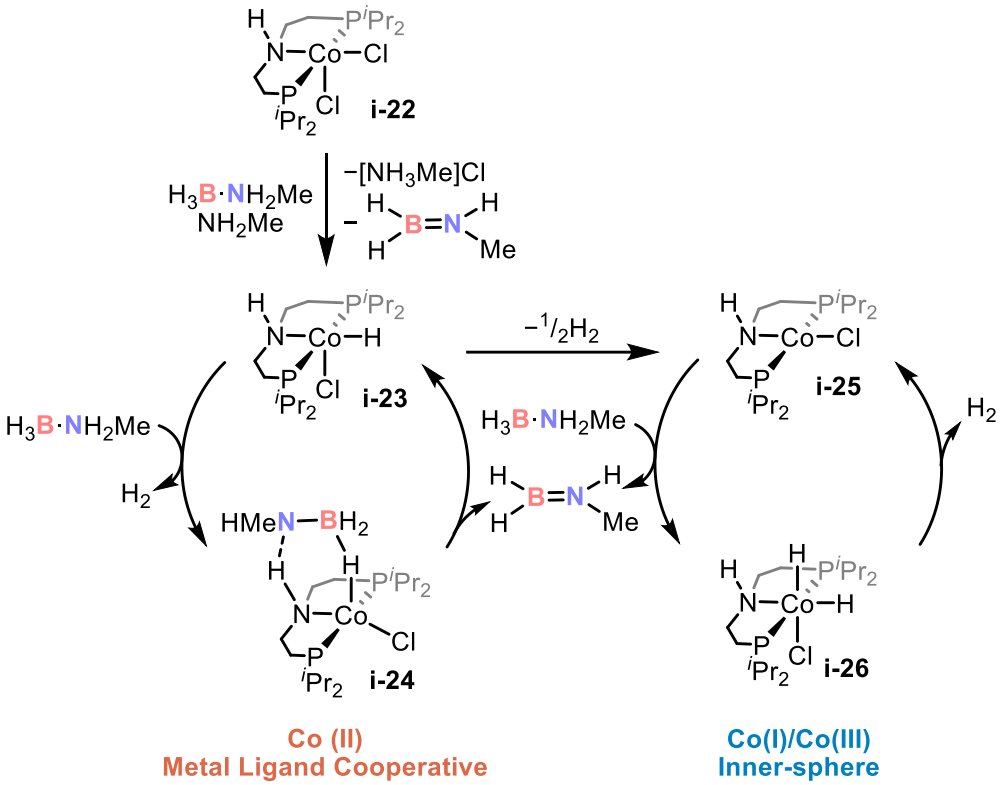

Scheme 1.9. Two potential mechanism for the dehydrogenation of $H_3B{\cdot}NH_2Me$ with Co(^{i}Pr-PN^{H}P)(Cl)$_2$.[68]

Weller and coworkers went on to report another system with this ligand motif, pre-catalyst [Rh(^{i}Pr-PN^{H}P)(NBD)]Cl.[51] Reaction with $H_3B{\cdot}NH_2Me$ resulted in an induction period followed by a pseudo zero-order regime and observation of Rh(^{i}Pr-PN^{H}P)(H)$_2$(Cl) (**i-27**) as the sole species on catalysis completion by various NMR spectroscopies. Synthesis and use of **i-27** in catalysis resulted in no observable induction period. Use of both catalysts resulted in the selective formation of polyaminoborane in all cases (M_n ~ 70,000, Đ = 1.6).

Investigation of the speciation during catalysis resulted in observation of Rh(^{i}Pr-PN^{H}P)(H)$_3$ (**i-28**) by NMR spectroscopy. The hydride shifts of this complex were observed to change marginally throughout catalysis which was attributed to formation of a H···H dihydrogen bound $H_3B{\cdot}NH_2Me$ adduct, Rh(^{i}Pr-PN^{H}P)($H_3B{\cdot}NH_2Me$)(H)$_3$ – **i-29** as the resting state. The authors supported this observation with DFT calculations which confirmed the adduct was thermodynamically favoured. Similar connectivity was observed by the authors for an iridium system discussed in Section 1.3.5.

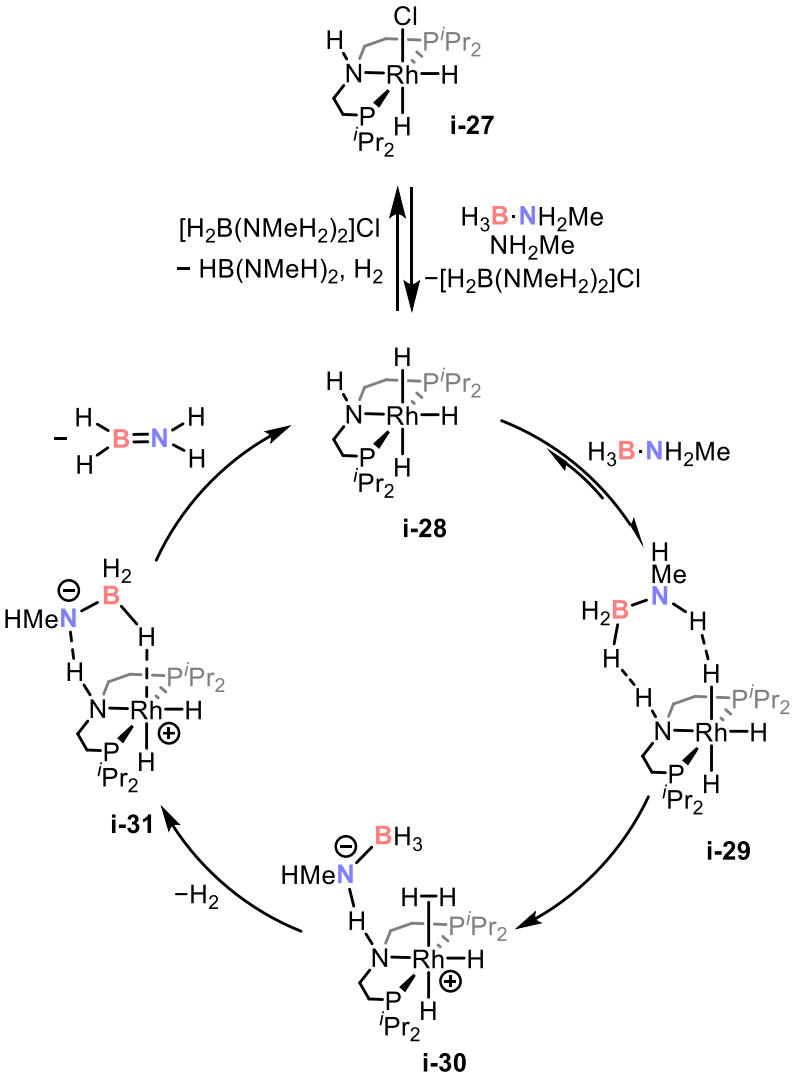

Scheme 1.10. Proposed mechanism for the dehydrogenation of $H_3B{\cdot}NH_2Me$ with [Rh(*i*Pr-PN^{H}P)$(H)_2$(Cl)].[51]

Building on the work of Schneider with the group 8 catalysts,[56, 58] Weller and co-workers proposed the mechanism in Scheme 1.10.[51] Rh(*i*Pr-PN^{H}P)$(H)_3$ (**i-28**) was formed through reaction of Rh(*i*Pr-PN^{H}P)$(H)_2$(Cl) (**i-27**) with $H_3B{\cdot}NH_2Me$ and NH_2Me. There is reversible outer-sphere binding of $H_3B{\cdot}NH_2Me$ to form the amine-borane bound adduct Rh(*i*Pr-PN^{H}P)$(H_3B{\cdot}NH_2Me)(H)_3$ (**i-29**). Proton transfer from N–H to Rh–H to form the cationic rhodium dihydrogen amidoborane complex (**i-30**) was followed by H_2 loss to form **i-31**. Loss of aminoborane reforms the proposed active catalyst (**i-28**). This mechanism was supported by DFT calculations, level of theory: BP86[D3BJ,THF]/Def2TZVP//BP86/SDD (Rh, P, with polarization on P); 6-31G** on other atoms.

The turnover-determining step was calculated to be the loss of H_2 with a barrier of 19 kcal mol^{-1}, this was consistent with a close to zero experimentally measured $\Delta S^{\ddagger}$ = −5(8) cal K^{-1} mol^{-1}. A KIE was observed for N–D (3.3) but not for B–D analogues, this was rationalised by a pre-equilibrium that featured an initial N–H deprotonation followed by rearrangement prior to the loss of H_2.[51]

1.3.7 Proton-Rebound catalysis

A third type of mechanism has also been proposed, involving hydride abstraction at a cationic metal centre to give a boronium cation $[H_2B(NRH_2)_2]^+$ and a neutral metal hydride.[69, 70] The metal hydride then deprotonates the boronium or ammonium to form aminoborane and the cationic metal centre (Scheme 1.11). Some examples will be discussed in this section.

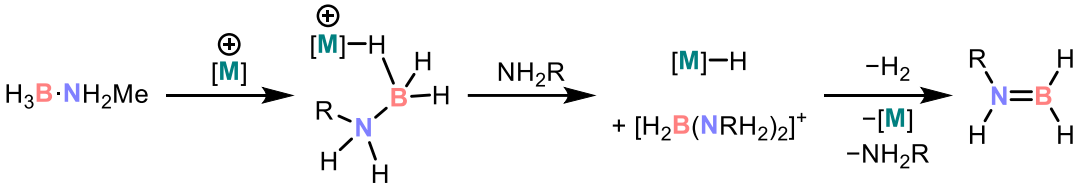

Scheme 1.11. General scheme illustrating the hydride abstraction/boronium co-catalysis pathway.

In 2013 Lopez-Serrano and Conjero reported formation of $(H_2BNMe_2)_2$ from $H_3B{\cdot}NMe_2H$ with a cationic cyclometallated platinum complex $[Pt(I^tBu')(I^tBu)][BAr^F{}_4]$ (I^tBu = 1,3-ditertbutylimidazol-2-ylidene, I^tBu' = cyclometallated) (**i-32**).[71] The reaction was carried out at 5 mol% catalyst loading and was complete in 15 minutes. The postulated mechanism is shown in Scheme 1.12. The addition of $H_3B{\cdot}NMe_2H$ to **i-32** results in the formation of the σ-amine-borane complex **i-33**. The transfer of a hydride from the borane to the platinum is facilitated by free $NHMe_2$ (from the cleavage of the B-N bond in the amine-borane). This results in the formation of the boronium cation $[BH_2(NMe_2H)_2]^+$ and the neutral platinum hydride (**i-34**). The boronium cation is in equilibrium with $[BH_2(THF)(NMe_2H)]^+$. This was illustrated by independent reaction of **i-34** and $[BH_2(THF)(NMe_2H)]^+$ resulting in immediate hydrogen release while reaction of **i-34** with $[BH_2(NMe_2H)_2]^+$ did not. This THF solvated boronium cation

protonates **i-34**, releasing aminobornane and hydrogen to reform **i-32**. DFT calculations support this proposed mechanism, the turnover limiting step was the abstraction of the hydride from the boron to the platinum with a barrier of 24.3 kcal mol^{-1} when assisted by NMe_2H (M06/6-31g(d,p)/SDD level).[71]

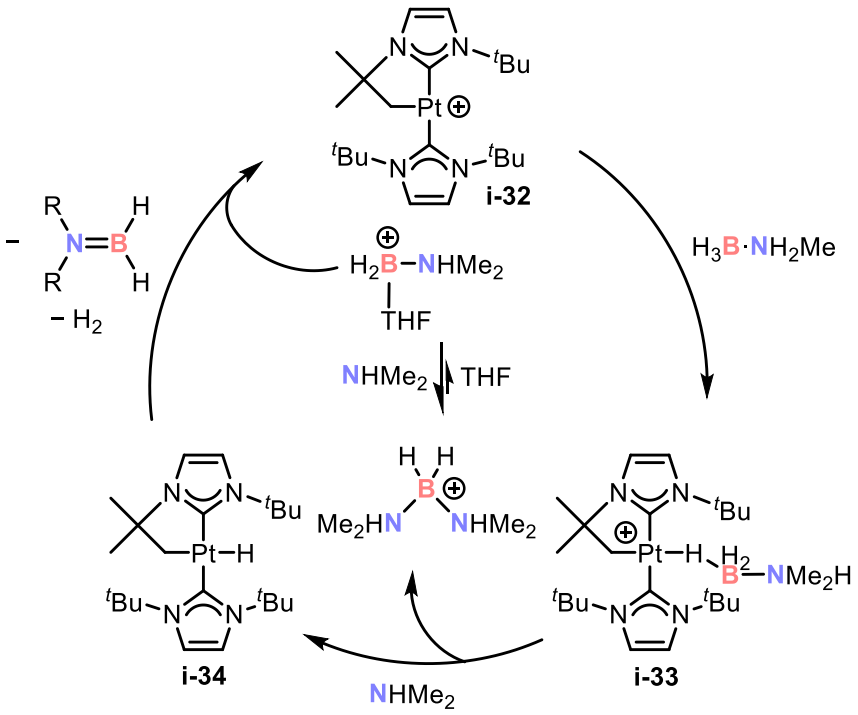

Scheme 1.12. Proposed mechanism for the dehydrogenation of $H_3B{\cdot}NMe_2H$ with $[Pt(I^tBu')(I^tBu)][BAr^F{}_4]$ (I^tBu = 1,3-ditertbutylimidazol-2-ylidene, I^tBu' = cyclometallated). $[BAr^F{}_4]^-$ anions not shown for clarity.[71]

Weller and coworkers reported a related mechanism for cationic rhodium Xantphos catalysts, $[Rh(\kappa^3\text{-P,O,P-Xantphos})(H)_2][BAr^F{}_4]$ where the R-group on the phosphorus was ethyl, isopropyl or *tert*-butyl.[69] The isopropyl and ethyl catalysts are in an equilibrium between $[Rh(\kappa^3\text{-P,O,P-Xantphos})(H)_2][BAr^F{}_4]$ and $[Rh(\kappa^3\text{-P,O,P-Xantphos})(H)_2(\eta^1\text{-}H_3B{\cdot}NMe_3)][BAr^F{}_4]$ (**i-35** and **i-36**, respectively). The authors found when added to $H_3B{\cdot}NH_2Me$ in 1,2-$F_2C_6H_4$, the isopropyl form of the catalyst was the most effective, forming polyaminoborane with >90% conversion in less than 30 minutes (M_n = 9,000, Đ = 2.9). Use of THF in place of 1,2-$F_2C_6H_4$ resulted in low conversion and a slower reaction, 40% conversion after 3 hours. This low conversion was proposed to be due to the competitive coordination of THF solvent. The *tert*-butyl derivative resulted in longer reaction times and was less selective for the formation of

polyaminoborane, while the ethyl derivative was catalytically inactive due to the lack of steric bulk that lead to formation of dimers.

The authors proposed a mechanism shown in Scheme 1.13. Addition of $H_3B{\cdot}NH_2Me$ to **i-35** results in a reversible B–H activation that forms the rhodium boryl/hydride **i-36**. Transfer of a hydride from the boron, assisted by NH_2Me, results in formation of boronium and neutral trihydride **i-38**. Protonation of **i-38** by the boronium results in reformation of cationic **i-35**, and the release of aminoborane and hydrogen.[69]

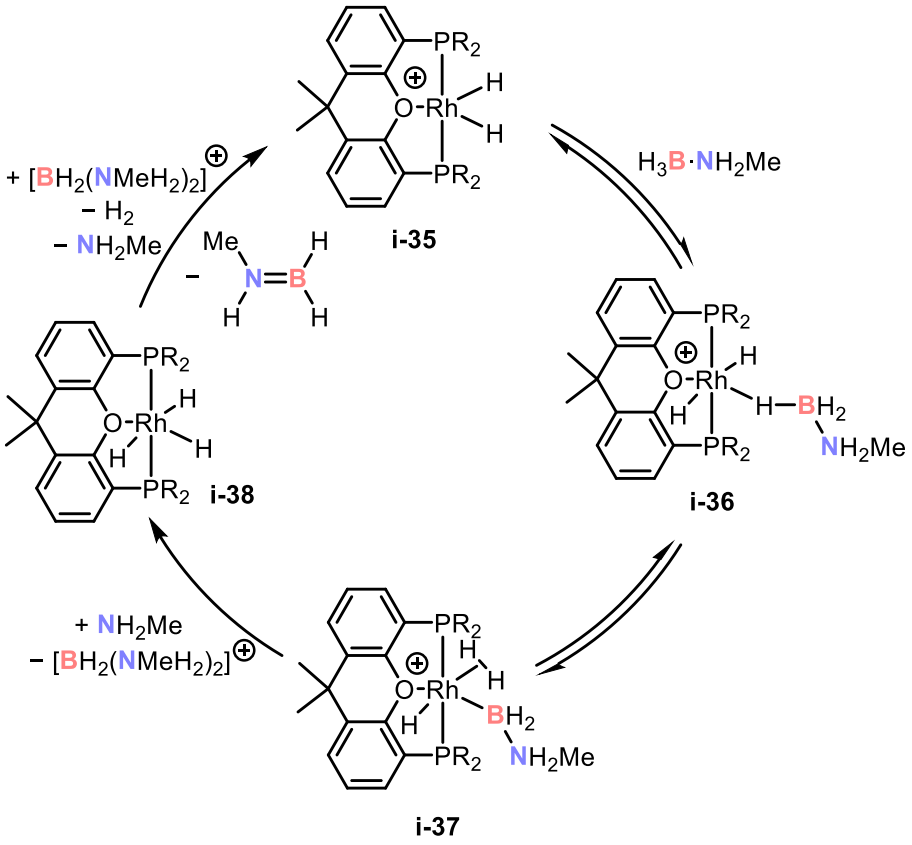

Scheme 1.13. Proposed mechanism for the dehydropolymerisation of $H_3B{\cdot}NH_2Me$ with a [Rh(κ^3-P,O,P-Xantphos)$(H)_2$][$BAr^F{}_4$] catalyst assisted by a boronium co-catalyst.[69]

1.4 Deactivation of catalysts – off-cycle borohydride complexes

The performance of catalysts can be greatly affected by deactivation or the formation of off-cycle 'dormant' species, as has been reported for multiple homogeneous catalyst systems.[72] Deactivation can be caused by several factors such as undesired reactions with the substrate; inadvertent admission of air and/or moisture and solvent incompatibilities/impurities.[72] Catalyst

deactivation during the dehydropolymerisation of amine-boranes will be discussed in this section.

As was alluded to in Section 1.2, amine-boranes have been shown to undergo dissociation of the B–N bond to form 'free' BH_3 and amine. This has been shown in the literature to be prevalent in solvents such as THF where the 'free' BH_3 is likely in the form of a stabilised $THF{\cdot}BH_3$ adduct.[73] The presence of 'free' BH_3 from B–N bond dissociation has led to the observation of borohydride complexes in amine-borane dehydropolymerisation chemistry. In most cases these borohydride complexes are inactive in catalysis or are dormant forms of the active catalyst that can be brought back onto cycle.[65, 74, 75]

1.4.1 Borohydride complexes

Common coordination modes of boranes to metal hydrides that have been identified in amine-borane dehydropolymerisation are shown in Figure 1.8, and featuring either primary η^1 B–H, secondary η^2 B–H or σ-borane connectivity.[76]

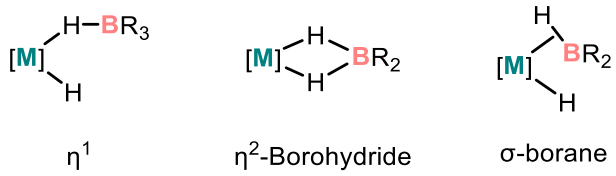

Figure 1.8. Potential binding modes of boranes to metal hydrides. No ligand structure shown for clarity.[77]

An initial report by Goldberg, Heinekey and coworkers, on use of an Ir(^{t}Bu-POCOP)$(H)_2$ complex (^{t}Bu-POCOP = κ^3-2,6-(^{t}Bu$_2$PO)$_2$C$_6$H$_3$) for the dehydrogenation of $H_3B{\cdot}NH_3$ identified a catalytic intermediate as an iridium borohydride complex, Ir(^{t}Bu-POCOP)$(H)(\eta^2\text{-}BH_4)$, see Figure 1.9.[78] The complex was synthesised independently by reaction of Ir(^{t}Bu-POCOP)$(H)_2$ (**1**) with $THF{\cdot}BH_3$. Use of this complex in catalysis with $H_3B{\cdot}NH_3$ resulted in negligible activity.

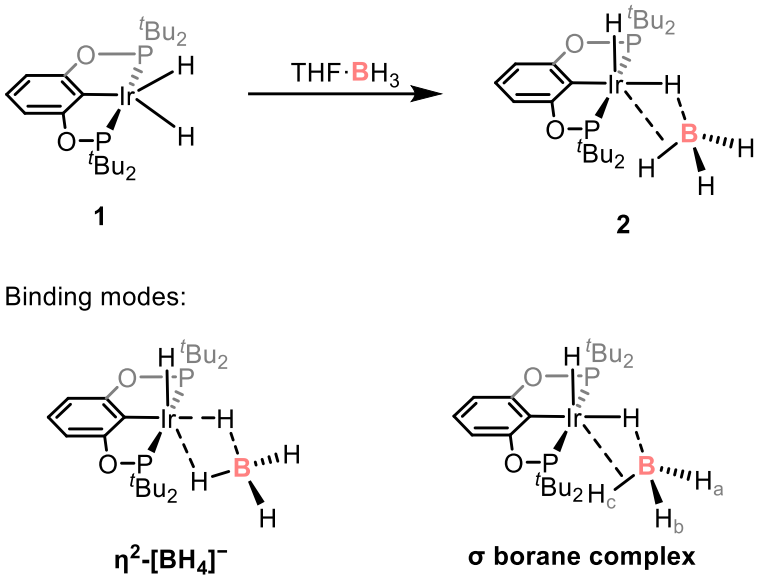

Figure 1.9. Synthesis of Ir(^{t}Bu-POCOP)(H)$_2$(BH$_3$) and the two proposed borane binding modes of BH$_3$ to Ir(^{t}Bu-POCOP)(H)$_2$.

Further work on the structural characterisation of this iridium borohydride complex was carried out and two likely descriptions of the complex arose (Figure 1.9):[79] an η^2-[BH$_4$]$^-$ adduct of a cationic [Ir(^{t}Bu-POCOP)(H)]$^+$ complex, or a BH$_3$ σ adduct of neutral Ir(^{t}Bu-POCOP)(H)$_2$. The ^{1}H NMR spectrum and the single crystal neutron diffraction structure of the complex indicate that the environment around the boron atom is highly unsymmetric. The authors comment that the distance between the iridium and boron atoms (2.37(3) Å) is longer than would be expected for an η^2-[BH$_4$]$^-$ complex (2.28 Å) and yet shorter than a monodentate binding mode (2.48 Å).[79] The lengths of the terminal B–H bonds (B–H$_a$ and B–H$_b$) are 1.22(5) Å and 1.18(8) Å, respectively. While the B–H$_c$ bond is noticeably longer (1.45(5) Å), the authors attribute this to a highly activated agostic bond between the BH$_3$ group and the iridium centre. The bond lengths between the iridium centre, the hydride and the boron are all elongated. The latter suggests that the borane fragment is not an η^2-[BH$_4$]$^-$ adduct. The authors propose that

the most consistent structure with the experimental data is the σ-borane complex (**2**).[79] Nevertheless it is likely that a borohydride structure is close in energy.

1.5 Role of additives in catalysis

There are many examples in the literature of the addition of additives to amine-borane dehydropolymerisation. Some examples include bases such as NH_2Me, and KO^tBu. There are also examples of proton sources such as ammonium $[NH_3Me]^+$, boronium $[H_2B(NMe_2H)_2]^+$ and water.

1.5.1 Bases

An initial report from Fagnou and co-workers reported the addition of K^tOBu (30 equivalents with regards to catalyst) to a ruthenium catalyst $Ru(Cl)_2(^iPr_2PCH_2CH_2NH)_2$ (**i-39**) prior to use in the dehydrogenation of amine-boranes, Figure 1.10.[60]

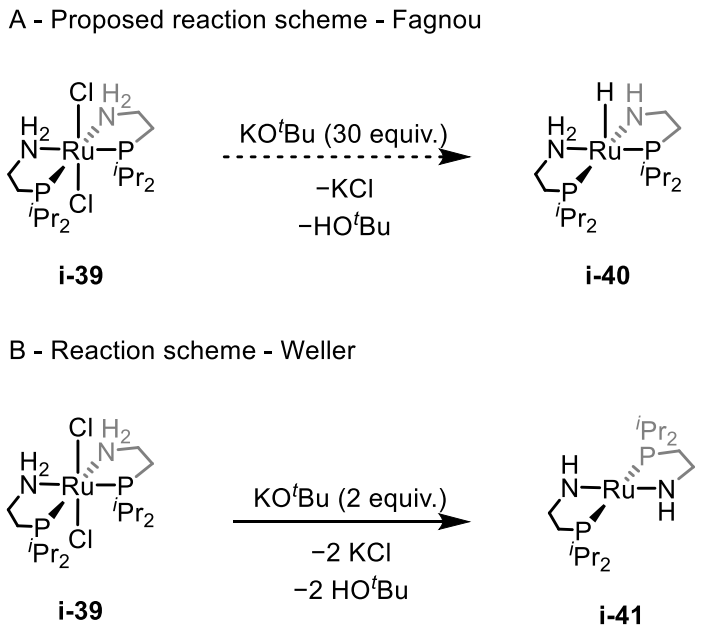

Figure 1.10. Proposed organometallic species formed from reaction of $Ru(Cl)_2(^iPr_2PCH_2CH_2NH)_2$ with K^tOBu, A – Fagnou, B – Weller.[54, 60]

Fagnou proposed that the 16-electron complex $Ru(H)(^iPr_2PCH_2CH_2NH)(^iPr_2PCH_2CH_2NH_2)$ (**i-40**) was formed. Use of proposed **i-40** to catalyse the dehydropolymerisation of amine-

boranes resulting in no induction period and rapid H_2 formation. However, the dehydrocoupled products formed were unselective.[60]

Very recent work from the group of Weller[54] identified the complex formed from reaction of **i-39** and KO^{t}Bu as the square-planar *P,P-trans*-Ru(^{i}Pr$_2$PCH$_2$CH$_2$NH)$_2$ complex (**i-41**). This dehydrohalogenation reaction was supported by various NMR spectroscopies, single-crystal X-ray diffraction studies and mass spectrometry. Use of the isolated product (**i-41**) in catalysis with $H_3B{\cdot}NH_2Me$ resulted in selective formation of polyaminoborane. There was no induction period and when added to $H_3B{\cdot}NH_2Me$, rapid H_2 production was observed. Similar dehydrodehalogenation reactions have been reported with other catalysts for other processes.[80, 81]

Another commonly used base in the dehydropolymerisation of amine-boranes is methylamine (NH_2Me). In most cases, addition of NH_2Me has a promoting effect on the dehydropolymerisation reaction, resulting in reduced/or no induction periods and increased rates of reaction in many cases.[52, 54, 56, 68, 74, 82, 83]

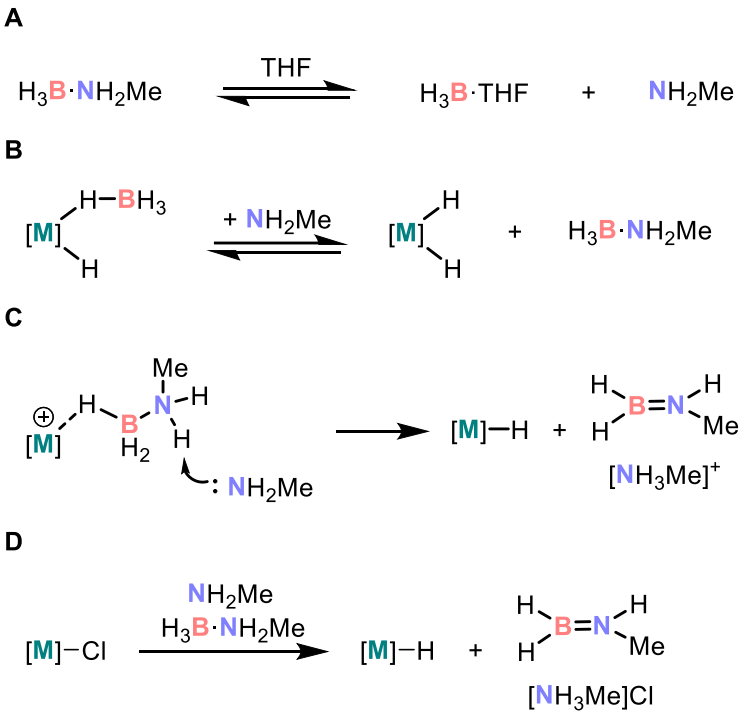

Scheme 1.14. Possible roles of NH_2Me in amine-borane dehydropolymerisation that may promote dehydrogenation catalysis.

One potential role that NH_2Me may play is to limit the extent of B–N bond dissociation by biasing the equilibrium towards the amine-borane adduct Scheme 1.14 (a). If there is less 'free' BH_3 in solution then there is less availability for interactions of the metal-hydrides with BH_3 that can cause catalyst deactivation *e.g.* formation of borohydride complexes as discussed in Section 1.4.1.[56] Another role is to bring an inactive form of the catalyst back on cycle, Scheme 1.14 (b). For example, if an inactive borohydride catalyst has formed, NH_2Me may play a role by reacting with this inactive complex to reform an active metal-hydride and an equivalent of substrate.[74] This would result in an increased concentration of active catalyst and therefore increased rate of reaction. Alternatively, NH_2Me may act as a base to deprotonate the metal bound amine-borane unit forming a metal-hydride, an equivalent of aminoborane and an ammonium species, Scheme 1.14 (c).[83, 84] NH_2Me can also promote formation of a catalytically active species from a metal chloride complex, forming an equivalent of amino borane, ammonium/boronium, and a metal hydride as shown in Scheme 1.14 (d).[51, 68] Addition of NH_2Me has also been shown to have an inhibitory effect on catalysis when it results in the formation of off-cycle catalytically inactive intermediates such as the cationic amine complex $[Ir(^{i}Pr\text{-}PN^{H}P)(H)_2(NH_2Me)][BAr^{F}_4]$ (**i-15**) discussed in section 1.3.5.[53]

1.5.2 Acids

Addition of $[NH_3Me]^+$ or $[H_2B(NMe_2H)_2]^+$ to amine-borane dehydropolymerisations as a proton source has been shown to have a promoting effect on the rate of catalysis in some cases and an inhibitory effect in others.

In systems where the addition of NH_2Me has a promoting effect on catalysis, boronium can act as a trapping agent reducing the concentration of available NH_2Me. Therefore the addition of excess $[H_2B(NMe_2H)_2]^+$ would have an inhibitory effect on catalysis.[83, 85] These interactions were confirmed by NMR titration experiments where interactions of $[H_2B(NMe_2H)_2]^+$ and $[NH_3Me]^+$ can occur with amine-boranes to form off-cycle adducts (Figure 1.11).[83]

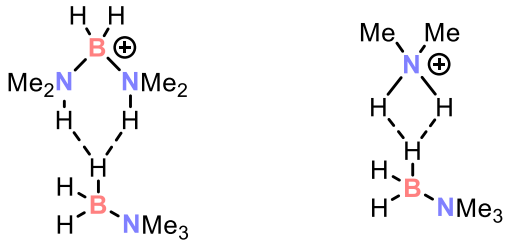

Figure 1.11. Amine-boranes forming adducts with $[H_2B(NMe_2H)_2]^+$ and $[NH_3Me]^+$ through B–H/N–H interactions.[83]

Examples of boronium having a promoting effect on catalysis were discussed in section 1.3.7, with catalysts that operate *via* the hydride abstraction/boronium co-catalyst pathway. Boronium plays an important role in the catalytic cycles to go from a neutral to a cationic catalytic intermediate *via* formation of aminoborane, NH_2Me and H_2 (Scheme 1.12 and 1.13).[69, 71] There are similar reactions where $[NH_3Me]^+$ plays a similar role, reacting with an off-cycle neutral iridium trihydride ($Ir(^iPr\text{-}PN^HP)H_3$, **i-14**) to form a cationic iridium dihydride amine complex and H_2. This cationic iridium complex can then react with $H_3B{\cdot}NH_2Me$ to get back on-cycle (see Scheme 1.5).[53]

1.5.3 Addition of H_2O

Many of the catalysts discussed so far are expected to be air and/or moisture sensitive. Addition of water to amine-boranes also results in the hydrolysis of borane to form borates which would hinder the synthesis of polyaminoborane. Thus, there is very little detail on the effect of adding small quantities of H_2O to amine-borane dehydropolymerisations as it has not been recognised or widely reported.

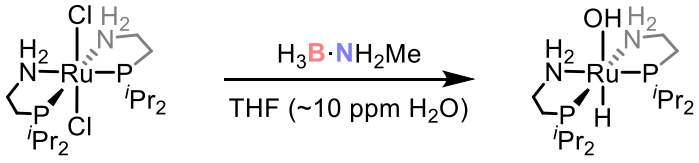

i-39 **i-42**

Scheme 1.15. Scheme showing reaction of adventitious H_2O with **i-39**.[54]

One example details the addition of H_2O to the dehydropolymerisation of $H_3B{\cdot}NH_2Me$ with $Ru(Cl)_2(^iPr_2PCH_2CH_2NH_2)_2$ (**i-39**).[54] The use of THF with <10 ppm H_2O content resulted in no induction period but the addition of 500 equivalents of H_2O to THF resulted in a very long induction period of 5 h. Weller and co-workers suggest this reactivity is due to the reaction of **i-39** with adventitious H_2O present in THF. This reaction resulted in the formation of a ruthenium hydroxyhydride ($Ru(OH)(H)(^iPr_2PCH_2CH_2NH_2)_2$) (**i-42**) that sits off-cycle during the induction period, as a resting state. This complex was synthesised independently and was observed to be a competent pre-catalyst after a significant induction period.[54]

Another example from Nolan and co-workers showed that addition of an iridium catalyst $[Ir(I^tBu')_2][PF_6]$ (I^tBu' – cyclometallated 1,3-ditertbutylimidazol-2-ylidene) to ammonia borane in a THF/H_2O 1:1 mixture led to the formation of borates.[86] The authors isolated crystals of ammonium borates with the structure $[NH_4][B_5O_{10}H_4]{\bullet}2H_2O$. The formation of borates was supported by resonances indicative of BO_3 and BO_4^- in the $^{11}B\{^1H\}$ NMR (δ 19.9 and δ 1.3, respectively) spectrum taken of the isolated borates.[86]

1.6 Dehydropolymerisation of amine-boranes with Ir(^{t}Bu-POCOP)(H)$_2$

1.6.1 Catalysis with Ir(^{t}Bu-POCOP)H$_2$

Ir(^{t}Bu-POCOP)(H)$_2$ (^{t}Bu-POCOP = κ^3-2,6-($^tBu_2PO)_2C_6H_3$) was initially reported as a transfer dehydrogenation catalyst of cyclooctane to cyclooctene with *tert*-butylethylene acting as the sacrificial hydrogen acceptor by Brookhart and co-workers.[87]

An initial report of the use of Ir(^{t}Bu-POCOP)(H)$_2$ (**1**) as a catalyst for the dehydrogenation of $H_3B{\cdot}NH_3$ was published in 2006 by Goldberg, Heinekey and co-workers.[78] Treatment of $H_3B{\cdot}NH_3$ at 0.5 M in THF, with **1** (0.5 mol%) resulted in one equivalent of hydrogen release in 14 minutes. Recharging the system with additional substrate resulted in further hydrogen production. No induction period for the reaction was noted and the rate of reaction increased as the catalyst loading increased. Elemental mercury was added to the reaction but there was no change to the rate of the reaction, suggesting a homogenous process.[88]

Through the course of the reactions the authors reported a white solid forming that was insoluble in H_2O and most organic solvents. Based on characterisation by solid state ^{11}B NMR spectroscopy (broad peak at −18 ppm), IR spectrum and X-ray powder diffraction pattern the authors assigned this precipitate as a cyclic pentamer $[H_2N{\cdot}BH_2]_5$, although subsequently this was found not to be correct.

Analysis of the organometallic species observed during catalysis by NMR spectroscopy resulted in some interesting observations. Upon mixing of **1** and $H_3B{\cdot}NH_3$, a new iridium species formed which was assigned as a tetrahydride complex, Ir(^{t}Bu-POCOP)$(H)_4$ (**3**). A third species was observed at long reaction times which was identified as borohydride complex Ir(^{t}Bu-POCOP)$(H)_2(BH_3)$ (**2**). The synthesis and structure of this complex was discussed in Section 1.4.1. Use of **2** in catalysis with $H_3B{\cdot}NH_3$ resulted in no H_2 production indicating that it was inactive in catalysis. The authors established an equilibrium shown in Scheme 1.16, that Ir(^{t}Bu-POCOP)$(H)_4$ (**3**) can be formed from the addition of H_2 (2 bar.) to Ir(^{t}Bu-POCOP)$(H)_2(BH_3)$ (**2**). The backwards reaction of this equilibrium can be achieved by the addition of $BH_3{\cdot}THF$. They also reported that removal of hydrogen from Ir(^{t}Bu-POCOP)$(H)_4$ (**3**) results in reformation of Ir(^{t}Bu-POCOP)$(H)_2$ (**1**).[78]

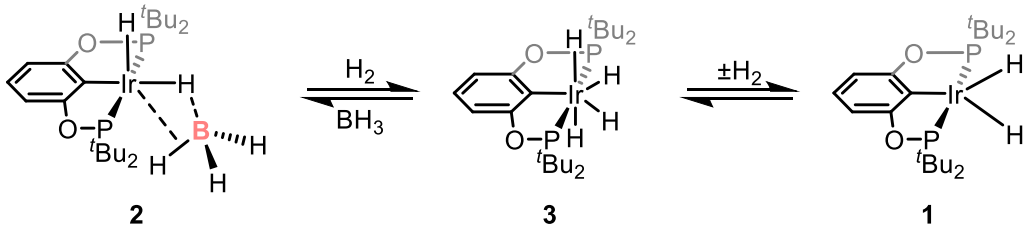

2 **3** **1**

Scheme 1.16. Established equilibrium of Ir(^{t}Bu-POCOP)$(H)_2(BH_3)$ with H_2.[78]

A further contribution from Goldberg and Heinekey followed in 2008,[89] focussing on the dehydropolymerisation of $H_3B{\cdot}NH_2Me$ and $H_3B{\cdot}NH_3$, as well as mixtures of the two. Substitution of an alkyl group to $H_3B{\cdot}NH_3$ was hypothesised to increase the solubility of the product (–$(H_2B$-NHMe)–) when compared to polymeric –$(H_2B$-$NH_2)$– allowing further modification.

The initial focus of the study was on the dehydropolymerisation of $H_3B{\cdot}NHMe_2$. However, this was refocused to $H_3B{\cdot}NH_2Me$ when the original reaction took over 24 hours and did not go to completion. The results achieved with $H_3B{\cdot}NH_2Me$ as a substrate were more similar to that shown in the previous contribution for $H_3B{\cdot}NH_3$ (at 0.5 mol% and 298 K the first-order rate constants were k_{obs} = 13.4(7) × 10^{-3} s^{-1} and 11(2) × 10^{-3} s^{-1} respectively). The measured k_{obs} were higher for $H_3B{\cdot}NH_2Me$ over $H_3B{\cdot}NH_3$ at all catalyst loadings (0.5, 1.0 and 2.0 mol%). The major difference between the two substrates was that the products from the reaction with $H_3B{\cdot}NH_2Me$ remained soluble throughout the reaction.

In agreement with the authors initial report, complexes **2** and **3** were the organometallic species observed during catalysis by ^{1}H NMR spectroscopy. In the ^{1}H NMR spectrum, the resonances for $H_3B{\cdot}NH_2Me$ rapidly disappeared, with new signals appearing. Two N–H resonances were observed, as well as a methyl resonance and a broad BH_2 resonance. Large numbers of methyl resonances were observed between 36 and 28 ppm in the $^{13}C\{^1H\}$ NMR spectrum. This was different to what was observed for the insoluble product formed from dehydropolymerisation of $H_3B{\cdot}NH_3$. The authors attributed these signals to the formation of cyclic and acyclic oligomeric material, $[MeHNBH_2]_n$ (n = 2–20) and $[MeH_2NBH_2][MeHNBH_2]_n[MeNH_2]$ (n = 4–48), respectively.

Interestingly, addition of a 1:1 ratio of $H_3B{\cdot}NH_3$ and $H_3B{\cdot}NH_2Me$ led to 1 equivalent of H_2 being produced and a soluble material formed. Increasing the ratios to 2:1 and 5:1 led to the formation of insoluble precipitate as described in the authors previous contribution. In all cases, analysis of the products by ^{1}H NMR spectroscopy indicated formation of oligomers with a 1:1 incorporation of $[H_2B{\cdot}NH_2]$ and $[H_2B{\cdot}NHMe]$ units. This observation was also supported by ESI-MS.[89]

Simultaneously, Manners and co-workers were also using **1** to form a material they characterised as polyaminoborane.[59] Addition of a concentrated solution of $H_3B{\cdot}NH_2Me$ in THF (2 M) to **1** (0.3 mol%) at 0 °C resulted in vigorous bubbling. The authors commented on the increased viscosity of the solution as the reaction went on. The reaction was allowed to stir at

20 °C for 20 minutes. A white solid was isolated from precipitation into n-butane or n-hexane at −78 °C. Characterisation of the solid was consistent with the formation of polyaminoborane. The ^{11}B NMR spectrum had a single broad resonance at δ 6.7. In the ^{1}H NMR spectrum in $CDCl_3$ three resonances were observed, δ 2.78, 2.18 and 1.68, assigned to the N–H, CH_3, and BH_2, respectively. Residual solvent signals, THF and n-alkanes were also observed after prolonged vacuum treatment. The ^{13}C NMR spectrum contained two methyl resonances at δ 36.8 and 35.8, attributed to the diastereomeric nitrogen centre. It is interesting to note that the isomers of the nitrogen centre are observed in the ^{13}C NMR but not the ^{1}H NMR in $CDCl_3$. The polymer produced was determined to be of high molecular weight as measured by GPC M_w = 160,000 g mol^{-1}, and the Đ was high 2.9.

The authors achieved some success in the dehydropolymerisation of $H_3B{\cdot}NH_3$, however the product remained insoluble. Instead focus pivoted to the formation of co-polymers using $H_3B{\cdot}NH_3$ and $H_3B{\cdot}NH_2Me$ as substrates. The polymer formed remained soluble in THF up to a 1:1 ratio. An attempt to expand the range of substrates to $H_3B{\cdot}NH_2{}^n$Bu was successful in polyaminoborane formation. However, isolation of the product was challenging due to its increased solubility. Co-polymers of $H_3B{\cdot}NH_2Me$ and $H_3B{\cdot}NH_2{}^n$Bu (1:1 ratio) were synthesised and found to be more insoluble in *n*-pentane allowing the desired purification and isolation by precipitation to be achieved.

In a further contribution by Manners and coworkers, some kinetic measurements had been carried out with a manometer (conditions $H_3B{\cdot}NH_2Me$ 0.5 M and Ir(^{t}Bu-POCOP)$(H)_2$ (**1**) 0.1 mol%). The kinetics were irreproducible over a number of runs. Additionally, an investigation had been carried out to determine conditions that affected polymerisation.[55] In the case where the substrate concentration was varied, the lowest concentration of $H_3B{\cdot}NH_2Me$ resulted in the shorter polymer M_n = 24,400 g mol^{-1}. In the range between 2 M and 10 M the molecular weight ranged from M_n = 51,500-71,800 g mol^{-1} with high Đ from 2.6-3.4. There was no discernible pattern between the substrate concentration and these

measured polymer properties. Alternatively, when the catalyst loading of **1** was increased the molecular weight of the polymer formed increased M_n = 55,400-187,400 g mol^{-1}, Đ = 1.9-2.5.

While the authors of this contribution expanded the understanding of how changing a limited number of conditions can affect the molecular weight of polymer, there was no insight into the dehydropolymerisation mechanism.

1.6.2 Proposed dehydrogenation mechanism based on DFT calculations

The initial report by Goldberg,[78, 89] prompted Paul and Musgrave to investigate the mechanism for the dehydropolymerisation of amine-borane with **1** computationally.[32] The calculations were carried out using $H_3B{\cdot}NH_3$ as the substrate and Ir(Me-POCOP)$(H)_2$ as a truncated model of the catalyst. The energies were calculated using B3LYP(CPCM)/B2//B3LYP/B1 with zero-point correction

The authors propose the catalytic process proceeds *via* an Ir(III) mechanism, Scheme 1.17. The combination of **1** and $H_3B{\cdot}NH_3$ to form an amine-borane bound complex (**i-43**) *via* the hydridic B–H bond was shown to be exergonic. This was computed to be energetically favourable by 10.2 kcal mol^{-1}. The formation of a six-membered transition state (**i-44**) through a concerted hydride transfer from the boron to the iridium and transfer of a proton on the nitrogen to an iridium bound hydride lies 16.5 kcal mol^{-1} in energy above the amine-borane bound complex, and goes on to form the more favourable iridium tetrahydride (**3**). The loss of hydrogen from the tetrahydride *via* an elongated transition state (**i-45**) returns **1**. Loss of H_2 *via* this transition state has a barrier of 20.7 kcal mol^{-1}. The two largest barriers come from the formation of the concerted transition state and the loss of H_2, the energy span for these is 18.8 kcal mol^{-1} and 20.7 kcal mol^{-1}, respectively. The authors comment that both lie within the error range of the computational model used. Therefore, it is likely that these two barriers would determine the rate of reaction for this catalytic process if the model is correct.

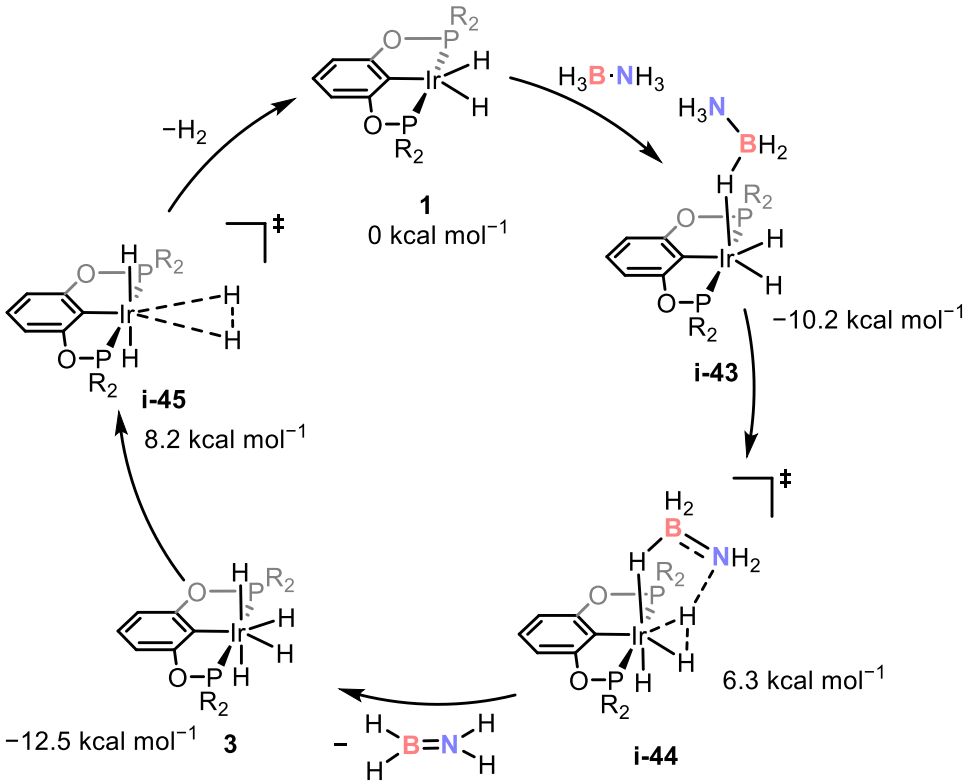

Scheme 1.17. Proposed mechanism for the dehydropolymerisation of amine-boranes by Ir(R-POCOP)H_2 (R = Me).[32] The energies were calculated using B3LYP(CPCM)/B2//B3LYP/B1 with zero-point correction

1.6.3 Polymerisation Mechanism

An initial study by Manners and coworkers gave some insight into the polymerisation mechanism that is acting in the case of **1**.[55] Catalytic reactions were carried out and halted at various progression points; the polymer molecular weight was measured by GPC and a molecular weight vs conversion graph plotted. The authors plotted both M_w and M_n against conversion. The relationship of M_w vs conversion has a similar linear-like relationship as would be expected for a living polymerisation, although there was a large range of dispersity values quoted for the polymers (2.6-4.6).

However, the evolution of M_n with conversion shows notable molecular weight polymer formed at low conversions (~20,000 g mol^{-1} at <25% conversion) and this gradually increased (~ 60,000 g mol^{-1} at 80% conversion). The authors note that this relationship is indicative of a chain growth polymerisation mechanism. However, due to the increase in molecular weight at

higher conversions the polymerisation mechanism they postulated that the mechanism may differ from a classical chain growth polymerisation mechanism.[55]

A computational study was carried out by Paul and coworkers to try to underpin the polymerisation mechanism of **1** assuming the real monomer $H_2B{=}NHMe$ is available (B3LYP/MO6L(CPCM,THF).[30] This study agrees with the observations of Manners,[55] that the polymerisation likely occurs *via* a head-to-tail chain growth mechanism, see Scheme 1.18. This mechanism initiates *via* activation of an aminoborane unit. From here the lone pair on the nitrogen can undergo nucleophilic attack on the electron deficient BH_2 of another molecule of aminoborane. This nucleophilic attack continues promoting the growth of long polyaminoborane chains. The authors found that the barrier for continued oligomerisation was much more favourable that formation of cyclic pentamer.

The suggested computed termination process involves a proton transfer from the amine unit closest to the metal centre to the terminal NH_2 group. The polymer chain dissociated from the metal centre forming a terminal aminoborane group. This reactive end then undergoes a proton transfer with an equivalent of amine-borane to form another aminoborane unit and polyaminoborane.

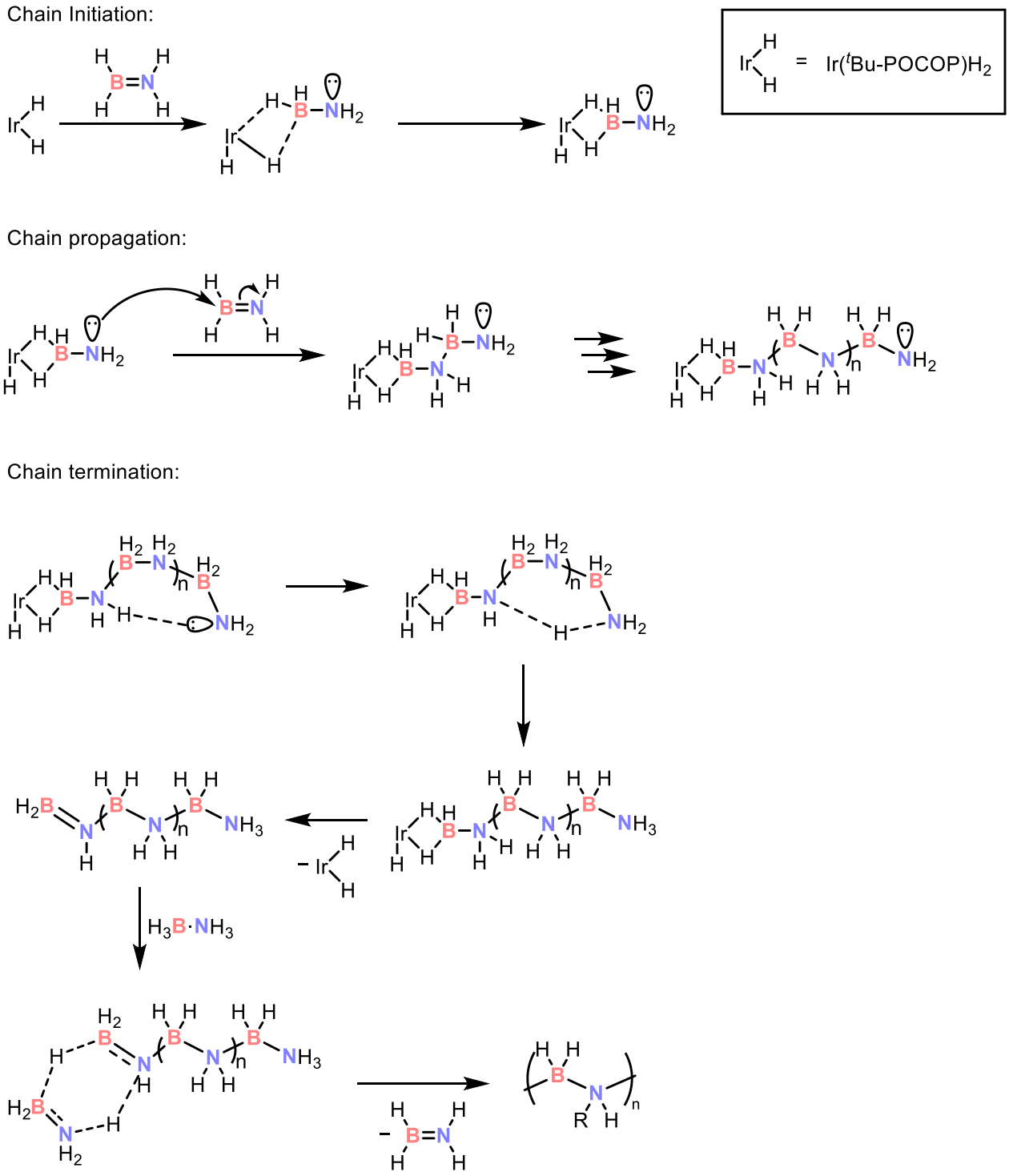

Scheme 1.18. Proposed polymerisation mechanism of aminoborane by Ir(^{t}Bu-POCOP)H_2.[30]

1.7 Applications of polyaminoboranes

Preceramic polymer or polymers that convert to ceramic materials often through pyrolysis are sought after due to their ability to be shaped prior to pyrolysis. The ceramic products are of interest as they have high thermal and chemical stability.[90] A common example is the pyrolysis of polysiloxanes to form silicon carbides and silicon oxicarbides. The formed silicon carbide is a very hard material and has many industrially relevant uses such as in car parts and bulletproof vests.[91]

Boron nitride is a boron and nitrogen containing ceramic that is chemically and thermally resistant. It has different morphologies, hexagonal, cubic and wurtzite. These are analogous to their isoelectronic carbon counterpart's graphite, diamond and hexagonal diamond (Lonsdaleite). Hexagonal boron nitride (*h*-BN) is of interest as it has low electrical conductivity, excellent heat conductivity, superhydrophobicity and has many applications in lubricants, medical imaging and electronics.[22, 23]

The typical synthetic route to boron nitride is the pyrolysis of boric acid/oxide and urea or melamine.[25, 26] This route requires calcium carbonate as a catalyst to promote crystallisation, and it offers little control in the shape or morphology of the boron nitride formed.[25] Use of ammonia borane as a precursor has also been shown.[92] A benefit of using polymeric precursors instead is that polymers can be more easily shaped and manipulated into forms that may be useful, *i.e.* coatings, thin films, fibres *etc.*, prior to pyrolysis.

Research into polymeric precursors for the synthesis of *h*-BN ceramics focused in on polyborazylene as an ideal precursor to *h*-BN as it already consists of a chain of six-membered B–N rings, the base structure of *h*-BN. While the synthesis of dimers and oligomers had been reported previously, it was not until Sneddon and coworkers reported their synthesis of polyborazylene that the material was isolated as a solid and characterised.[93] Borazine was heated at 70 °C *in vacuo* until it was viscous. Any volatiles were removed and a white powder remained that could be purified by dissolution in glyme followed by precipitation into pentane.

Polyborazylene was formed in 61% yield as a white solid that was water sensitive and decomposed when exposed to moist air.[93] A later contribution from Sneddon found that pyrolysis of polyborazylene under argon or ammonia at 1200 °C resulted in formation of white boron nitride powders with high purity and ceramic yields.[94] Polyborazylene was able to form coatings on preexisting ceramic fibres such as alumina fibres through dip coating.[94] However, attempts at using polyborazylene to form fibres by the authors through melt spinning were unsuccessful. This was due to a crosslinking stage that occurred at low temperatures.[95] Further research was carried out by Sneddon with post synthetically modified polyborazylenes, which were much more amenable to melt spinning processing.[96] Simultaneously, work carried out by Miele and co-workers using asymmetric alkylaminoborazines was more adept at forming boron nitride fibres,[97-100] though with various processing issues caused by the materials tendency to crosslink. All manipulations were carried out under an argon atmosphere due to the air and moisture sensitivity of the polyborazylene.[100]

Similarly, polyaminoboranes are considered to be an alternative polymeric precursor to boron nitride. Manners and coworkers studied the thermal decomposition behaviour of polyaminoborane, noting that the materials had low ceramic yields of ~36% at 900 °C.[28] The authors attribute the low ceramic yield to a polymer with low amounts of crosslinking. A pellet of polyaminoborane was treated in a furnace, this resulted in the formation of boron nitride as identified by loss of N–H and B–H stretches in the IR spectrum and the powder X-ray diffraction pattern.[28] The authors found that crosslinking the polyaminoborane with hydrazine-diborane increased the ceramic yield up to 52%. In a later contribution, Manners illustrated that polyaminoboranes could be successfully electrospun, evidenced with an optical light microscopic image of the electro spun fibres.[21]

1.8 Summary and outlook

The previous sections have provided an exploration into the existing literature on the dehydropolymerisation of amine-boranes, highlighting the use of transition metal catalysts for

this reaction, with emphasis on the three types of mechanistic pathways proposed. The examples described in this chapter present catalysts that can be used for the synthesis of polyaminoborane however control of polymer properties has yet to be achieved. Further mechanistic understanding of amine-borane dehydropolymerisation is required to gain control over catalysis and allow for the synthesis of polyaminoborane with tuneable polymer properties. This understanding will be essential to advance the use of polyaminoborane as precursors to ceramics (boron nitride). It remains unclear how polymer properties such as; molecular weight, dispersity, glass transition temperature and solubility may affect the formation of boron nitride.

This contribution aims to take a known catalyst system (Ir(^{t}Bu-POCOP)(H)$_2$)[55, 59, 78, 89] (**1**) and the development of novel systems to synthesise various polyaminoboranes with control over molecular weight and dispersity. The mechanism of dehydropolymerisation of amine-boranes with Ir(^{t}Bu-POCOP)(H)$_2$ remains unknown, with limited experimental and computational attempts over a decade ago.[32] This work will combine kinetic data and speciation to gain understanding of the mechanism of **1** and allow the optimisation of reaction conditions to gain control of polymer properties *i.e.* molecular weight and polydispersity (Đ). Scale-up of polymer production from promising catalyst systems will allow the materials properties to be investigated.

1.9 References

1. S. Aldridge, A. J. Downs, C. Y. Tang, S. Parsons, M. C. Clarke, R. D. L. Johnstone, H. E. Robertson, D. W. H. Rankin and D. A. Wann, *J. Am. Chem. Soc.*, 2009, **131**, 2231–2243.
2. M. E. Bowden, I. W. M. Brown, G. J. Gainsford and H. Wong, *Inorg. Chim. Acta*, 2008, **361**, 2147–2153.
3. A. Staubitz, A. P. M. Robertson, M. E. Sloan and I. Manners, *Chem. Rev.*, 2010, **110**, 4023–4078.
4. H. C. Brown, H. I. Schlesinger and S. Z. Cardon, *J. Am. Chem. Soc.*, 1942, **64**, 325–329.
5. R. Baldwin and R. Washburn, *J. Org. Chem.*, 1961, **26**, 3549–3550.
6. A. Haaland, *Angew. Chem. Int. Ed.* , 1989, **28**, 992–1007.
7. A. Staubitz, M. Besora, J. N. Harvey and I. Manners, *Inorg. Chem.*, 2008, **47**, 5910–5918.
8. H. Flores-Segura and L. A. Torres, *Struct. Chem.*, 1997, **8**, 227–232.
9. C. Tantardini and A. R. Oganov, *Nat. Commun.*, 2021, **12**, 2087.
10. R. D. Suenram and L. R. Thorne, *Chem. Phys. Lett.*, 1981, **78**, 157–160.
11. X. Chen, J. C. Zhao and S. G. Shore, *Acc. Chem. Res.*, 2013, **46**, 2666–2675.
12. D. J. Grant and D. A. Dixon, *J. Phys. Chem. A*, 2006, **110**, 12955–12962.
13. R. O. Hutchins, K. Learn, B. Nazer, D. Pytlewski and A. Pelter, *Org. Prep. Proced. Int.*, 2009, **16**, 335–372.
14. L. Euzenat, D. Horhant, Y. Ribourdouille, C. Duriez, G. Alcaraz and M. Vaultier, *Chem. Commun.*, 2003, 2280–2281.
15. S. Lau, D. Gasperini and R. L. Webster, *Angew. Chem. Int. Ed.*, 2021, **60**, 14272–14294.
16. L. Monnier, J.-G. Delcros and B. Carboni, *Tetrahedron*, 2000, **56**, 6039–6046.
17. P. V. Ramachandran, M. P. Drolet and A. S. Kulkarni, *Chem. Commun.*, 2016, **52**, 11897–11900.
18. P. V. Ramachandran, S. Choudhary and A. Singh, *J. Org. Chem.*, 2021, **86**, 4274–4280.
19. A. Staubitz, A. P. Robertson and I. Manners, *Chem. Rev.*, 2010, **110**, 4079–4124.
20. F. H. Stephens, V. Pons and R. Tom Baker, *Dalton Trans.*, 2007, 2613–2626.
21. E. M. Leitao, T. Jurca and I. Manners, *Nat. Chem.*, 2013, **5**, 817–829.
22. L. H. Li and Y. Chen, *Adv. Funct. Mater.*, 2016, **26**, 2594–2608.
23. S. Roy, X. Zhang, A. B. Puthirath, A. Meiyazhagan, S. Bhattacharyya, M. M. Rahman, G. Babu, S. Susarla, S. K. Saju, M. K. Tran, L. M. Sassi, M. A. S. R. Saadi, J. Lai, O. Sahin, S. M. Sajadi, B. Dharmarajan, D. Salpekar, N. Chakingal, A. Baburaj, X. Shuai, A. Adumbumkulath, K. A. Miller, J. M. Gayle, A. Ajnsztajn, T. Prasankumar, V. V. J. Harikrishnan, V. Ojha, H. Kannan, A. Z. Khater, Z. Zhu, S. A. Iyengar, P. A. d. S. Autreto, E. F. Oliveira, G. Gao, A. G. Birdwell, M. R. Neupane, T. G. Ivanov, J. Taha-Tijerina, R. M. Yadav, S. Arepalli, R. Vajtai and P. M. Ajayan, *Adv. Mater.*, 2021, **33**, 2101589.
24. D. Han, F. Anke, M. Trose and T. Beweries, *Coord. Chem. Rev.*, 2019, **380**, 260–286.
25. S. Bernard and P. Miele, *Materials*, 2014, **7**, 7436–7459.
26. R. T. Paine and C. K. Narulat, *Chem. Rev.*, 1990, **90**, 73–91.
27. A. L. Colebatch and A. S. Weller, *Chem. Eur. J.*, 2019, **25**, 1379–1390.
28. V. Pons and R. T. Baker, *Angew. Chem. Int. Ed.*, 2008, **47**, 9600–9602.
29. G. I. Peterson and T. L. Choi, *Chem. Sci.*, 2020, **11**, 4843–4854.
30. S. Bhunya, T. Malakar and A. Paul, *Chem. Commun.*, 2014, **50**, 5919–5922.
31. M. Devillard, C. A. De Albuquerque Pinheiro, E. Caytan, C. Roiland, C. Dinoi, I. Del Rosal and G. Alcaraz, *Adv. Synth. Catal.*, 2021, **363**, 2417–2426.
32. A. Paul and C. B. Musgrave, *Angew. Chem. Int. Ed.*, 2007, **46**, 8153–8156.
33. A. Ravve, *Principles of Polymer Chemistry Third Edition*, Springer, New York, 2012.

34. T. N. Hooper, A. S. Weller, N. A. Beattie and S. A. Macgregor, *Chem. Sci.*, 2016, **7**, 2414–2426.
35. J. J. Race, A. Heyam, M. A. Wiebe, J. Diego-Garcia Hernandez, C. E. Ellis, S. Lei, I. Manners and A. S. Weller, *Angew. Chem. Int. Ed.*, 2023, **62**, e202216106.
36. C. W. Bielawski and R. H. Grubbs, *Prog. Polym. Sci.*, 2007, **32**, 1–29.
37. F. Vidal and F. Jäkle, *Angew. Chem. Int. Ed.*, 2019, **58**, 5846–5870.
38. H. I. Schlesinger, D. M. Ritter and A. B. Burg, *J. Am. Chem. Soc.*, 1938, **60**, 2297–2300.
39. G. W. Schaeffer and L. J. Basile, *J. Am. Chem. Soc.*, 1955, **77**, 331–332.
40. A. K. Holliday and N. R. Thompson, *J. Chem. Soc.*, 1960, **0**, 2695–2699.
41. A. J. Miller and J. E. Bercaw, *Chem. Commun.*, 2010, **46**, 1709–1711.
42. C. Appelt, J. C. Slootweg, K. Lammertsma and W. Uhl, *Angew. Chem. Int. Ed.*, 2013, **52**, 4256–4259.
43. R. J. Less, R. L. Melen and D. S. Wright, *RSC Adv.*, 2012, **2**.
44. P. Bellham, M. S. Hill and G. Kociok-Kohn, *Dalton Trans.*, 2015, **44**, 12078–12081.
45. Z. Mo, A. Rit, J. Campos, E. L. Kolychev and S. Aldridge, *J. Am. Chem. Soc.*, 2016, **138**, 3306–3309.
46. O. J. Metters, A. M. Chapman, A. P. M. Robertson, C. H. Woodall, P. J. Gates, D. F. Wass and I. Manners, *Chem. Commun.*, 2014, **50**, 12146–12149.
47. C. A. De Albuquerque Pinheiro, C. Roiland, P. Jehan and G. Alcaraz, *Angew. Chem. Int. Ed.*, 2018, **57**, 1519–1522.
48. T. Jurca, T. Dellermann, N. E. Stubbs, D. A. Resendiz-Lara, G. R. Whittell and I. Manners, *Chem. Sci.*, 2018, **9**, 3360–3366.
49. T. Kakizawa, Y. Kawano, K. Naganeyama and M. Shimoi, *Chem. Lett.*, 2011, **40**, 171–173.
50. G. M. Adams, A. L. Colebatch, J. T. Skornia, A. I. McKay, H. C. Johnson, G. C. Lloyd Jones, S. A. Macgregor, N. A. Beattie and A. S. Weller, *J. Am. Chem. Soc.*, 2018, **140**, 1481–1495.
51. C. N. Brodie, T. M. Boyd, L. Sotorríos, D. E. Ryan, E. Magee, S. Huband, J. S. Town, G. C. Lloyd-Jones, D. M. Haddleton, S. A. Macgregor and A. S. Weller, *J. Am. Chem. Soc.*, 2021, **143**, 21010–21023.
52. M. J. Cross, C. N. Brodie, D. G. Crivoi, J. C. Goodall, D. E. Ryan, A. J. Martinez-Martinez, A. Johnson and A. S. Weller, *Chem. Eur. J.*, 2023, **29**, e202302110.
53. C. N. Brodie, L. Sotorrios, T. M. Boyd, S. A. Macgregor and A. S. Weller, *ACS Catal.*, 2022, **12**, 13050–13064.
54. M. J. Cross, M. A. Sajjad, S. A. Macgregor and A. S. Weller, *Angew. Chem. Int. Ed.*, 2025, **64**, e202500019.
55. A. Staubitz, M. E. Sloan, A. P. M. Robertson, A. Friedrich, S. Schneider, P. J. Gates, J. S. A. D. Günne and I. Manners, *J. Am. Chem. Soc.*, 2010, **132**, 13332–13345.
56. A. Glüer, M. Förster, V. R. Celinski, J. Schmedt auf der Günne, M. C. Holthausen and S. Schneider, *ACS Catal.*, 2015, **5**, 7214–7217.
57. A. N. Marziale, A. Friedrich, I. Klopsch, M. Drees, V. R. Celinski, J. Schmedt auf der Günne and S. Schneider, *J. Am. Chem. Soc.*, 2013, **135**, 13342–13355.
58. M. Käß, A. Friedrich, M. Drees and S. Schneider, *Angew. Chem. Int. Ed.*, 2009, **48**, 905–907.
59. A. Staubitz, A. Presa Soto and I. Manners, *Angew. Chem. Int. Ed.*, 2008, **47**, 6212–6215.
60. N. Blaquiere, S. Diallo-Garcia, S. I. Gorelsky, D. A. Black and K. Fagnou, *J. Am. Chem. Soc.*, 2008, **130**, 14034–14035.
61. G. J. Kubas, *Metal Dihydrogen and σ-Bond Complexes*, Springer, New York, 2001.
62. R. N. Perutz and S. Sabo-Etienne, *Angew. Chem. Int. Ed.*, 2007, **46**, 2578–2592.
63. H. C. Johnson, A. P. Robertson, A. B. Chaplin, L. J. Sewell, A. L. Thompson, M. F. Haddow, I. Manners and A. S. Weller, *J. Am. Chem. Soc.*, 2011, **133**, 11076–11079.
64. A. Kumar, H. C. Johnson, T. N. Hooper, A. S. Weller, A. G. Algarra and S. A. Macgregor, *Chem. Sci.*, 2014, **5**, 2546–2553.

65. L. Luconi, E. S. Osipova, G. Giambastiani, M. Peruzzini, A. Rossin, N. V. Belkova, O. A. Filippov, E. M. Titova, A. A. Pavlov and E. S. Shubina, *Organometallics*, 2018, **37**, 3142–3153.
66. M. R. Elsby and R. T. Baker, *Chem. Soc. Rev.*, 2020, **49**, 8933–8987.
67. J. R. Khusnutdinova and D. Milstein, *Angew. Chem. Int. Ed.*, 2015, **54**, 12236–12273.
68. T. M. Boyd, K. A. Andrea, K. Baston, A. Johnson, D. E. Ryan and A. S. Weller, *Chem. Commun.*, 2020, **56**, 482–485.
69. G. M. Adams, A. L. Colebatch, J. T. Skornia, A. I. McKay, H. C. Johnson, G. C. Lloyd-Jones, S. A. Macgregor, N. A. Beattie and A. S. Weller, *J. Am. Chem. Soc.*, 2018, **140**, 1481–1495.
70. A. Kumar, N. A. Beattie, S. D. Pike, S. A. Macgregor and A. S. Weller, *Angew. Chem. Int. Ed.*, 2016, **55**, 6651–6656.
71. M. Rosello-Merino, J. Lopez-Serrano and S. Conejero, *J. Am. Chem. Soc.*, 2013, **135**, 10910–10913.
72. R. H. Crabtree, *Chem. Rev.*, 2015, **115**, 127–150.
73. J. Li, S. M. Kathmann, H. S. Hu, G. K. Schenter, T. Autrey and M. Gutowski, *Inorg. Chem.*, 2010, **49**, 7710–7720.
74. P. Hasche, J. Haak, F. Anke, C. Kubis, W. Baumann, H. J. Drexler, H. Jiao and T. Beweries, *Cat. Sci. Technol.*, 2021, **11**, 3514–3526.
75. F. Anke, D. Han, M. Klahn, A. Spannenberg and T. Beweries, *Dalton Trans.*, 2017, **46**, 6843–6847.
76. A. Johnson, A. J. Martinez-Martinez, S. A. Macgregor and A. S. Weller, *Dalton Trans*, 2019, **48**, 9776–9781.
77. S. D. Thomas, R. C. Da Costa and G. R. Owen, *Organometallic Chemistry: Volume 43*, The Royal Society of Chemistry, 2020.
78. M. C. Denney, V. Pons, T. J. Hebden, D. M. Heinekey and K. I. Goldberg, *J. Am. Chem. Soc.*, 2006, **128**, 12048–12049.
79. T. J. Hebden, M. C. Denney, V. Pons, P. M. B. Piccoli, T. F. Koetzle, A. J. Schultz, W. Kaminsky, K. I. Goldberg and D. M. Heinekey, *J. Am. Chem. Soc.*, 2008, **130**, 10812–10820.
80. T. Li, R. Churlaud, A. J. Lough, K. Abdur-Rashid and R. H. Morris, *Organometallics*, 2004, **23**, 6239–6247.
81. E. H. Kwan, H. Ogawa and M. Yamashita, *ChemCatChem*, 2017, **9**, 2457–2462.
82. D. E. Ryan, K. A. Andrea, J. J. Race, T. M. Boyd, G. C. Lloyd-Jones and A. S. Weller, *ACS Catal.*, 2020, **10**, 7443–7448.
83. E. A. K. Spearing-Ewyn, N. A. Beattie, A. L. Colebatch, A. J. Martinez-Martinez, A. Docker, T. M. Boyd, G. Baillie, R. Reed, S. A. Macgregor and A. S. Weller, *Dalton Trans.*, 2019, **48**, 14724–14736.
84. C. Peng, W. Liu and Y. Wang, *New J. Chem.*, 2023, **47**, 6661–6672.
85. G. M. Adams, D. E. Ryan, N. A. Beattie, A. I. McKay, G. C. Lloyd-Jones and A. S. Weller, *ACS Catal.*, 2019, **9**, 3657–3666.
86. G. C. Fortman, A. M. Z. Slawin and S. P. Nolan, *Organometallics*, 2011, **30**, 5487–5492.
87. I. Göttker-Schnetmann, P. S. White and M. Brookhart, *Organometallics*, 2004, **23**, 1766–1776.
88. J. A. Widegren and R. G. Finke, *J. Mol. Catal. A: Chem.*, 2003, **198**, 317–341.
89. B. L. Dietrich, K. I. Goldberg, D. M. Heinekey, T. Autrey and J. C. Linehan, *Inorg. Chem.*, 2008, **47**, 8583–8585.
90. P. Colombo, G. Mera, R. Riedel and G. D. Sorarù, *J. Am. Ceram. Soc.*, 2010, **93**, 1805–1837.
91. E. Papanasam, P. K. B, C. B, E. Manikandan and L. Agarwal, *Silicon*, 2022, **14**, 12887–12900.
92. S. Frueh, R. Kellett, C. Mallery, T. Molter, W. S. Willis, C. King'ondu and S. L. Suib, *Inorg. Chem.*, 2011, **50**, 783–792.

93. P. J. Fazen, J. S. Beck, A. T. Lynch, E. E. Remsen and L. G. Sneddon, *Chem. Mater.*, 1990, **2**, 96–97.
94. L. G. Sneddon, M. G. L. Mirabelli, A. T. Lynch, P. J. Fazen, K. Su and J. S. Beck, *Pure Appl. Chem.*, 1991, **63**, 407–410.
95. P. J. Fazen, E. E. Remsen, J. S. Beck, P. J. Carroll, A. R. McGhie and L. G. Sneddon, *Chem. Mater.*, 1995, **7**, 1942–1956.
96. T. Wideman and L. G. Sneddon, *Chem. Mater.*, 1996, **8**, 3–5.
97. P. M. B. Toury, D. Cornu, H. Vincent, J. Bouix, *Adv. Funct. Mater.*, 2002, **12**, 228–234.
98. B. Toury, S. Bernard, D. Cornu, F. Chassagneux, J.-M. Létoffé and P. Miele, *J. Mater. Chem.*, 2003, **13**.
99. D. Cornu, S. Bernard, S. Duperrier, B. Toury and P. Miele, *J. Eur. Ceram. Soc.*, 2005, **25**, 111–121.
100. V. Salles, S. Bernard, A. Brioude, D. Cornu and P. Miele, *Nanoscale*, 2010, **2**, 215–217.

Chapter 2: Baselining of kinetics and speciation

The *in situ* flow NMR experiments presented in this chapter were carried out in collaboration with Dr Ulrich Hintermair at the DReaM Facility, situated at the University of Bath. The experimental work was conducted by myself with Dr Catherine Lyall and Dr John Lowe carrying out the NMR data acquisition. The EXSY NMR experiments were conducted by Professor Simon Duckett at the University of York.

2.1 Introduction

As discussed in section 1.3, precise gearing of both the dehydrogenation and the polymerisation step of the 'cascade' dehydropolymerisation reaction to form polyaminoborane is required to achieve control over the polymer properties. These processes need to be understood in order to achieve control. The relative barriers for the dehydrogenation of amine-boranes and polymerisation of aminoborane are $\Delta G^{\ddagger}$ >17 kcal mol^{-1} and ~8 kcal mol^{-1}, respectively.[1-3] This means that dehydrogenation is rate limiting, while polymerisation determines the selectivity of product formation. The use of eudiometric measurements allows for the interrogation of the dehydrogenation process in the reaction, whereas the ability to monitor and understand the polymerisation reaction is much more challenging. The monomer ($H_2B{=}NHMe$) that is formed by the dehydrogenation step is very reactive and transient; it is not observed by analytical techniques such as ^{11}B NMR spectroscopy. In the following Chapters 2 and 3, based on kinetics studies and mechanistic interpretation, the two processes will be decoupled. The kinetic and mechanism discussion refers only to the dehydrogenation process. The polymerisation process will be discussed in more detail in Chapter 4.

Ir(^{t}Bu-POCOP)$(H)_2$ (**1**) was shown by both Goldberg and Manners to be a competent dehydrocoupling catalyst for amine-boranes as discussed in section 1.6.[4-7] Based on the evidence presented, at low concentrations of amine-borane (*e.g.* 0.5 M), cyclic pentamer $[H_2N{\cdot}BH_2]_5$, was formed while at higher concentrations (*e.g.* 2 M) the formation of linear

polyaminoborane was favoured. Goldberg identified two complexes present during the reaction, Ir(^{t}Bu-POCOP)(H)$_2$(BH$_3$) (**2**) and Ir(^{t}Bu-POCOP)(H)$_4$ (**3**). There was limited kinetic data discussed for the substrates ($H_3B{\cdot}NH_3$ and $H_3B{\cdot}NH_2Me$), and no conclusions drawn in terms of a mechanism. This chapter includes the baselining of the kinetics of this reaction, and the determination of an unexpected induction period. These observations are followed by an in-depth report on the speciation of Ir(^{t}Bu-POCOP)(H)$_2$ (**1**) during the dehydropolymerisation of $H_3B{\cdot}NH_2Me$.

2.2 Initial findings from reaction of Ir(^{t}Bu-POCOP)(H)$_2$ with $H_3B{\cdot}NH_2Me$

Ir(^{t}Bu-POCOP)(H)$_2$ was synthesised as a red/brown microcrystalline powder (81% yield) according to the reported synthetic route outlined in Scheme 2.1.[8, 9]

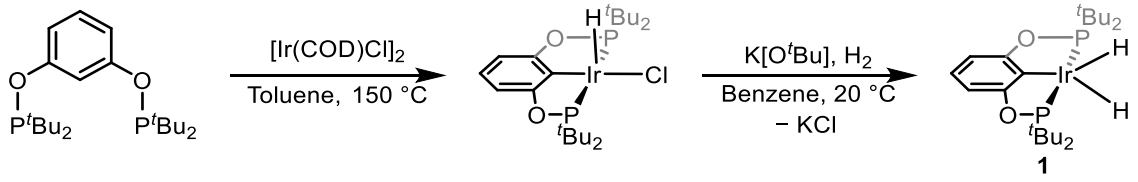

Scheme 2.1. Synthetic route to form complex **1**.[8, 9]

Initial experiments were carried out to gain a basic understanding of the kinetic profile and length/duration of the dehydropolymerisation of $H_3B{\cdot}NH_2Me$. Conditions were chosen that mirrored some of those reported by Manners[10] so that the molecular weight of the polymer could be compared (See Chapter 4).

In all cases the reaction reached completion, as shown by >99% conversion observed in the ^{11}B NMR spectrum that was recorded from an aliquot of the reaction mixture at the end of catalysis. The spectrum also highlighted the selectivity of the catalyst with <1% of other BN products observed such as borazine (δ 33.2),[11] see Figure 2.1 for a representative example. Precipitation of the THF/polymer solution into pentane yielded an off-white powder (yields of 52-74%). This reduction is attributed to loss of material during the precipitation, as the ^{11}B NMR spectrum shows that >99% of the monomer was converted to polymer in the reaction.

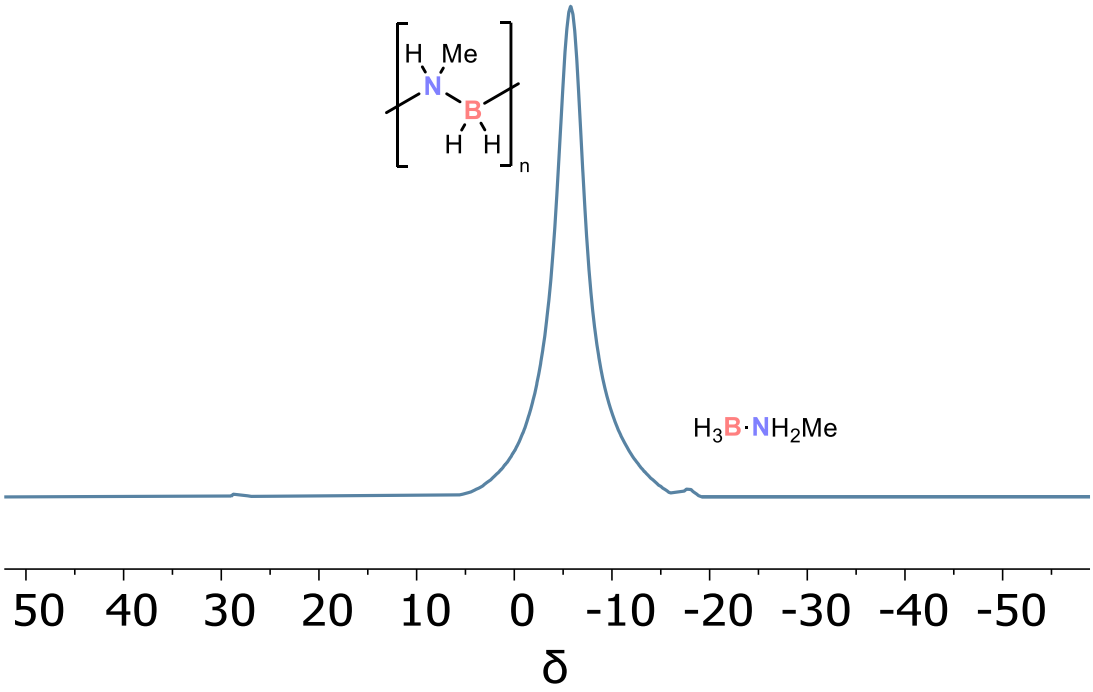

Figure 2.1. Representative ^{11}B NMR spectrum taken on catalysis completion showing >99% conversion and >99% selectivity for formation of polyaminoborane under standard conditions, H^8-THF, 193 MHz, 298 K.

In order to measure the kinetics of the reaction, the volume of hydrogen gas produced was measured eudiometrically. As the moles of hydrogen produced are proportional to the moles of aminoborane that are formed, the evolution of hydrogen can be used to monitor kinetics and thus polymer formation. All of the kinetic plots in this thesis are presented in equivalents of hydrogen evolved rather than [aminoborane], see Figure 2.2. As mentioned in section 1.3.1 the release of more than one equivalent of hydrogen gas in the dehydropolymerisation reaction can result in the formation of other dehydrocoupled products such as borazine (2 equivalents) and polyborazylene (>2 equivalents). However, if there is more than one equivalent of hydrogen released but no evidence in the ^{11}B NMR spectrum of formation of dehydrocoupled by-products, then there must be another cause. Two potential explanations are THF evaporation (see experimental) or formation of hydrogen during the induction period. Due to the additional gas evolved the [aminoborane] would be higher than the [amine-borane] starting material. Therefore, graphs of equivalents of hydrogen evolved against time are

presented in all cases to show the kinetic profile and the relationships between different conditions. Graphs of [aminoborane] against time were used to determine the rate of reaction from the pseudo-zero order regime of the linear region of the kinetic profile (the area of maximum rate). A representative example of the two graphs can be found in Figure 2.2. In all cases the raw data is presented without normalisation. Error for the rates were calculated in Microsoft Excel using the linear regression function (LINEST). For detailed discussion into conditions and experimental set up see Chapter 7.

Initial studies were carried out using catalyst **1** for the dehydropolymerisation of $H_3B{\cdot}NH_2Me$ (THF, 20 °C, 2 M [$H_3B{\cdot}NH_2Me$], 0.1 mol% [Ir] (2 mM)), and from this point on these will be referred to as standard conditions. A solution of **1** in THF was added to solid $H_3B{\cdot}NH_2Me$, this resulted in an induction period of ~300 s before fast H_2 release (k_{obs} = 5.93(3) mM s^{-1}). The start of hydrogen release is a sharp event; this suggests that the catalyst is being conscripted elsewhere. The release of H_2 clearly exhibits a pseudo zero order regime before deceleration, Figure 2.1.

Reproducibility of the reaction was exemplified in Figure 2.2, there are three overlayed kinetic profiles that show the reproducibility of the kinetics (k_{obs} = 6.1 ± 0.2 mM s^{-1}). The starting material was purified by dissolution in minimal OEt_2 and recrystallisation at –20 °C before filtering and drying of the solids *in vacuo*. Recrystallised $H_3B{\cdot}NH_2Me$ was used for all kinetic experiments but there were some observed differences in the kinetic profiles with regards to induction periods with variation between 100 s and 300 s dependant on the 'batch' of $H_3B{\cdot}NH_2Me$ (Figure 2.1). This is likely due to different water contents in the material; attempts were made to quantify this but a peak residual water peak was not visible in the ^1H NMR spectrum of the starting material in dry deuterated solvent. The effect of water on the reaction kinetics will be discussed in more detail in section 2.5. To limit the effect if this on kinetic analysis, all kinetic experiments were carried out using the same crop of recrystallised material.

Analysis of the reaction mixtures by ^{11}B NMR spectroscopy shows that the reactions are in almost all cases >99% selective for polymer formation, with full conversion of monomer to polymer. The isolated yields of the reactions are between 40 to 80%, the lower-than-expected isolated yield is proposed to be due to material loss on precipitation of the polymer by pentane, prior to filtering and drying *in vacuo*. There may also be some material loss when transferring the polymer from the reaction vessel to a weighing boat.

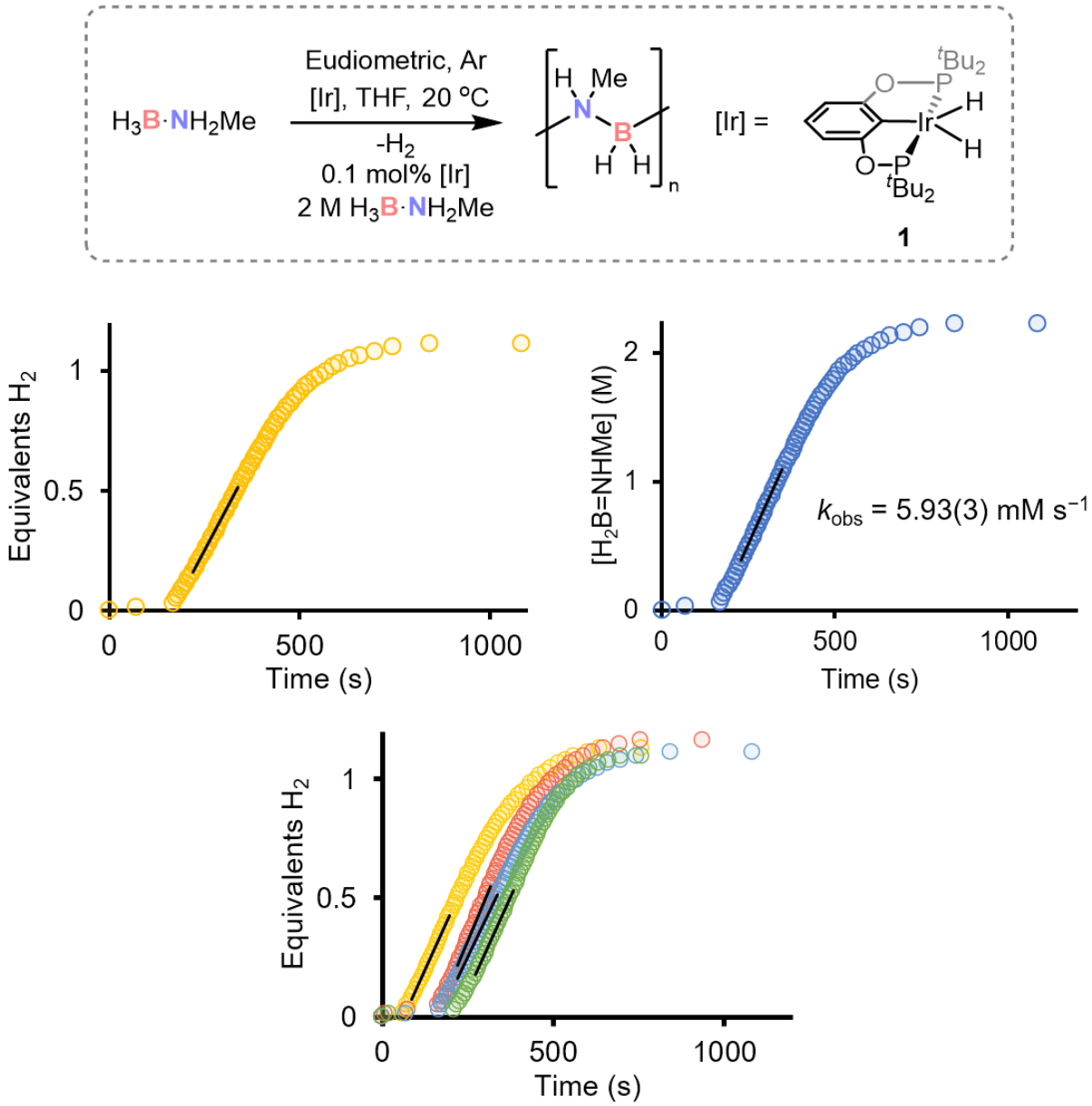

Figure 2.2. Representative kinetic profile for the dehydropolymerisation of $H_3B{\cdot}NH_2Me$ with **1** under standard conditions (THF, 20 °C, 2 M [$H_3B{\cdot}NH_2Me$], 0.1 mol% [Ir] (2 mM)).

Although induction periods are not uncommon for amine-borane dehydropolymerisations,[3, 12-16] the observed induction period was unexpected for this catalyst, as it had not been reported previously by either Goldberg or Manners.[4-7] In most cases the induction periods observed in amine-borane dehydropolymerisation are due to the slow initial formation of the active homogeneous catalyst. Alternatively, they can be attributed to formation of nanoparticles which often result in sigmoidal shaped kinetic profiles,[17] and would be indicative of a heterogeneous *i.e.* Ir(0) colloidal process rather than homogeneous catalysis.[16, 18]

2.2.1 Poisoning experiments

Visual inspection of the catalysis mixture on addition of **1** to $H_3B{\cdot}NH_2Me$ revealed a clear, light-yellow solution (Figure 2.3 A). No darkening or particles indicative of the formation of iridium nanoparticles were observed.[16] Additionally, a series of poisoning experiments were carried out to determine the nature of the catalysis.[17] Hg(0) can be used to identify heterogeneous processes through the suppression of catalysis by Hg(0) adsorption onto the metal surface blocking the reactive sites. The mercury poisoning experiment is not definitive by itself; while Hg(0) forms amalgams with other metals (*e.g.* Pt and Pd), it does not form amalgams with iridium.[17] Alternatively, the use of <1 equivalent of PMe_3 in catalysis can identify a heterogenous system by binding strongly to the nanoparticle, covering its surface and halting catalysis, but will only partially suppress a homogenous system if the PMe_3 binds strongly to the metal.[17] An alternate indicator of nanoparticle formation is a sigmoidal kinetic profile, reported by Finke and coworkers.[18, 19]

These experiments were carried out under the standard with the addition of excess Hg(0) or 0.5 equivalents of PMe_3 after ~50 and ~25% conversion respectively, conditions chosen to allow for the formation of nanoparticles. As can be seen in Figure 2.3, neither Hg(0) or PMe_3 had an effect on catalysis, with similar profiles under standard conditions without the addition of the additives. It is important to note that while addition of 0.5 equivalents of PMe_3 had no

effect on catalysis the addition of 5 equivalents of PMe_3 shuts down catalysis, likely through the formation of Ir(^{t}Bu-POCOP)$(H)_2(PMe_3)$ similar to the PPh_3 analogue reported by Findlater and co-workers.[20] This indicates that PMe_3 does not bind strongly to dihydride complex **1**.

The negative results for heterogeneous catalysis from the Hg(0) and PMe_3 tests in combination with the absence of visual nanoparticle formation, and a lack of a sigmoidal kinetic profile,[18] suggests that catalysis is homogeneous.

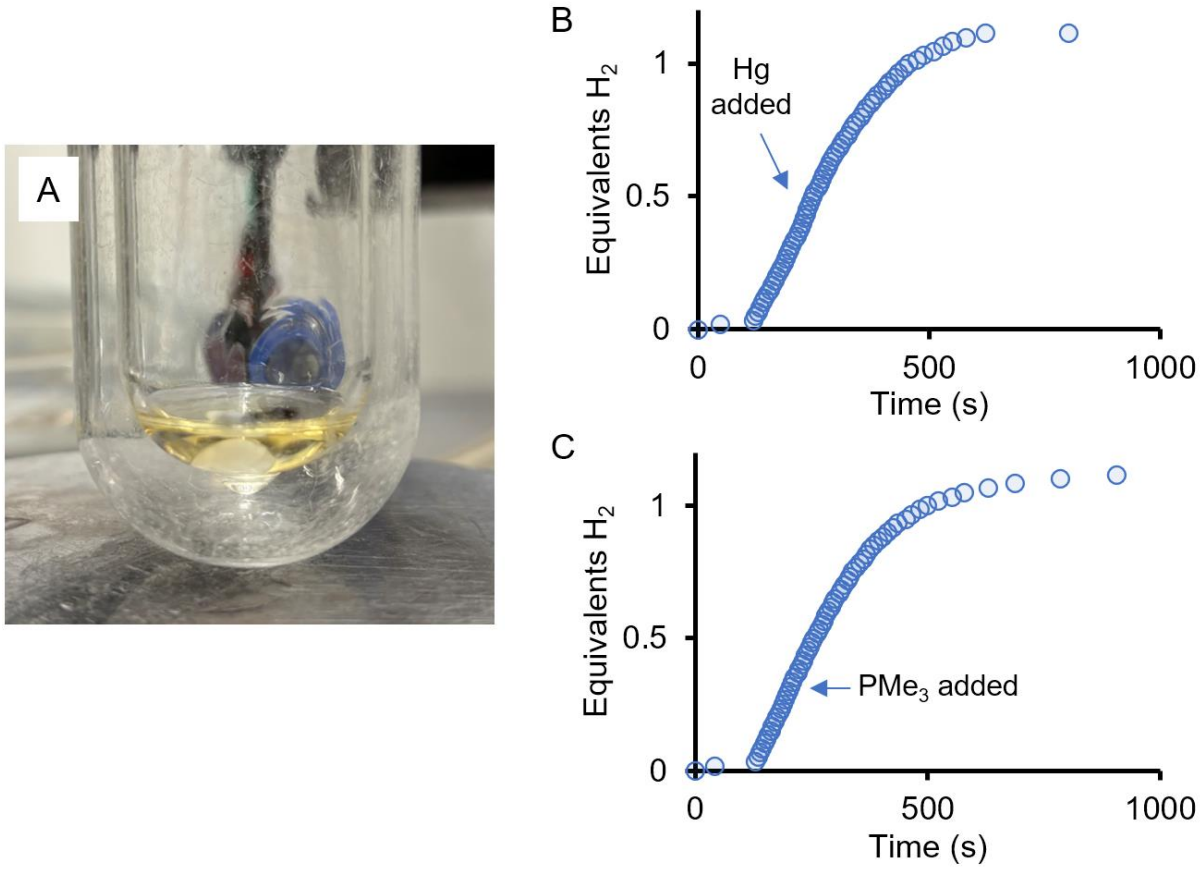

Figure 2.3. A) Image of reaction solution at the end of catalysis, showing a clear, light-coloured solution. Poisoning experiments to determine if the dehydropolymerisation of $H_3B{\cdot}NH_2Me$ with **1** is homogeneous or heterogeneous. B) excess Hg(0), C) 0.5 equivalents PMe_3.

2.3 Speciation

2.3.1 Speciation on completion of catalysis

All dehydropolymerisation catalytic experiments were analysed by NMR spectroscopies upon catalysis completion (under standard condition ~20 minutes). Two different iridium hydride complexes were routinely observed in the ^1H and $^{31}P\{^1H\}$ NMR spectra (Figure 2.4). The first

was observed as a broad singlet in the ^{1}H NMR spectrum at δ –8.6, and a singlet in the ^{31}P{^{1}H} NMR spectrum at δ 183. These signals were assigned to previously reported Ir(^{t}Bu-POCOP)(H)$_4$ (**3**), as evident by independent synthesis from the reaction of **1** and H_2 (4 bar) in THF.[21] For the other complex, a hydride resonance was observed in the ^{1}H NMR spectrum (triplet, δ –20.7) and a singlet resonance in the ^{31}P{^{1}H} NMR spectrum at δ 170. These signals were assigned as previously reported Ir(^{t}Bu-POCOP)(H)$_2$(BH$_3$) (**2**), after independent synthesis from reaction of **1** with THF·BH$_3$.[22] The other hydride signals associated with **2** were not observed at this catalyst concentration as they are broadened by interactions with quadrupolar boron (spin – ^{11}B = 3/2, ^{10}B = 3). The observation of complexes **2** and **3** at the end of catalysis was in agreement with that which Goldberg and coworkers reported for reactions of **1** with H$_3$B·NH$_3$.[4] The formation of complex **2** occurs due to the dissociation of H$_3$B·NH$_2$Me as discussed in Chapter 1, with formation of NH$_2$Me as a by-product when borohydride complex **2** is formed. Interestingly, complex **2** is not always present at the end of catalysis and the amount observed is variable, even for repeat experiments of the same reaction conditions.

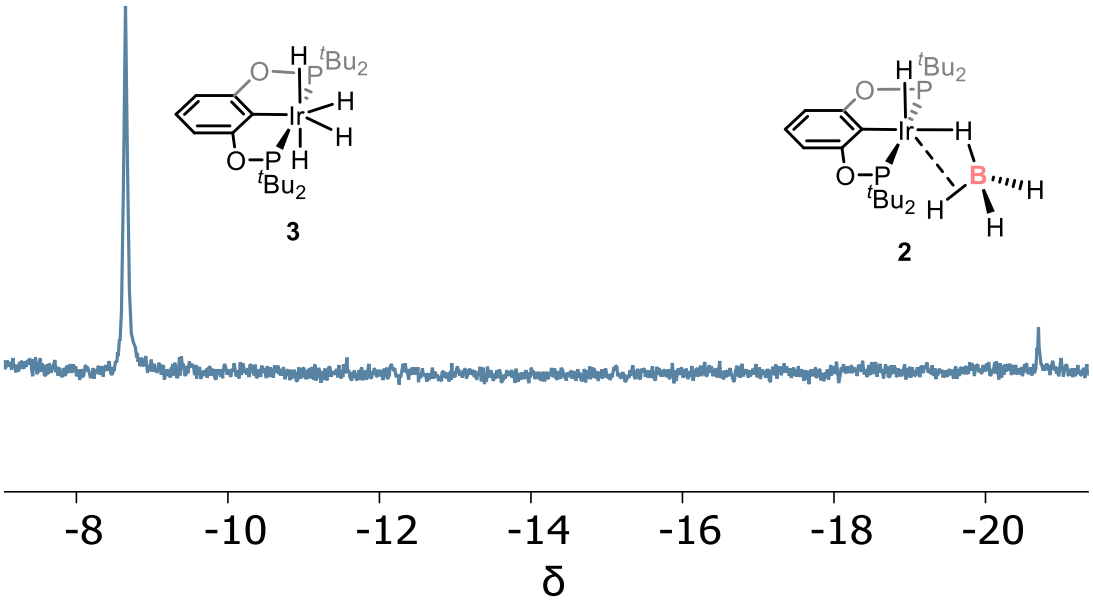

Figure 2.4. Hydride region of an example ^{1}H NMR spectrum (THF-H^{8}, 600 MHz, 298 K) taken on catalysis completion showing **2** and **3**. Conditions: 2 M [H$_3$B·NH$_2$Me], 0.1 mol% [Ir] (2 mM), THF, 20 °C.

The observation of complex **3** as the major species was rationalised in Paul and Musgrave's theoretical study of the dehydropolymerisation of $H_3B{\cdot}NH_3$ with catalyst **1,** discussed in Chapter 1, due to **3** being the most thermodynamically stable complex (resting state).[2] Whilst Paul and Musgrave propose that there are two barriers that influence the rate of reaction, the experimental observation of complex **3** as the resting state might indicate that hydrogen loss is the rate determining step, as has been shown in other reported amine-borane dehydropolymerisation mechanisms; this will be returned to later.[3, 23]

2.3.2 *In situ* speciation studies

The most useful form of analysis used to identify catalytic intermediates for this type of reaction is NMR spectroscopy, especially in cases where the catalysts contain phosphorus atoms and/or hydride signals as the latter are shifted significantly up-field in a region of the ^{1}H NMR spectrum that is generally clear of aliphatic or aromatic signals. These two factors allow for the signals from the catalyst to be deconvoluted from the protio solvent, as well as the formed polymer signals themselves. One challenge of studying the speciation of dehydropolymerisation reactions using NMR spectroscopy is the hydrogen production, as not only does this result in large pressure build up in NMR tubes, but effervescence can also cause issues with spectral resolution.[24]

2.3.3 Low-temperature speciation studies by NMR spectroscopies

To gain some insight into the speciation of complex **1** during the catalytic cycle, three separate catalytic runs were set up under the following conditions (2 M $H_3B{\cdot}NH_2Me$, 2 mM [Ir], 10 °C). The temperature was controlled to 10 °C to slow the rate of reaction and allow an aliquot to be taken from the reaction mixture. The reactions were allowed to run to a desired point of conversion (Figure 2.5), as informed by the production of measured hydrogen gas evolution, then an aliquot of the catalyst solution was transferred into a pre-cooled NMR tube (179 K) to thermally quench the reaction and stop further hydrogen production. The NMR tubes were then stored in liquid nitrogen until rapidly thawed in a liquid nitrogen/ethyl acetate mixture and

put into a pre-cooled NMR spectrometer at 198 K for analysis. To limit the risk of explosion through build-up of pressure, NMR experiments were carried out in high pressure NMR tubes rated up to 12 bar pressure and the taps were fitted with HPLC tubing that was connected to a 5 bar pressure release valve as a safety precaution. The NMR tube, HPLC tubing and pressure release valve were all under an argon atmosphere.

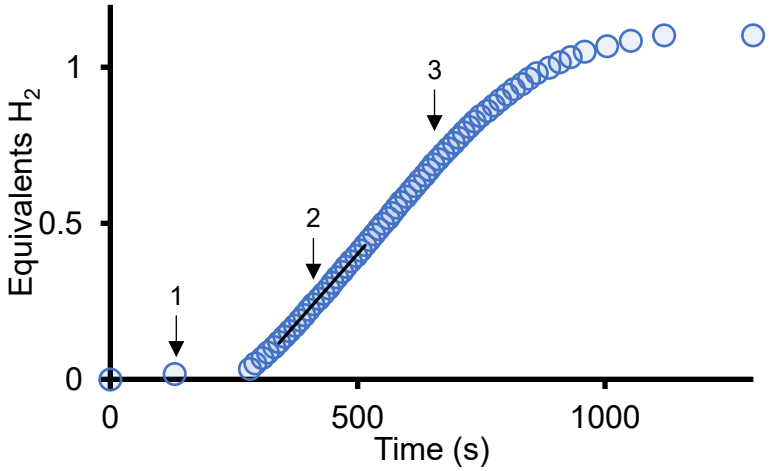

Figure 2.5. Eudiometric measurement of H_2 release using pre-catalyst Ir(^{t}Bu-POCOP)$(H)_2$ Conditions: 2M $H_3B{\cdot}NH_2Me$, 0.1 mol% catalyst loading, 20 °C. Each arrow indicates a sampling point.

Analysis of time point 1 (150 s) showed that there were three species present in the ^{1}H NMR spectrum, complexes **2** and **3**, and a third unknown complex with a resonance at δ –10.5 (Figure 2.6 A). The spectrometer was warmed to –15 °C and catalysis allowed to resume for 20 minutes and followed by ^{1}H NMR spectroscopy (Figure 2.6 B). In Figure 2.6 B at the 0-minute time point, borohydride complex **2** is observed with a broad peak at δ –20.2 that integrated to 1H. This shows that borohydride complex **2** is formed during the induction period, which is in contrast with Goldberg's report that **2** is formed only at long reaction times.[4] The other resonances associated with complex **2** at δ –5 and δ –6 were not observed as the resonances are broadened due to interactions with quadrupolar boron. The resonance at δ –8.2 indicated the presence of tetrahydride complex **3**, which at 258 K resolves as a triplet.[21] This resonance grows in over time, indicating that turnover occurs during this 20 minute time frame at –15 °C. A hydride resonance at δ –9.9 is present in the early time points of the

reaction (<10 minutes) and the identity of this species is unknown; it has a corresponding peak in the $^{31}P\{^{1}H\}$ NMR spectrum (δ 177). One possible identity of this complex may be a H_2O or $[OH]^-$ complex, formed from adventitious water in the substrate and the solvent. An example of a hydroxide complex formed from a dehydropolymerisation reaction was discussed in Chapter 1.[15]

The only iridium complex observed in the ^{1}H and $^{31}P\{^{1}H\}$ NMR spectra of timepoints 2 (25% conversion) and 3 (75% conversion) was complex **3**. As previously stated, this is proposed to be the catalyst resting state.

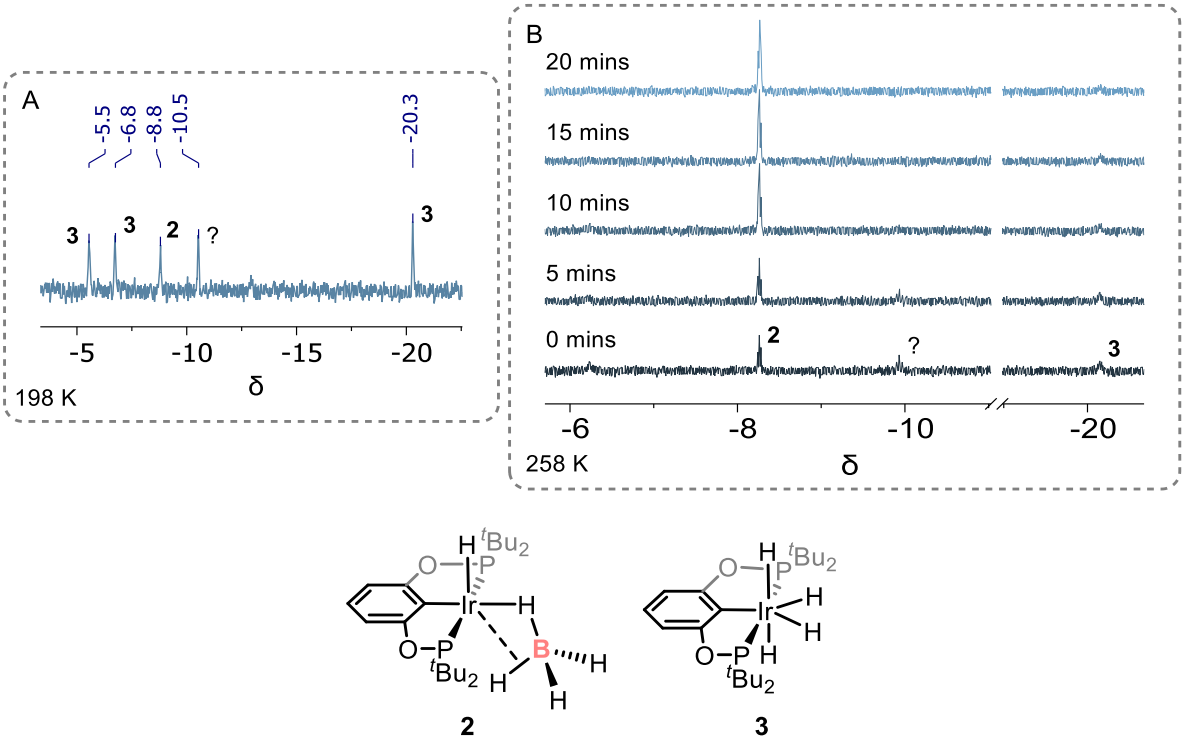

Figure 2.6. Hydride region of the ^{1}H NMR spectra (500 MHz, 198 K, THF-H^8) of Ir(^{t}Bu-POCOP)$(H)_2$ and $H_3B{\cdot}NH_2Me$ a) sampled at 150 s (500 MHz, 198 K, THF-H^8) b) progressing at –15 °C (500 MHz, 258 K, THF-H^8).

2.3.4 *In operando* speciation by flow NMR

The experiments discussed in section 2.3.3 give an indication of the speciation at three points during catalysis. However, these data are sparse and may not be an accurate representation of the speciation during catalysis, as these reactions were carried out in a sealed NMR tube, whereas all kinetic measurements are carried out eudiometrically under isobaric conditions

(1 bar H_2). In order to gain more information about the speciation during catalysis, the reaction was monitored by ^{1}H, $^{31}P\{^{1}H\}$ and ^{11}B NMR spectroscopy under continuous, looped flow conditions, using ^{1}H selective excitation experiments to increase signal intensities in the hydride region. The ability to monitor the reaction in flow allowed for dense data collection as well as *in operando* monitoring and the mitigation of the risk of hydrogen gas build up in a static system. The reaction was carried out in a round-bottom flask cooled to –7 °C using a circulating cooler. The flow apparatus allowed for constant mixing of the bulk reaction mixture while simultaneous data collection occurred in the spectrometer. This allowed for a more accurate picture of speciation during catalysis as well as reaction monitoring. The flow NMR experiments were carried out in collaboration with Dr Ulrich Hintermair at the DReaM Facility, situated at the University of Bath. The experimental work was conducted by myself with Dr Catherine Lyall and Dr John Lowe carrying out the NMR data acquisition. Further experimental details and information about the flow set-up can be found in Chapter 7.

The catalytically relevant complexes identified (*e.g.* **2** and **3**) have diagnostic hydride signals, therefore the upfield region (δ –6 to –26) was selected as the focus of the ^{1}H selective excitation experiments. The use of the selective excitement experiment over a standard ^{1}H NMR experiment results in significant signal enhancement. The resulting data is represented in Figure 2.7 as a graph of the normalised hydride signal ratios (optimal conditions: 0.5 M $H_3B{\cdot}NH_2Me$, 0.1 mol% [Ir], –7 °C (measured at the probe), and $Cr(tmhd)_3$ as a relaxation agent).[25] Further experimental details can be found in Chapter 7 and the original spectra can be found in the appendix.

It is evident from the integral vs time plot (Figure 2.7) that borohydride complex **2** was formed immediately upon addition of $H_3B{\cdot}NH_2Me$ to complex **1** at 332 s. There is also a small amount of tetrahydride complex **3** formed at this time. At around 950 s there is a sharp change and the relative concentration of **3** increases while the relative concentration of **2** decreases rapidly until it is no longer seen in the spectra. After ~1500 s **3** is the major species, similar to that

observed for timepoints 2 and 3 in the static low temperature NMR experiments as discussed in section 2.3.3. Complex **3** is also the major species observed in the NMR spectra taken at the end of catalysis. As was observed for the low-temperature experiments discussed in section 2.3.3, during the induction period small amounts of an unknown hydride signal were observed at δ –10.4, the identity of the species remains unknown. The reaction was repeated under flow conditions and $^{31}P\{^{1}H\}$ NMR spectra recorded; the data were in agreement with the speciation identified during the selective excitation ^{1}H NMR spectroscopy experiments.

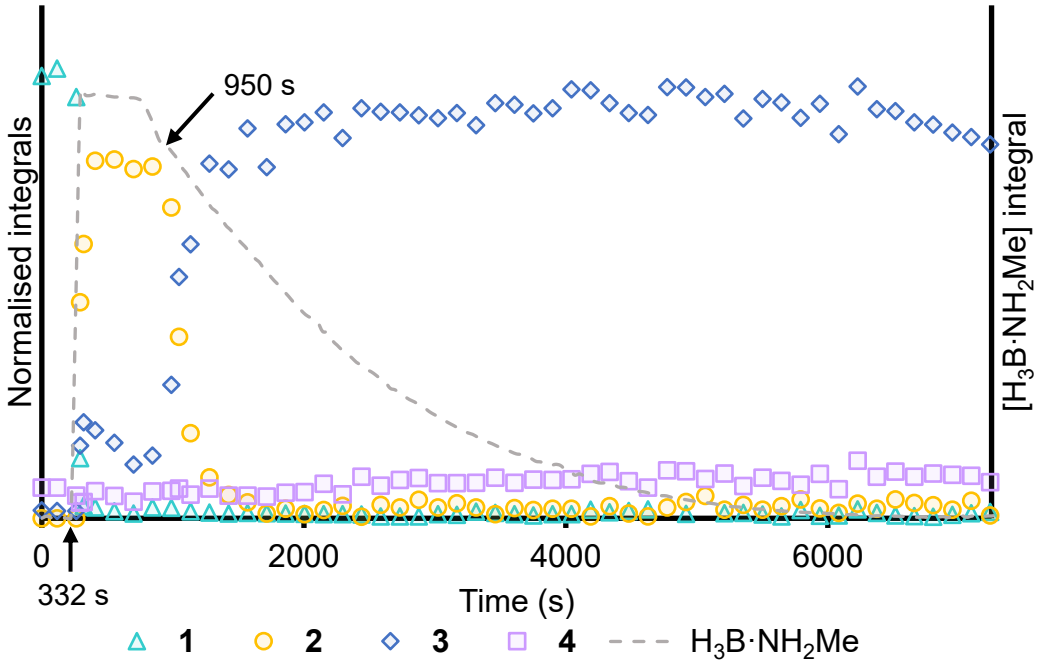

Figure 2.7. Graph showing speciation of catalyst throughout reaction from ^{1}H NMR spectroscopy (500 MHz, 266 K, THF-H^8) selective excitation experiments, with $H_3B{\cdot}NH_2Me$ consumption from ^{11}B NMR spectra (160 MHz, 266 K, THF-H^8).

The ^{11}B NMR data (Figure 2.7) shows the concentration of $H_3B{\cdot}NH_2Me$ in the solution measured from the integral of $H_3B{\cdot}NH_2Me$ in the ^{11}B NMR spectra. Addition of $H_3B{\cdot}NH_2Me$ at 332 s is indicated by an arrow; the concentration of $H_3B{\cdot}NH_2Me$ remains constant during the induction period until ~730 s where the substrate starts to be consumed. The speciation data paired with the conversion data from the ^{11}B NMR spectra (Figure 2.7) shows that the major species during the induction period is borohydride complex **2** with minor amounts (<25%) of tetrahydride **3**. As the catalyst starts turning over, consuming $H_3B{\cdot}NH_2Me$ and producing

hydrogen, the relative amount of **2** decreases while the amount of **3** increases. **3** remains the major species for the duration of catalysis.

Upon catalysis completion, as shown by the complete consumption of $H_3B{\cdot}NH_2Me$ (^{11}B NMR spectroscopy), small amounts of Ir(^{t}Bu-POCOP)$(H)_2(NH_2Me)$ (**4**) and complex **1** grow in. A reason for this is potential H_2 gas loss from the system that results in the favourable binding of NH_2Me over H_2. Equilibria between the discussed complexes (**1**-**4**) will be discussed in section 2.7.

2.4 Dehydropolymerisation of $H_3B{\cdot}NH_2Me$ with Ir(^{t}Bu-POCOP)$(H)_2(BH_3)$ (2)

To further understand the role of the borohydride complex **2** in catalysis during the induction period, **2** was synthesised independently according to the literature procedure[4] and used in a set of eudiometric experiments under standard conditions. Catalysis with complex **2** (Figure 2.8) resulted in a 10-fold increased induction period of ~3000 s compared to catalysis with **1** (~300 s). The eventual rate of reaction of catalysis with pre-catalyst **2** is also lower than **1**, k_{obs} = 4.44(2) mM s^{-1} and 5.93(3) mM s^{-1}, respectively. In conjunction with the insight gained from the flow NMR data discussed in section 2.3.4 this indicates that formation of complex **2** and then its consumption is involved in the induction period.

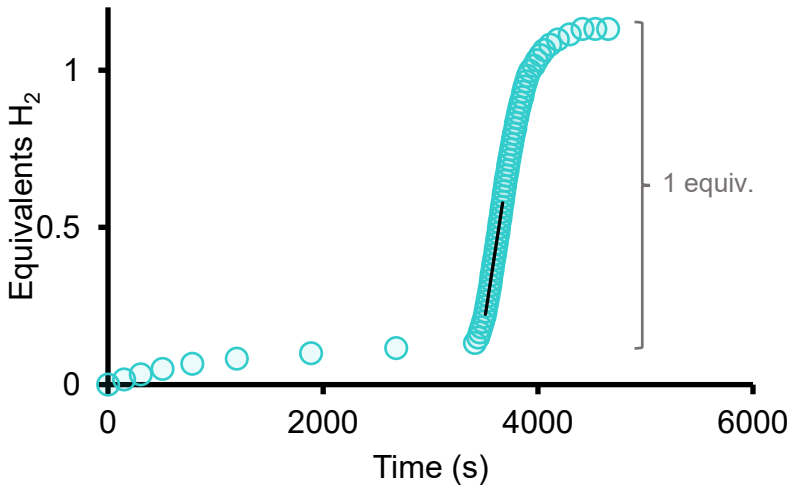

Figure 2.8. Dehydropolymerisation of $H_3B{\cdot}NH_2Me$ with Ir(^{t}Bu-POCOP)$(H)_2(BH_3)$ (**2**). Conditions: 0.1 mol% catalyst, 2 M $H_3B{\cdot}NH_2Me$, 293 K, 1.25 mL THF.

As evident in Chapter 1, the addition of NH_2Me to amine-borane dehydropolymerisations is well documented. The addition commonly results in the reduction of induction periods and/or an increased rate of turnover. Addition of NH_2Me (5 equiv.) to the reaction of **2** and $H_3B{\cdot}NH_2Me$ resulted in a significant decrease in the induction period and an increased rate of turnover (k_{obs} = 6.55(2) mM s^{-1}), Figure 2.9. This is in agreement with literature examples where NH_2Me is used to avoid or reverse formation of catalytically inactive borohydride species.[12, 13, 16, 26]

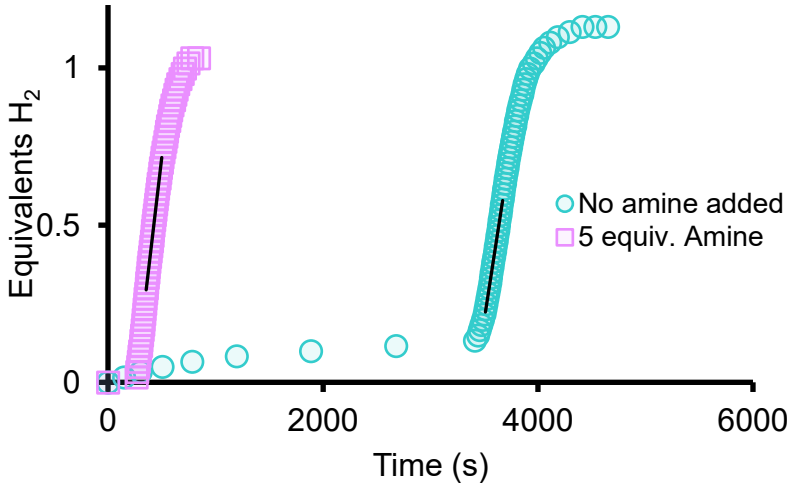

Figure 2.9. Dehydropolymerisation of $H_3B{\cdot}NH_2Me$ with Ir(^{t}Bu-POCOP)$(H)_2(BH_3)$ (**2**), showing the effect of 5 equivalents of NH_2Me (2 M in THF) on the rate and induction period.

The data collected indicates that NH_2Me present in the reaction affects the induction period. It is postulated that amine is required to form the active species in catalysis from dormant **3**. This would imply that the induction period is related to a lack of NH_2Me at the start of catalysis, then catalysis begins once NH_2Me builds up, potentially from dissociation of $H_3B{\cdot}NH_2Me$ or conscription of the catalyst in a process that forms NH_2Me.

2.5 Role of Ir(^{t}Bu-POCOP)$(H)_2(BH_3)$ during the induction period

In recent work from the Weller group, trace water has been shown to have a significant effect on the length of induction periods and turnover,[15] this was discussed in section 1.5.3. The authors found that adventitious water in 'dry' THF resulted in the formation of a catalytically

inactive species (ruthenium hydroxyhydride (Ru(OH)(H)(^{i}Pr$_2$PCH$_2$CH$_2$NH$_2$)$_2$) (**i-42**)) that the authors proposed as a resting state during the induction period as was discussed in Chapter 1.

A series of eudiometric measurements were carried out where the concentration of water in the THF solvent differed. The results of these experiments can be seen in Figure 2.10. A higher concentration of water in the THF resulted in faster turnover and a reduction in the induction period (Table 2.1). The promoting effect of excess water on catalysis with complex **1** was surprising as it contrasted what had been reported previously for another amine-borane dehydropolymerisation catalyst,[15] therefore further investigation was required to understand the role of water in catalysis with **1**.

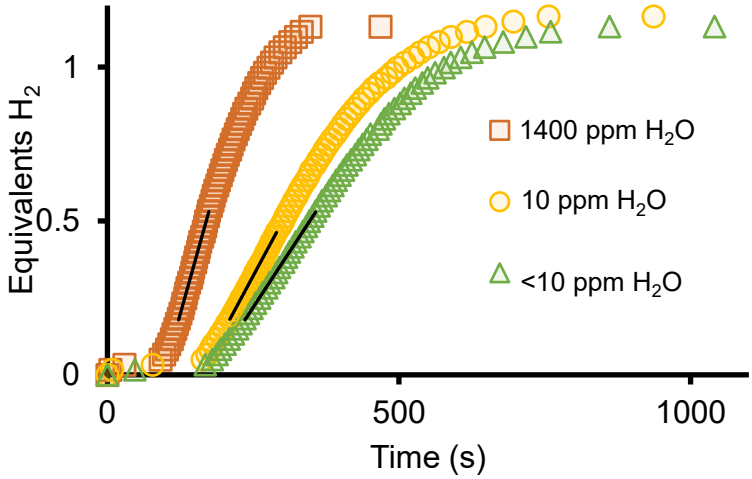

Figure 2.10. Dehydropolymerisation of $H_3B{\cdot}NH_2Me$ with Ir(^{t}Bu-POCOP)$(H)_2$, showing the effect of H_2O concentration in THF. Conditions: 2 M $H_3B{\cdot}NH_2Me$, 2 mM catalyst, THF, 293 K □ 1400 ppm H_2O ○ 10 ppm H_2O (stills) △ <10 ppm H_2O (dried over NaH, stored over K and distilled prior to use).

Table 2.1. Effect of [H_2O] on dehydropolymerisation with Ir(^{t}Bu-POCOP)$(H)_2$. Conditions: 2 M $H_3B{\cdot}NH_2Me$, 2 mM (0.1 mol%) of **1**, 293 K, THF. [a]Determined by the pseudo zero order region of the profile [b]Measured by ^{11}B NMR spectroscopy

Entry	H_2O (ppm)	Rate[a] (mM s^{-1})	Induction period (s)	Conv.[b] (%)	Selectivity[b] (%)	Isolated yield (%)
1	1400	13.5(1)	77	>99	>98	60
2	10	6.61(3)	163	>99	>99	59
3	<10	5.89(2)	168	>99	>99	70

Given that borohydride complex **2** has been shown to be the major species present during the induction period, experiments were carried out to analyse the effect of the addition of water to **2**. The addition of 20 equivalents of water to **2** resulted in immediate effervescence and formation of a white precipitate (Figure 2.11 A). Analysis of the THF solution by $^{31}P\{^{1}H\}$ NMR spectroscopy showed the formation of tetrahydride complex **3** as the only phosphorus-containing product (Figure 2.11 B). A resonance at δ 20.2 was observed in the ^{11}B NMR spectrum of the initial solution (THF, Figure 2.11 C), indicating the formation of boric acid.[27] Dissolution of the precipitate showed evidence of boric acid and borates (δ 20.2 and 2.7 respectively) in the ^{11}B NMR spectrum (ethanol, Figure 2.11 D).[27] A resonance (δ 1.8) suggestive of borate formation was also observed in the ^{11}B NMR spectrum (THF) taken after completion of catalysis for the dehydropolymerisation of $H_3B{\cdot}NH_2Me$ with **1** using THF with an additional 1400 ppm H_2O.

These observations combined with the flow NMR speciation data provide insight into what may be happening during the induction period. Catalytically inactive **2** forms readily on addition of $H_3B{\cdot}NH_2Me$ to **1**. It has been evidenced that the processing of adventitious water by borohydride complex **2** results in formation of tetrahydride complex **3**, borates and H_2, similar to that reported by Nolan and co-workers for the hydrolysis of $H_3B{\cdot}NH_3$ with an Ir(III)-NHC catalyst.[28] This process may explain the presence of **3** during the induction period in the flow NMR data, when there is little significant H_2 production from the dehydrogenation of $H_3B{\cdot}NH_2Me$ until ~780 s. This also may signal that during the induction period, borohydride complex **2** is conscripted away from the catalytic cycle processing H_2O from the starting material/solvent. A consequence of borohydride complex **2** being formed is the build-up of 'free' NH_2Me. NH_2Me may then allow for catalysis to start once the H_2O has been processed, this is observed as catalysis starting as a sharp event after the induction period.

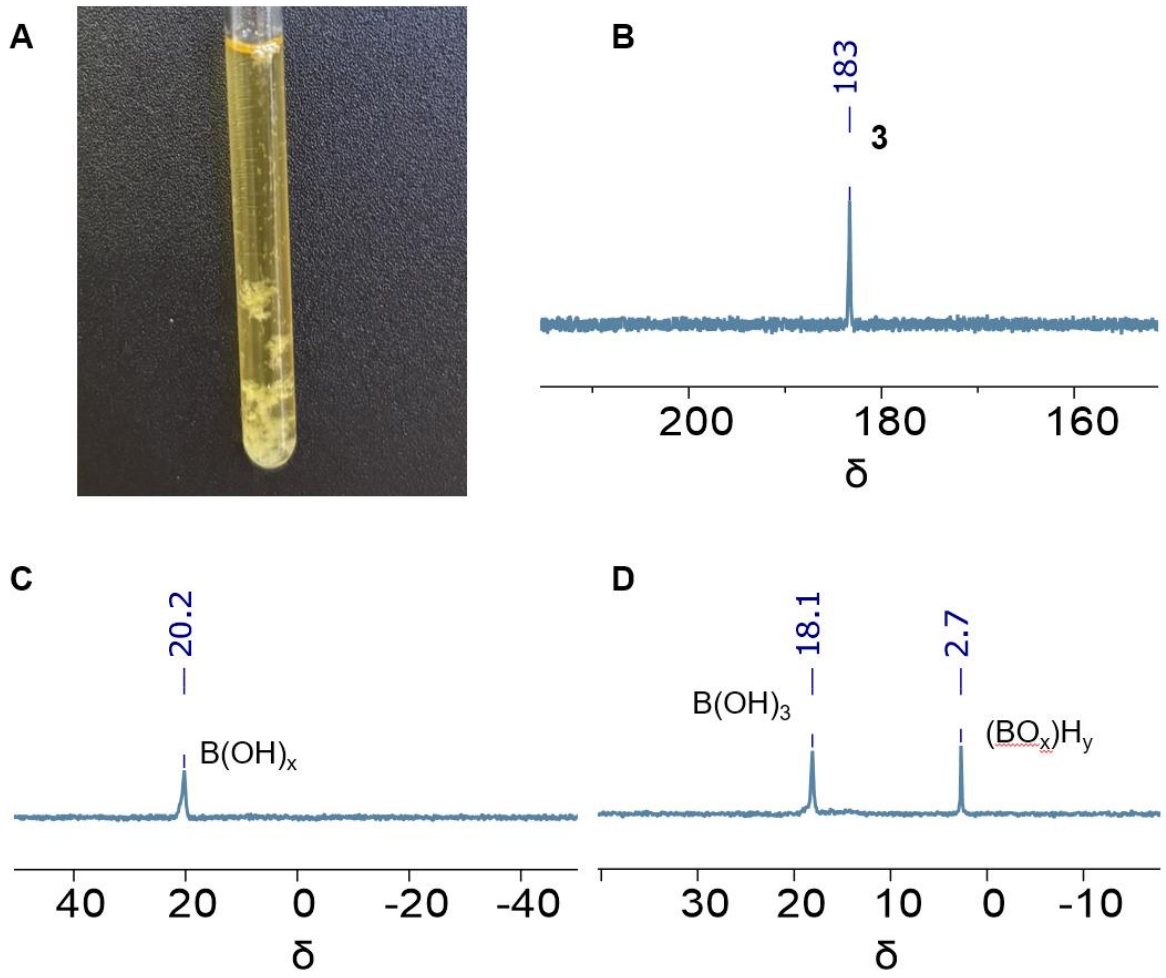

Figure 2.11. Reaction of Ir(^{t}Bu-POCOP)(H)$_2$(BH$_3$) with H$_2$O (20 equiv.) in THF. A) observed effervescence and precipitate. B) ^{31}P{^{1}H} NMR spectrum (THF-H^8, 203 MHz, 298 K). C) ^{11}B NMR spectrum (THF-H^8, 193 MHz, 298 K) of Ir(^{t}Bu-POCOP)(H)$_2$(BH$_3$) with H$_2$O. D) ^{11}B NMR spectrum (EtOH-H^6, 193 MHz, 298 K) of resulting white precipitate.

2.6 Dehydropolymerisation of H$_3$B·NH$_2$Me with Ir(^{t}Bu-POCOP)(H)$_4$ (3)

To investigate catalysis using tetrahydride complex **3**, proposed to be the resting state during catalysis, the catalyst was made *in-situ* as it cannot be isolated. A THF solution of complex **1** was placed under 4 bar H$_2$ and shaking of the solution resulted in an instant colour change from red/orange to pale yellow/colourless and 100% conversion of **1** to **3** as measured by ^{1}H and ^{31}P{^{1}H} NMR spectroscopies.

The solution of thus-formed complex **3** was added to H$_3$B·NH$_2$Me as a solid under standard conditions (0.1 mol% [Ir], 2 M H$_3$B·NH$_2$Me, 20 °C, THF). The resulting eudiometrically determined kinetic profile is shown in Figure 2.12. The rate of reaction is higher using

tetrahydride **3** than with dihydride **1**, 8.47(7) mmol s^{-1} and 5.93(3) mM s^{-1} respectively, while induction periods remained comparable. The presence of an induction period similar to that observed for complex **1** indicates that **3** is a competent pre-catalyst that still operates with an induction period. This is likely caused by the rapid formation of borohydride complex **2** on addition of pre-catalyst **3** to $H_3B{\cdot}NH_2Me$. This, in combination with **3** being observed as the major species during and after catalysis, is in agreement with the observations of Goldberg and Paul that **3** is the resting state of the catalyst.[2, 4]

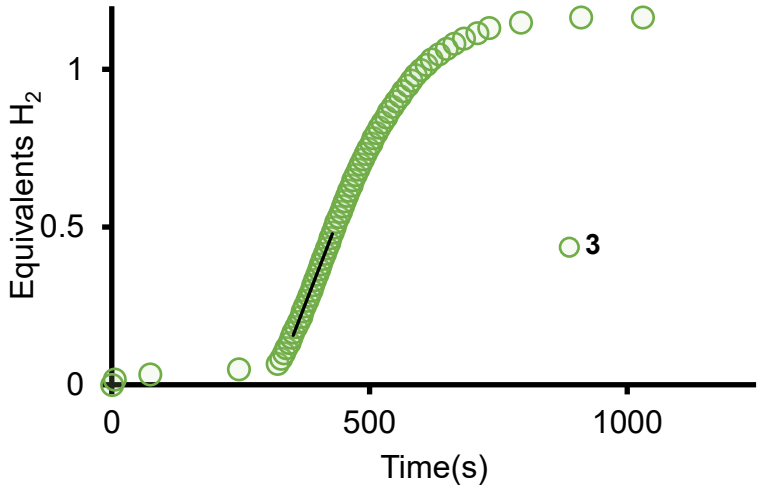

Figure 2.12. Eudiometric measurement of H_2 release using pre-catalyst Ir(^{t}Bu-POCOP)$(H)_4$. Conditions: 2 M $H_3B{\cdot}NH_2Me$, 0.1 mol% catalyst loading, 20 °C.

2.7 Understanding the reaction manifold that connects complexes 1-4

As discussed in Chapter 1, Goldberg and co-workers identified the relationships between complexes **1** to **3** (Scheme 2.2) as discussed in Chapter 1.[4] In this section a further catalytically relevant intermediate has been identified and synthesised, Ir(^{t}Bu-POCOP)$(H)_2(NH_2Me)$ (**4**), initially observed in the flow NMR data. A series of NMR experiments were carried out to determine the relationships between complexes **1** to **4.**

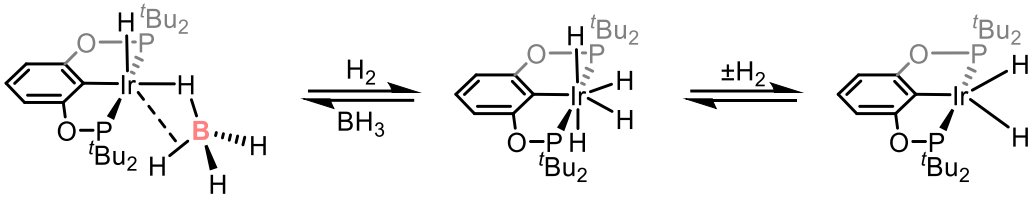

2 **3** **1**

Scheme 2.2. Established equilibrium of Ir(^{t}Bu-POCOP)(H)$_2$(BH$_3$) with H$_2$.[4]

2.7.1 Synthesis of 4 and establishing an equilibrium between 1 and 4

The initial *in-situ* synthesis of complex **4** was carried out by the addition of NH$_2$Me (2 M in THF) to complex **1**. This resulted in a colour change from red to yellow and the full conversion of **1** to **4** as measured by NMR spectroscopy. In the resulting ^{1}H NMR spectrum (Figure 2.13), a triplet and doublet ($^3J_{HH}$ = 7.7 Hz) are observed at δ 6.31 (1H) and δ 6.07 (2H), respectively, assigned to the protons of the aryl ring. Signals corresponding to the bound NH$_2$Me are observed as a broad singlet at δ 3.23 (2H) corresponding to the NH$_2$ and a triplet (J = 6.6 Hz) at δ 2.88 assigned to the CH$_3$ group. The ^{t}Bu groups are equivalent with a triplet (J = 6.6 Hz) at δ 1.41 (36 H). The hydride resonance is located at δ –9.19 as a triplet ($^2J_{HP}$ = 16.1 Hz) that collapses to a singlet on ^{31}P{^{1}H} decoupling. Signals for excess 'free' NH$_2$Me are observed at δ 2.34 and 0.73. The resonance in the ^{31}P{^{1}H} NMR spectrum is a singlet at δ 169. The hydride and phosphorus resonances of complex **4** are similar to related *trans* dihydride amine complex Ir(^{t}Bu-POCOP)(H)$_2$(NH$_2$^{i}Bu) (^{1}H δ –8.84, ^{31}P{^{1}H} δ 170.7).[29]

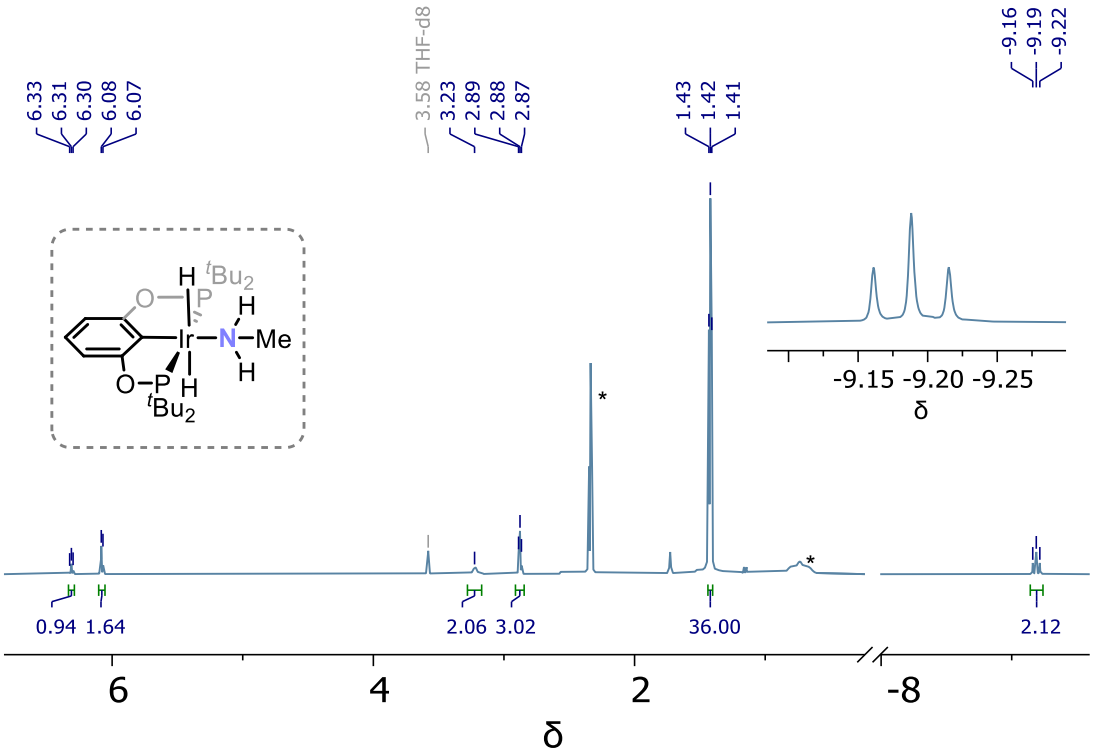

Figure 2.13. ^{1}H NMR spectrum (THF-d^{8}, 600 MHz, 298 K) of Ir(^{t}Bu-POCOP)H$_2$(NH$_2$Me) – NH$_2$Me gas dissolved in THF indicated by *.

Crystals suitable for single crystal X-ray crystallography were isolated following the addition of excess NH$_2$Me (2 M in THF) to 1, removal of THF under a flow of argon, and addition of pentane to the residues. Crystallisation from pentane at –80 °C afforded a small number of colourless crystals of **4**. To our understanding this is the first crystallographically characterised example of a primary amine-bound iridium complex bearing the POCOP ligand framework (Figure 2.14). Comparison with a related cationic [Ir(^{t}Bu-PONOP)(NH$_2$Me)]$^{+}$ (^{t}Bu-PONOP = κ^{3}-2,6-(^{t}Bu$_2$PO)$_2$C$_6$H$_3$N) complex showed similar bond lengths between the central iridium atom and the surrounding pincer ligand.[30] The Ir–P distances of complex **4** are 2.289(2) and 2.288(3) Å, similar to [Ir(^{t}Bu-PONOP)(NH$_2$Me)]$^{+}$ (2.279(2) and 2.262(2) Å). The Ir–N bond length of complex **4** was 2.22(1) Å, similar to [Ir(^{t}Bu-PONOP)(NH$_2$Me)]$^{+}$ (2.104(6) Å). It is difficult to compare these bond lengths as there are a number of differing factors: cationic vs neutral, Ir(I) vs Ir(III), and the effects of a carbon vs a nitrogen atom in the trans position.

The hydrides were not located in the molecular structure, so by single crystal X-ray diffraction alone it is unclear whether the molecular structure is of an Ir(III) *trans* dihydride amine complex

or an Ir(I) amine complex. The ^{1}H and $^{31}P\{^{1}H\}$ NMR spectra were taken of an independent sample not the crystals. However, applying a vacuum to a sample of dihydride amine complex **4** results in loss of amine to form dihydride complex **1**, so the amine is labile and loss of H_2 does not occur. This observation gives confidence that the molecular structure is that of dihydride amine complex **4**.

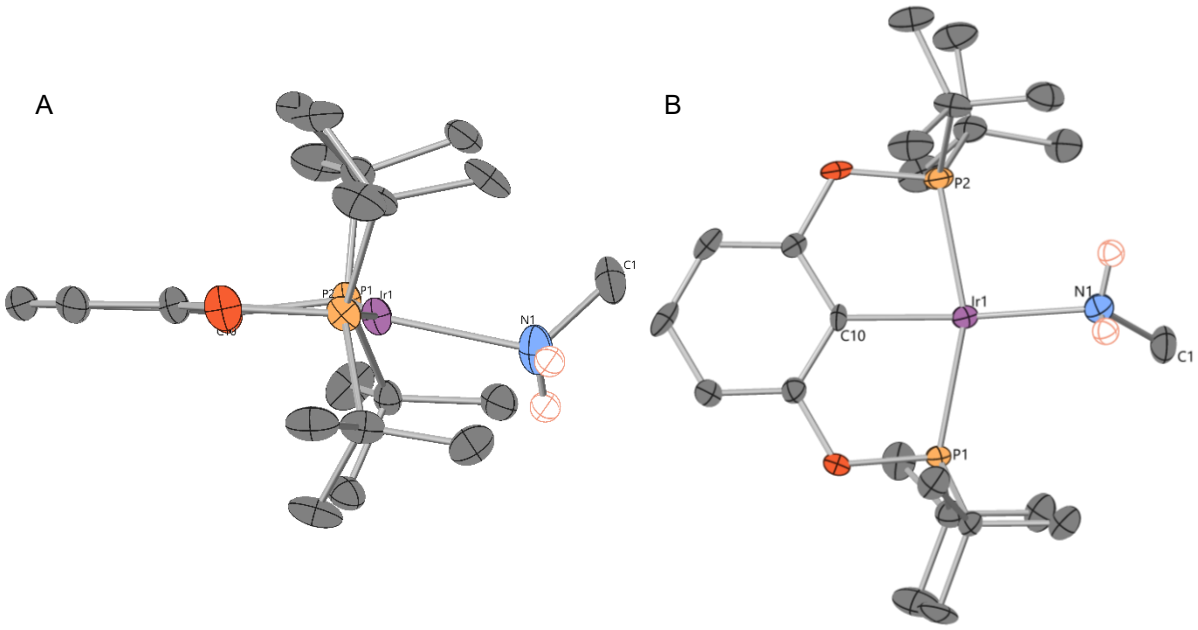

Figure 2.14. The molecular structure of Ir(^{t}Bu-POCOP)$(H)_2(NH_2Me)$ A) side on view and B) above view of the molecular structure. Displacement ellipsoids are set at 50% probability, hydrogen atoms are removed for clarity. Selected bond lengths (Å): Ir1-N1 2.22(1), Ir1-P1 2.289(2), Ir1-P2 2.288(3), N1-C1 1.48(2), Ir1-C10 2.048(9). Selected bond angles (°): Ir1-N1-C1 121.8(8).

Synthesis of complex **4** by addition of excess NH_2Me to complex **1** resulted in the full conversion of **1** to **4** as measured by NMR spectroscopy. Removal of the THF by a flow of argon and dissolution in d^8-THF showed two products (**4** and **1**, ~10:1) observed in the ^{1}H and $^{31}P\{^{1}H\}$ NMR spectra. To characterise complex **4** by NMR spectroscopy in deuterated solvent in isolation of complex **1**, an excess of NH_2Me was required (Scheme 2.3). Methylammonium chloride and sodium hydride were dissolved in d^8-THF and the J-Youngs NMR tube inverted overnight to form $NH_2Me_{(l)}$ in d^8-THF. The $NH_2Me_{(g)}$ in d^8-THF was transferred onto solid **1** *via* a trap-to-trap distillation to cleanly form **4** with excess NH_2Me. A related approach has been used to prepare PH_3 gas *in situ* for the synthesis of organometallic complexes.[31]

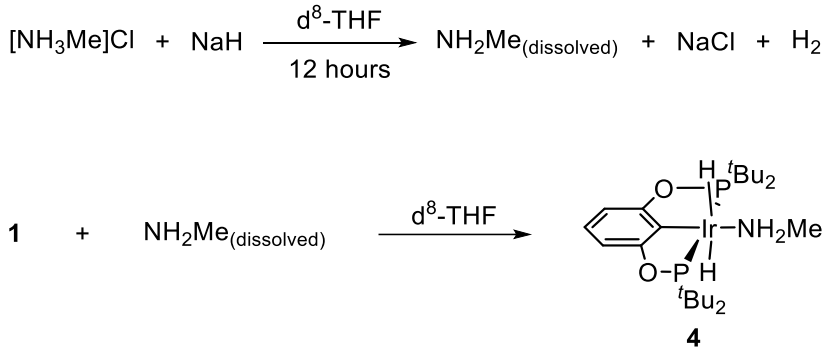

Scheme 2.3. Synthesis of **4** for analysis by NMR spectroscopy.

2.7.2 Establishing equilibria between Complexes 1-4

To fully investigate the equilibrium between complexes **1** and **4**, exchange spectroscopy (EXSY) NMR was carried out with the assistance of Professor Simon Duckett at the University of York (Scheme 2.4). The EXSY data shows that complexes **1** and **4** are in exchange on the NMR time scale in d^8-THF. These data provide exchange constants for the forward and backward reaction that can be used to estimate the rate constants in the manner of Wendt.[32] The rate constants are 0.33 M^{-1} s^{-1} for the forwards reaction and 6.6 × 10^{-2} s^{-1} for the backwards reaction (Scheme 2.4). While these two rate constants cannot be directly compared as one is a first-order process while the other is a second-order process, they will be used in Chapter 3 to model the proposed mechanism with kinetic modelling software COPASI.[33]

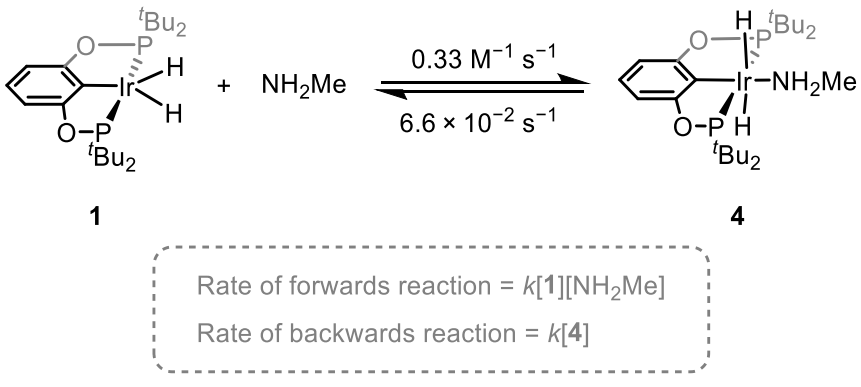

Scheme 2.4. Equilibrium between **1** and **4**, with equilibrium constants measured by EXSY NMR.

The groups of Brookhart, Goldberg, and Wendt have described the reversible reaction of **1** with H_2 to form complex **3**.[4, 9, 32] Wendt and co-workers reported NMR-kinetic data from 2D-EXSY experiments, allowing rate constants to be estimated from the measured exchange constants (this will be discussed later). The reaction between **2** and H_2O (20 equiv.) resulting in the formation of **3** was discussed in section 2.5 and has also been included in Scheme 2.5.

The reaction of borohydride **2** with NH_2Me (2 equiv.) in THF resulted in the formation of **3** and **4** (65:35), evidenced by ^{1}H and $^{31}P\{^{1}H\}$ NMR spectroscopies. This supports the hypothesis that the addition of NH_2Me to **2** in the dehydropolymerisation of $H_3B{\cdot}NH_2Me$ reduces the induction period as it converts the inactive catalyst to catalytically relevant intermediates **3** and **4**. The ^{11}B NMR spectrum showed the formation of borazine and $H_3B{\cdot}NH_2Me$.[11] A summary of findings from the above experiments can be found in Scheme 2.5.

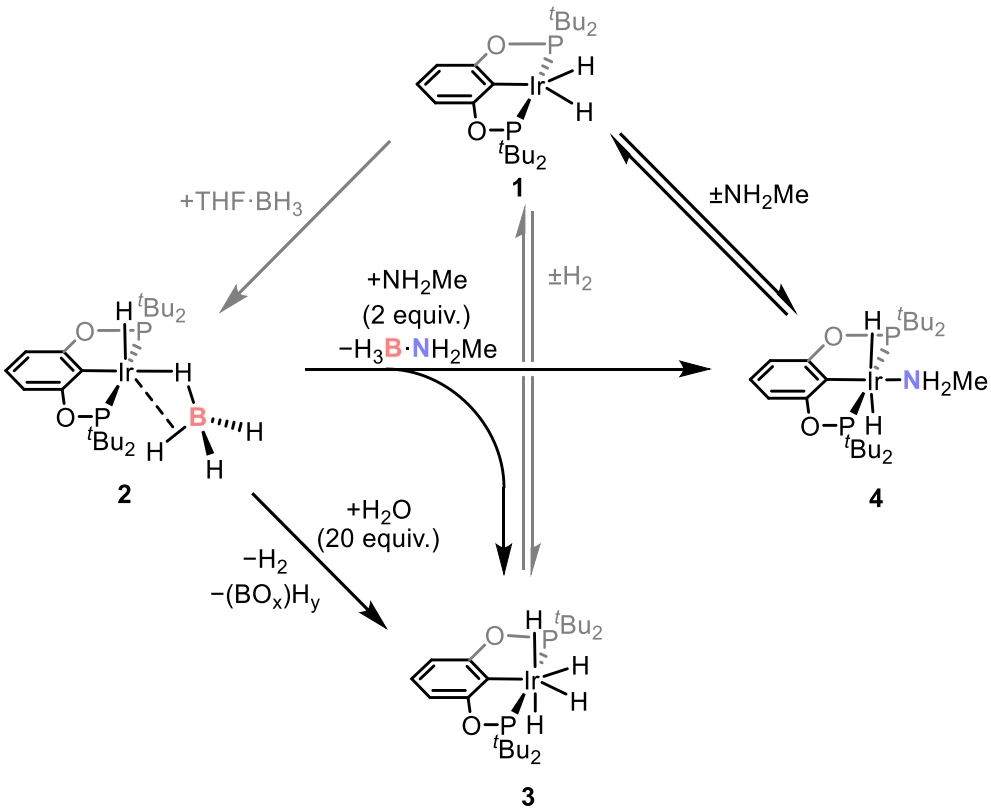

Scheme 2.5. Summary of interactions/equilibria between catalytically relevant iridium complexes **1** to **4**. Grey lines indicate relationships identified in the literature.

2.8 Summary and conclusions

This chapter has presented the general considerations that will apply to the eudiometric measurements carried out for this thesis and provided a baseline of what can be expected in term of catalysis. The eudiometric measurements carried out with **1** under standard conditions (THF at 20 °C, 2 M [$H_3B{\cdot}NH_2Me$], 0.1 mol% [Ir] (2 mM)), indicate the presence of an induction period before a pseudo zero order regime during turnover, followed by a deceleration in rate at the end of catalysis. Poisoning experiments (Hg(0) and PMe_3) determined catalysis with **1** to be homogeneous in nature.

Speciation studies show the presence of borohydride complex **2** and tetrahydride complex **3** during the induction period, after which **3** dominates as the resting state of the catalyst. *In-operando* flow NMR experiments allowed for the speciation of the catalyst and the consumption of the pre-monomer to be mapped in a way that has not been done before. An additional catalytically relevant intermediate, **4**, was also identified. Catalysis with **2** revealed a longer induction period (~55 minutes) compared to **1** (2-3 minutes), showing that **2** is the predominant species present during the induction period. It was also revealed that water has an unexpected promoting effect on catalysis, as it reacts with **2** to form **3**, reducing the induction period and bringing inactive **2** back onto cycle. NMR experiments were carried out to establish the relationships between complexes **1** and **4**, including measuring the rate constants between **1** and **4** by EXSY NMR.

The observations and understanding outlined in this chapter will be used as a foundation to analyse the kinetics of this reaction, followed by outlining of a proposed mechanism in Chapter 3.

2.9 References

1. S. Bhunya, T. Malakar and A. Paul, *Chem. Commun.*, 2014, **50**, 5919–5922.
2. A. Paul and C. B. Musgrave, *Angew. Chem. Int. Ed.*, 2007, **46**, 8153–8156.
3. C. N. Brodie, T. M. Boyd, L. Sotorríos, D. E. Ryan, E. Magee, S. Huband, J. S. Town, G. C. Lloyd-Jones, D. M. Haddleton, S. A. Macgregor and A. S. Weller, *J. Am. Chem. Soc.*, 2021, **143**, 21010–21023.
4. M. C. Denney, V. Pons, T. J. Hebden, D. M. Heinekey and K. I. Goldberg, *J. Am. Chem. Soc.*, 2006, **128**, 12048–12049.
5. B. L. Dietrich, K. I. Goldberg, D. M. Heinekey, T. Autrey and J. C. Linehan, *Inorg. Chem.*, 2008, **47**, 8583–8585.
6. V. Pons and R. T. Baker, *Angew. Chem. Int. Ed.*, 2008, **47**, 9600–9602.
7. A. Staubitz, M. E. Sloan, A. P. M. Robertson, A. Friedrich, S. Schneider, P. J. Gates, J. S. A. D. Günne and I. Manners, *J. Am. Chem. Soc.*, 2010, **132**, 13332–13345.
8. I. Göttker-Schnetmann, P. White and M. Brookhart, *J. Am. Chem. Soc.*, 2004, **126**, 1804–1811.
9. I. Göttker-Schnetmann, P. S. White and M. Brookhart, *Organometallics*, 2004, **23**, 1766–1776.
10. A. Staubitz, A. Presa Soto and I. Manners, *Angew. Chem. Int. Ed.*, 2008, **47**, 6212–6215.
11. C. A. Jaska, K. Temple, A. J. Lough and I. Manners, *J. Am. Chem. Soc.*, 2003, **125**, 9424–9434.
12. G. M. Adams, D. E. Ryan, N. A. Beattie, A. I. McKay, G. C. Lloyd-Jones and A. S. Weller, *ACS Catal.*, 2019, **9**, 3657–3666.
13. E. A. K. Spearing-Ewyn, N. A. Beattie, A. L. Colebatch, A. J. Martinez-Martinez, A. Docker, T. M. Boyd, G. Baillie, R. Reed, S. A. Macgregor and A. S. Weller, *Dalton Trans.*, 2019, **48**, 14724–14736.
14. D. E. Ryan, K. A. Andrea, J. J. Race, T. M. Boyd, G. C. Lloyd-Jones and A. S. Weller, *ACS Catal.*, 2020, **10**, 7443–7448.
15. M. J. Cross, M. A. Sajjad, S. A. Macgregor and A. S. Weller, *Angew. Chem. Int. Ed.*, 2025, **64**, e202500019.
16. M. J. Cross, C. N. Brodie, D. G. Crivoi, J. C. Goodall, D. E. Ryan, A. J. Martinez-Martinez, A. Johnson and A. S. Weller, *Chem. Eur. J.*, 2023, **29**, e202302110.
17. J. A. Widegren and R. G. Finke, *J. Mol. Catal. A: Chem.*, 2003, **198**, 317–341.
18. M. A. Watzky and R. G. Finke, *J. Am. Chem. Soc.*, 1997, **119**, 10382–10400.
19. M. A. Watzky, E. E. Finney and R. G. Finke, *J. Am. Chem. Soc.*, 2008, **130**, 11959–11969.
20. S. Shafiei-Haghighi, L. M. Singer, S. R. Tamang and M. Findlater, *Polyhedron*, 2018, **143**, 126–131.
21. T. J. Hebden, K. I. Goldberg, M. D. Heinekey, X. Zhang, T. J. Emge, A. S. Goldman and K. Krogh-Jespersen, *Inorg. Chem.*, 2010, **49**, 1733–1742.
22. T. J. Hebden, M. C. Denney, V. Pons, P. M. B. Piccoli, T. F. Koetzle, A. J. Schultz, W. Kaminsky, K. I. Goldberg and D. M. Heinekey, *J. Am. Chem. Soc.*, 2008, **130**, 10812–10820.
23. C. N. Brodie, L. Sotorrios, T. M. Boyd, S. A. Macgregor and A. S. Weller, *ACS Catal.*, 2022, **12**, 13050–13064.

24. W. Baumann, S. Mansel, D. Heller and S. Borns, *Magn. Reson. Chem.*, 1998, **35**, 701–706.
25. A. Bara-Estaun, M. C. Harder, C. L. Lyall, J. P. Lowe, E. Suturina and U. Hintermair, *Chem. Eur. J.*, 2023, **29**, e202300215.
26. A. Glüer, M. Förster, V. R. Celinski, J. Schmedt auf der Günne, M. C. Holthausen and S. Schneider, *ACS Catal.*, 2015, **5**, 7214–7217.
27. F. Wang, O. Planas and J. Cornella, *J. Am. Chem. Soc.*, 2019, **141**, 4235–4240.
28. G. C. Fortman, A. M. Z. Slawin and S. P. Nolan, *Organometallics*, 2011, **30**, 5487–5492.
29. W. H. Bernskoetter and M. Brookhart, *Organometallics*, 2008, **27**, 2036–2045.
30. K. M. Altus, M. A. Sajjad, M. R. Gyton, A. C. Whitwood, S. J. Page, S. A. Macgregor and A. S. Weller, *Organometallics*, 2024, **43**, 3137–3142.
31. S. Lau, M. F. Mahon and R. L. Webster, *Inorg. Chem.*, 2024, **63**, 6998–7006.
32. A. Spangenberg, O. O. Kovalenko, M. S. G. Ahlquist and O. F. Wendt, *Organometallics*, 2024, **43**, 3242–3250.
33. S. Hoops, S. Sahle, R. Gauges, C. Lee, J. Pahle, N. Simus, M. Singhal, L. Xu, P. Mendes and U. Kummer, *Bioinformatics*, 2006, **22**, 3067–3074.

Chapter 3: Mechanism

The numerical simulations (kinetic modelling) presented later in this chapter were carried out by Professor Andrew Weller using the kinetic modelling software COPASI.[1] The DFT calculations were conducted by Dr M. Arif Sajjad and Professor Stuart Macgregor at the University of St Andrews. The collection and refinement of single crystal X-ray diffraction data was carried out by Dr Joe Goodall at the University of York.

In Chapter 2, a series of eudiometric measurements were performed to baseline the dehydropolymerisation of $H_3B{\cdot}NH_2Me$ using catalyst Ir(^{t}Bu-POCOP)$(H)_2$ (**1**). The kinetic profiles measured indicated the presence of an induction period before a pseudo zero order regime during turnover, followed by a deceleration in rate at the end of catalysis. The use of *in operando* flow NMR spectroscopy experiments allowed for the speciation of the catalyst to be mapped alongside the conversion of the pre-monomer $H_3B{\cdot}NH_2Me$ to the monomer $H_2B{=}NHMe$. The flow NMR experiments identified borohydride Ir(^{t}Bu-POCOP)$(H)_2(BH_3)$ (**2**) as the major species observed during the induction period and tetrahydride Ir(^{t}Bu-POCOP)$(H)_4$ (**3**) as the resting state of the catalyst during active turnover. Experiments were also carried out that identified H_2O as an important additive to catalysis, having a promoting effect by converting borohydride complex **2** to tetrahydride complex **3**, releasing NH_2Me in the process, alongside borates. An equilibrium was also established between complex **1**/free NH_2Me and Ir(^{t}Bu-POCOP)$(H)_2(NH_2Me)$ (**4**).

These findings will be built upon in the following chapter, where the kinetics of the dehydropolymerisation of $H_3B{\cdot}NH_2Me$ with catalyst **1** will be analysed, followed by the outlining of two proposed mechanisms, numerical modelling using COPASI and DFT calculations. Combined, this allows for a mechanism to be proposed.

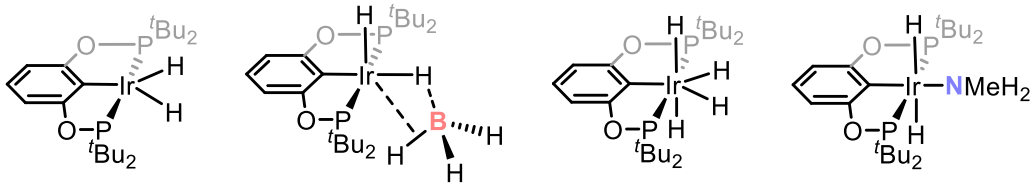

Chart 3.1. Complexes discussed in Chapter 2.

3.1 Establishing the order in catalyst and substrate

3.1.1 [Ir(^{t}Bu-POCOP)(H)$_2$]

To probe the effect of the concentration of Ir(^{t}Bu-POCOP)(H)$_2$ (**1**) on the dehydrogenation of $H_3B{\cdot}NH_2Me$, experiments were carried out that varied the concentration of complex **1**, while the concentration of $H_3B{\cdot}NH_2Me$ remained constant. To measure the kinetics of the reactions, the volume of hydrogen gas produced was measured eudiometrically. The kinetic profiles of these reactions along with a table of rates and induction periods can be found in Figure 3.1 (conditions: 2 M $H_3B{\cdot}NH_2Me$, THF, 20 °C). The $H_3B{\cdot}NH_2Me$ was recrystallised from OEt_2 at –20 °C prior to use, the THF contained ~10 ppm H_2O as measured by Karl Fisher titration, and the temperature of the reaction was maintained by a circulating chiller filled with a 1:1 ethylene glycol/water mix.

Increasing [Ir] in the reaction resulted in a higher rate of turnover, *e.g.* k_{obs} = 5.95(3) and 49.8(9) mM s^{-1} for 0.1 mol% and 0.5 mol%, respectively. The induction periods increased significantly at lower [Ir], 167 s and 4577 s for 0.1 mol% and 0.01 mol%, respectively. For the kinetic profiles with longer reaction times (0.05 and 0.01 mol%) the effect of vapour evolution from the THF and the induction period processes (borate formation), as discussed in Chapter 2, is more prominent but during active turnover ~1 equivalent of H_2 was released. Due to the additional gas evolved the [aminoborane] would be higher than the [amine-borane] starting material. Therefore, graphs of equivalents of hydrogen evolved against time are presented in all cases to show the kinetic profile and the relationships between different conditions. Graphs of [aminoborane] against time are used to determine the maximum rate as measured by k_{obs} from the linear region of the kinetic profile (*i.e.* the maximum rate).

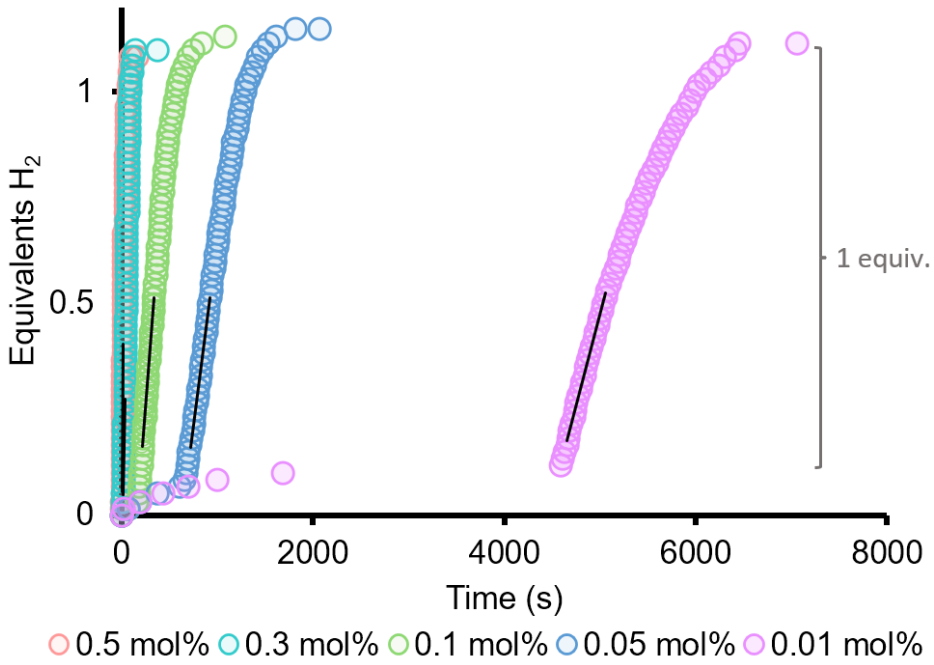

Entry	[Ir] (mM)	Cat. loading (mol %)	Rate[a] (mM s^{-1})	Induction period (s)	Conv.[b] (%)	Selectivity[b] (%)	Isolated Yield (%)
1	10	0.5	49.8(9)	0	>99	>99	65
2	6	0.3	25.1(5)	36	>99	>99	56
3	2.0	0.1	5.95(3)	167	>99	>99	62
4	1	0.05	3.36(2)	658	>99	>99	47
5	0.2	0.01	1.69(2)	4577	>99	>99	62

Figure 3.1. Dehydropolymerisation of $H_3B{\cdot}NH_2Me$ with Ir(^{t}Bu-POCOP)$(H)_2$ (**1**) at different catalyst concentrations, (0.2 mM – 10 mM, 0.01 mol%-0.5 mol%). Conditions: 2 M $H_3B{\cdot}NH_2Me$, THF, 293 K. [a]Determined by the pseudo zero order region of the profile [b]Measured by ^{11}B NMR spectroscopy. Yield is isolated yield of polymer from precipitation.

There is an acceptable first-order relationship identified when plotting k_{obs} against [Ir] that is supported by an average fit of the data to a variable time normalisation analysis (VTNA) model.[2] To model the data using VTNA, the induction period was removed and each data point is time normalised. A good fit for VTNA modelling would result in complete overlap of the kinetic profiles, and requires the [catalyst] to remain constant (or known) throughout the reaction. The relationship is approximately first-order, consistent with a unimolecular process with no off-cycle equilibria changing the molecularity. The average fit may be caused by the reaction being more complex, such as off-cycle equilibria taking the catalyst off-cycle meaning the [Ir_{ACTIVE}]

would not remain constant throughout the reaction. Overall, the catalysis shows a first order relationship for catalyst **1**.

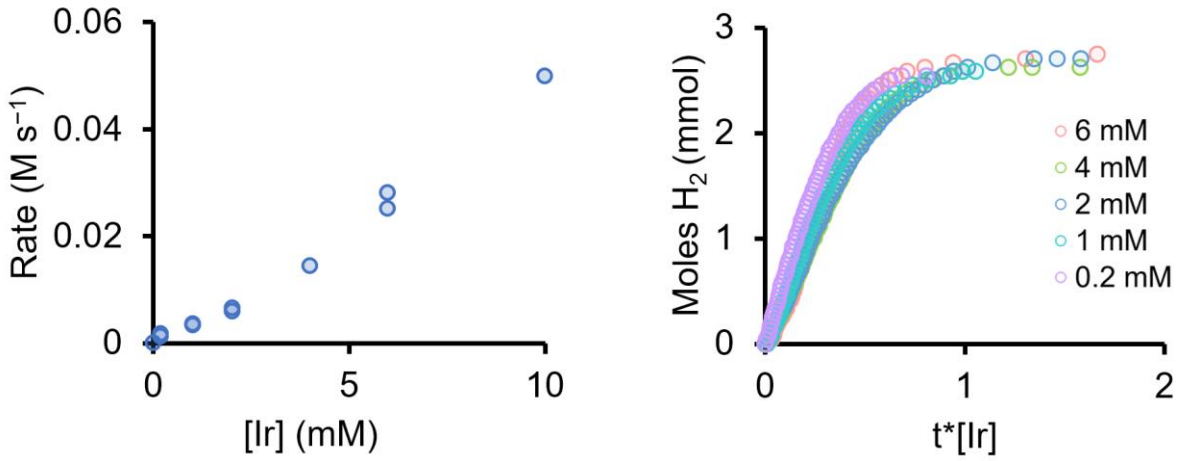

Figure 3.2. Comparison of concentration rate graphs and VTNA plots for [Ir].

3.1.2 [$H_3B{\cdot}NH_2Me$]

In Chapter 1, limited kinetic data that was previously reported for the dehydropolymerisation of amine-borane with catalyst **1** was discussed. Goldberg and co-workers carried out experiments with catalyst **1** and $H_3B{\cdot}NH_2Me$ at 0.5 M substrate concentration and catalyst loadings between 0.5 and 2.0 mol%.[3, 4] The rate constants reported for the reactions with $H_3B{\cdot}NH_2Me$ are first-order rate constants,[4] indicating that the kinetic profile is first order in nature, similar to that observed for reactions of **1** with $H_3B{\cdot}NH_3$ by Goldberg and co-workers.[3] However, temporal profiles were not given for $H_3B{\cdot}NH_2Me$ but were provided for $H_3B{\cdot}NH_3$. Kinetic measurements using a manometer carried out by Manners and co-workers with $H_3B{\cdot}NH_2Me$ (0.5 M) and catalyst **1** (0.1 mol%) resulted in irreproducible kinetics reported over multiple runs.[5]

To investigate the effect of [$H_3B{\cdot}NH_2Me$] on the dehydropolymerisation of $H_3B{\cdot}NH_2Me$ with catalyst **1**, experiments were carried out where the concentration of substrate was varied (0.5 M – 2.0 M) while the catalyst concentration remained constant (2 mM) (Figure 3.3). The measured rate of reaction increased with increased substrate concentration, at 0.5 M

[$H_3B{\cdot}NH_2Me$] k_{obs} = 3.53(10) mM s^{-1}, while at 1.0 M [$H_3B{\cdot}NH_2Me$] k_{obs} = 5.38(5) mM s^{-1}. A further increase to 2 M [$H_3B{\cdot}NH_2Me$] (as used in the standard conditions) resulted in k_{obs} = 5.95(3) mM s^{-1} *i.e.* essentially no increase. The relationship between [$H_3B{\cdot}NH_2Me$] and rate exhibits saturation-type kinetics. This may indicate that the binding of $H_3B{\cdot}NH_2Me$ to the iridium centre is exergonic, fast and reversible. At low [$H_3B{\cdot}NH_2Me$] (0.5 M), an equilibrium position is established between complex **1** and a $H_3B{\cdot}NH_2Me$-bound complex. At higher [$H_3B{\cdot}NH_2Me$] (2.0 M) the equilibrium is pushed exclusively over to a $H_3B{\cdot}NH_2Me$-bound complex, thought to be an important catalytic intermediate in many examples of amine-borane dehydropolymerisation.[6-9] The turnover limiting step must come after this equilibrium, otherwise a first-order relationship would be observed.

It is interesting to note that at higher [$H_3B{\cdot}NH_2Me$] (*e.g.* 2.0 M), there is a clear pseudo zero order regime, where the kinetic profile is almost linear during active turnover before deceleration. However, at low [$H_3B{\cdot}NH_2Me$] (*e.g.* 0.5 M), there is more curvature in the kinetic profile, typically what would be expected for a first-order kinetic profile.[10] This first-order profile is similar to that reported by Goldberg and co-workers at the same concentration of $H_3B{\cdot}NH_3$.[3, 4]

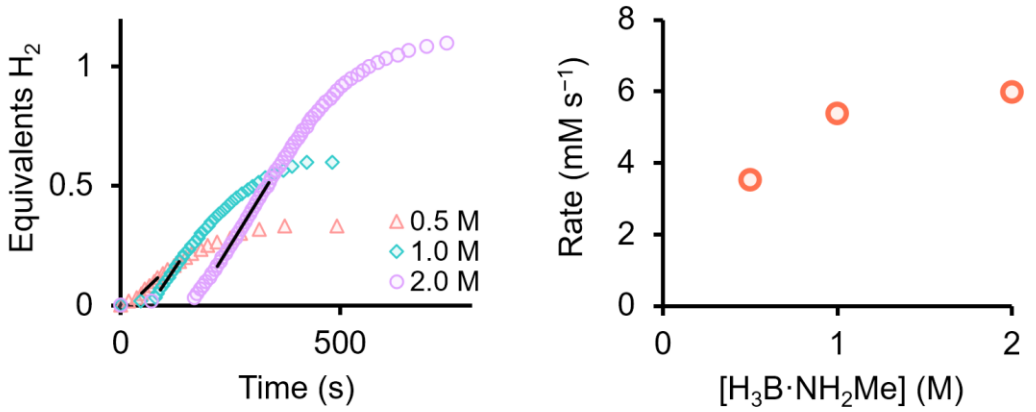

Entry	[$H_3B{\cdot}NH_2Me$] (M)	Rate[a] (mM s^{-1})	Induction period (s)	Conv.[b] (%)	Selectivity[b] (%)	Isolated yield (%)
1	0.5	3.53(10)	17	>99	>99	52
2	1.0	5.38(5)	79	>99	>99	60
3	2.0	5.95(3)	167	>99	>99	62

Figure 3.3. Dehydropolymerisation of $H_3B{\cdot}NH_2Me$ with Ir(^{t}Bu-POCOP)$(H)_2$ (**1**) at different substrate concentrations, (0.5 M – 2 M). Conditions: 2 mM [Ir], THF, 293 K. [a]Determined by the pseudo zero order region of the profile [b]Measured by ^{11}B NMR spectroscopy. Yield is isolated yield of polymer from precipitation.

The addition of NH_2Me to these reactions results in faster turnover and shorter induction periods in all cases. A similar effect was observed with the addition of NH_2Me to catalysis with borohydride complex **2**. It is interesting to note that the addition of NH_2Me causes the relationship between [$H_3B{\cdot}NH_2Me$] and maximum rate to change (Figure 3.4). 10 mM of NH_2Me was added to reactions where the concentration of substrate ranged from 0.25 M to 2.0 M. The rates show an upward trend, but overall, there is less of the saturation-type kinetics observed with the experiments without amine. This may be due to the binding of $H_3B{\cdot}NH_2Me$ being reversible and the presence of amine in the reaction pushing the equilibrium over in favour of an amine-borane bound complex instead of complex **1**. The levelling indicates a more complex relationship with NH_2Me, that possibly involves a change in off-cycle speciation and/or rate acceleration by direct involvement of NH_2Me in the turnover limiting step.

As discussed in the previous chapters, NH_2Me can play many roles in the dehydropolymerisation of amine-boranes and further investigation is required to understand its complete role in catalysis with **1**.

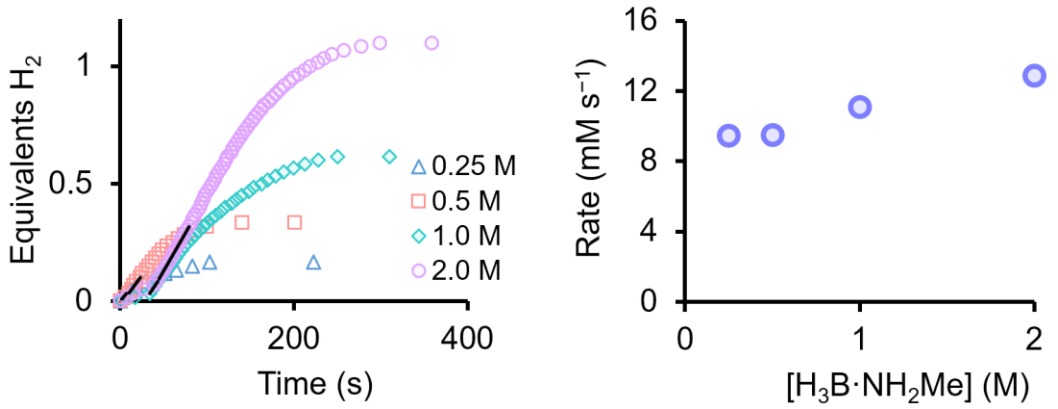

Entry	[$H_3B{\cdot}NH_2Me$] (M)	[NH_2Me] (mM)	Rate[a] (mM s^{-1})	Induction period (s)	Conv.[b] (%)	Selectivity[b] (%)	Isolated yield (%)
1	0.25	10	9.4(8)	0	>99	>99	30
2	0.5	10	9.5(3)	6	>99	>99	56
3	1.0	10	11.1(2)	37	>99	>99	63
4	2.0	10	12.9(1)	53	>99	>99	67

Figure 3.4. Dehydropolymerisation of $H_3B{\cdot}NH_2Me$ with Ir(^{t}Bu-POCOP)$(H)_2$ (**1**) at different substrate concentrations (0.5 M – 2 M) with added NH_2Me (10 mM). Conditions: 2 mM [Ir], THF, 293 K. [a]Determined by the pseudo zero order region of the profile [b]Measured by ^{11}B NMR spectroscopy. Yield is isolated yield of polymer from precipitation.

3.2 Role of NH_2Me in catalysis with 1

In the literature, the addition of NH_2Me to amine-borane dehydropolymerisation reactions is common, resulting in shorter induction periods, higher rates of turnover and in some cases bringing dormant catalysts on-cycle (for a more in-depth overview of the relevant literature see section 1.5.1).[7, 9, 11-15]

As discussed in Chapter 2, addition of NH_2Me to borohydride complex **2** resulted in a significant reduction of the induction period and an increase in the rate of reaction. Additionally, in section 3.1.2 addition of NH_2Me resulted in a change in the saturation-type profile of a plot of [$H_3B{\cdot}NH_2Me$] against rate for reaction with catalyst **1** to one that is more levelled.

To investigate the role NH_2Me plays in the dehydropolymerisation of amine-boranes with catalyst **1**, experiments were carried out that varied the concentration of NH_2Me while keeping

[Ir] and [$H_3B{\cdot}NH_2Me$] constant. In agreement with previous literature observations and the observation with borohydride pre-catalyst **2**, the induction period shortens when NH_2Me is added. This supports the hypothesis put forward in Chapter 2 that the induction period is caused by the formation of inactive borohydride complex **2**, that can then be brought back on-cycle by amine formed from the dissociation of the B–N bond (*via* hydrolysis or B–N dissociation in THF), or in this case, from the independent addition of NH_2Me. In terms of catalytic turnover, the addition of NH_2Me has an interesting effect. The addition of NH_2Me up to the concentration of 40 mM has a promoting effect on catalysis, increasing the rate from 5.52(2) mM s^{-1} at 0.5 mM [NH_2Me] to 14.6(1) mM s^{-1} at 40 mM [NH_2Me]. The further addition of NH_2Me results in a lower maximum rate of turnover of 13.6(1) mM s^{-1} at 60 mM [NH_2Me] and 12.2(1) mM s^{-1} at 120 mM [NH_2Me].

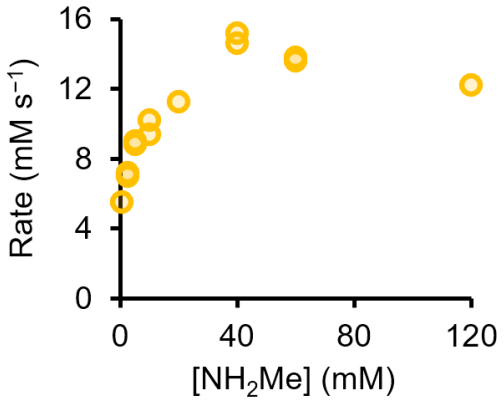

Entry	[NH_2Me] (mM)	Rate[a] (mM s^{-1})	Induction period (s)	Conv.[b] (%)	Selectivity[b] (%)	Isolated yield (%)
1	0.5	5.52(2)	317	>99	>99	45
2	2.5	7.20(5)	298	>99	>99	50
3	5	8.80(3)	139	>99	>99	46
4	10	10.2(1)	100	>99	>99	74
5	20	11.3(1)	41	>99	>99	63
6	40	14.6(1)	20	>99	>99	60
7	60	13.6(1)	19	>99	98	55
8	120	12.2(1)	7	>99	96	52

Figure 3.5. Dehydropolymerisation of $H_3B{\cdot}NH_2Me$ with Ir(^{t}Bu-POCOP)$(H)_2$ (**1**) at different added concentrations of NH_2Me, (0.5 mM – 120 mM). Conditions: 2 mM [Ir], 2 M $H_3B{\cdot}NH_2Me$, THF, 293 K. [a]Determined by the pseudo zero order region of the profile [b]Measured by ^{11}B NMR spectroscopy. Yield is isolated yield of polymer from precipitation.

A hypothesis for the promoting effect of NH_2Me addition on catalysis is that the NH_2Me reacts with inactive borohydride complex **2** to form tetrahydride complex **3**, resulting in more catalyst on-cycle and higher rates of reaction. NH_2Me may also be involved in the catalytic cycle as a co-catalyst, so addition of NH_2Me would promote faster turnover. Alternatively, additional NH_2Me would also bias the equilibrium of the dissociation of the B–N bond in $H_3B{\cdot}NH_2Me$, resulting in this occurring to a lesser degree. The inhibitory effect observed with the highest concentrations of NH_2Me may be due to the equilibrium between catalyst **1** and Ir(^{t}Bu-POCOP)$(H)_2(NH_2Me)$ (**4**), established in section 2.7, resulting in the favourable formation of Ir(^{t}Bu-POCOP)$(H)_2(NH_2Me)$ (**4**). This is supported by observation of complex **4** in the ^1H and $^{31}P\{^1H\}$ NMR spectra taken at the end of catalysis for the reaction with the highest concentration of added NH_2Me (120 mM). This illustrates the complex role of NH_2Me in the dehydropolymerisation of amine-boranes with catalyst **1**.

3.3 Eyring and KIE

3.3.1 Eyring Analysis

Using an Eyring analysis (Figure 3.6), the activation parameters of the transition state were calculated. $\Delta H^{\ddagger}$ was 11(1) kcal mol^{-1}, $\Delta S^{\ddagger}$ was –17(2) cal K^{-1} mol^{-1} and the overall $\Delta G^{\ddagger}$ at 298 K was 16(1) kcal mol^{-1}. The significant negative $\Delta S^{\ddagger}$ is indicative of an associative mechanism for the transition state. The $\Delta H^{\ddagger}$ and $\Delta G^{\ddagger}$ are comparable to those reported for dehydrogenation of $H_3B{\cdot}NH_2Me$ using rhodium and iridium catalysts in the literature, with a $\Delta H^{\ddagger}$ of 16.0 kcal mol^{-1} and a $\Delta G^{\ddagger}$ of 17.0 kcal mol^{-1} for the rhodium system discussed in Chapter 1 (**i-27**).[8, 16]

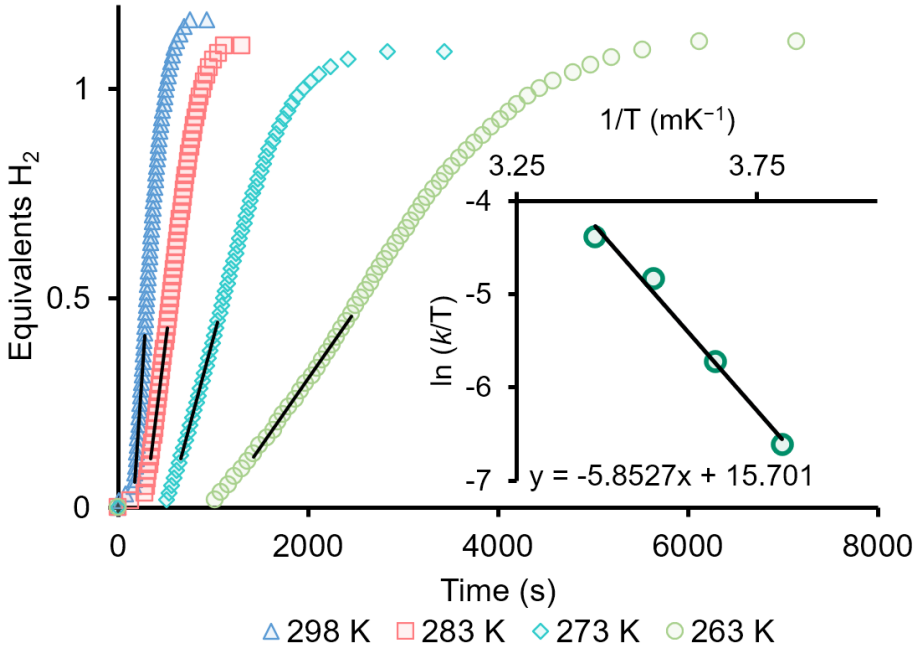

Entry	Temp. (K)	Rate[a] (mM s^{-1})	Induction period (s)	Conv.[b] (%)	Selectivity[b] (%)	Isolated yield (%)
1	293	6.61(6)	163	>99	>99	59
2	283	3.60(2)	282	>99	>99	54
3	273	1.68(1)	506	>99	>99	55
4	263	0.65(1)	1020	>99	>99	49

Figure 3.6. Dehydropolymerisation of $H_3B{\cdot}NH_2Me$ with Ir(^{t}Bu-POCOP)$(H)_2$ (**1**) at varied temperatures (298 K – 263 K), inset: Eyring plot (where k was calculated from $k = k_{obs}/[Ir]$) Conditions: 2 mM [Ir], 2 M $H_3B{\cdot}NH_2Me$, THF. [a]Determined by the pseudo zero order region of the profile [b]Measured by ^{11}B NMR spectroscopy. Yield is isolated yield of polymer from precipitation.

3.3.2 Effect of isotopic substitution on the dehydropolymerisation of $H_3B{\cdot}NH_2Me$ with Ir(POCOP)H_2

The effect of isotopic substitution on the dehydropolymerisation of amine-borane with catalyst **1** was probed using isotopologues $H_3B{\cdot}ND_2Me$ and $D_3B{\cdot}NH_2Me$ (Figure 3.7). Using $D_3B{\cdot}NH_2Me$ as the substrate resulted in a significant lengthening of the induction period from 57 s for $H_3B{\cdot}NH_2Me$ to 325 s for the isotopically substituted substrate ($D_3B{\cdot}NH_2Me$).[17] The maximum rates remained comparable however, 6.4(3) mM s^{-1} and 6.6(2) mM s^{-1} for

$D_3B{\cdot}NH_2Me$ and $H_3B{\cdot}NH_2Me$, respectively. The lengthening of the induction period was likely caused by formation of the borohydride complex **2** (with deuterated borane). The isotopic substitution would result in stronger interactions with the metal due to deuterium forming stronger bonds than hydrogen,[18] and so the position of the equilibrium would lie more heavily towards formation of complex **2**, causing the induction period to lengthen. Alternatively, the hydrolysis of the borohydride complex to form borates could be slower with BD_3 than with BH_3, leading to a longer induction period.

The reaction with $H_3B{\cdot}ND_2Me$ had a noticeable deceleratory curvature, as has been noted with other amine-borane dehydropolymerisation systems.[16, 17] This has previously been attributed to a change in speciation or a change in the rate-determining step that is isotopologue dependent. The reaction was repeated, and the kinetic profiles overlapped. The rate taken from the pseudo zero order regime of the kinetic profile was 4.6 mM s^{-1}, which was slower than with $H_3B{\cdot}NH_2Me$ (6.6(2) mM s^{-1}).

Deuteration at the borane resulted in little to no effect on the rate of reaction, with the k_{Hobs}/k_{Dobs} ~1, while substitution at the nitrogen results in a kinetic isotope effect (KIE) of ~1.4. Due to the change in kinetic profile, these results must be interpreted with caution; however, they suggest that N–H may be involved within the turnover determining manifold. This assumes that the same amount of active catalyst is present at the maximum rate from which k_{obs} is measured, which may not be the case as seen for Rh(^{i}Pr-PN^{H}P)$(H)_2$(Cl) (**i-27**).[16]

There was no change in the speciation of the iridium catalyst in the NMR spectra taken at the end of catalysis on isotopic substitution of the substrates. In the case of both $H_3B{\cdot}ND_2Me$ and $D_3B{\cdot}NH_2Me$, tetrahydride **3** was observed in the ^{1}H NMR spectrum and there was no evidence of a deuteride complex in the ^{2}H NMR spectrum. However, this would likely be in exchange and below the limit of detection.

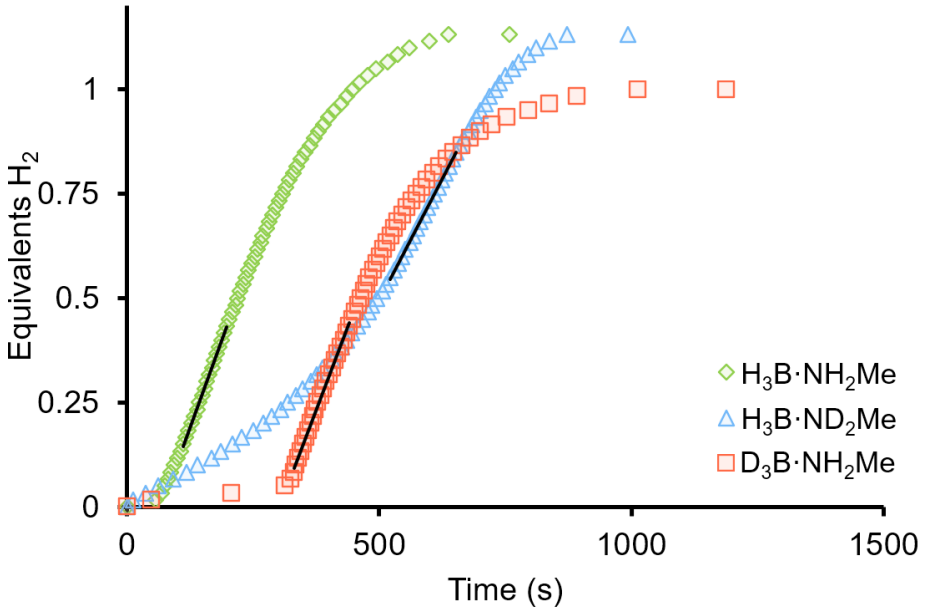

Entry	Substrate	Rate[a] (mM s^{-1})	Induction period (s)	Conv.[b] (%)	Selectivity[b] (%)	Isolated yield (%)
1	$H_3B{\cdot}NH_2Me$	6.6(2)	57	>99	>99	54
2	$D_3B{\cdot}NH_2Me$	6.4(3)	325	>99	>99	56
3	$H_3B{\cdot}ND_2Me$	4.6(1)	0	>99	>99	30

Figure 3.7. Dehydropolymerisation of $H_3B{\cdot}NH_2Me$ (isotopically substituted) with Ir(^{t}Bu-POCOP)$(H)_2$ (**1**) Conditions: 2 M substrate, 2 mM cat., THF, 293 K. [a]Determined by the pseudo zero order region of the profile [b]Measured by ^{11}B NMR spectroscopy. Yield is isolated yield of polymer from precipitation.

3.4 Possible proposed mechanisms of dehydrogenation

There are two proposed mechanisms that are consistent with the experimental data reported in the previous sections. One is based on an inner-sphere concerted mechanism similar to that proposed by Paul and Musgrave (discussed in section 1.6.2),[19] while the other is closely related to the proton rebound mechanisms discussed in section 1.3.7.[6, 7, 20]

In the case of both mechanisms, complex **1** initially binds $H_3B{\cdot}NH_2Me$ reversibly to form a σ-complex, supported by the saturation kinetics observed when the [$H_3B{\cdot}NH_2Me$] was varied. This formation of a σ-complex (**5**) is the initial step in many reported mechanisms for the dehydrogenation of amine-boranes.[6-9] After this point, the two mechanisms bifurcate

(Figure 3.8). Mechanism A involves B–H/N–H activation to form tetrahydride complex **3**, similar to the mechanism proposed by Paul and Musgrave.[19] Mechanism B forms an anionic trihydride [NH_3Me][Ir(^{t}Bu-POCOP)$(H)_3$] **[NH_3Me][6]** *via* an outer-sphere base promoted hydride transfer, which then forms tetrahydride complex **3** *via* a proton transfer (rebound). The mechanisms, as well as the computational calculations and kinetic modelling that support them, will be discussed in a later section.

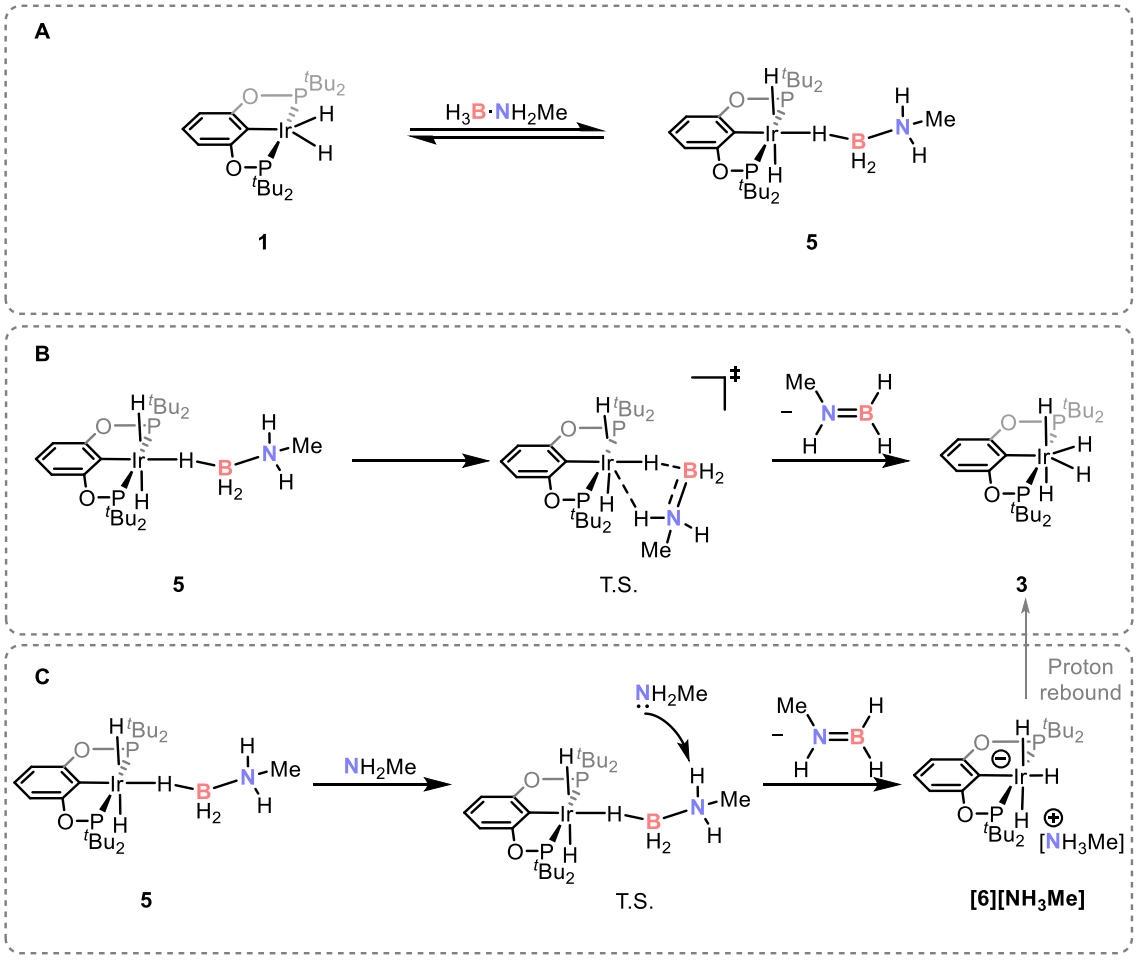

Figure 3.8. Two proposed mechanistic paths from the σ-complex (**5**) for the release of aminoborane. A) Reversible binding of $H_3B{\cdot}NH_2Me$ to **1** B) B–H/N–H activation to form tetrahydride complex **3** C) anionic trihydride [NH_3Me][Ir(^{t}Bu-POCOP)$(H)_3$] **[NH_3Me][6]** *via* an outer-sphere base promoted hydride transfer, which then forms tetrahydride complex **3** *via* a proton transfer (rebound).

Anionic iridium (POCOP) trihydrides have previously been reported (Figure 3.9). An example from Brookhart and co-workers with a sodium cation was generated *in-situ* by treating Ir(^{t}Bu-POCOP)HCl (**7**) with NaH.[21] Another example used complex **1** treated with Verkade's

base (^{i}Pr-VB, Figure 3.9) and H_2 (10 bar) to form the anionic trihydride [Ir(^{t}Bu-POCOP)$(H)_3$][^{i}Pr-VBH] (*iso*-propylimino-tri(pyrrolidino)phosphorane = ^{i}Pr-VB).[22] Cantat and coworkers postulated that [Ir(^{t}Bu-POCOP)$(H)_3$][^{i}Pr-VBH] was a catalytic intermediate in their catalytic cycle for the hydrogenolysis of chlorosilanes to hydrosilanes.[22] The authors proposed that the anionic trihydride formed by deprotonation of tetrahydride **3** by ^{i}Pr-VB, effectively the microscopic reverse of what is being proposed here. The subsequent section will report the synthesis and investigation of an anionic trihydride in catalysis for amine-borane dehydrogenation.

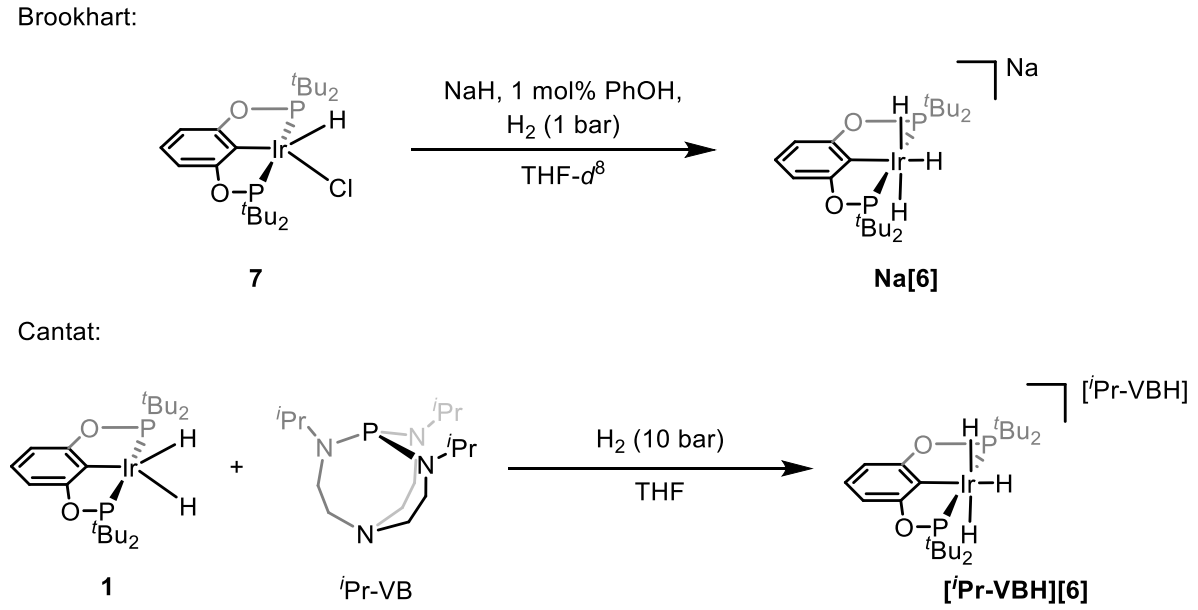

Figure 3.9. Synthetic routes to anionic iridium POCOP trihydrides.[21, 22]

3.4.1 Synthesis of an anionic iridium trihydride complex [Na-18-crown-6-$(THF)_2$][Ir(^{t}Bu-POCOP)H_3].

The synthesis of **[Na][6]** by Brookhart and coworkers allowed the generation of **[Na][6]** *in-situ*. To attempt to isolate **[6]**$^{-}$, 18-crown-6 was added to [Ir(^{t}Bu-POCOP)HCl] (**7**) with NaH in THF. However, this did not result in successful formation of **[6]**$^{-}$, with the formation of [Na-18-crown-6][Ir(^{t}Bu-POCOP)Cl] instead, identified by single crystal X-ray diffraction of crystals isolated from a THF/pentane solution (see the appendix for details).

Complex **[6]**$^-$ was successfully isolated by the addition of complex **1** in THF to a slurry of NaH, 18-crown-6 and THF. The reaction was stirred overnight at room temperature, with the ^{1}H and ^{31}P{^{1}H} NMR spectra of the reaction mixture showing the quantitative formation of [Ir(^{t}Bu-POCOP)H$_3$][Na-18-crown-6-(THF)$_2$] **[Na-18-crown-6][6]**.

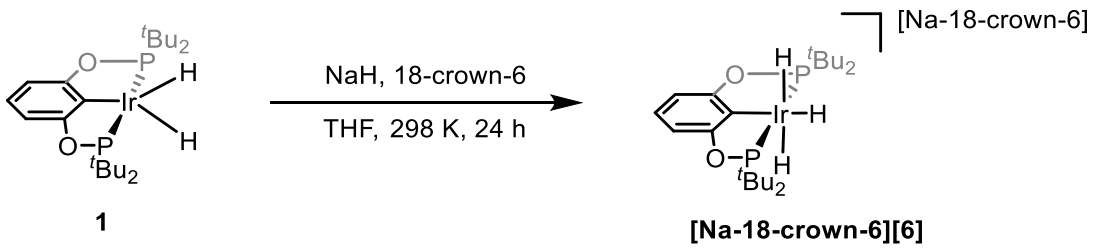

1 **[Na-18-crown-6][6]**

Scheme 3.1. The synthesis of [Na-18-crown-6-(THF)$_2$][Ir(^{t}Bu-POCOP)H$_3$] (**[Na-18-crown-6][6]**).

Crystallisation from a THF/hexane solution afforded colourless crystals (62% yield) of complex **[Na-18-crown-6][6]** (Figure 3.10). To our knowledge this is the first isolated example of an anionic iridium trihydride complex bearing the POCOP ligand framework. The data was of sufficient quality for the hydrides to be located (R(2σ) = 4.26, R(int) = 3.39%).

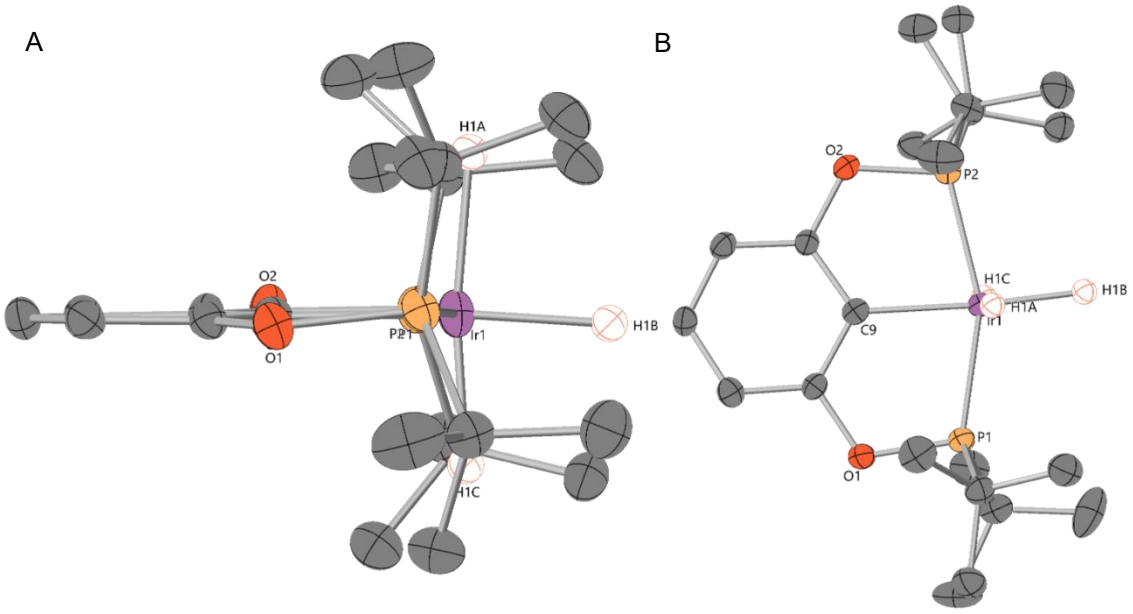

Figure 3.10. A view of the molecular structure of **[Na-18-crown-6][6]** A) side on view and B) view from above. Displacement ellipsoids are set at 50% probability, some hydrogen atoms and the cation are omitted for clarity. Selected bond lengths (Å): Ir1–P1 2.2514(12), Ir1–P2 2.2468(12), Ir1–C9 2.062(5), Ir1–H1A 1.83(8), Ir1–H1B 1.74(7), Ir1–H1C 1.73(7). Selected bond angles (°): P1–Ir1–P2 158.06(5), P1–Ir1–C9 78.97(14), P2–Ir1–C9 79.21(14).

[Na-18-crown-6][6] displays a pseudo square-planar geometry around the iridium(III) centre with a P1–Ir1–P2 angle of 158.06(5)°. The Ir–C distance of **[Na-18-crown-6][6]** is similar to that of dihydride complex **1** (2.062(5) Å and 2.059(4) Å, respectively).[23] The Ir–P distances are 2.2514(12) and 2.2468(12) Å, which are slightly shorter compared to neutral dihydride complex **1** (2.270(1) and 2.271(1) Å),[23] although it is difficult to draw a comparison as one is anionic and the other is neutral.

The ^{1}H NMR (THF-d^8) spectrum of **[Na-18-crown-6][6]** (Figure 3.11) shows a triplet ($^{3}J_{HH}$ = 7.5 Hz) and doublet ($^{3}J_{HH}$ = 7.5 Hz) at δ 6.16 (1 H) and δ 6.03 (2 H), assigned to H1 and H2 on the phenyl ring, respectively. Signals corresponding to the THF molecules bound to the [Na-18-crown-6]$^{+}$ are observed at δ 3.61 and δ 1.77. The ^{t}Bu groups are equivalent with a triplet at δ 1.33 (36 H). The hydride signals are observed at δ –11.58 (1H) and δ –13.22 (2H). The first as an apparent septet due to a small ^{1}H coupling constant ($^{2}J_{HH}$ = 5.1 Hz), that collapses to a broad triplet with ^{31}P decoupling ($^{2}J_{HP}$ = 11.6 Hz). This signal is attributed to the hydride *trans* to the phenyl ring. A triplet of doublets at δ –13.22 (2H, $^{2}J_{HP}$ = 16.7 Hz, $^{2}J_{HH}$ = 5.1 Hz) is assigned to the *cis* hydrides. The chemical shifts of the hydride signals are similar to those observed for **[^{i}Pr-VBH][6]** [δ –11.60 and δ –13.24 (CD_3CN)].[22] However, comparison to the chemical shifts for the hydride signals observed by Brookhart for **Na[6]** in d^8 THF (δ –13.33 and –13.55) shows a downfield shift for both signals, with the hydride *trans* to the phenyl ring showing the largest shift.[21] This may indicate dihydrogen $H^{\delta+}\cdots H^{\delta-}$ interactions between the hydride and the cation in complexes **[Na-18-crown-6][6]** and **[^{i}Pr-VBH][6]**. The resonance in the ^{31}P{^{1}H} NMR spectrum of **[Na-18-crown-6][6]** is a singlet at δ 192.31, which is more similar to that of **[^{i}Pr-VBH][6]** δ 194.40,[22] both are shifted downfield compared to the ^{31}P{^{1}H} NMR signal reported of **Na[6]** at δ 185.9.[21] There is also a noticeable chemical shift change in the ^{23}Na NMR spectra of **[Na-18-crown-6][6]** and **Na[6]** of δ –15 and δ –16, respectively.

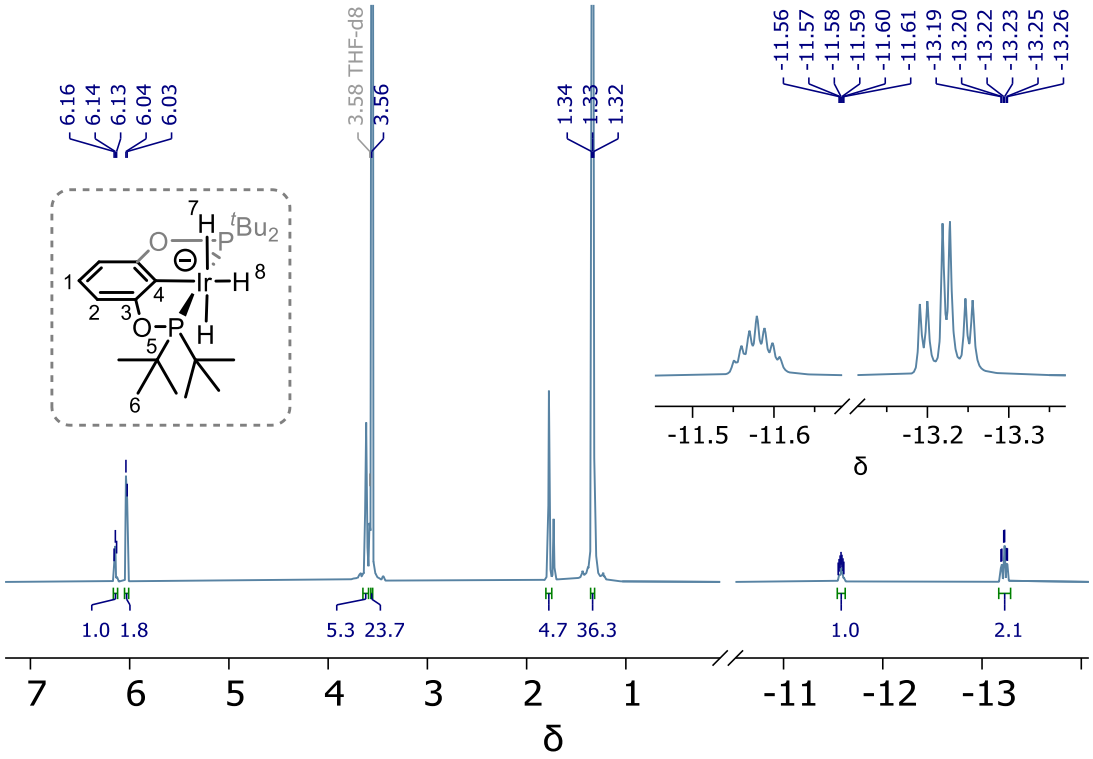

Figure 3.11. ^{1}H NMR spectrum (THF-d^{8}, 600 MHz, 298 K) of [Na(18-crown-6)(THF)$_2$][Ir(^{t}Bu-POCOP)H$_3$].

To investigate the downfield shift in the hydride signals observed in the ^{1}H NMR spectrum of **[Na-18-crown-6][6]**, Rotating-frame Overhauser Effect Spectroscopy (ROESY) NMR spectroscopy was employed. By selectively exciting each hydride signal in turn and recording a 1D ROESY NMR spectrum (Figure 3.12), signals for protons that experience through-space interactions with the excited hydride signals are observed. The selective excitation of both hydride resonances resulted in observed resonances for the ^{t}Bu groups (δ 1.33) and the protons associated with the crown ether (δ 3.56), indicating that there are through-space interactions between the iridium hydrides and the protons of the crown. This may be the cause of the downfield shift in the chemical shifts relative to the hydride shifts of Na**[6]**. However, in the solid-state molecular structure there are no observable H···H interactions <2.7 Å that would indicate an interaction (Figure 3.12).[24, 25]

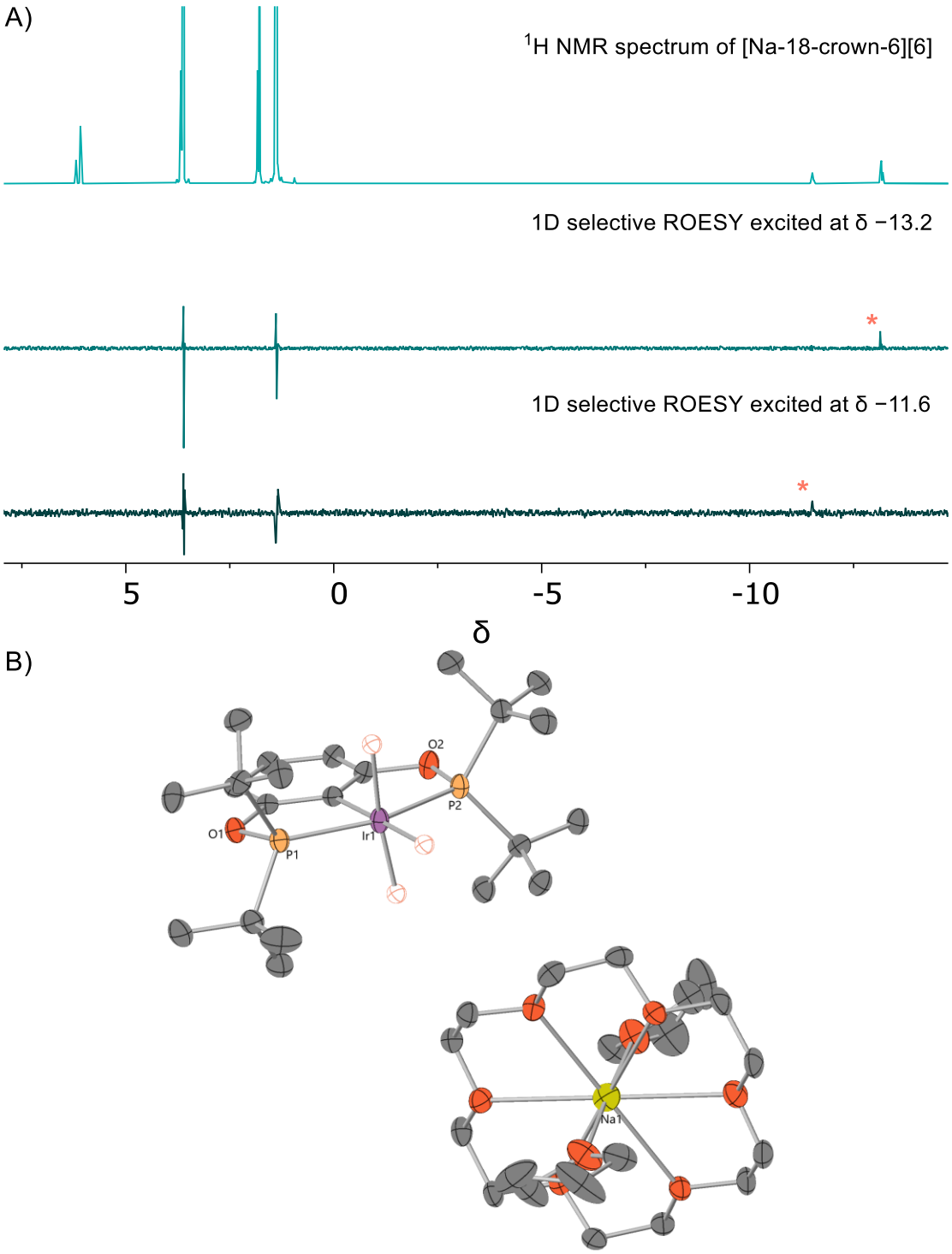

Figure 3.12. A) Stacked ^{1}H NMR spectra (THF-d^8, 500 MHz, 298 K) of [Na(18-crown-6)(THF)$_2$][Ir(^{t}Bu-POCOP)H$_3$] showing correlation between the hydride signals and crown protons, ^{1}H NMR spectrum (top), 1D selective ROESY excited at δ –13.2 hydride (middle), 1D selective ROESY excited at δ –11.6 hydride (bottom). Selectively excited peak indicated by *. B) Molecular structure of **[Na(18-crown-6)(THF)$_2$][Ir(^{t}Bu-POCOP)H$_3$]**. Displacement ellipsoids are set at 50% probability, some hydrogen atoms and the cation are omitted for clarity.

There are examples of anion hydride transition metal complexes with sodium or potassium crown cations. One structural feature that these examples have in common is that in most of them the face of the crown approaches the metal hydrides, to allow the formation of an ion pair (Figure 3.13).[26] One example [K(18-crown-6)][Ir(H)$_4$(P^{i}Pr$_3$)$_2$] presents a face-on crown spatial relationship with a Ir–K distance of 3.450(2) Å (Figure 3.13).[26] Another example of a face-on interaction is [K(18-crown-6)][W(H)$_5$(PMe$_3$)$_3$] which has a W–K distance of 3.660(1) Å,[27] and a ruthenium example [K(18-crown-6)][Ru(H)$_3$(PPh$_3$)$_3$] had a Ru–K distance of 3.613 Å.[28] Alternatively, in an example that contains a THF molecule co-ordinated to the cation, [K(THF)(18-crown-6)][Os(H)$_5$(P^{i}Pr$_3$)$_2$] (Figure 3.13), the crown faces the osmium side on and the closest distance between a hydride and a hydrogen on the crown is 2.4 Å.[26] This type of interaction is not observed in the solid-state molecular structure of **[Na-18-crown-6][6]**.

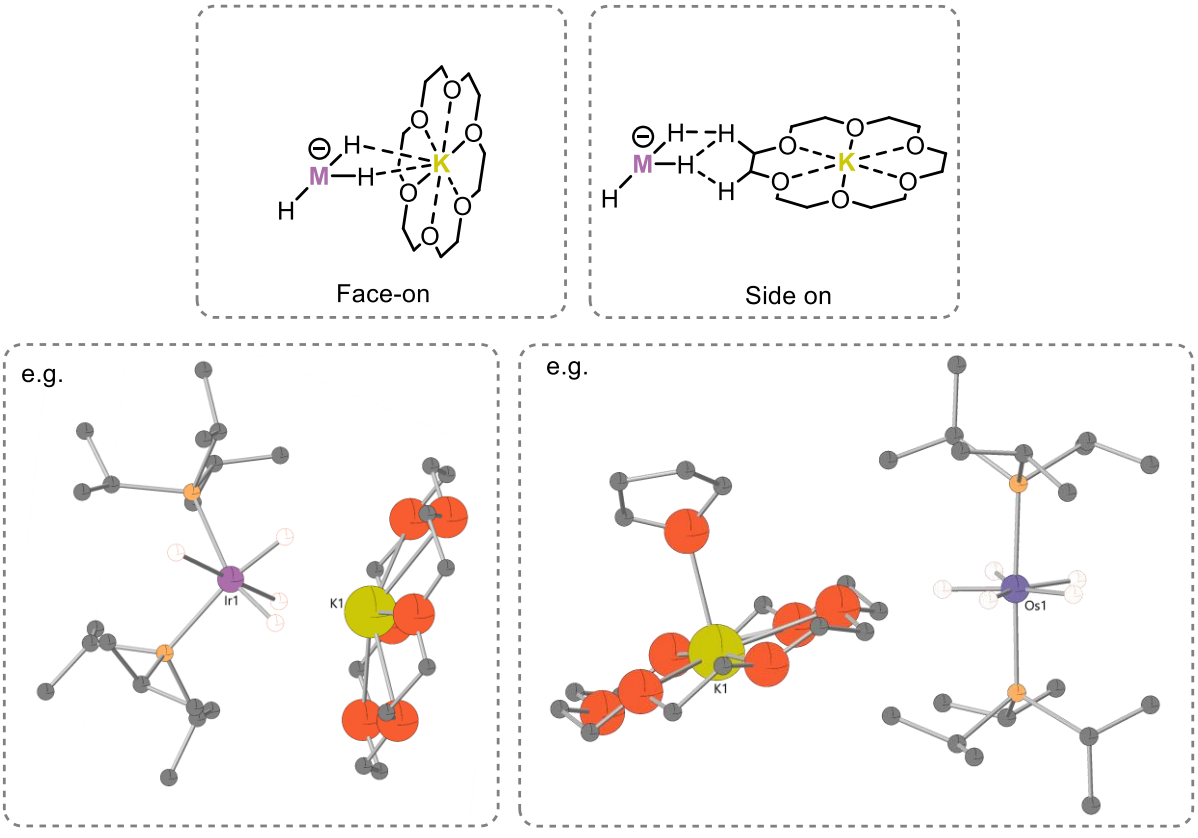

Figure 3.13. The two arrangements of hydride containing transition metal anions and K-crown cations with example molecular structures recreated from the reported cif.[26]

The promoting effect of crowns has been reported for other catalytic examples in the literature.[29, 30] To determine if a close interaction between the anion and cation is deemed to

be important to promoting the dehydrogenation of $H_3B{\cdot}NH_2Me$ with catalyst **1**, azacrowns should be considered as they promote interactions due to the formation of favourable N–H···H–Ir interactions.[26]

3.4.2 Probing the use of [Na-18-crown-6][6] in catalysis

With the synthesis and characterisation of **[Na-18-crown-6][6]** in hand, the kinetics of **[Na-18-crown-6][6]** in catalysis with $H_3B{\cdot}NH_2Me$ were recorded (Figure 3.14). Reaction with **[Na-18-crown-6][6]** resulted in >99% conversion of $H_3B{\cdot}NH_2Me$ to polyaminoborane, supported by ~1 equivalent of H_2 release. The induction period was 274 s, within the range of that seen for catalyst **1** (200-300 s) and the rate was comparable to that noted for catalyst **1** (5.97(3) mM s^{-1} and 5.95(3) mM s^{-1}, respectively). The observed speciation at the end of catalysis echoed that shown for catalyst **1**, with only tetrahydride complex **3** observed. This shows that **[Na-18-crown-6][6]** can be used as a competent pre-catalyst for the dehydrogenation of amine-boranes.

Interestingly, the addition of 1 equivalent of $[NH_3Me][BAr^F{}_4]$ to the reaction with **[Na-18-crown-6][6]** resulted in complete removal of the induction period and a three times increase in the rate of reaction (19.2(3) mM s^{-1}). The use of ammonium as an additive has previously been reported to have a promoting effect in some cases,[8] and an inhibitory effect in others,[7] as discussed in Chapter 1.

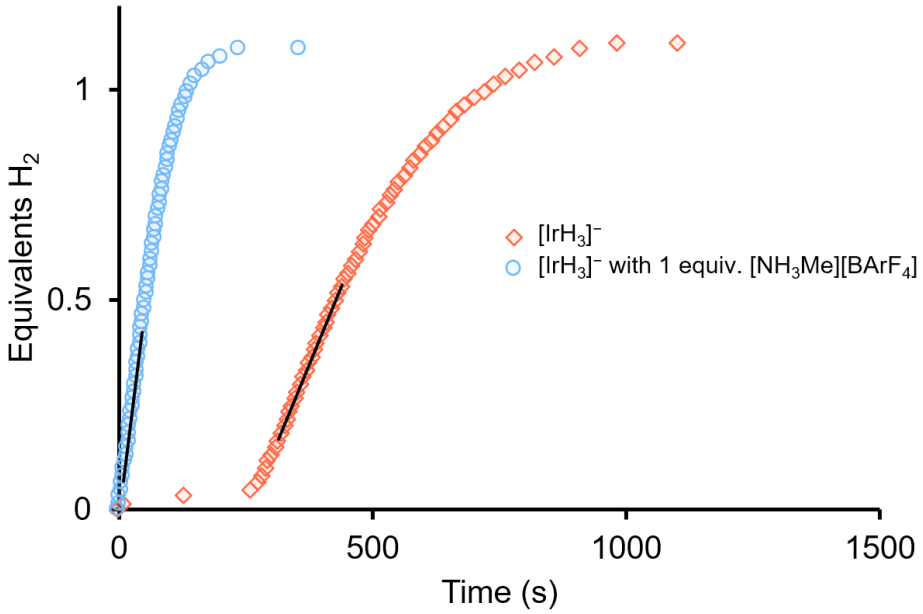

Entry	$[NH_3Me][BAr^F_4]$ Equiv.	Rate[a] (mM s^{-1})	Induction period (s)	Conv.[b] (%)	Selectivity[b] (%)	Isolated yield (%)
1	0	5.97(3)	274	>99	>99	63
2	1	19.2(3)	0	>99	>99	59

Figure 3.14. Dehydropolymerisation of $H_3B{\cdot}NH_2Me$ with **[Na-18-crown-6][6]**, with and without the addition of $[NH_3Me][BAr^F_4]$ (1 equiv.). Conditions: 2 mM [Ir] (0.1 mol%), 2 M $H_3B{\cdot}NH_2Me$, THF, 293 K. [a]Determined by the pseudo zero order region of the profile [b]Measured by ^{11}B NMR spectroscopy. Yield is isolated yield of polymer from precipitation.

The addition of $[NH_3Me][BAr^F_4]$ (1 equiv.) to **[Na-18-crown-6][6]** in the absence of $H_3B{\cdot}NH_2Me$ resulted in the formation of dihydride-amine complex **4**, tetrahydride complex **3** and dihydride complex **1** (90:7:3) observed by ^1H NMR spectroscopy (Figure 3.15). This indicates that $[NH_3Me]^+$ may act as a proton source to protonate **[Na-18-crown-6][6]** to form tetrahydride **3** and NH_2Me, this results in participation in the established equilibrium between complexes **1**, **3** and **4** as discussed in section 2.7.2.

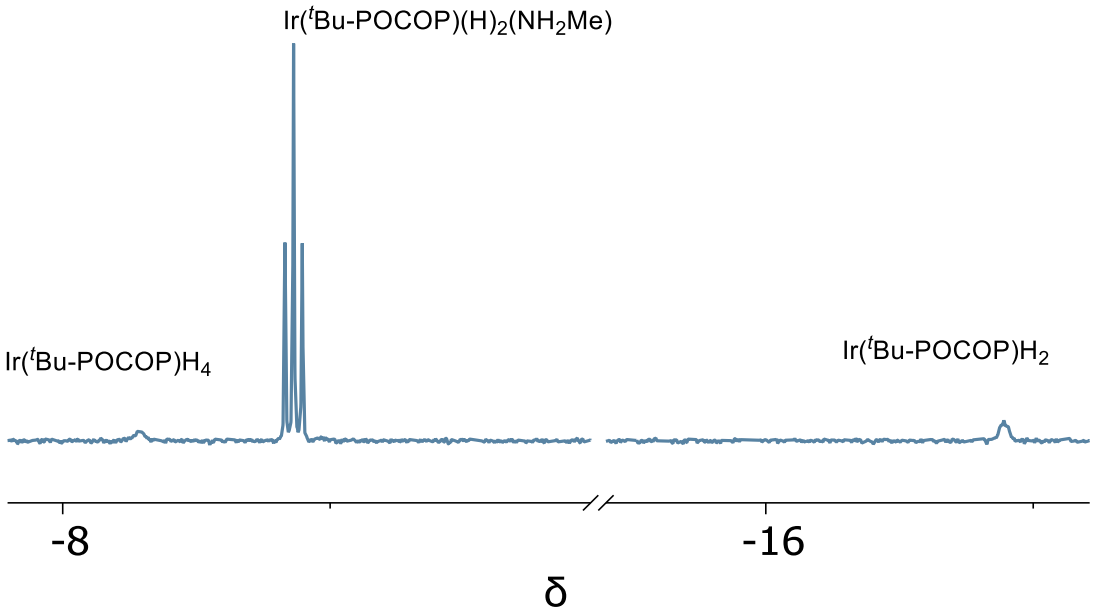

Figure 3.15. ^{1}H NMR spectrum (THF-H^{8}, 500 MHz, 298 K) of an NMR scale reaction of **[Na-18-crown-6][6]** and [NH$_3$Me][BAr$^F{}_4$] (1 equiv.).

If a proton source (*e.g.* [NH$_3$Me]$^+$) is required for **[Na-18-crown-6][6]** to turn over, this may explain the induction period observed in catalysis with **[Na-18-crown-6][6]**. Adventitious H_2O in the solvent may act as this proton source, allowing for a limited number of turnovers. If the formation of **[6]**$^-$ is part of the catalytic cycle, as suggested in Figure 3.8, then once the catalyst begins to turnover, one equivalent of [NH$_3$Me]$^+$ would form for each equivalent of **[6]**$^-$ allowing the catalyst to turn over freely. The addition of 1 equivalent of [NH$_3$Me][BAr$^F{}_4$] would provide a proton source on addition of the catalyst to the substrate, allowing the catalyst to turn over without an induction period and at the fastest rate of turn over observed for the different conditions tested so far. Further investigation into the addition of [NH$_3$Me]$^+$ to catalyst **1** will be discussed later in this chapter.

3.4.3 Two proposed mechanisms

The two proposed mechanisms for the dehydropolymerisation of $H_3B{\cdot}NH_2Me$ are shown in Figure 3.16. Following the initial reversible coordination of $H_3B{\cdot}NH_2Me$ to the metal, Mechanism A proceeds *via* a concerted B–H/N–H activation to form tetrahydride complex **3** (in Mechanism A K_4 (k_4/k_{-4}) follows k_2 for ease of comparison to Mechanism B). In Mechanism B an anionic trihydride $[NH_3Me][Ir(^tBu\text{-}POCOP)(H)_3]$ is formed *via* an outer-sphere base promoted hydride transfer, which then protonates to form tetrahydride complex **3**. Both mechanisms feature the loss of H_2 from tetrahydride complex **3** to re-form the dihydride, and the off-cycle equilibrium between dihydride complex **1** and dihydride amine complex **4**. This is supported by the EXSY NMR experiments discussed in section 2.7.2 and the inhibitory effect on the rate of reaction when NH_2Me is added (>60 mM) to catalysis with complex **1**. A further off-cycle reaction occurs from σ-complex **5** to form borohydride complex **2** *via* loss off NH_2Me from the σ-complex.

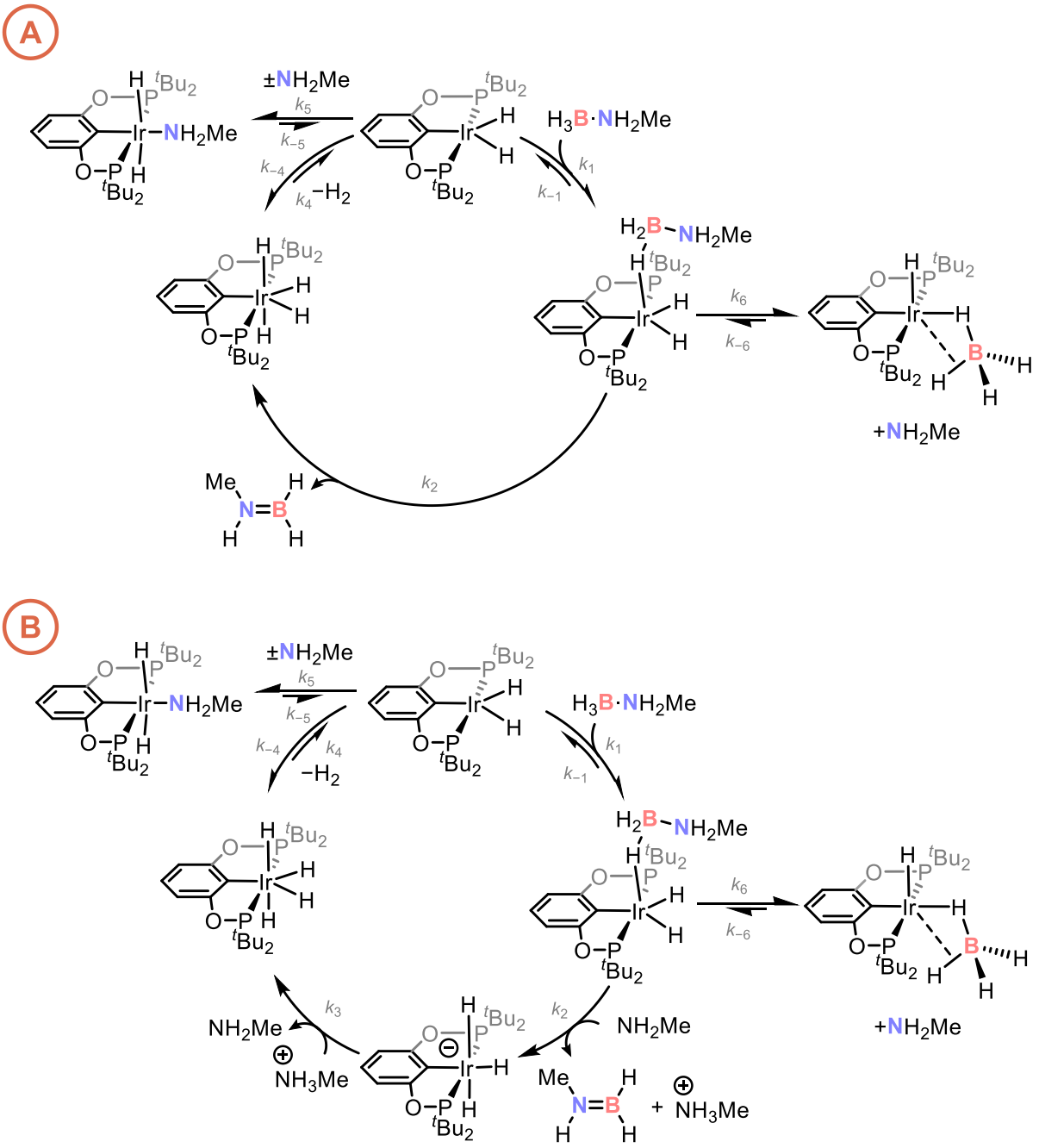

Figure 3.16. Proposed mechanisms for the dehydrogenation of amine-borane with catalyst **1**. A) B–H/N–H activation B) Base promoted hydride transfer. In Mechanism A K_4 *(k_4/k_{-4})* follows k_2 for ease of comparison to Mechanism B.

In section 3.4.2, trihydride **[Na-18-crown-6][6]** was shown to be a competent catalyst for the dehydrogenation of $H_3B{\cdot}NH_2Me$. However, this does not provide evidence of its active participation in turnover as it may sit as a pre-catalyst outside the catalytic cycle. To further investigate both proposed mechanisms, other methods were required, and so both proposed mechanisms were modelled using COPASI.[1] All data modelling was carried out by Professor

Andrew Weller at the University of York. Eight independent data sets with varying conditions (*i.e.* catalyst loading, [$H_3B{\cdot}NH_2Me$], [$H_3B{\cdot}NH_2Me$] with 10 mM NH_2Me, and [NH_2Me]), were holistically modelled against the experimental data. The experimental conditions are shown in Table 3.1. All of the experimental data was time-shifted to remove the induction period and, where possible, experimentally determined rate constants were used and fixed to avoid over parameterisation (k_4, k_{-4}, k_5, k_{-5}).[31] The rate constants estimated for the equilibrium between **1** and **4** in d^8 THF from EXSY NMR experiments (as discussed in section 2.7.2) were included. The flow NMR data evidenced that catalysis was not active during the induction period with little/no conversion of monomer, thus it was reasonable that the induction periods be removed for the modelling with COPASI. The solution phase H_2 concentration was limited to 0.04 M to reflect eudiometric conditions, and the very slow dissociation of $H_3B{\cdot}NH_2Me$ was included.[32] The B–H/N–H activation was simplified to a single step for ease of modelling. All data was normalised to 1 equivalent of H_2 formed (2 M [$H_2B{=}NHMe$]). This is justified as the reaction goes to completion and is >99% selective.

Table 3.1. Experimental conditions for the dehydropolymerisation of $H_3B{\cdot}NH_2Me$ in THF using catalyst **1** under eudiometric conditions used in the COPSAI simulations.

Entry	$[Ir]_{TOTAL}$ (mM)	$[H_3B{\cdot}NMeH_2]$ (M)	$[NMeH_2]$ (mM)
a	2.0	2.0	1.0
b	2.0	2.0	10
c	2.0	2.0	20
d	2.0	2.0	60
e	2.0	1.0	3.0
f	2.0	0.5	1.8
g	2.0	1.0	10
h	1.0	2.0	2.2

Both mechanisms can be sufficiently modelled using COPASI by holistically fitting the simulated (line) and experimental (marker) data from the measured hydrogen evolution, expressed as [$H_2B{=}NHMe$] (Figure 3.17). Both mechanisms show an acceptable fit to the

experimental data. The values for the equilibrium constants that COPASI produces based on the mechanisms show that both mechanisms strongly favour the formation of σ-complex **5** from **1** (k_1/k_{-1} = 10^9 M^{-1}). The formation of borohydride complex **2** is favoured in Mechanism B over Mechanism A (k_6/k_{-6} = 10^3 M and 0.03 M respectively). In Mechanism B $k_2<k_1<k_3$ and in Mechanism A $k_2 \approx k_1$.

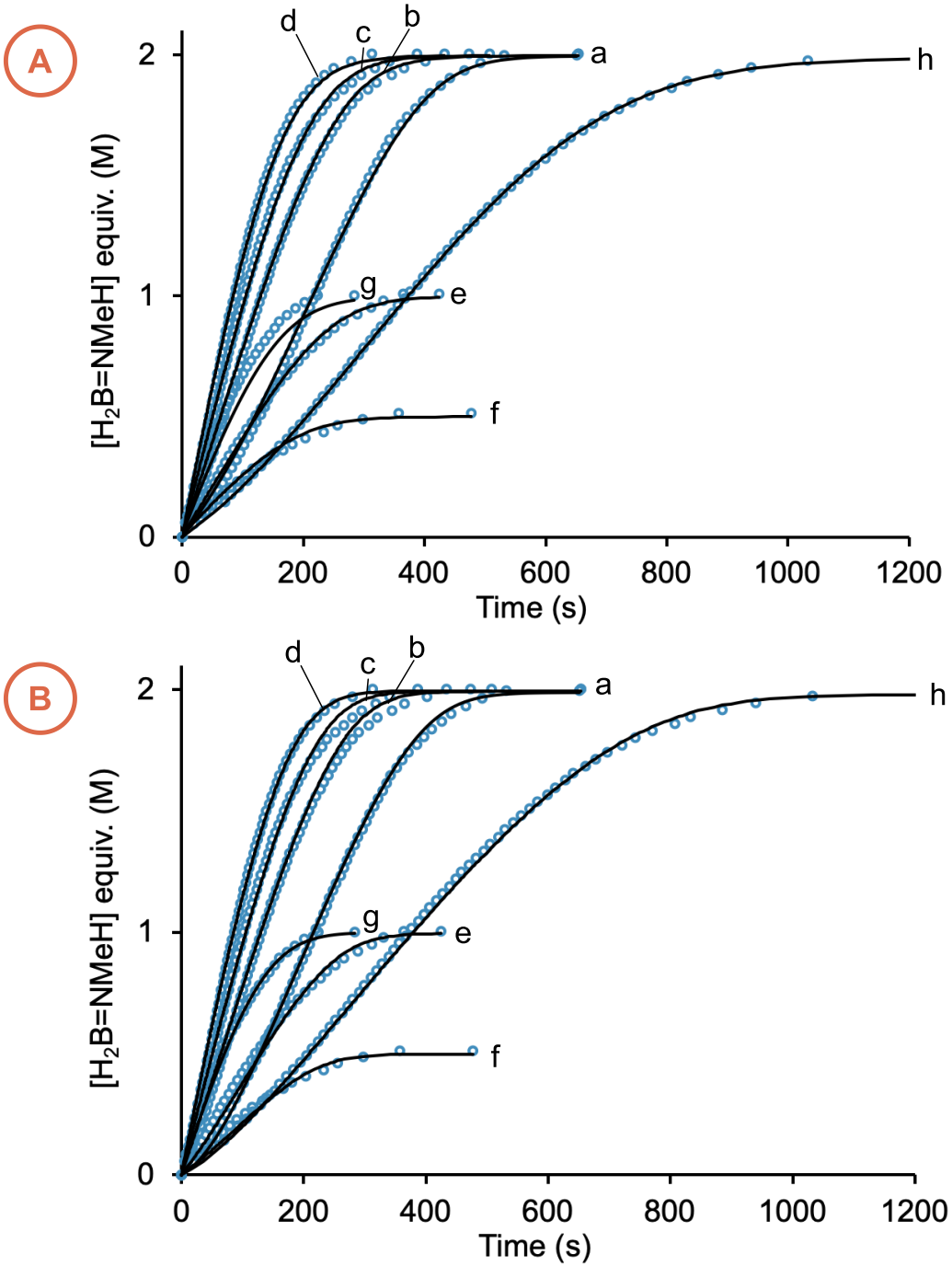

Figure 3.17. [H_2B=NMeH] as a proxy for H_2 evolution *versus* time for eight different starting concentrations of $H_3B{\cdot}NH_2Me$ listed in Table 3.1. [H_2] limited to 0.04 M using the "Events" function in COPASI. Open circles = experimental data; solid lines = holistically simulated data

derived for the two catalytic manifolds A and B. Data is time-shifted to remove induction periods.

To gain further understanding of the mechanisms DFT calculations were performed by Professor Stuart Macgregor and Dr M. Arif Sajjad at the University of St Andrews.

The DFT calculations suggest that in the case of catalyst **1**, borohydride complex **2** forms from the loss of amine from σ-complex **5** (Figure 3.18). Both complexes **5** and **2** have a similar relative energy and involve an overall barrier (relative to complex **5**) of 13.9 kcal mol^{-1}. This is consistent with borohydride complex **2** being off-cycle but the equilibrium being established rapidly. The calculated K_{eq} values for these reactions would be 3.65 ×10^{-3} and 2.44 ×10^{-3} for the forwards and backwards reaction, respectively. Complex **2** is slightly lower in energy (ΔG = –1 kcal mol^{-1}), indicating that formation of complex **2** and 'free' NH_2Me is slightly favoured, which is consistent with what was observed experimentally in the flow NMR data discussed in Section 2.3.4.

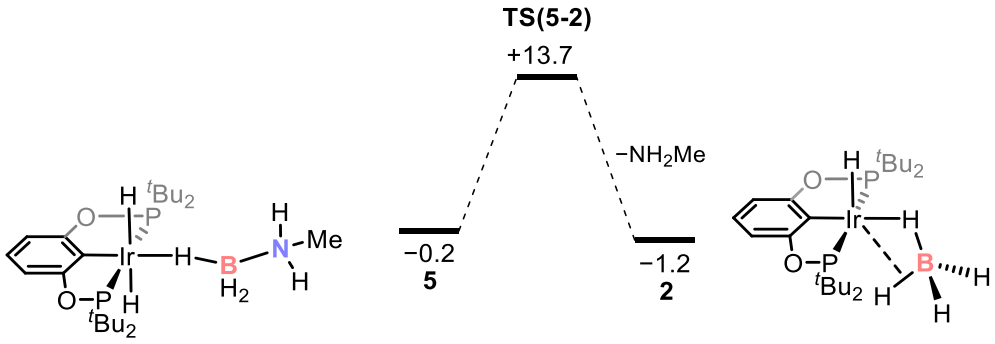

Figure 3.18. Computed free energy profile (kcal mol^{-1}) for the interconversion between complexes **5** and **2**. Level of theory: PBE0-D3BJ(def2-tzvp,THF)//BP86/SDD (Ir, P with polarization on P); 6-31G** other atoms).

The computed pathways for Mechanisms A and B are shown in Figure 3.19. The formation of σ-complex **5** is the first step in both computed pathways, then the B–H/N–H activation pathway forms tetrahydride **3** (–8.0 kcal mol^{-1}) *via* **TS(5-3)** (+11.0 kcal mol^{-1}). The alternate pathway (Mechanism B) results in deprotonation of amine-borane to form the anionic trihydride **[NH$_3$Me][6]** (+7.7 kcal mol^{-1}) *via* **TS(5-6)** (+14.6 kcal mol^{-1}). The structure of **[NH$_3$Me][6]** was

computed to be a dihydrogen-bonded ion pair from which a proton transfer releases NH_2Me to form tetrahydride complex **3**. Complex **3** is a common intermediate in both mechanistic pathways, and the reductive coupling of complex **3** to complex **3'** is the rate determining step in both processes prior to the loss of H_2. This is consistent with observation of tetrahydride complex **3** as the resting state and the experimentally determined $\Delta S^{\ddagger} = -17(2)$ cal K^{-1} mol^{-1}, indicative of an associative mechanism towards the transition state. The computed energy span of both mechanisms (**3** to **TS(3-3')**) is in good agreement with the experimentally determined value, 16.1 kcal mol^{-1} and 16(2) kcal mol^{-1}, respectively.

While the B–H/N–H activation pathway *via* **TS(5-3)** is more accessible that the base assisted pathway *via* **TS(5-6)**, +11.0 kcal mol^{-1} and +14.6 kcal mol^{-1}, respectively, both proposed mechanisms are plausible.

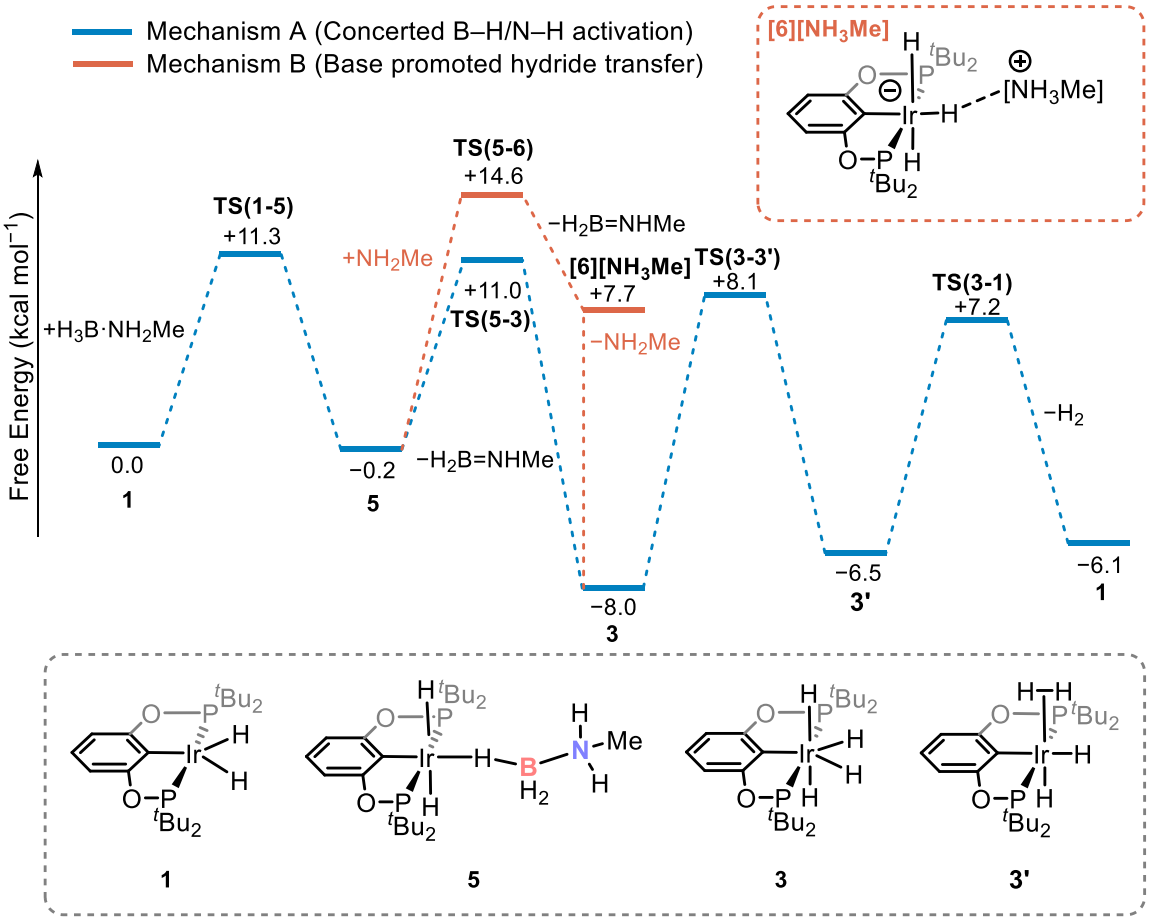

Figure 3.19. Computed free energy profiles (kcal mol^{-1}) for Mechanisms A and B. Level of theory: BP86-D3BJ(DEF2-TZVP, THF)//BP86/SDD (Ir, P with polarization on P); 6-31G** other atoms).

The experimental observations, numerical simulations and DFT calculations cannot differentiate between the two mechanisms, with both providing an acceptable fit for the data. However, the rate constants generated by the models created can be used to simulate catalyst speciation with COPASI. The models do not consider the induction period. Under the reaction conditions used to collect the flow NMR data ([**1**] = 0.5 mM, [$H_3B{\cdot}NH_2Me$] = 0.5 M, [NH_2Me] = 0.5 mM, $[H_2]_{dissolved}$ limited to 0.2 M), COPASI can provide a simulation of expected speciation for each model (Figure 3.20). Mechanism A provides a much closer fit to the observed speciation in the flow NMR data (see section 2.3.4), where there is a high concentration of borohydride complex **2** observed at early reaction times. This transforms to tetrahydride complex **3** early in the reaction and remains as complex **3** for the duration of catalysis. This very close fit between the simulated and experimental data provides some justification for not

considering the induction period in the model. Mechanism B shows more complex speciation that does not fit the observed data, showing high concentrations of σ-complex **5** and trihydride complex **[6]**$^-$ at early reaction times that forms a mixture of complexes **2** and **3** over time. This suggests that the operation of proposed Mechanism A is more likely.

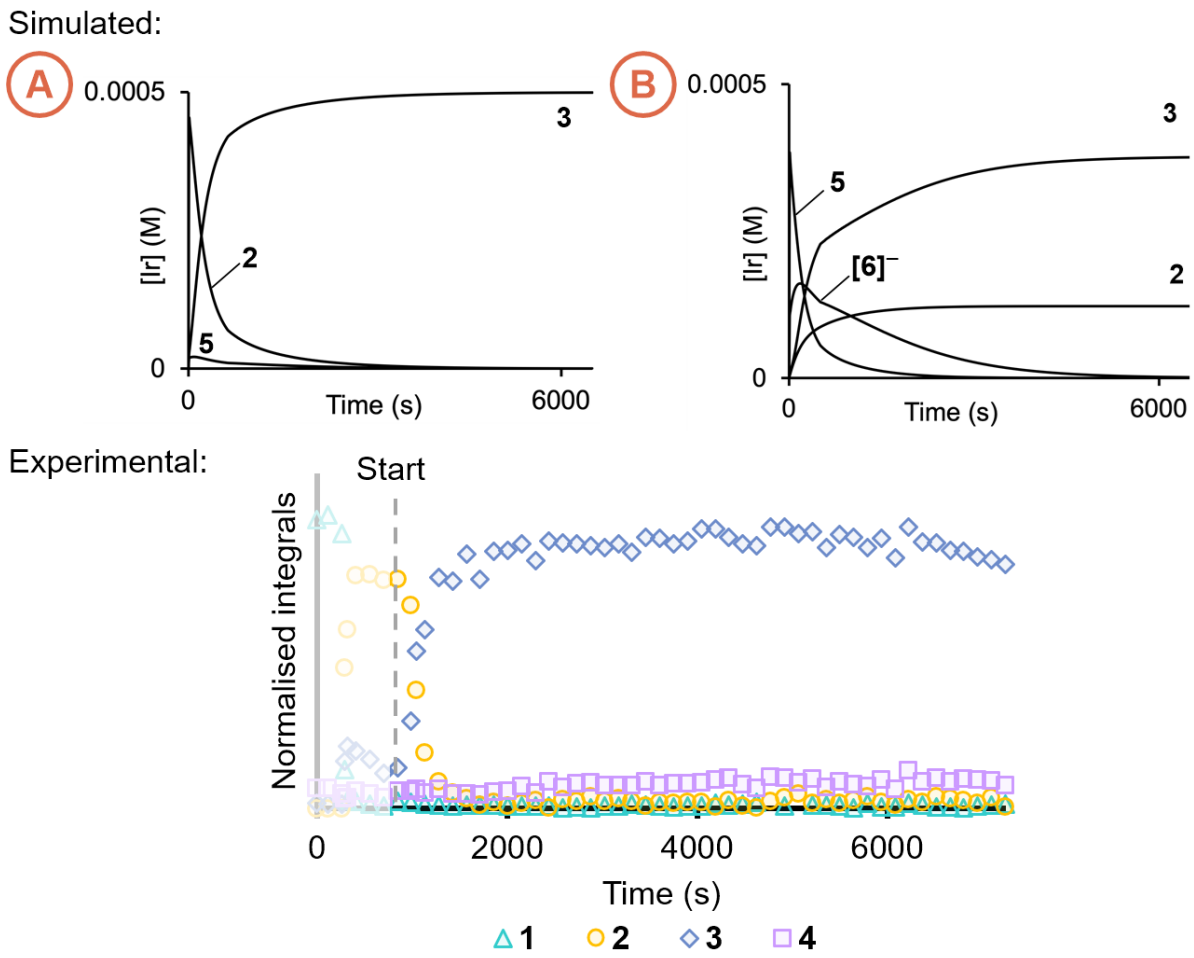

Figure 3.20. Simulated species *versus* time-shifted plots for mechanism A and B under Flow NMR conditions: [**1**] = 0.5 mM, [$H_3B{\cdot}NH_2Me$] = 0.5 M, [NH_2Me] = 0.5 mM, $[H_2]_{dissolved}$ limited to 0.2 M.

3.5 Role of Additives in the dehydropolymerisation of amine-boranes with catalyst 1

3.5.1 Addition of $[NH_3Me]^+$

The addition of $[NH_3Me]^+$ to the dehydropolymerisation reaction using catalyst **[Na-18-crown-6][6]** resulted in some interesting observed reactivity, leading to catalysis with no induction period and a high rate of turnover. To further investigate this the reactivity of $[NH_3Me]^+$ in catalysis with complex **1** was investigated (Figure 3.21).

The addition of $[NH_3Me]Cl$ (5 equiv. relative to **1**) to the dehydropolymerisation of $H_3B{\cdot}NH_2Me$ with catalyst **1** resulted in no induction period and a high rate of turnover compared to the reaction with complex **1** without additives (8.17(3) mM s^{-1} and 5.93(3) mM s^{-1}, respectively). There was slight curvature to the kinetic profile at lower conversion <25% (0.25 equiv. H_2). This curvature was also observed when bis(triphenylphosphine)iminium chloride ([PNP]Cl) was added to catalysis with **1**, although with a significant induction period. The addition of [PNP]Cl (5 equiv.) resulted in slower turnover compared to a standard reaction with catalyst **1** without additives (4.63(4) mM s^{-1} and 5.93(3) mM s^{-1}, respectively). The observed curvature may be due to a competing reaction that is taking place, potentially the formation of reported complex Ir(^{t}Bu-POCOP)HCl (**7**) taking active catalyst off-cycle. Meanwhile, addition of 5 equivalents of $[NH_3Me][BAr^F{}_4]$ to catalysis resulted in no observable change compared to when no additive was added. This demonstrates that there is a requirement for both $[NH_3Me]^+$ and Cl^- to remove the induction period and promote turnover with catalyst **1**. While $[NH_3Me]Cl$ has a promoting effect on catalysis with **1**, the rate does not reach that achieved with trihydride **[Na-18-crown-6][6]** with 1 equivalent of $[NH_3Me][BAr^F{}_4]$, k_{obs} = 19.2(3) mM s^{-1}.

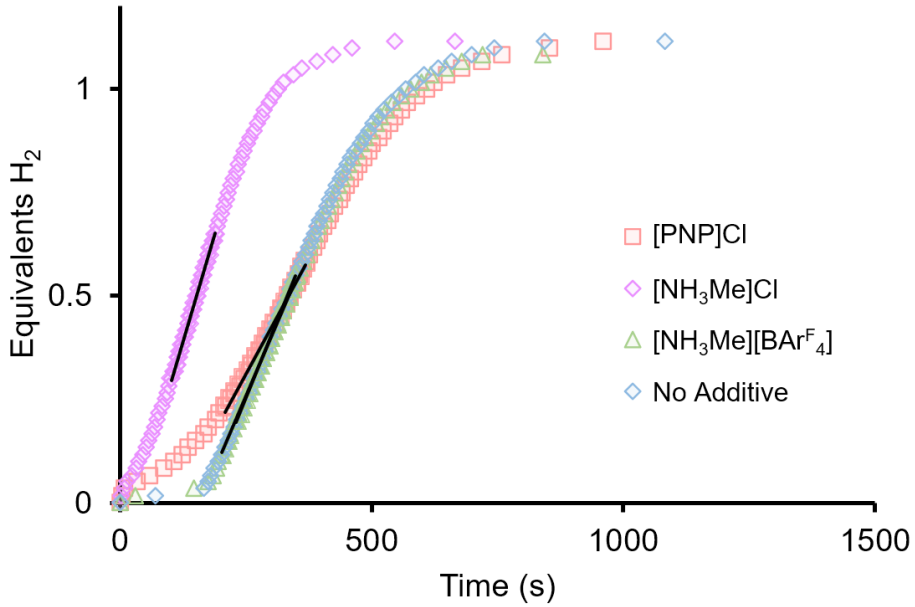

Entry	Additive	Rate[a] (mM s^{-1})	Induction period (s)	Conv.[b] (%)	Selectivity[b] (%)	Isolated yield (%)
1	None	5.93(3)	167	>99	>99	62
2	[NH_3Me]Cl	8.17(3)	0	>99	>99	56
3	[NH_3Me][BAr^F_4]	5.73(2)	179	>99	>99	72
4	[PNP]Cl	4.63(4)	139	>99	>99	66

Figure 3.21. Dehydropolymerisation of $H_3B{\cdot}NH_2Me$ with **1**, with and without the addition of additives (5 equiv. [NH_3Me][BAr^F_4], [NH_3Me]Cl, [PNP]Cl). Conditions: 2 mM [Ir] (0.1 mol%), 2 M $H_3B{\cdot}NH_2Me$, THF, 293 K. [a]Determined by the pseudo zero order region of the profile [b]Measured by ^{11}B NMR spectroscopy. Yield is isolated yield of polymer from precipitation.

In Chapter 2, it was established that the formation of borohydride complex **2** was the cause of the induction period. The addition of five equivalents of sparingly soluble [NH_3Me]Cl to complex **2** in THF led to the formation of hydrido-chloride complex **7** and unreacted complex **2** observed by ^1H NMR spectroscopy (Figure 3.22 A). This reaction would produce H_2, however this was not observed by ^1H NMR spectroscopy, this is due to it being below the limit of detection or other peaks (*i.e.* THF) obscuring the chemical shift range (δ ~4). The formation of $H_3B{\cdot}NH_2Me$ was observed in the ^{11}B NMR spectrum (Figure 3.22 B). This suggests that addition of [NH_3Me]Cl to catalysis with **1** results in the formation of hydrido-chloride complex **7** from initially formed borohydride complex **2**, from which complex **7** can undergo a dehydrodehalogenation reaction to form complex **1**. This type of activation has been proposed

for other amine-borane dehydropolymerisation catalysts that contain chloride ligands,[11, 13, 16] examples of which were discussed in Chapter 1.

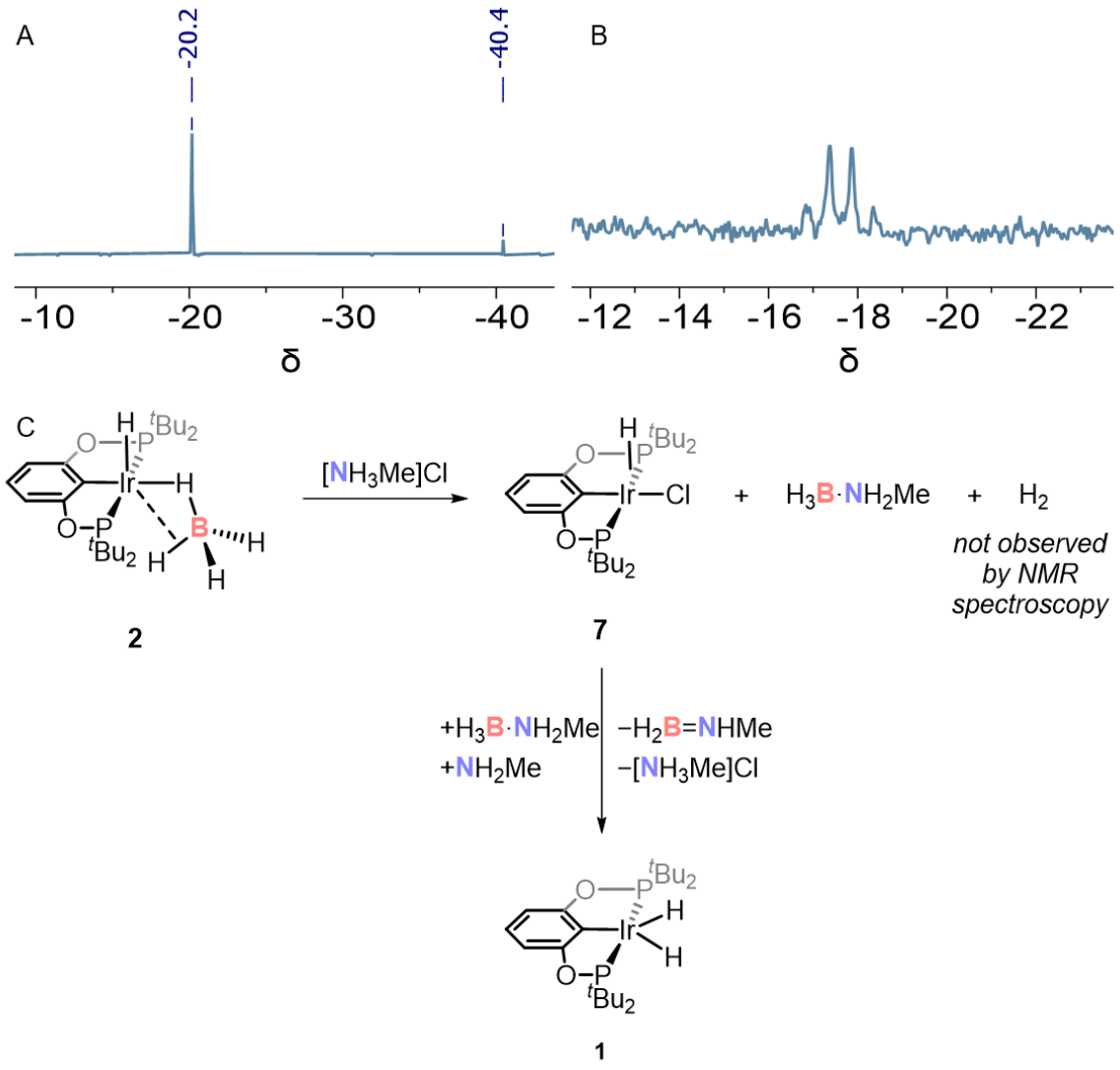

Figure 3.22. Reaction of Ir(ᵗBu-POCOP)(H)$_2$(BH$_3$) with [NH$_3$Me]Cl (5 equiv.) in THF. A) ^{1}H NMR spectrum (THF-H^8, 600 MHz, 298 K) B) ^{11}B NMR spectrum (THF-H^8, 193 MHz, 298 K) C) Proposed activation of complex **2** under [NH$_3$Me]Cl/NH$_2$Me conditions.

3.5.2 Addition of Na^+

In the previous section, it has been shown that addition of $[NH_3Me]Cl$ has a promoting effect on catalysis with **1**, although the rate of reaction does not reach the same rate of reaction as when 1 equivalent of $[NH_3Me][BAr^F_4]$ was added to trihydride **[Na-18-crown-6][6]** in catalysis (Rate = 19.2(3) mM s^{-1}). Therefore, it was important to determine if the cation may be playing a role in promoting the dehydrogenation of amine-boranes.

Addition of 5 equivalents of $[Na\text{-}18\text{-}crown\text{-}6][BAr^F_4]$ to the dehydropolymerisation of $H_3B{\cdot}NH_2Me$ with catalyst **1** resulted in a reduced induction period, 167 s and 92 s for no additive and with additive, respectively (Figure 3.23). Adding $[Na\text{-}18\text{-}crown\text{-}6][BAr^F_4]$ also resulted in a higher rate of turnover, 8.52(3) mM s^{-1} and 5.93(3) mM s^{-1} with and without $[Na\text{-}18\text{-}crown\text{-}6][BAr^F_4]$, respectively. This promoting effect still did not rival the higher rate seen with **[Na-18-crown-6][6]**. As has been discussed previously, NH_2Me has a promoting effect on the dehydrogenation of amine-boranes, and the addition of **[Na-18-crown-6][6]** and $[NH_3Me][BAr^F_4]$ would produce NH_2Me based on the proposed Mechanism B. Thus, 5 equivalents of $[Na\text{-}18\text{-}crown\text{-}6][BAr^F_4]$ and 5 equivalents of NH_2Me were added to catalysis with **1**, resulting in a further increase in rate of reaction (Rate = 12.9(1) mM s^{-1}) and reduction in induction period (42 s).

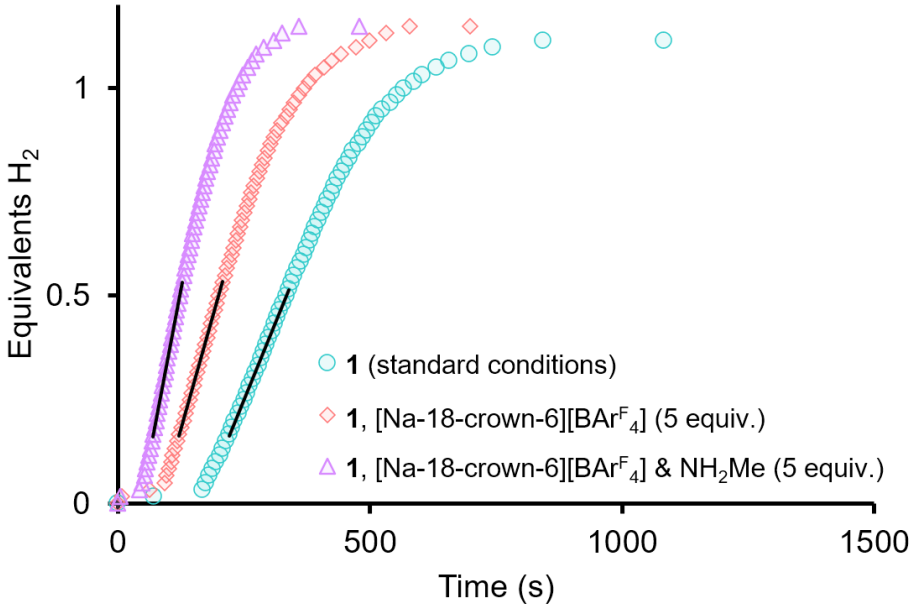

Entry	Additive	Rate[a] ($mM\ s^{-1}$)	Induction period (s)	Conv.[b] (%)	Selectivity[b] (%)	Isolated yield (%)
1	None	5.93(3)	167	>99	>99	62
2	[Na-18-crown-6][BAr^F_4]	8.52(3)	92	>99	>99	69
3	[Na-18-crown-6][BAr^F_4] & NH_2Me	12.9(1)	42	>99	>99	82

Figure 3.23. Dehydropolymerisation of $H_3B{\cdot}NH_2Me$ with **1**, with and without the addition of additives (5 equiv. [Na-18-crown-6][BAr^F_4] and 5 equiv. of NH_2Me). Conditions: 2 mM [Ir] (0.1 mol%), 2 M $H_3B{\cdot}NH_2Me$, THF, 293 K. [a]Determined by the pseudo zero order region of the profile [b]Measured by ^{11}B NMR spectroscopy. Yield is isolated yield of polymer from precipitation.

There are examples in the literature of group 1 salts and/or crown ethers having a promoting effect on catalysis with organometallic complexes.[29, 30, 33, 34] Although the observed rate of reaction with added $[Na\text{-}18\text{-}crown\text{-}6]^+$ and NH_2Me is higher than with catalyst **1** alone, it is still not as high as the combination of **[Na-18-crown-6][6]** and $[NH_3Me][BAr^F_4]$ in catalysis. The solution NMR data may suggest a close ion-pairing for complex **[Na-18-crown-6][6]** however, the role of this interaction in promoting the dehydrogenation of amine-boranes remains unclear.

3.6 Summary and conclusions

This chapter has presented the kinetics of the dehydrogenation of $H_3B{\cdot}NH_2Me$ with catalyst **1**. The reaction is first order in catalyst and shows saturation kinetics with varied substrate concentration. The role of NH_2Me in catalysis with **1** was shown to be complex, with a promoting effect up to 40 mM, then an inhibitory effect for higher concentrations >40 mM.

Activation parameters were determined from Eyring analysis, indicating there was an associative mechanism towards the transition state. It was also determined that there was a N–H/N–D KIE, indicative of N–H activation being involved in or up to the rate determining step. Two mechanisms were proposed based of the experimental evidence collected, both of which were supported by kinetic modelling using COPASI and DFT calculations. The combined experimental and computational data indicate that both mechanisms are plausible. The simulated versus observed speciation favours operation of Mechanism A.

The synthesis of a novel anionic iridium trihydride was carried out and characterised, followed by an investigation into its behaviour in catalysis. **[Na-18-crown-6][6]** is a competent pre-catalyst and can be used to reach very high rates of turnover with the addition of one equivalent of $[NH_3Me][BAr^F{}_4]$. Further investigation into the effect of $[NH_3Me]^+$ on catalysis with **1** identified $[NH_3Me]Cl$ as a convenient additive to increase the rate of reaction and remove the induction period, while the role of Na^+ as an additive remains elusive.

However, further work would be required to understand the true cause of the induction period. Is it an off-cycle process as discussed in the preceding chapters or is there something else happening that the current proposed catalytic cycle does not capture. One way that this could be probed is to try to fit the data in COPASI including the induction period to see if the model can fit a pre-equilibrium or intermediates to simulate slow activation of a catalyst, dissociation of an inhibitor, or the reaction with H_2O to form tetrahydride **3**, borates and NH_2Me. The work in this chapter has contributed to the mechanistic understanding of how this system works, supported by speciation and kinetic data. This understanding will form a basis of

understanding to rationalise the reaction outcomes for the polymerisation step discussed in Chapter 4.

3.7 References

1. S. Hoops, S. Sahle, R. Gauges, C. Lee, J. Pahle, N. Simus, M. Singhal, L. Xu, P. Mendes and U. Kummer, *Bioinformatics*, 2006, **22**, 3067–3074.
2. J. Burés, *Angew. Chem. Int. Ed.*, 2016, **55**, 2028–2031.
3. M. C. Denney, V. Pons, T. J. Hebden, D. M. Heinekey and K. I. Goldberg, *J. Am. Chem. Soc.*, 2006, **128**, 12048–12049.
4. B. L. Dietrich, K. I. Goldberg, D. M. Heinekey, T. Autrey and J. C. Linehan, *Inorg. Chem.*, 2008, **47**, 8583–8585.
5. A. Staubitz, M. E. Sloan, A. P. M. Robertson, A. Friedrich, S. Schneider, P. J. Gates, J. S. A. D. Günne and I. Manners, *J. Am. Chem. Soc.*, 2010, **132**, 13332–13345.
6. G. M. Adams, A. L. Colebatch, J. T. Skornia, A. I. McKay, H. C. Johnson, G. C. Lloyd Jones, S. A. Macgregor, N. A. Beattie and A. S. Weller, *J. Am. Chem. Soc.*, 2018, **140**, 1481–1495.
7. E. A. K. Spearing-Ewyn, N. A. Beattie, A. L. Colebatch, A. J. Martinez-Martinez, A. Docker, T. M. Boyd, G. Baillie, R. Reed, S. A. Macgregor and A. S. Weller, *Dalton Trans.*, 2019, **48**, 14724–14736.
8. C. N. Brodie, L. Sotorrios, T. M. Boyd, S. A. Macgregor and A. S. Weller, *ACS Catal.*, 2022, **12**, 13050–13064.
9. M. J. Cross, C. N. Brodie, D. G. Crivoi, J. C. Goodall, D. E. Ryan, A. J. Martinez-Martinez, A. Johnson and A. S. Weller, *Chem. Eur. J.*, 2023, **29**, e202302110.
10. M. R. Wright, *An Introduction to Chemical Kinetics*, John Wiley & Sons, England, 2004.
11. M. J. Cross, M. A. Sajjad, S. A. Macgregor and A. S. Weller, *Angew. Chem. Int. Ed.*, 2025, **64**, e202500019.
12. A. Glüer, M. Förster, V. R. Celinski, J. Schmedt auf der Günne, M. C. Holthausen and S. Schneider, *ACS Catal.*, 2015, **5**, 7214–7217.
13. T. M. Boyd, K. A. Andrea, K. Baston, A. Johnson, D. E. Ryan and A. S. Weller, *Chem. Commun.*, 2020, **56**, 482–485.
14. P. Hasche, J. Haak, F. Anke, C. Kubis, W. Baumann, H. J. Drexler, H. Jiao and T. Beweries, *Cat. Sci. Technol.*, 2021, **11**, 3514–3526.
15. D. E. Ryan, K. A. Andrea, J. J. Race, T. M. Boyd, G. C. Lloyd-Jones and A. S. Weller, *ACS Catal.*, 2020, **10**, 7443–7448.
16. C. N. Brodie, T. M. Boyd, L. Sotorríos, D. E. Ryan, E. Magee, S. Huband, J. S. Town, G. C. Lloyd-Jones, D. M. Haddleton, S. A. Macgregor and A. S. Weller, *J. Am. Chem. Soc.*, 2021, **143**, 21010–21023.
17. A. L. Colebatch, B. W. Hawkey Gilder, G. R. Whittell, N. L. Oldroyd, I. Manners and A. S. Weller, *Chem. Eur. J.*, 2018, **24**, 5450–5455.
18. C.-H. Chen, *Deuterium Bonding Versus Hydrogen Bonding*, Springer, Cham, 2022.
19. A. Paul and C. B. Musgrave, *Angew. Chem. Int. Ed.*, 2007, **46**, 8153–8156.
20. M. Rosello-Merino, J. Lopez-Serrano and S. Conejero, *J. Am. Chem. Soc.*, 2013, **135**, 10910–10913.
21. I. Göttker-Schnetmann, P. S. White and M. Brookhart, *Organometallics*, 2004, **23**, 1766–1776.
22. G. Durin, J.-C. Berthet, E. Nicolas and T. Cantat, *ACS Catal.*, 2021, **11**, 10855–10861.
23. A. V. Polukeev, S. C. Capelli and O. F. Wendt, *Chem. Sci.*, 2023, **14**, 12308–12320.
24. S. E. Landau, K. E. Groh, A. J. Lough and R. H. Morris, *Inorg. Chem.*, 2002, **41**, 2995–3007.

25. N. V. Belkova, L. M. Epstein, O. A. Filippov and E. S. Shubina, *Chem. Rev.*, 2016, **116**, 8545–8587.
26. K. Abdur-Rashid, D. G. Gusev, S. E. Landau, A. J. Lough and R. H. Morris, *J. Am. Chem. Soc.*, 1998, **120**, 11826–11827.
27. J. A. Bandy, A. Berry, M. L. H. Green and K. Prout, *J. Chem. Soc., Chem. Commun.*, 1985, 1462–1464.
28. A. S. C. Chan and H.-S. Shieh, *J. Chem. Soc., Chem. Commun.*, 1985, 1379–1380.
29. Y. Gao, C. Guan, M. Zhou, A. Kumar, T. J. Emge, A. M. Wright, K. I. Goldberg, K. Krogh-Jespersen and A. S. Goldman, *J. Am. Chem. Soc.*, 2017, **139**, 6338–6350.
30. S. Acosta-Calle and A. J. M. Miller, *Acc. Chem. Res.*, 2023, **56**, 971–981.
31. A. Spangenberg, O. O. Kovalenko, M. S. G. Ahlquist and O. F. Wendt, *Organometallics*, 2024, **43**, 3242–3250.
32. R. G. Potter, D. M. Camaioni, M. Vasiliu and D. A. Dixon, *Inorg. Chem.*, 2010, **49**, 10512–10521.
33. F. Fiorentini, W. T. Diment, A. C. Deacy, R. W. F. Kerr, S. Faulkner and C. K. Williams, *Nat. Commun.*, 2023, **14**, 4783.
34. Y. Ma and A. A. Hussein, *Phys. Chem. Chem. Phys.*, 2023, **25**, 3110–3120.

Chapter 4: Polymer properties

As discussed in Chapter 1, catalyst **1** has previously been reported by Manners and co-workers to form polyaminoborane on reaction with $H_3B{\cdot}NH_2Me$.[1, 2] However, there was limited control of molecular weight and large dispersities. Computational work carried out by Paul and coworkers identified that the most likely polymerisation mechanism for the reaction was a head-to-tail chain-growth mechanism similar to an anionic polymerisation from an iridium centre.[3]

In the literature there is limited information concerning the polymerisation mechanism for the dehydropolymerisation of amine-boranes due to difficulties in monitoring this fast reaction. The loss of hydrogen from the pre-monomer $H_3B{\cdot}NH_2Me$ allows for the kinetics of the dehydrogenation reaction to be accurately monitored, but gives no indication of what happens once the true monomer, $H_2B{=}NHMe$, has formed. In almost all cases, the true monomer $H_2B{=}NHMe$ is not observed by NMR spectroscopy and/or other analytical techniques, as it is a reactive and short-lived intermediate.[4] This makes the study of the polymerisation mechanism challenging.

There are many competent catalysts in the literature that can be used to dehydropolymerise amine-boranes. However, there is limited evidence of fine control of molecular weight of polyaminoborane. In this chapter, reaction conditions are explored that allow for such fine control of the molecular weight of polyaminoborane. This is followed by the scale up of polymer production from 100 mg to 20 g to allow for an initial investigation into processing the material and its properties.

4.1 Determining the polymerisation mechanism

As was previously discussed in Chapter 1, the dehydropolymerisation of amine-boranes by catalyst **1** is thought to proceed *via* a chain-growth mechanism from an amido end group; for more detail on polymerisation mechanisms see section 1.3.2. This was determined by the molecular weight versus conversion plot reported by Manners and co-workers (Figure 4.1, left),[1] where the relationship between conversion and M_w showed a weak positive correlation between the variables that would usually indicate a living polymerisation mechanism (see section 1.3.2), albeit with large dispersities. The authors acknowledged that the results for the polymerisation mechanism were complex. Living polymerisations have not been suggested for themechanism for polyaminoboranes in the literature. Meanwhile the relationship between conversion and M_n showed the formation of polymer from ~20,000 g mol^{-1} at 25% conversion that increased to ~60,000 g mol^{-1} at 80% conversion. This observation led to the authors reporting the polymerisation mechanism as chain growth (*i.e.* high molecular weight polymer produced at low conversions), with the caveat that, due to the molecular weight increase at higher conversions the mechanism may differ from a classical chain-growth mechanism. The proposed chain-growth mechanism was supported by DFT calculations carried out by Paul and co-workers.[3] For more details see section 1.6.3.

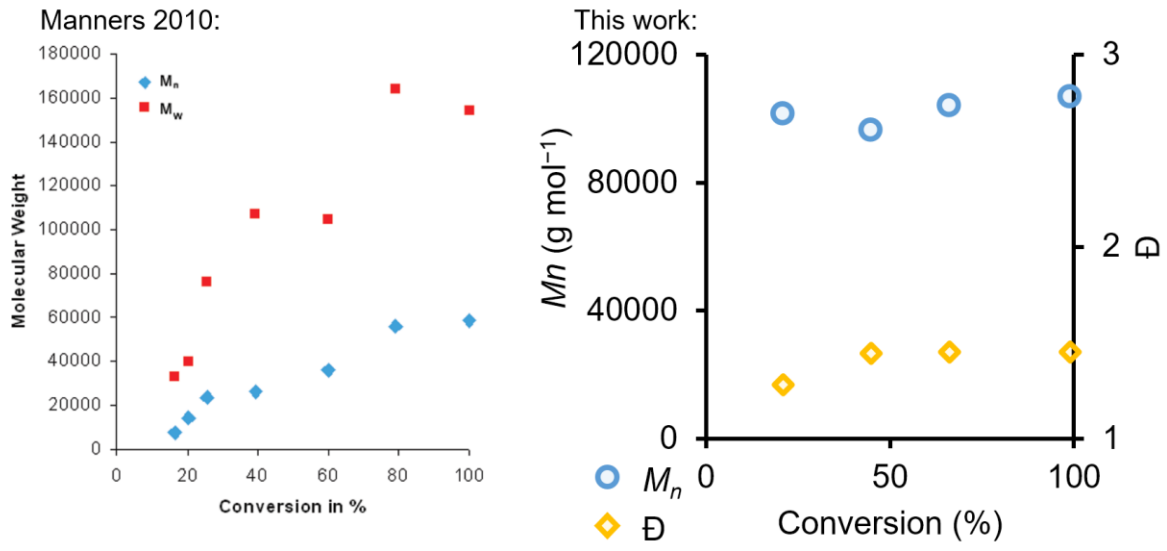

Figure 4.1. Molecular weight versus conversion graph Manners (left)[1] this work (right).

Prior to establishing relationships between reaction variables and the control of molecular weight, it was important to reconstruct the molecular weight against conversion graph under the experimental conditions used in this study to confirm the type of polymerisation mechanism that is occurring. This required a set of experiments to be carried out where catalysis was successfully halted at a pre-determined time/conversion. This was done by adding PMe_3 to quench the reaction. Thus, five equivalents of PMe_3 were added to catalysis at the desired conversion point, tracked by the amount of hydrogen produced. It was established in Chapter 2 that 0.5 equivalents of PMe_3 had no effect on catalysis in terms of rate. The addition of five equivalents halted catalysis completely. The potential formation of Ir(^{t}Bu-POCOP)$(H)_2(PMe_3)$ was indicated by peaks similar to those reported for Ir(^{t}Bu-POCOP)$(H)_2(PPh_3)$ in the resulting ^{1}H and ^{31}P{^{1}H} NMR spectra taken at the end of catalysis.[5] The conversion was determined by ^{11}B NMR spectroscopy of an aliquot of reaction mixture once the PMe_3 had been added. Polymer was isolated by precipitation with pentane; the isolated polymer was analysed by GPC to determine the molecular weight.

Figure 4.1 shows the results from these molecular weight-versus-conversion experiments. The lower molecular weight at ~25% conversion reported by Manners and co-workers was not observed in these independent experiments. The experiments carried out by Manners and co-workers were done in a closed system whereas the experiments presented in this study were carried out with a eudiometer and it is unclear how the build-up of H_2 may affect the propagation and termination events.

It is clear from the molecular weight vs conversion graph (Figure 4.1, right) that high molecular weight polymer is formed at low conversions (~25%). This molecular weight of polymer remains constant at higher conversion, too. This relationship is indicative of a chain-growth mechanism,[6] and is in broad agreement with the previously proposed mechanism.[1, 3]

4.2 Factors affecting the molecular weight of polyaminoborane

There are three key steps in polymerisation mechanisms: initiation, propagation and termination. From DFT calculations of amine-borane dehydropolymerisations, initiation is thought to occur at the metal centre or from an NH_2Me initiator by coordination of a nucleophile to an aminoborane.[3, 7] Propagation is proposed to proceed *via* a chain growth mechanism with a head-to-tail addition from the nucleophilic lone pair on the nitrogen of the aminoborane monomer. Termination has been proposed to occur *via* proton transfer (back biting) from the amido end chain to the amine-borane unit co-ordinated to the metal (see section 1.6.3 for more details).[3] Alternatively, it could occur *via* a chain terminating agent such as 'BH_3' or boronium ($[H_2B(NRH_2)_2]^+$, a proton source), both of which would cap the nucleophilic amido end group.[8]

A simplified way to conceptualise the kinetics of chain growth polymerisation kinetics is that the degree of polymerisation (D.P.) is proportional to the rate of propagation divided by rate of termination (D.P. $\propto R_{prop}/R_{term}$).[6] In the case of the dehydropolymerisation of amine-boranes, this may equate to factors that increase the rate of dehydrogenation, essentially the rate of formation of monomer, having an effect on the degree of polymerisation (if the initiation and termination events remain constant). This is due to the formation of true monomer $H_2B{=}NHMe$ being rate limiting compared to chain growth ($\Delta G^{\ddagger}_{exp}$ = 16(1) kcal mol^{-1} and ~8 kcal mol^{-1},[3] respectively).

The molecular weight of the polyaminoboranes was measured using a GPC (gel permeation chromatography), a type of size exclusion chromatography that separates polymers by size with the highest molecular weight material eluting first. The values of M_n quoted in this chapter are relative to polystyrene standards, as there are no polyaminoborane standards available. Thus, the values are treated with a larger error than 'normal', values are considered the same molecular weight ± 5,000 g mol^{-1}.

4.2.1 Temperature

For the reactions carried out between 293 K and 263 K, polyaminoborane was formed in all cases as an off-white solid, in isolated yields of 49 to 59%. Analysis of the reaction mixture by ^{11}B NMR spectroscopy shows that the reaction was >99% selective for polymer formation, with full conversion of monomer to polymer. The lower-than-expected isolated yield is proposed to be due to material loss on precipitation of the polymer by pentane. The molecular weight of the polymer increased as the temperature of the reaction was decreased (Figure 4.2). This relationship is typically seen with anionic chain-growth polymerisation mechanisms due to a lower barrier for propagation compared to the barrier for termination.[6] Reaction at lower temperatures disfavours the latter,[6] and so longer polymer is formed. The use of temperature is a useful way to control the molecular weight of the polymer formed without using additives, as has been shown previously with boronium addition.[8] These observations further support the propagation as being chain growth.

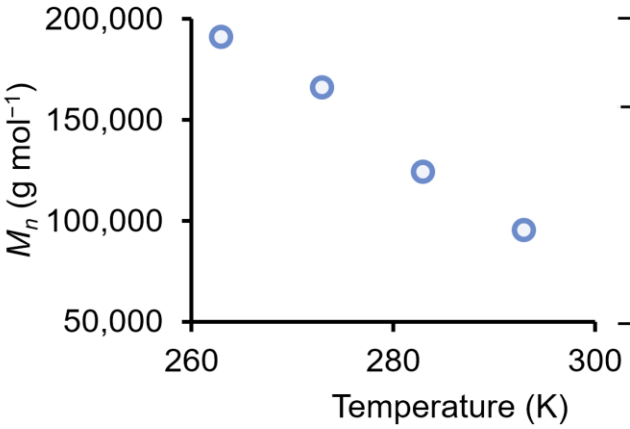

Temp. (K)	M_n (g mol^{-1})	Đ	Yield (mg (%))
293	95,000	1.4	63(59)
283	124,000	1.4	58(54)
273	166,000	1.5	59(55)
263	191,000	1.5	53(49)

Figure 4.2. A graph showing the relationship between temperature and M_n (g mol^{-1}) of polyaminoborane formed and a table of the details (conditions – 0.1 mol% (2 mM [Ir]), 2 M $H_3B{\cdot}NH_2Me$, THF, varied temperatures). Yield is isolated yield of polymer from precipitation.

4.2.2 Catalyst loading

4.2.2.1 Relationship between catalyst loading and molecular weight

The dehydropolymerisation of $H_3B{\cdot}NH_2Me$ at different catalyst loadings (0.2 mM – 10 mM *i.e.* 0.01 mol% - 0.5 mol%) resulted in the selective formation of polyaminoborane in all cases (yields = 47 to 65%). Analysis of the reaction mixture by ^{11}B NMR spectroscopy shows that the reaction was >99% selective for polymer formation, with full conversion of monomer to polymer. Material loss by precipitation of the polymer from pentane is the proposed cause of the lower isolated yield compared with the conversion. At lower [Ir] (0.2 mM, *i.e.* 0.01 mol%) relatively short polymer was formed (M_n = 57,300 g mol^{-1}) which increased to M_n = 103,100 g mol^{-1} at 2 mM [Ir] (*i.e.* 0.1 mol%). The relationship between catalyst loading and molecular weight seemed to reach a plateau (Figure 4.3) where above 6 mM [Ir] the M_n did not increase further (M_n = 131,600 g mol^{-1} at 6 mM [Ir], M_n = 125,700 g mol^{-1} at 10 mM [Ir]). The relationship observed where the M_n increases with increased catalyst loading follows a similar trend to the effect of [Ir] on k_{obs} (discussed in Chapter 3). This can be rationalised through the kinetics of chain growth polymerisations (D.P. $\propto R_{prop}/R_{term}$). More catalyst results in a faster dehydrogenation, the first step of the cascade reaction, which in turn results in more available monomer ($H_2B{=}NHMe$). So, the rate of propagation would be larger than the rate of termination, as long as the termination event remains constant. There is evidence that the termination event does remain constant and the terminating agent does not form from the catalyst itself, as the molecular weight of the polymer would be expected to remain constant if the terminating agent was formed by the catalyst.[8] In the case of catalyst **1** this relationship is not observed (Figure 4.3).

The reactions at high catalyst loadings 6 mM (0.3 mol%) and 10 mM (0.5 mol%) are very fast, the full reaction is complete within 2 minutes and is accompanied by very vigorous bubbling. This may suggest that mass transport effects are important and may explain the plateauing of the molecular weights and also the rates (discussed in Chapter 3).

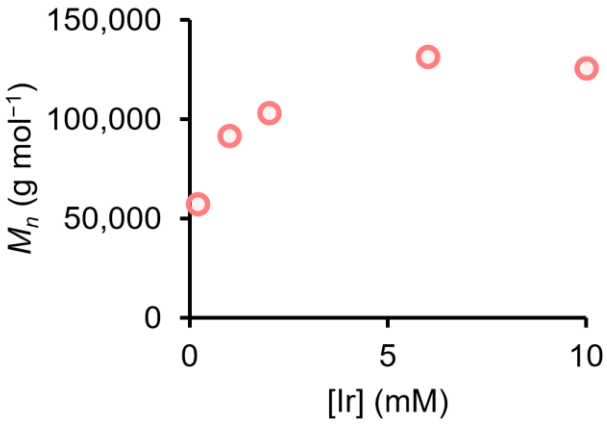

[Ir] (mM)	M_n (g mol^{-1})	Đ	Yield (mg (%))
10	126,000	1.4	70(65)
6	132,000	1.4	60(56)
2	103,000	1.3	66(50)
1	92,000	1.3	50(47)
0.2	57,000	1.5	66(62)

Figure 4.3. A graph showing the relationship between temperature and M_n (g mol^{-1}) of polyaminoborane formed and a table of the details (conditions – 293 K, 2 M $H_3B{\cdot}NH_2Me$, THF, varied [Ir]). Yield is isolated yield of polymer from precipitation.

4.2.2.2 ICP-OES analysis of isolated polymers with different catalyst loadings

Evidence of the iridium catalyst remaining entrained within the isolated polymer after precipitation came from analysis by inductively coupled plasma optical emission spectroscopy (ICP-OES) carried out by Niall Donaldson at the University of York. Polyaminoborane formed with a catalyst loading of 1 mol% gave polyaminoborane that contained 11063 ppm of Ir by ICP-OES, while polymer formed with 0.01 mol% catalyst loading gave polyaminoborane that contained 89 ppm of iridium *i.e.* 100 times less (Table 4.1). In some cases, low or high iridium content in the polyaminoborane may be useful for an application, such as in catalysis where higher concentrations of iridium may be favourable.

There have been previous reports of post modification of polyaminoborane with activated carbon that allow for the removal of residual metals, however, the reported procedure results in a large loss of material.[9] The ability to selectively form polyaminoborane at 0.01 mol% catalyst loading, resulting in polymer with 89 ppm [Ir], forms the basis of polyaminoborane synthesis with a low residual concentration of iridium without the large loss of material that has previously been reported. The formation of polyaminoborane with lower catalyst loadings will be discussed in a later section.

Table 4.1. ICP-OES analysis of polymer samples with different catalyst loadings to show residual [Ir].

Catalyst Loading (mol%)	[Ir] (weight ppm)	Ir ppm/mol
1.0	11063	2464
0.1	1002	223
0.01	89	20

4.3 Additives

4.3.1 NH_2Me

It is understood that the addition of NH_2Me to the dehydropolymerisation of $H_3B{\cdot}NH_2Me$ increases the rate of dehydrogenation in many cases.[9-15] In Chapter 3 it was shown that this stood true for the dehydropolymerisation of $H_3B{\cdot}NH_2Me$ with catalyst **1**, with complex kinetics that were discussed in Section 3.2.

The addition of NH_2Me also had an effect on the molecular weight of the polyaminoborane formed (Conditions: 0.1 mol% (2 mM [Ir]), 2 M $H_3B{\cdot}NH_2Me$, 293 K, THF). The dehydropolymerisation of $H_3B{\cdot}NH_2Me$ was carried out with a varied [NH_2Me] = 0.5 mM to 120 mM, resulting in the formation of polyaminoborane as an off-white solid in yields of 46-74%. Lower [NH_2Me] (up to 2.5 mM) resulted in the formation of isolated polyaminoborane with M_n ~112,000 g mol^{-1}. Higher concentrations of NH_2Me (>5 mM) resulted in polyaminoborane formed with M_n ~160,000 g mol^{-1}. This increase may be explained by two potential hypotheses. Firstly, that the addition of NH_2Me increases the rate of reaction, resulting in the enhanced availability of the true monomer $H_2B{=}NHMe$ and so based on the proposed relationship of D.P. $\propto R_{prop}/R_{term}$, the propagation term would be favoured, resulting in longer polyaminoborane. An alternative is that 'BH_3' is a terminating agent, and so the addition of NH_2Me will result in a reduced [BH_3] by formation of $H_3B{\cdot}NH_2Me$, causing less availability of the terminating agent.

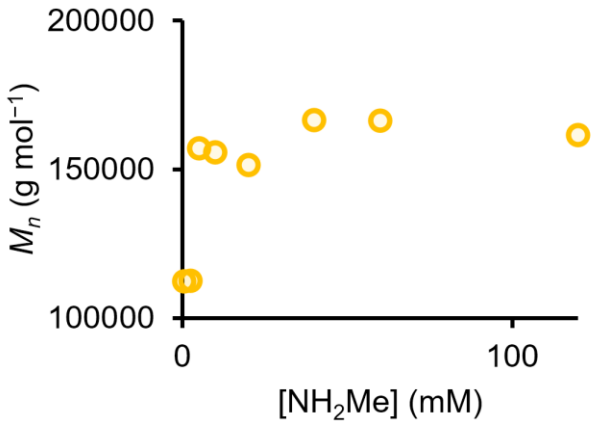

[NH$_2$Me] (mM)	M_n (g mol^{-1})	Đ	Yield (mg (%))
0.5	112,000	1.6	48 (45)
2.5	113,000	1.6	54 (50)
5	157,000	1.5	49 (46)
10	156,000	1.5	79 (74)
20	152,000	1.7	67 (63)
40	167,000	1.6	64 (60)
60	166,000	1.6	59 (55)
120	162,000	1.6	56 (52)

Figure 4.4. A graph showing the relationship between temperature and M_n (g mol^{-1}) of polyaminoborane formed and a table of the details (conditions – 0.1 mol% (2 mM [Ir]), 2 M $H_3B{\cdot}NH_2Me$, 293 K, THF, varied [NH_2Me]). Yield is isolated yield of polymer from precipitation.

4.3.2 Addition of [NH$_3$Me][BAr$^F{}_4$]

As part of the kinetic investigation into the dehydropolymerisation of $H_3B{\cdot}NH_2Me$, $[NH_3Me]^+$ was identified as an additive of interest. The addition of 1 equivalent of [NH$_3$Me][BAr$^F{}_4$] (relative to cat.) to the reaction catalysed by **[Na-18-crown-6][6]** under standard conditions resulted in the highest observed k_{obs} of this iridium POCOP system (Table 4.2). Based on the proposed relationship between k_{obs} and M_n observed with these catalysts thus far, it is not surprising that this dehydropolymerisation resulted in high molecular weight polyaminoborane (M_n = 185,200 g mol^{-1}, Đ = 1.4).

It is interesting to note that the addition of [NH$_3$Me][BAr$^F{}_4$] to the dehydropolymerisation of $H_3B{\cdot}NH_2Me$ with catalyst **1** resulted in a reduction of the molecular weight of the polyaminoborane compared to **1** alone but at an equivalent rate (M_n = 57,700 g mol^{-1}, Đ = 1.4 and M_n = 103,100 g mol^{-1}, Đ = 1.3, respectively), Table 4.1. This does not follow the proposed relationship of k_{obs} affecting M_n observed for this system so far, as the rates of the two reactions are comparable. The cause of this remains unclear, although it may be due to the addition of ammonium changing the speciation of the catalyst or the involvement of ammonium in the

termination event, potentially by hydrogen bonding to the end of the polymer chain essentially capping it, or protonating the end group. It should be noted that $[BAr^F_4]^-$ resolves in the GPC chromatograms and in this case cannot be deconvoluted from the polymer peaks, and so can lead to an artificially skewed distribution.[16]

Table 4.2. Observed k_{obs} and molecular weights for different reaction conditions focused on the $[NH_3Me]^+$ cation.

Reaction conditions	k_{obs}[a] (mM s^{-1})	M_n[b] (g mol^{-1})	Đ	Yield (mg (%))
[Na-18-crown-6][6], 1 equiv. $[NH_3Me][BAr^F_4]$	19.2(3)	185,000[c]	1.4	63(59)
1	5.93(3)	103,000	1.3	66(62)
1, 5 equiv. $[NH_3Me][BAr^F_4]$	5.73(2)	58,000[c]	1.4	77(72)

[a]Determined by the pseudo zero order region of the profile [b]Relative to polystyrene standards. [c]Some overlap from $[BAr^F_4]^-$ signal in GPC. Yield is isolated yield of polymer from precipitation.

4.3.3 Addition of Na^+

Reactions carried out with the addition of [Na-18-crown-6]$[BAr^F_4]$ were also performed as part of the kinetic investigation. The addition of 5 equivalents of [Na-18-crown-6]$[BAr^F_4]$ (relative to cat.) to catalysis with **1** did not lead to a large increase in polymer M_n compared to reaction with **1** alone (M_n = 109,900 g $mol^{-1}$and 103,100 g mol^{-1}, respectively), see Table 4.3. It is important to note that $[BAr^F_4]^-$ resolves in the GPC chromatograms and in this case cannot be deconvoluted from the polymer peaks, and so can lead to an artificially skewed distribution.[16] However, the reaction of $H_3B{\cdot}NH_2Me$ with **1** with the addition of 5 equivalents of [Na-18-crown-6]$[BAr^F_4]$ and 5 equivalents of NH_2Me resulted in the formation of polyaminoborane M_n = 220,400 g mol^{-1}, Đ = 1.5 (Table 4.3). It is unclear why this reaction would produce such high molecular weight polyaminoborane, as it does not follow the proposed relationship of k_{obs} affecting M_n. Further investigation is required to understand the role of alkali metal salts in the dehydropolymerisation of amine-boranes.

Table 4.3. Observed k_{obs} and molecular weights for different reaction conditions focused on [Na-18-crown-6][BAr^F_4],

Reaction conditions	k_{obs}[a] (mM s^{-1})	M_n[b] (g mol^{-1})	Đ	Yield (mg (%))
1	5.93(3)	103,000	1.3	66(62)
1, 5 equiv. [Na-18-crown-6]	8.53(3)	110,000[c]	1.3	61(57)
1, 5 equiv. [Na-18-crown-6], 5 equiv. NH_2Me	12.9(1)	220,00[c]	1.5	72(67)

[a]Determined by the pseudo zero order region of the profile [b]Relative to polystyrene standards. [c]Some overlap from $[BAr^F_4]^-$ signal in GPC. Yield is isolated yield of polymer from precipitation.

4.4 Control of molecular weight

The proposed relationship between k_{obs} and M_n is shown in Figure 4.5. At 20 °C, it is clear that higher rates of reaction tend to result in higher M_n of polyaminoborane. This relationship has been previously demonstrated by Weller and co-workers with a ruthenium catalyst discussed in Chapter 1, $Ru(Cl)_2(^iPr_2PCH_2CH_2NH_2)_2$ (**i-39**).[17] Here, a wider set of data are available to demonstrate the relationship.

The current investigation has found a number of conditions that can be used to control the M_n of polyaminoborane formed with catalyst **1** (*e.g.* temperature, catalyst loading, additive). Further investigation is required to understand the role of additives, such as Na^+ ions in the polymerisation process, and to identify routes to higher molecular weight polyaminoborane. Not only does this provide a basis that can practically inform polymer formation, it also exemplifies the degree of control in the M_n of the polyaminoborane using catalyst **1**, with a range over 57,300-185,200 g mol^{-1}. Such control over polyaminoborane molecular weight has not yet been reported for a single catalyst system.

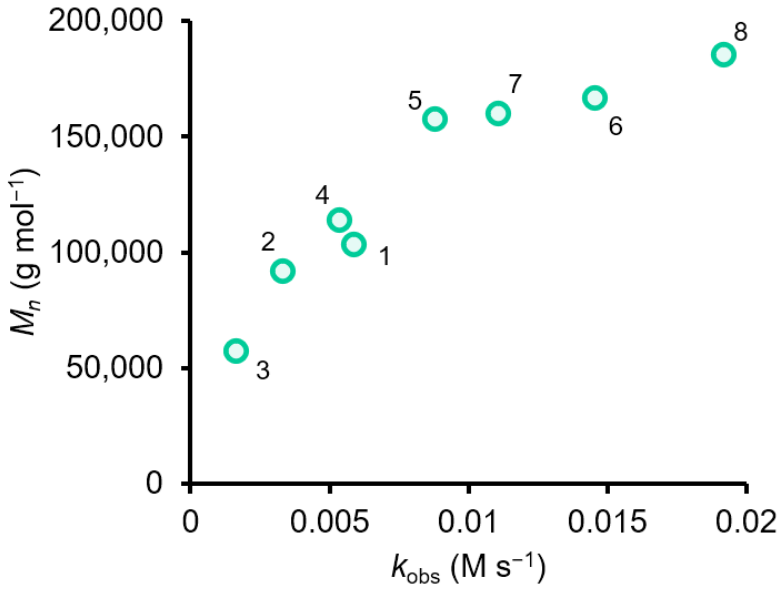

Entry	Catalyst	[Ir] (mM)	[$H_3B{\cdot}NH_2Me$][a] (M)	[NH_2Me][b] (mM)	k_{obs}[c] (mM s^{-1})	M_n[d] (g mol^{-1})
1	**1**	2	2.0	-	5.9	103,000
2	**1**	1	2.0	-	3.4	92,000
3	**1**	0.2	2.0	-	1.7	57,000
4	**1**	2	1.0	-	5.4	114,000
5	**1**	2	2.0	5.0	8.8	157,000
6	**1**	2	2.0	40.0	14.6	167,000
7	**1**	2	1.0	10.0	11.1	160,000
8	**[6]$^-$**[e]	2	2.0	-	19.2	185,000

Figure 4.5. Relationship between k_{obs} and M_n carried out at 20 °C, shown graphically with details in the table underneath. [a]Reactions carried out at 112 mg scale [b]Added as a 2 M solution in THF at time of catalyst addition [c]Measured from the pseudo zero-order regime [d]Relative to polystyrene standards [e]**[Na-18-crown-6][6]**/ 1 equiv. [NH_3Me][$BAr^F{}_4$]

4.5 Characterisation of polyaminoborane

4.5.1 NMR spectroscopy and GPC

All of the reactions shown in table of Figure 4.5 were selective for polymer formation, as observed in the ^{11}B NMR spectrum taken on catalysis completion, see Figure 4.6 A for a representative example. The polymers were analysed by GPC chromatography and were shown to have a molecular weight range of 57,300-185,200 g mol^{-1}, (Figure 4.6 B).

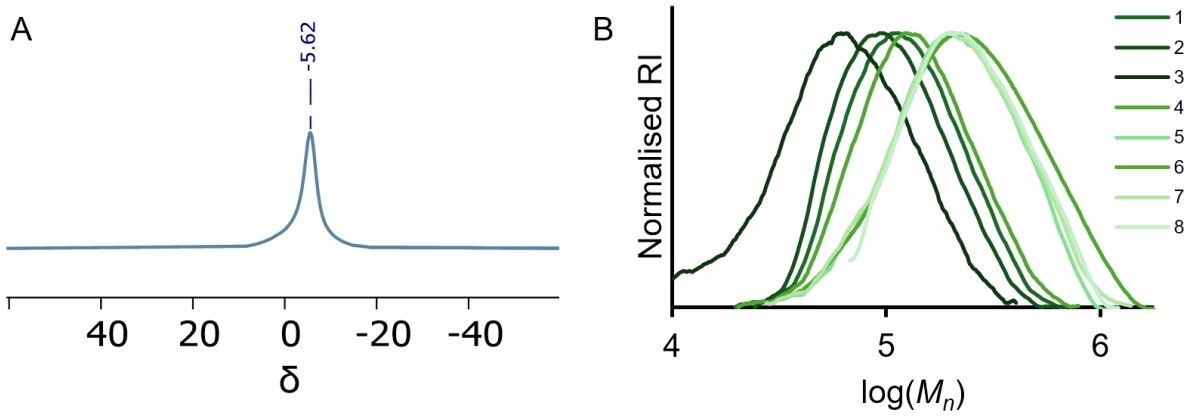

Figure 4.6. A) Representative ^{11}B NMR spectrum taken on catalysis completion showing >99% conversion and >99% selectivity for formation of polyaminoborane under standard conditions, H^8-THF, 193 MHz, 298 K. B) GPC trace showing the range of M_n for entries 1-8 in Figure 4.5 (relative to polystyrene standards).

4.5.2 TGA and DSC

Analysis of the materials by thermogravimetric analysis (TGA) yielded similar results for all polymer samples in Figure 4.5 regardless of molecular weight (see Figure 4.7 A for a representative example). All samples exhibited low ceramic (char) yields <6.5% at 500 °C, and showed a 50% mass loss event between 178 – 185 °C. This is similar to what has previously been reported for polyaminoboranes.[1,8] Differential scanning calorimetry (DSC) was also carried out but glass transitions, if present, could not be reliably observed as the signal was weak and inconclusive (see Figure 4.7 B for a representative example). No further conclusions will be drawn from this data.

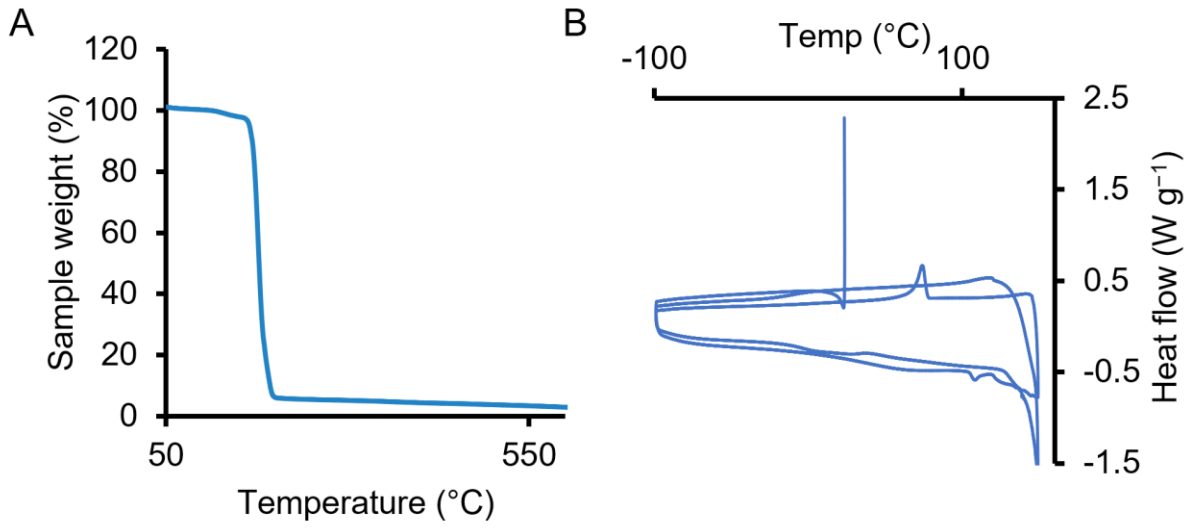

Figure 4.7. A) TGA data of Entry 1 in Figure 4.5 B) DSC data for Entry 1 in Figure 4.5, M_n = 103,20.

4.5.3 Mass Spectrometry

The polyaminoboranes formed (Figure 4.5) were analysed by electrospray ionization mass spectrometry (ESI-MS) carried out by Dr Charles Killeen at the University of Victoria, Canada. The ESI-MS data show that the polyaminoborane presents as two polymer distributions $[H(NMe\text{-}HBH_2)_nNH_2Me]^+$ and $[H(NMe\text{-}HBH_2)_n]$ (Figure 4.8), similar to those reported by Manners and co-workers.[1] The repeat units are consistent with a H_2B-NMeH repeating unit. Polyaminoborane of different molecular weights was analysed but all samples showed essentially the same distribution. This indicates that analysis of polyaminoborane by ESI-MS does not allow a true estimation of molecular weight, and this is supported by observations by Manners and co-workers.[1]

An alternative explanation for the distributions could be due to *in situ* fragmentation occurring of the polymers during the analysis by ESI-MS, as has been previously noted for polymers.[18] In some cases this *in situ* fragmentation has allowed for the end groups of the polymer chains to be identified.[18] If this were the case here that would indicate that the polyaminoboranes are capped by a terminal amine and a terminal ammonium group.

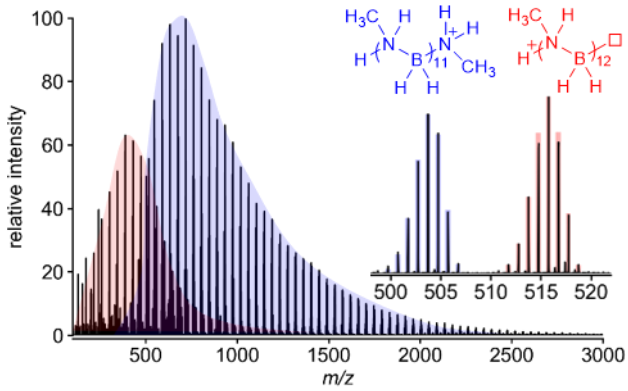

Figure 4.8. ESI-MS (positive mode, CH_2Cl_2) of a representative example of polyaminoborane formed using **1**.

4.6 Scale up and low [Ir] polyaminoborane

With the mechanism of the dehydrogenation of $H_3B{\cdot}NH_2Me$ and control of molecular weight in hand, focus turned to the practical use of catalyst **1**. To achieve this, polyaminoborane was to be formed selectively on a 20 g scale using the smallest amount of catalyst possible. Polyaminoborane has previously been made on the 10 g scale with 0.01 mol% catalyst loading of [Rh{(^{i}Pr$_2$PCH$_2$CH$_2$)$_2$NH}(NBD)]Cl.[8] It should be noted that catalyst loadings of 0.001 mol% have been achieved in the dehydrogenation/hydrolysis of $H_3B{\cdot}NH_3$ with [Ir(I^{t}Bu')$_2$][BAr$^F{}_4$] and Ir(I^{t}Bu')$_2$Cl (I^{t}Bu′ = cyclometallated 1,3-ditertbutylimidazol-2-ylidene) on a 21 mg scale in a THF/H_2O mixture resulting in a mixture of $B_xO_yH_z$ products.[19, 20]

4.6.1 Reaction on scale

To facilitate the reaction on a 20 g scale, a reaction vessel with a mechanical overhead stirrer was used at 20 °C (Figure 4.9 A). Prior to the reaction, the compatibility of catalyst **1** with commercial, unpurified $H_3B{\cdot}NH_2Me$ was determined, resulting in selective formation of polyaminoborane at 0.1 mol%, 0.2 mM [Ir] (M_n = 100,000 g mol^{-1}, Đ = 1.5), indistinguishable from the polymer formed from the recrystallised starting material.

Kinetic analysis at different catalyst loadings established that lower catalyst loadings resulted in longer induction periods. To minimise this catalysis was initiated by the addition of **1** (2.6 mg) to a portion of the $H_3B{\cdot}NH_2Me$ in a THF solution (10%), with the remaining 90% added slowly

over 3 hours as a THF solution. Additionally, $[NH_3Me]Cl$ (5 equivalents with regards to catalyst) was added at the start of catalysis, as it was shown in Chapter 3 to promote turnover with catalyst **1** without an induction period. The reaction started almost immediately (visible H_2 bubbles), and NH_2Me (0.1 mL) was added every 6 h *via* Hamilton syringe to ensure continued turnover, and the reaction progress was monitored every ~8 h (aliquot analysed by ^{11}B NMR spectroscopy). The reaction was complete after 2 days, forming polyaminoborane (16 g, 80%) as a free-flowing white powder (Figure 4.9 B). The molecular weight of the polyaminoborane was M_n = 35,000 g mol^{-1}, Đ = 1.9 (Figure 4.9 C). This is considerably shorter than that formed under standard conditions, but is not surprising considering the correlation between catalyst loading and M_n discussed in section 4.2.2. The lower molecular weight may also be due to the scale-up conditions, such as mass transport effects in the reaction vessel.[21] Support for the latter comes from an alternate experiment carried out, experimental conditions: 1 g (90% added slowly), 0.001 mol% cat., 0 °C, $[NH_3Me]Cl/NH_2Me$ addition. The resulting polyaminoborane had a higher M_n (856 mg, 81%, M_n = 122,300 g mol^{-1}, Đ = 1.5), although the effect of temperature would also need to be taken into account.

ICP-OES analysis of the isolated polyaminoborane indicated that there was a very low residual iridium content (21 ppm w/w). Polyaminoborane with a lower residual metal content has previously been reported, but this required post-synthetic processing and resulted in large material loss.[9]

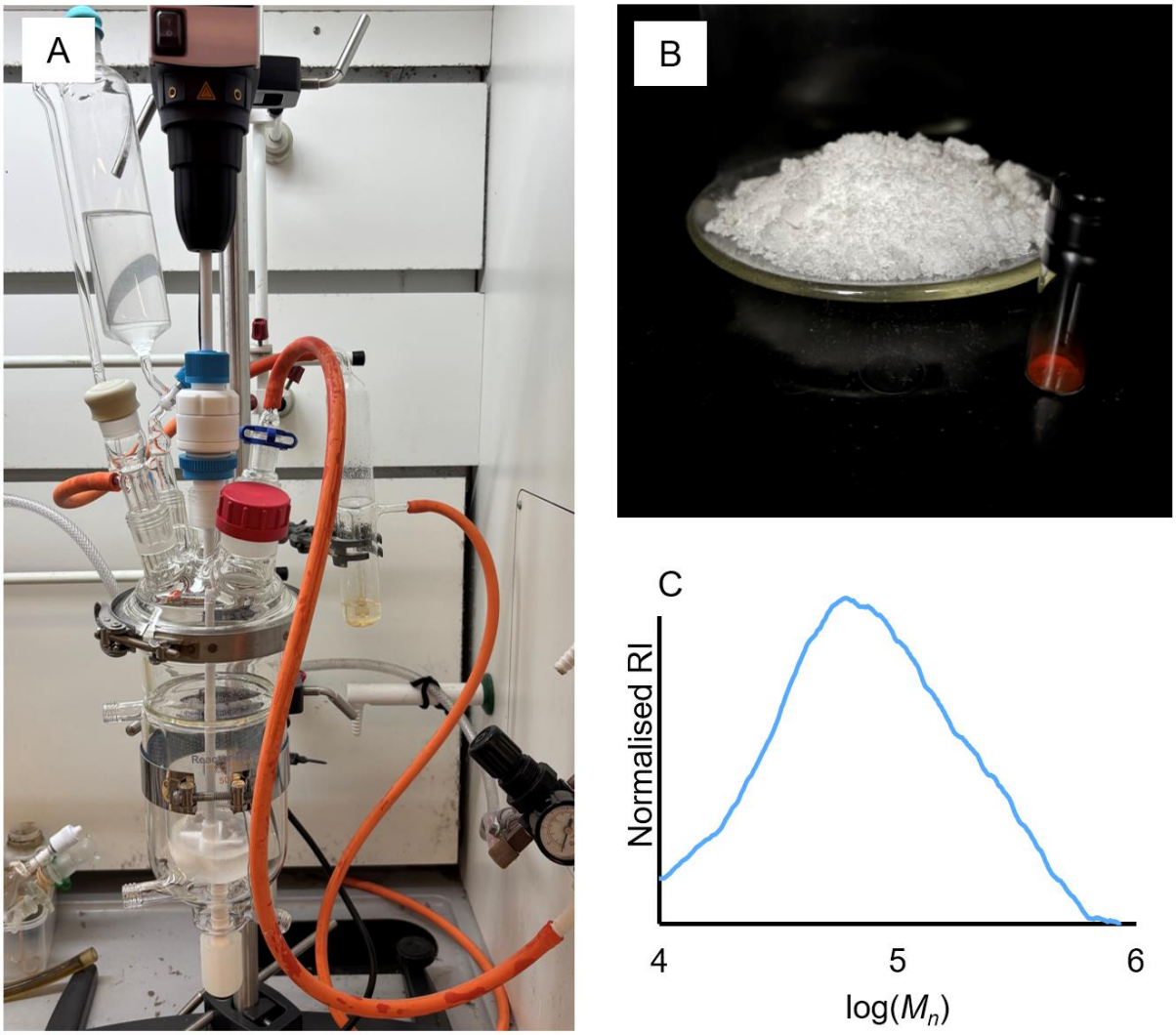

Figure 4.9. A) 20 g reaction vessel (500 mL capacity) B) 16 g polyaminoborane formed compared with 2.6 mg of catalyst **1** C) GPC trace of polyaminoborane (M_n = 35,000 g mol^{-1}).

4.7 Application

4.7.1 Boron nitride fibers

The potential use of polyaminoboranes as precursors to ceramic boron nitride is well reported in the literature: see Section 1.7 for discussion of the relevant literature. The formation of boron nitride fibres from polyaminoborane precursors has been hinted at by Manners and co-workers.[22] Other routes are available although they require high temperatures and pressures, and/or air and moisture sensitive polymeric materials.[23-25]

The previous work discussed in this chapter formed the basis of a collaboration with the Grobert Group at the University of Oxford that resulted in a publication in Advanced Composites and Hybrid Materials.[26] The polyaminoborane formed in a range of molecular weights was required to investigate the formation of *h*-BN fibers *via* electrospray methods. The formation and characterisation of the fibers was carried out by Dr Ping-Yuan Lee at the University of Oxford.

The polymers were electrosprayed from a $CHCl_3$ solution at different viscosities and polyaminoborane fibers were formed. Solid-state ^{11}B NMR spectra of the polyaminoborane and electrospun fiber show no difference to the boron environment of the material, with both showing a broad resonance at δ –8.35, indicative of polyaminoborane (Figure 4.10). An ideal molecular weight range was identified that resulted in the formation of homogenous fibers (M_w = 172,000-250,500 g mol^{-1}). Analysis of polyaminoboranes by TGA show that they have low ceramic yields (<6.5% at 500 °C),[8] but this can be combatted by the curing of the spun-fibers in a vacuum oven (10^{-1} bar) at 100 °C for 48 hours prior to ammonolysis. Analysis of the materials pre- and post-vacuum oven treatment by solid-state NMR spectroscopy indicated that the thermal treatment resulted in crosslinking of the polymer. Peaks present at δ 9.72 and 1.54 in the solid-state ^{11}B NMR spectra of the cured fibre (Figure 4.10 A and B), indicate the presence of boron coordinated by 3 and 4 nitrogen atoms, respectively.[27, 28]

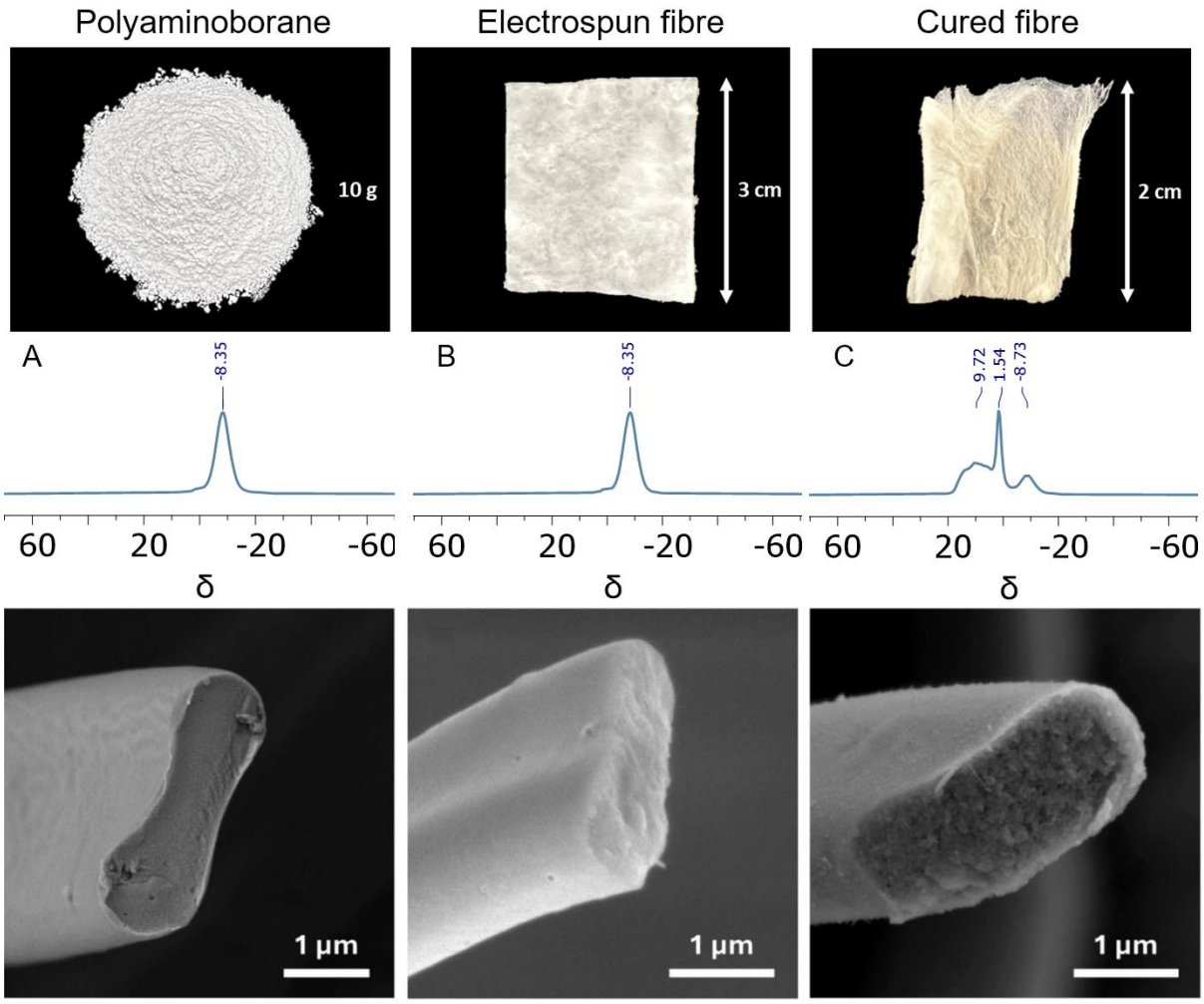

Figure 4.10. ^{11}B Solid state NMR spectrum (128 MHz, 12 kHz spin rate, 303K), and SEM images of A) Polyaminoborane, B) polyaminoborane fibre C) Cured polyaminoborane fibre.

Crosslinking of the polyaminoborane lead to an increased ceramic yield of ~70% at 500 °C observed by TGA. Subsequent heating to 1400 °C under a flow of ammonia resulted in the formation of *h*-BN fibres. Analysis of the fibres were consistent with the formation of boron nitride; the powder X-ray diffraction pattern was broadened compared with the commercial sample. The broadening indicates that the boron nitride is turbostractic in nature, meaning there is less ordered stacking of the sheets. (Figure 4.11 A). The IR spectrum acquired showed characteristic peaks at 1354 cm^{-1} and 798 cm^{-1} (Figure 4.11 B) for the in-plane B–N stretching vibration and the out-of-plane B–N–B bending vibration, respectively, consistent with BN.[29]

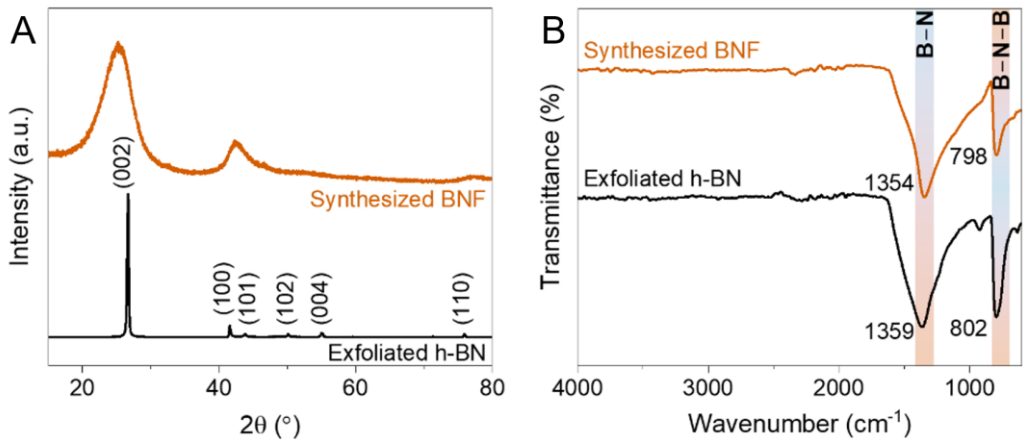

Figure 4.11. A) Powder X-ray diffraction pattern of polymer derived *h*-BN compared to a commercial sample B) Infrared spectrum of polymer derived *h*-BN compared to a commercial.

The ability to control the molecular weight of polyaminoborane allowed access to polymers in an ideal spinnable range to form homogeneous fibers. Vacuum curing of the polyaminoborane prior to ammonolysis allowed for higher ceramic yields to be achieved, and analysis of the materials by NMR spectroscopies gave insight into the crosslinking that was happening during this step. Finally, boron nitride fibres were formed from easily accessible and air-stable materials that provides a practical improvement in the synthesis of boron nitride fibres, and opens avenues into new investigations into these materials.

4.7.2 Iridium-doped boron nitride

Catalytic applications of *h*-BN have previously been reported, such as: the selective oxidative dehydrogenation of alkanes,[30] CO methanation,[31] and the synthesis and decomposition of ammonia and formic acid.[32] Additionally, there are reports of *h*-BN acting as a support for metal nanoparticles in catalysis, namely Ag, Au, Pt, and Pd.[29, 33, 34] Having previously determined that iridium from the catalyst remains entrained in the formed polyaminoborane, it was of interest to determine if the iridium remained after the conversion of polyaminoborane into boron nitride and if it had catalytic potential.

The synthetic approach to the formation of boron nitride took inspiration from the collaboration with the Grobert group at the University of Oxford. The polyaminoborane was cured in a

vacuum oven (10^{-1} bar at 100 °C) for 48 hours (59% yield by mass) prior to ammonolysis at 1200 °C (48% yield by mass). The resulting boron nitride was grey in colour (Figure 4.12), likely due to carbon impurity from the methyl group on the polymer.

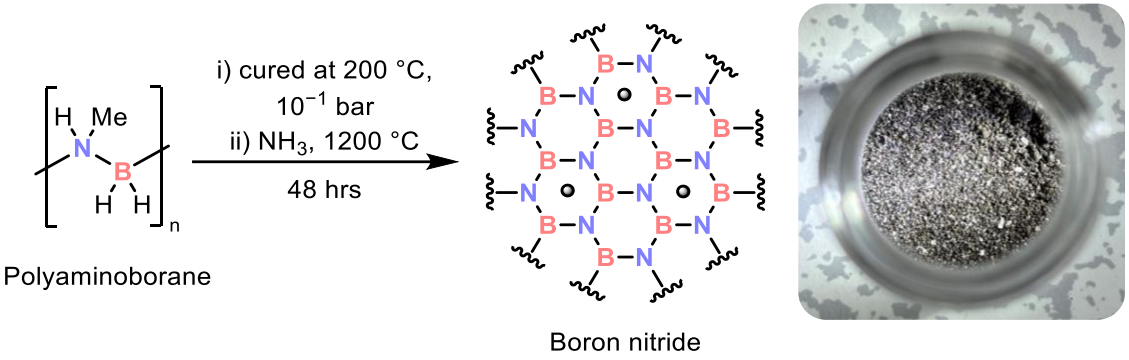

Figure 4.12. Synthesis of Ir@*h*-BN and an image of the product.

The composition of the boron nitride was analysed using X-ray photoelectron spectroscopy (XPS) at HarwellXPS, with the data processing carried out by Professor Richard Douthwaite at the University of York. The calculated elemental content (Figure 4.13 A) shows a large oxygen content in the boron nitride (27.48%) that in the high-resolution boron 1s spectra can be seen as B-O (Figure 4.13 B). This is likely due to oxidation occurring, forming B-O impurities, as the material was stored in air. The boron and nitrogen content are different (37.37% and 23.72%, respectively), indicating that the material is boron rich. It is interesting to note that the BN fibres were also boron rich.[26] The elemental mapping also shows that the iridium from the catalyst remains entrained in the boron nitride (Figure 4.13 D). The aluminium content is an impurity that comes from removal of the boron nitride from the ceramic boat that the cross-linked polymer undergoes ammonolysis in.

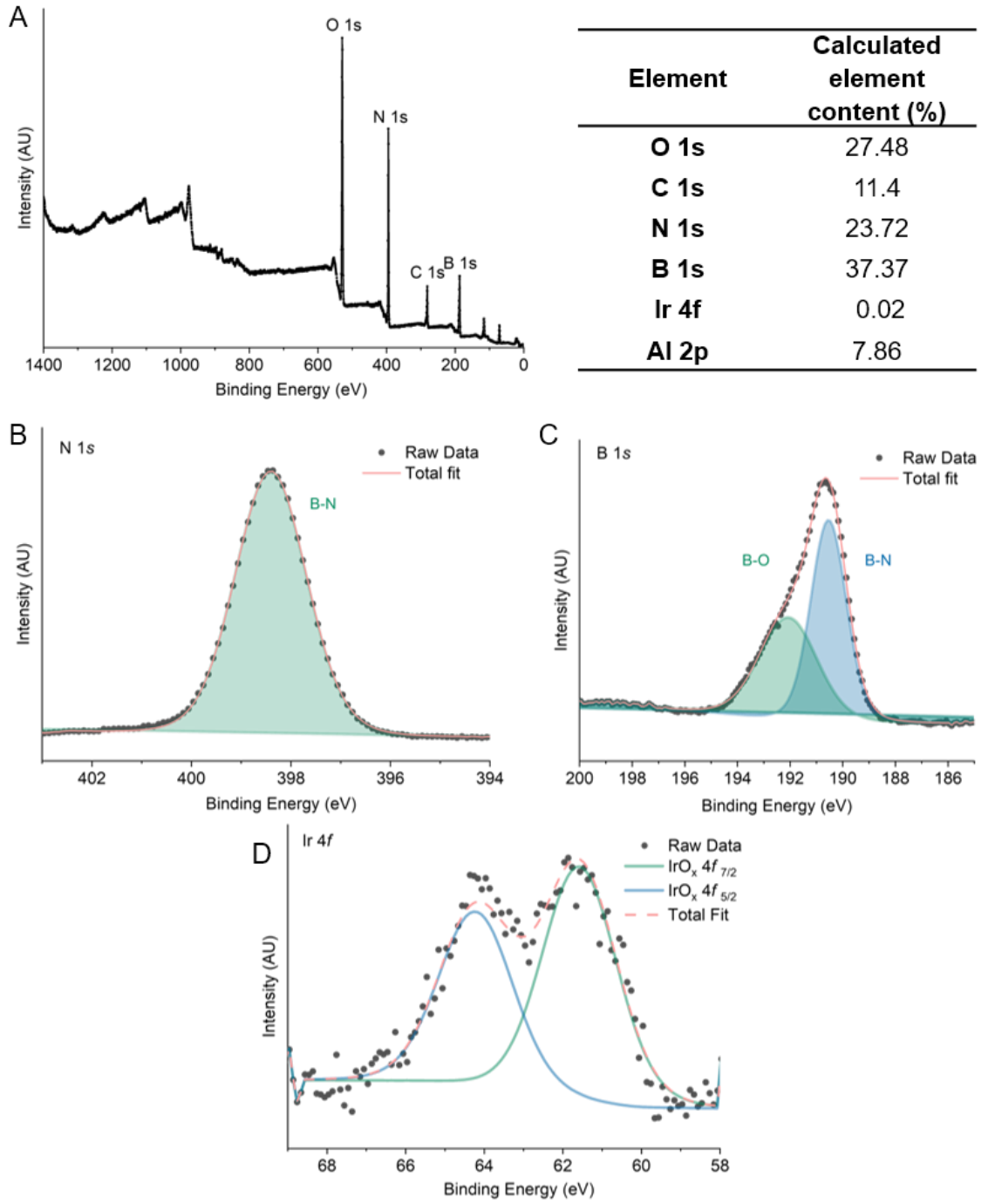

Element	Calculated element content (%)
O 1s	27.48
C 1s	11.4
N 1s	23.72
B 1s	37.37
Ir 4f	0.02
Al 2p	7.86

Figure 4.13. A) XPS survey spectrum with table of calculated element content B) High resolution spectrum N 1s C) High resolution spectrum of B 1s D) High resolution spectrum of Ir 4f.

The content of iridium in the material was quantified by ICP-OES analysis. The initial polyaminoborane had an iridium content of 891 ppm; this increased to 1501 ppm in the sample of boron nitride (Table 4.4). This increase is likely due to the B/N mass loss through the curing and ammonolysis process, 41% and 48% mass loss, respectively.

Table 4.4. ICP-OES Analysis of polyaminoborane and Ir@hBN for [Ir] (ppm).

Material	[Ir] (ppm)
Polyaminoborane	891
Ir@*h*-BN	1501

Analysis of the material by infrared spectroscopy indicated the formation of boron nitride, with the spectrum comparable to that of a commercial sample of *h*-BN (Figure 4.14). The IR spectrum taken shows characteristic peaks at ~1300 cm^{-1} and ~750 cm^{-1} (Figure 4.11 B) indicative of the in-plane B–N stretching vibration and the out-of-plane B–N–B bending vibration, respectively.[29]

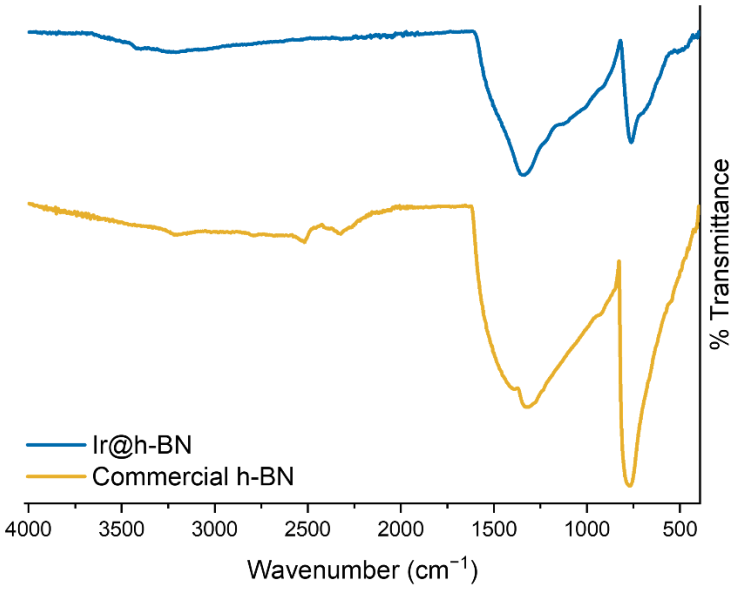

Figure 4.14. IR spectrum of Ir@*h*-BN (top) and commercial *h*-BN sample (bottom).

Scanning transmission electron microscopy (STEM) imaging carried out by Dr Leonardo Lari at the York JEOL Nanocentre at the University of York, shows that iridium is present in the boron nitride samples (supported by energy dispersive X-ray spectroscopy (EDX) and electron energy loss spectroscopy (EELS)). The images of the boron nitride flakes show a good iridium distribution over the surface with iridium clusters ~2-3 nm (Figure 4.15 B) and single atom sites visible on the surface (Figure 4.15 C).

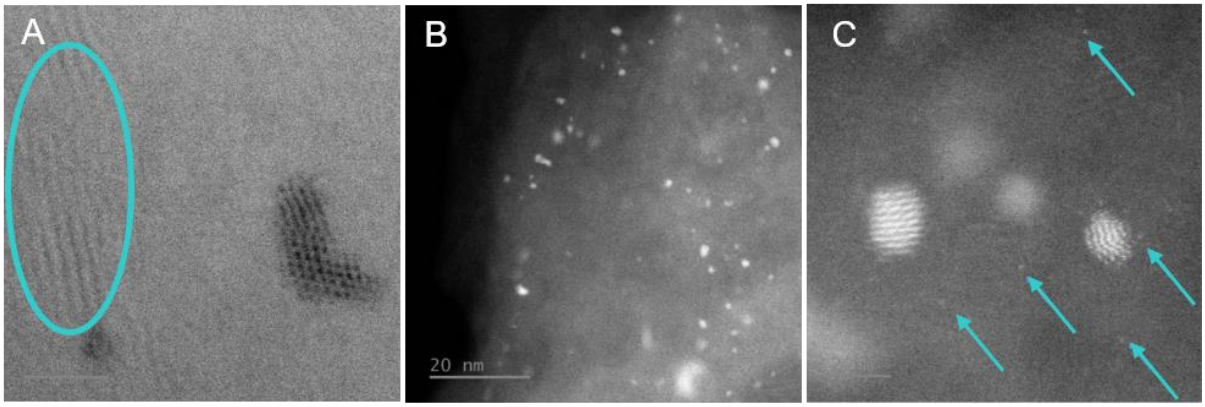

Figure 4.15. A) BF STEM image showing layers and atom channels, B) HAADF STEM image showing iridium clusters, C) blue arrows indicate iridium single atom sites. Graphitised carbon present increased conductivity to prevent charging.

With the understanding that the iridium remained entrained in the boron nitride formed (Ir@*h*-BN), focus shifted to reactions that the material may catalyse. There are similar materials (iridium-doped boron nitride reported in the literature) that catalyse the hydrogenation of aldehydes.[35, 36] To test the Ir@*h*-BN synthesised from polyaminoboranes, the hydrogenation of propene was chosen as the reaction could easily be monitored by gas phase ^{1}H NMR spectroscopy. Additionally, performing the reaction as a solid-gas reaction (without the use of solvent) negated the possibility of iridium nanoparticles leeching into solution and catalysing the reaction.

An NMR tube was charged with Ir@*h*-BN (5 mg), propene was added (1 bar) and the NMR tube was cooled to 77 K prior to hydrogen addition (2 bar). The reaction was carried out at room temperature and resulted in no formation of propane after 24 hours. Heating the reaction to 100 °C for 24 hours led to the full conversion of propene to propane (Figure 4.16). A control experiment was carried out with a commercial sample of boron nitride which resulted in a 22% conversion from propene to propane at 100 °C over 24 hours. This shows that the Ir@*h*-BN formed from polyaminoborane is more active for the hydrogenation of propene than the commercial *h*-BN sample.

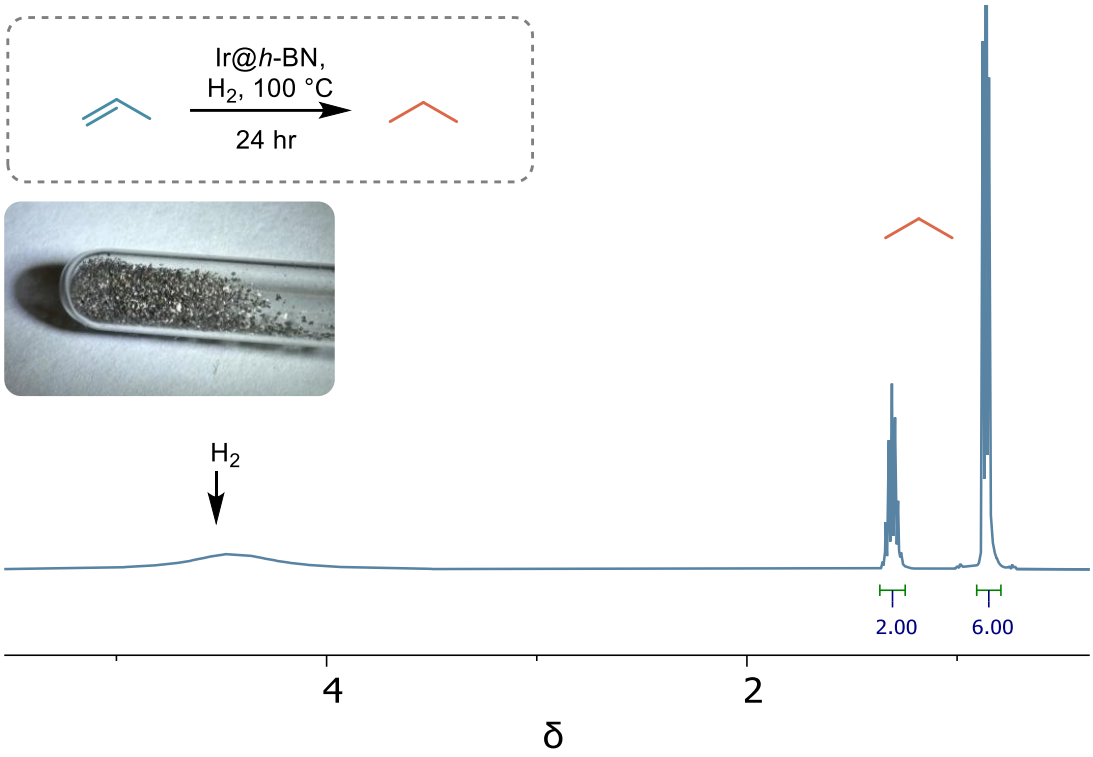

Figure 4.16. Gas-phase ^{1}H NMR spectra (500 MHz, 298 K) showing full hydrogenation of propene to propane over 24 hours.

Analysis of the Ir@*h*-BN pre- and post-catalysis by p-XRD shows a very similar powder pattern to that recorded for the boron nitride fibers.[26] The broadness of the pattern indicates that the boron nitride is amorphous and is suggestive of a turbostratic structure, not crystalline like the commercial sample. Further work would be required to identify synthetic conditions or post synthetic modifications that forms more ordered, crystalline *h*-BN.

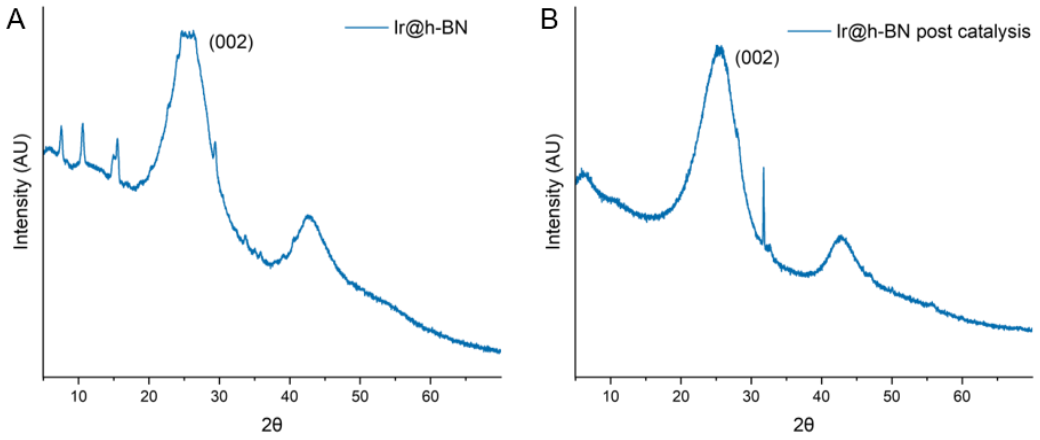

Figure 4.17. Powder X-ray diffraction pattern of Ir@h-BN A) Pre- B) Post- propene hydrogenation catalysis.

This initial result provides a proof of principle that polyaminoborane derived boron nitride can be used to catalyse reactions and provides an 'additive free' route to iridium doped boron nitride. Further work is required to increase the activity of the catalyst, such as higher [Ir], thin films to increase the surface area, increased crystallinity and doping of other metals (*e.g.* Rh and Ru).

4.8 Summary and conclusions

In this chapter the polymerisation mechanism for aminoborane polymerisation was determined to be a chain growth mechanism, in agreement with previous reports.[1, 3] The termination event is believed to be consistent with a termination agent such as BH_3 or boronium ($[H_2B(NRH_2)_2]^+$). This meant that the kinetics of the chain growth mechanism could be rationalised by the term D.P. ~ R_{prop}/R_{term}.[6]

Reaction conditions and additives have been identified that can control the molecular weight of polyaminoborane formed with catalyst **1**. As part of this investigation the relationship between k_{obs} and M_n was established with catalyst **1**. This has allowed for the control of M_n to this extent for the first time with a range of 57,300-185,200 g mol^{-1}, using easily tuneable reaction conditions. Prior to this the molecular weights of polyaminoborane with catalyst **1** varied widely from run-to-run with the same reaction conditions. The scaled-up synthesis of polyaminoborane with catalyst **1** unlocked further range with polyaminoborane M_n = 35,000 g mol^{-1}.

The control of M_n that has been achieved in this study has enabled new applications to be investigated for polyaminoboranes, including the synthesis of boron nitride fibres from an easily assessable and air stable precursor, something that had previously only been alluded to.[22] Boron nitride fibres are alternatives to carbon fibre and can be used in place of carbon fibre in environments where carbon fibre fails (*i.e.* corrosive environments and very high

temperatures).[37] These findings may open up a new avenue of research into the use of polyaminoboranes as precursors to BN ceramics.

Additionally, initial results have shown that polyaminoborane can act as a precursor to Ir@*h*-BN, providing an 'additive free' route to catalytically active iridium doped boron nitride catalysts for the hydrogenation of alkenes. Further work would be required to investigate how the Ir content in the Ir@*h*-BN, the crystallinity and co-doping of other metals may affect catalysis with these metal-doped *h*-BN materials, also what range of reactions the materials can catalyse.

Finally, a thorough understanding of the mechanism of catalyst **1** allowed for the reaction to be taken to extremes, forming polyaminoborane selectively on scale (20 g) with extremely low catalyst loading (0.001 mol%) for the first time. This signals a step towards potential transfer to an industrial where sustainability and cost are both important factors in taking a reaction from the bench to

4.9 References

1. A. Staubitz, M. E. Sloan, A. P. M. Robertson, A. Friedrich, S. Schneider, P. J. Gates, J. S. A. D. Günne and I. Manners, *J. Am. Chem. Soc.*, 2010, **132**, 13332–13345.
2. A. Staubitz, A. Presa Soto and I. Manners, *Angew. Chem. Int. Ed.*, 2008, **47**, 6212–6215.
3. S. Bhunya, T. Malakar and A. Paul, *Chem. Commun.*, 2014, **50**, 5919–5922.
4. O. J. Metters, A. M. Chapman, A. P. M. Robertson, C. H. Woodall, P. J. Gates, D. F. Wass and I. Manners, *Chem. Commun.*, 2014, **50**, 12146–12149.
5. S. Shafiei-Haghighi, L. M. Singer, S. R. Tamang and M. Findlater, *Polyhedron*, 2018, **143**, 126–131.
6. A. Ravve, *Principles of Polymer Chemistry Third Edition*, Springer, New York, 2012.
7. M. Devillard, C. A. De Albuquerque Pinheiro, E. Caytan, C. Roiland, C. Dinoi, I. Del Rosal and G. Alcaraz, *Adv. Synth. Catal.*, 2021, **363**, 2417–2426.
8. C. N. Brodie, T. M. Boyd, L. Sotorríos, D. E. Ryan, E. Magee, S. Huband, J. S. Town, G. C. Lloyd-Jones, D. M. Haddleton, S. A. Macgregor and A. S. Weller, *J. Am. Chem. Soc.*, 2021, **143**, 21010–21023.
9. M. J. Cross, C. N. Brodie, D. G. Crivoi, J. C. Goodall, D. E. Ryan, A. J. Martinez-Martinez, A. Johnson and A. S. Weller, *Chem. Eur. J.*, 2023, **29**, e202302110.
10. D. E. Ryan, K. A. Andrea, J. J. Race, T. M. Boyd, G. C. Lloyd-Jones and A. S. Weller, *ACS Catal.*, 2020, **10**, 7443–7448.
11. C. N. Brodie, L. Sotorrios, T. M. Boyd, S. A. Macgregor and A. S. Weller, *ACS Catal.*, 2022, **12**, 13050–13064.
12. E. A. K. Spearing-Ewyn, N. A. Beattie, A. L. Colebatch, A. J. Martinez-Martinez, A. Docker, T. M. Boyd, G. Baillie, R. Reed, S. A. Macgregor and A. S. Weller, *Dalton Trans.*, 2019, **48**, 14724–14736.
13. T. M. Boyd, K. A. Andrea, K. Baston, A. Johnson, D. E. Ryan and A. S. Weller, *Chem. Commun.*, 2020, **56**, 482–485.
14. A. Glüer, M. Förster, V. R. Celinski, J. Schmedt auf der Günne, M. C. Holthausen and S. Schneider, *ACS Catal.*, 2015, **5**, 7214–7217.
15. P. Hasche, J. Haak, F. Anke, C. Kubis, W. Baumann, H. J. Drexler, H. Jiao and T. Beweries, *Cat. Sci. Technol.*, 2021, **11**, 3514–3526.
16. G. M. Adams, A. L. Colebatch, J. T. Skornia, A. I. McKay, H. C. Johnson, G. C. Lloyd Jones, S. A. Macgregor, N. A. Beattie and A. S. Weller, *J. Am. Chem. Soc.*, 2018, **140**, 1481–1495.
17. M. J. Cross, M. A. Sajjad, S. A. Macgregor and A. S. Weller, *Angew. Chem. Int. Ed.*, 2025, **64**, e202500019.
18. G. Montaudo and R. P. Lattimer, *Mass Spectrometry of Polymers*, CRC Press, Florida, 2002.
19. G. C. Fortman, A. M. Z. Slawin and S. P. Nolan, *Organometallics*, 2011, **30**, 5487–5492.
20. D. J. Nelson, B. J. Truscott, J. D. Egbert and S. P. Nolan, *Organometallics*, 2013, **32**, 3769–3772.
21. V. A. Cherepanova, E. G. Gordeev and V. P. Ananikov, *JACS Au*, 2025, **5**, 3789–3798.
22. E. M. Leitao, T. Jurca and I. Manners, *Nat. Chem.*, 2013, **5**, 817–829.
23. S. Bernard and P. Miele, *Materials*, 2014, **7**, 7436–7459.
24. R. T. Paine and C. K. Narulat, *Chem. Rev.*, 1990, **90**, 73–91.
25. P. J. Fazen, J. S. Beck, A. T. Lynch, E. E. Remsen and L. G. Sneddon, *Chem. Mater.*, 1990, **2**, 96–97.
26. P.-Y. Lee, B. M. Maciejewska, M. J. Cross, C. M. van Beek, C. N. Brodie, A. S. Bhaskaran, G. T. Tebbutt, R. M. Schofield, S. J. Page, E. Darnbrough, M. Swart, A. S. Weller and N. Grobert, *Adv. Compos. Hybrid Mater.*, 2025, **8**.
27. R. Knitsch, D. Han, F. Anke, L. Ibing, H. Jiao, M. R. Hansen and T. Beweries, *Organometallics*, 2019, **38**, 2714–2723.

28. D. Han, M. Joksch, M. Klahn, A. Spannenberg, H. J. Drexler, W. Baumann, H. Jiao, R. Knitsch, M. R. Hansen, H. Eckert and T. Beweries, *Dalton Trans.*, 2016, **45**, 17697–17704.
29. D. Fan, J. Feng, J. Liu, T. Gao, Z. Ye, M. Chen and X. Lv, *Ceram. Int.*, 2016, **42**, 7155–7163.
30. J. T. Grant, C. A. Carrero, F. Goeltl, J. Venegas, P. Mueller, S. P. Burt, S. E. Specht, W. P. McDermott, A. Chieregato and I. Hermans, *Science*, 2016, **354**, 1570–1573.
31. J. Sheng, W.-C. Li, B. He, X.-Q. Gao, W.-D. Lu, B. Qiu, R.-P. Zhang, L. He, X. Liu and A.-H. Lu, *ACS Catal.*, 2023, 9201–9212.
32. M. Yruela-Garrido, E. Campos-Castellanos, M. V. Morales, I. Rodriguez-Ramos and A. Guerrero-Ruiz, *Nanomaterials*, 2025, **15**, 212.
33. C. Huang, C. Chen, X. Ye, W. Ye, J. Hu, C. Xu and X. Qiu, *J. Mater. Chem. A*, 2013, **1**, 12192–12197.
34. W. Sun, Y. Meng, Q. Fu, F. Wang, G. Wang, W. Gao, X. Huang and F. Lu, *ACS Appl. Mater. Interfaces*, 2016, **8**, 9881–9888.
35. Y.-M. Hu, W.-B. Zheng, A.-P. Jia, M.-F. Luo, C. Tang and J.-Q. Lu, *React. Kinet. Mech. Catal.*, 2021, **132**, 301–315.
36. X. Ning, Y.-M. Xu, A.-Q. Wu, C. Tang, A.-P. Jia, M.-F. Luo and J.-Q. Lu, *Appl. Surf. Sci.*, 2019, **463**, 463–473.
37. P. Colombo, G. Mera, R. Riedel and G. D. Sorarù, *J. Am. Ceram. Soc.*, 2010, **93**, 1805–1837.

Chapter 5: Derivatives of iridium POCOP complexes in catalysis

In Chapters 2, 3 and 4, an in-depth study was carried out into the dehydropolymerisation of amine-boranes with catalyst **1**, Ir(^{t}Bu-POCOP)(H)$_2$. This study was split into two parts, the dehydrogenation reaction and the polymerisation reaction. In Chapter 4, study of the relationship between the two reactions demonstrated that k_{obs} has an effect on the molecular weight of the polyaminoborane formed. The investigation into the dehydropolymerisation of amine-boranes with catalyst **1** identified a number of external variables that can be used to control the rate and the molecular weight of the polymer (*e.g.* catalyst loading, NH_2Me addition, *etc.*). Under standard reaction conditions (2 mM [Ir], 2 M $H_3B{\cdot}NH_2Me$, 20 °C, THF) the highest observed k_{obs} combined with highest molecular weight came from using anionic trihydride **[Na-18-crown-6][6]** and 1 equivalent of $[NH_3Me][BAr^F{}_4]$ (k_{obs} = 19.2(3) mM s^{-1} and M_n = 185,200 g mol^{-1}, Đ = 1.4). The following chapter details the synthesis of alternate iridium POCOP catalysts, before determining if changes to the pincer ligand structure can be used as another way to control k_{obs} and consequently molecular weight of polymer. The complexes presented in Chart 5.1 were selected due to the different steric demands of the R-groups on the phosphine, effectively changing the accessibility of the iridium centre.

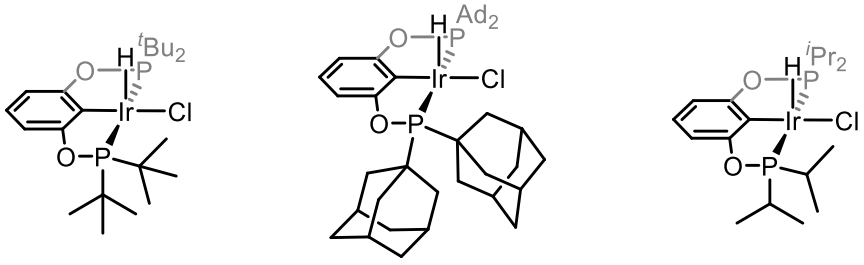

7 **8** **9**

Chart 5.1. Complexes of interest for Chapter 5.

5.1 Synthesis of Ad-POCOP derivative

5.1.1 Synthesis of Ad-POCOP ligand

The synthesis of 1,3-bis[(di-adamantylphosphino)oxy]benzene (Ad-POCOP) was carried out with inspiration from Brookhart and co-workers and their synthesis of ^{t}Bu-POCOP.[1] Ad-POCOP was prepared in high purity and moderate isolated yield (43%) from the treatment of resorcinol with NaH in THF at 76 °C for 1 hour followed by the addition of diadamantylchlorophosphine (PAd_2Cl) and further reflux for 1 hour (Scheme 5.1). Removal of the solvent *in vacuo*, followed by washing with pentane at 0 °C, and extraction into toluene before removal of the volatiles yielded the Ad-POCOP ligand as a white powder (151 mg, 43% yield). The purity of the ligand was determined by NMR spectroscopy and was used in the synthesis of Ir(Ad-POCOP)HCl without further purification.

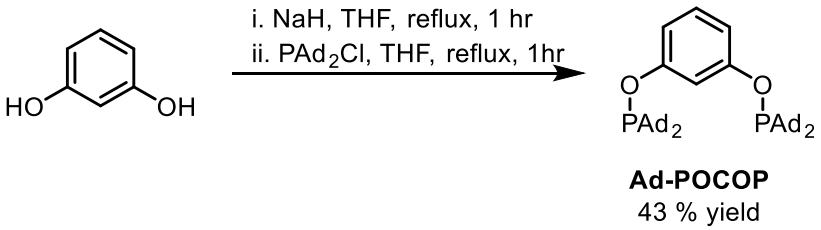

Scheme 5.1. The synthesis of new phosphine 1,3-bis[(di-adamantylphosphino)oxy]benzene (Ad-POCOP).

The ^{1}H NMR spectrum (Figure 5.1) shows a pentet (apparent) at δ 7.65 that integrates for 1H. This resonance collapses to a triplet ($^{4}J_{HH}$ = 2.2 Hz) on ^{31}P decoupling. This signal was assigned to H1 of the phenyl ring. The other protons of the aryl ring (H2 and H3) are observed as a multiplet (δ 7.15-7.07) that integrates for 3H that collapses down to a doublet and triplet, respectively, on ^{31}P decoupling ($^{3}J_{HH}$ = 2.3 Hz). In solution the adamantyl groups are equivalent as they show as one set of signals: three broad singlets at δ 2.07, 1.85 and 1.65 that integrate for 24H, 12H and 24H, respectively. There are persistent signals assigned to toluene (δ 7.02 and 7.05) that remained after drying the product *in vacuo* (10^{-3} mbar) at 40 °C for 12 hours. A singlet was observed at δ 149.15 in the ^{31}P{^{1}H} NMR spectrum, similar to that reported for ^{t}Bu-POCOP (δ 153.1).[1]

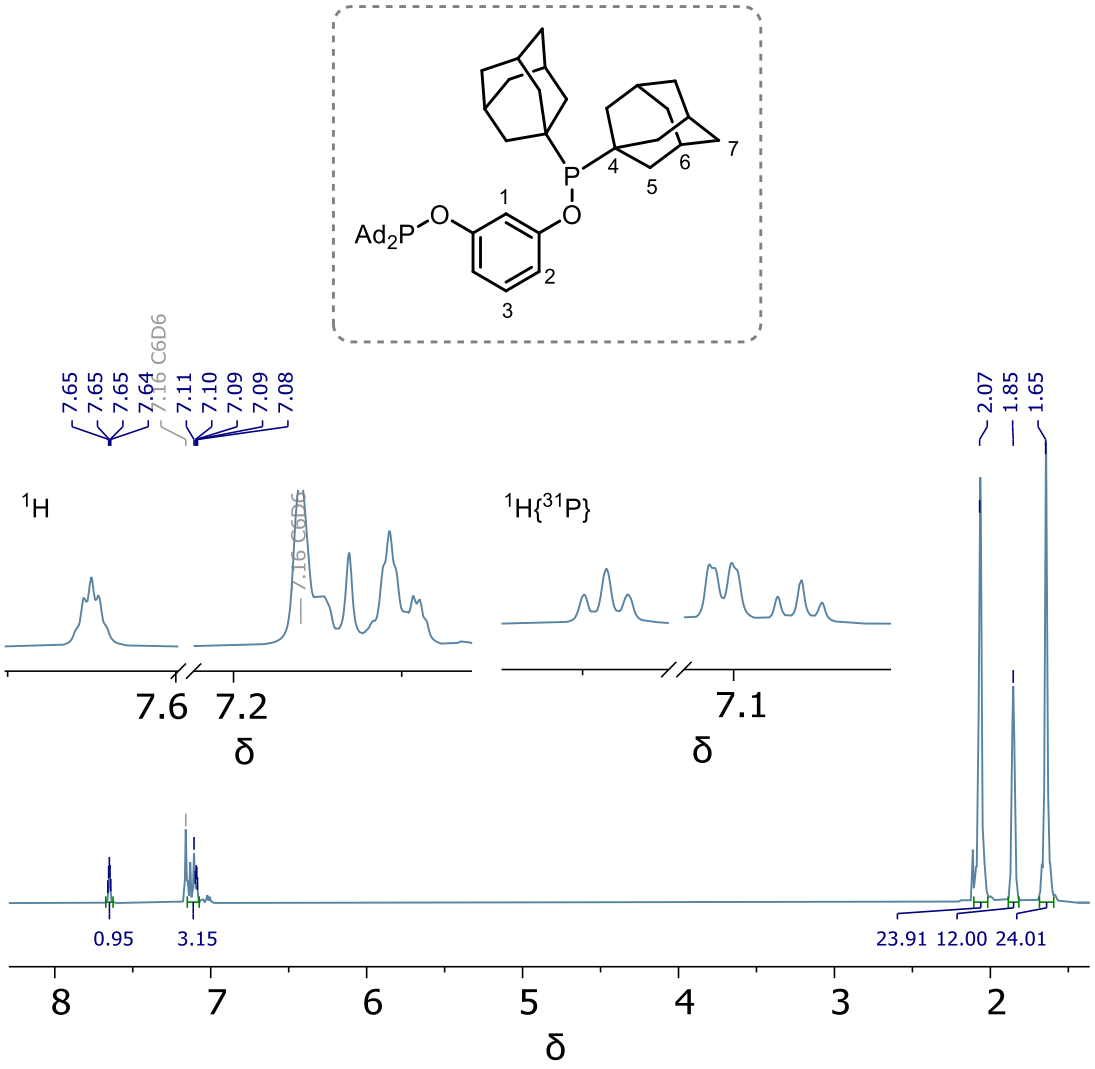

Figure 5.1. ^{1}H NMR spectrum (C_6D_6, 500 MHz, 298 K) of Ad-POCOP.

Crystals suitable for single crystal X-ray diffraction were obtained by cooling (4 °C) a concentrated pentane solution of Ad-POCOP. The ligand crystalises in the $P\bar{1}$ space group (Figure 5.2) with a molecule of pentane in its asymmetric unit, which is not shown for clarity. The phosphorus atoms are crystallographically inequivalent, with one in the plane of the phenyl ring and the other pointing below the plane of the phenyl ring. The P–C distances (1.863(2) Å, 1.875(2) Å, 1.868(2) Å and 1.867(2) Å) are comparable to those reported for ^{t}Bu-POCOP (1.864(2) Å, 1.875(1) Å, 1.873(2) Å and 1.873(2) Å.[2] The P–O distances are also similar to those reported for ^{t}Bu-POCOP (Ad-POCOP = 1.677(1) Å, 1.681(2) Å and ^{t}Bu-POCOP 1.675(1) Å and 1.679(1) Å).[2]

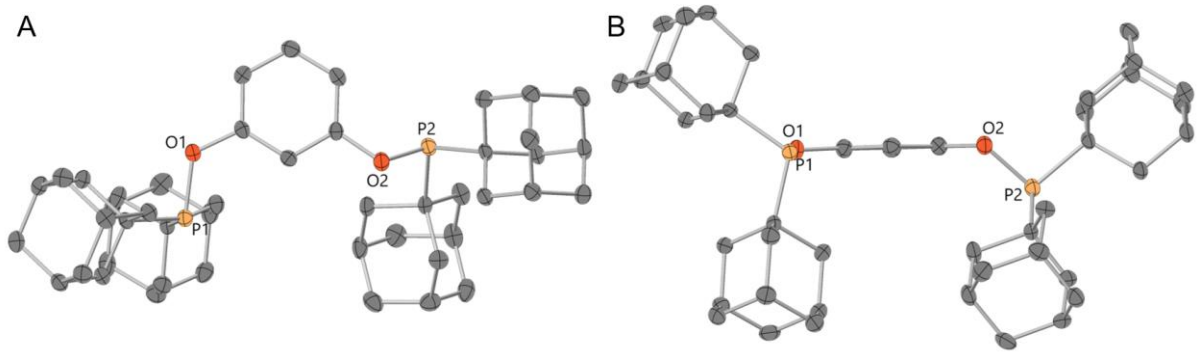

Figure 5.2. A view of the molecular structure of **Ad-POCOP** A) view from above and B) looking down the plane of the phenyl ring. Displacement ellipsoids are set at 50% probability, hydrogen atoms and co-crystallised pentane are omitted for clarity. Selected bond lengths (Å): P1–O1 1.677(1), P2–O2 1.681(2), P1–C7 1.863(2), P1–C17 1.875(2), P2–C27 1.868(2), P2–C37 1.867(2).

5.1.2 Synthesis of Ir(Ad-POCOP)HCl

The synthesis of Ir(Ad-POCOP)HCl was carried out with inspiration form Brookhart and co-workers based on their synthesis of Ir(^{t}Bu-POCOP)HCl.[1] Ir(Ad-POCOP)HCl was prepared by treatment of $[Ir(COD)Cl]_2$ with Ad-POCOP in toluene at 150 °C (Scheme 5.2). Reaction at lower temperatures results in a loss of selectivity for the formation of Ir(Ad-POCOP)HCl, indicated by a large number of impurities observed by $^{31}P\{^1H\}$ NMR spectroscopy. Subsequent removal of solvent and washing with pentane yielded Ir(Ad-POCOP)HCl (**8**) as a red/brown microcrystalline solid.

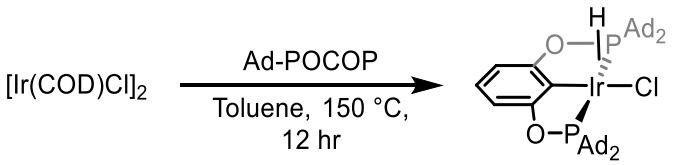

8
76 % yield

Scheme 5.2. The synthesis of Ir(Ad-POCOP)HCl.

Crystals suitable for single crystal X-ray diffraction were obtained from slow evaporation of a concentrated pentane solution. The complex crystallised in the $P\bar{1}$ space group (Figure 5.3). The Ad-POCOP and chloride ligands were arranged around the metal in a distorted square-

planar geometry, with a P1–Ir1–P2 bond angle of 160 °. The chloride atom is positioned *trans* to the phenyl group of the pincer ligand, with the chloride atom pointed below the plane of the pincer ligand. The Ir–P distances are 2.287(2) Å and 2.285(1) Å similar to the *tert*-butyl derivative (**7**) 2.292(1) Å and 2.290(1) Å.[3] The Ir–Cl bond length of complex **8** and complex **7** are also comparable (2.409(1) Å and 2.395(1) Å respectively).[3]

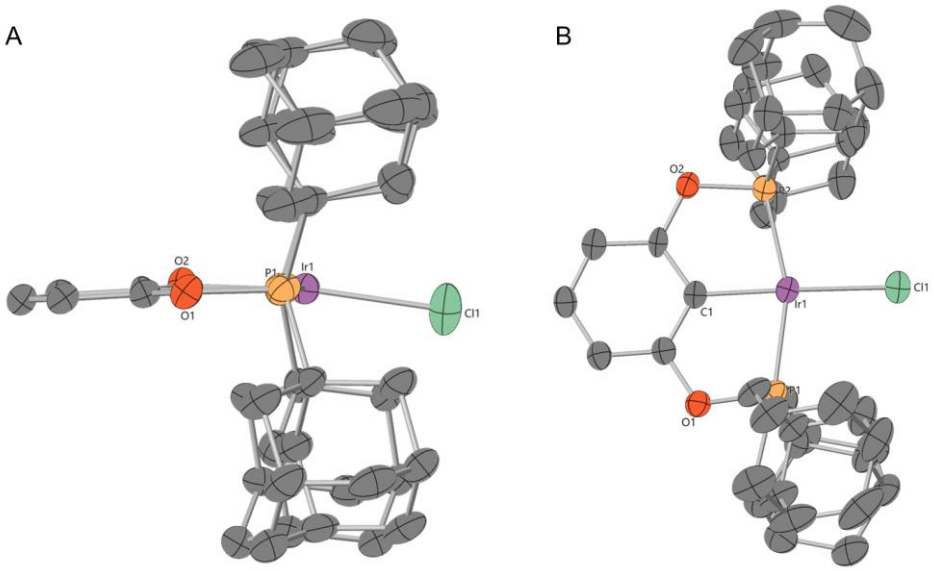

Figure 5.3. A view of the molecular structure of Ir(Ad-POCOP)HCl (**8**) A) side on view and B) view from above. Displacement ellipsoids are set at 50% probability, hydrogen atoms are omitted for clarity. Selected bond lengths (Å): Ir1–P1 2.287(2), Ir1–P2 2.285(1), Ir1–C1 1.997(4), Ir1–Cl1 2.409(1). Selected bond angles (°): P1–Ir1–P2 160.21(5), P1–Ir1–C1 79.9(1), P2–Ir1–C1 80.3(1).

The ^{1}H NMR spectrum of **8** shows a complex multiplet (Figure 5.4) that integrates for 3H assigned to the aromatic protons of the phenyl ring (H1 and H2) at δ 6.88. This multiplet collapses down to a broad singlet on ^{31}P decoupling. The signals for the protons of the phenyl ring overlap, unlike the *tert*-butyl derivative where they appear at different chemical shifts. The hydride signal at δ –40.17 presents as a broad singlet that sharpens on ^{31}P decoupling. This chemical shift is similar to that recorded for the *tert*-butyl derivative, however with the *tert*-butyl complex the signal resolves as an apparent triplet. The signals attributed to the adamantyl groups are complex, likely due to the adamantyl groups being chemically inequivalent above and below the plane of the phenyl ring. There are two overlapping sets of doublets of doublets

assigned to H7. Each set of doublets integrates for 12H, and each doublet shows correlation to another in the COSY NMR. The coupling constants of the dd at *δ* 2.42 are *J* = 174.1 Hz and *J* = 11.8 Hz. The other dd assigned to H7 is found at *δ* 2.35, with coupling constants of *J* = 69.4 Hz, *J* = 12.2 Hz. Both sets of doublets of doublet do not collapse on ^{31}P decoupling. There are two broad singlets at *δ* 1.94 and *δ* 1.87 that each integrate for 6H. Each singlet shows correlation in the COSY NMR to one set of doublets that is assigned to H7. The remaining signals from the adamantyl group are found as an overlapping doublet of doublets that are highly roofed at *δ* 1.59. Each set of dd shows correlation in the COSY NMR to one 'set' of the other signals attributed to the adamantyl groups (Figure 5.5).

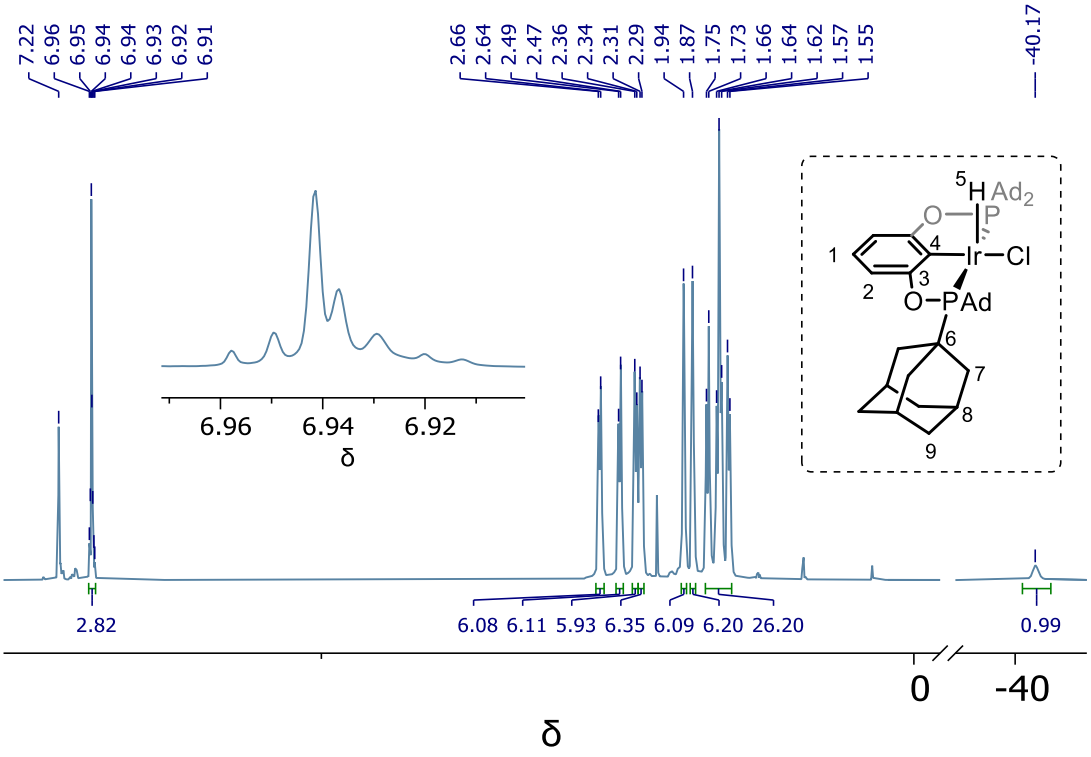

Figure 5.4. ^{1}H NMR spectrum (C_6D_6, 600 MHz, 298 K) of Ir(Ad-POCOP)HCl.

The adamantyl groups are inequivalent highlighted in the ^{1}H-^{1}H COSY NMR spectrum (Figure 5.5), and one phosphorus environment (singlet) was observed at *δ* 165.7 in the ^{31}P{^{1}H} NMR spectrum. This was expected as the molecule has a symmetry plane, and C_s symmetry.

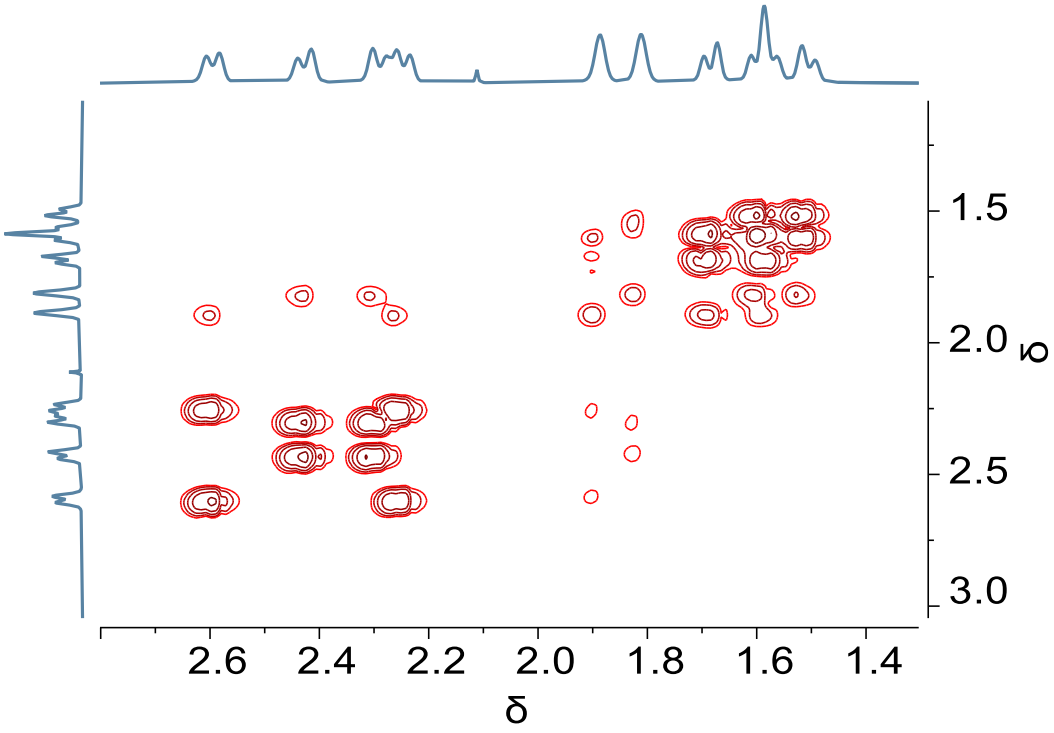

Figure 5.5. Expansion of the section relating to the adamantyl groups in the ^{1}H-^{1}H COSY NMR spectrum (C_6D_6, 600 MHz, 298 K) of of Ir(Ad-POCOP)HCl.

In the molecular structure obtained from single crystal X-ray diffraction, the chlorine atom is pointing below the plane of the pincer ligand, indicating that the hydride identified in the ^{1}H NMR spectrum but not observed in the molecular structure is positioned above the plane of the pincer ligand in the representation (Figure 5.3). There may be a preference for this hydride to be above the plane causing the chloride to point below the plane.

5.2 Other POCOP derivative in catalysis

5.2.1 Varying the R group on the phosphine of the pincer ligand

This section will investigate how small changes to the catalyst may affect k_{obs} and M_n, focussing on changes to the R-group on the phosphine of the pincer ligand. With insight into catalysis by the *tert*-butyl derivative already established, focus was transferred to the adamantyl and *iso*-propyl derivatives.

The synthesis of Ad-POCOP and Ir(Ad-POCOP)HCl (**8**) were described in section 5.1. The synthesis of Ir(*i*Pr-POCOP)HCl (**9**), although previously reported in the literature,[4, 5] was challenging. Reported procedures in the literature, similar to the synthetic route of the *tert*-butyl derivative, resulted in unselective formation of Ir(*i*Pr-POCOP)HCl (**9**) and other unidentified hydride containing iridium POCOP species.[4, 5] An alternative approach from the literature first formed a pyridine adduct before formation of hydridochloride **9** (Scheme 5.3).[6]

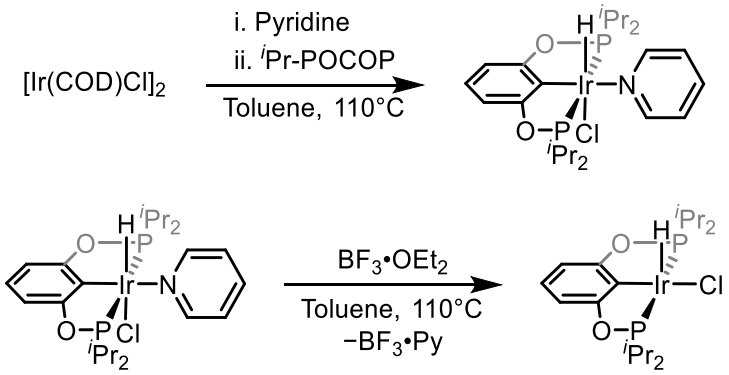

Scheme 5.3. Synthesis of Ir(*i*Pr-POCOP)HCl (**9**).[6]

Attempts to prepare the unreported dihydride complex of the *i*Pr derivative were unsuccessful. Addition of K[O*t*Bu] and H_2 (4 bar) resulted in unselective formation of tetrahydride Ir(*i*Pr-POCOP)H_4, with similar shifts observed in the ^{1}H and ^{31}P{^{1}H} NMR spectra to those reported in the literature.[4] However, application of a vacuum to remove the hydrogen to form the dihydride complex resulted in a breakdown to products that remain unidentified. This indicates that unlike the *tert*-butyl derivative, the dihydride form of Ir(*i*Pr-POCOP)H_2 is not stable or isolable. This is supported by there being no record of Ir(*i*Pr-POCOP)H_2 in the

literature, likely due to the lack of steric bulk from the *iso*-propyl groups. Congruently, the molecular structure of complex **9** reported by Waterman and co-workers[5] forms a dimer co-ordinated through the chloride ligands. Here the isolation and analysis of crystals of complex **9** by single crystal XRD resulted in the same arrangement of molecules in the asymmetric unit.

5.2.2 The effect of R-group on the phosphine of the pincer ligand on the dehydropolymerisation of amine-boranes

The three catalysts, Ir(^{t}Bu-POCOP)HCl (**7**), Ir(Ad-POCOP)HCl (**8**), Ir(^{i}Pr-POCOP)HCl (**9**) were tested in catalysis under the standard conditions established in Chapter 2 (0.1 mol% [Ir], 2 M $H_3B{\cdot}NH_2Me$, 20 °C, THF), see Figure 5.6. Polyaminoborane was formed cleanly with each catalyst, identified by a peak observed around δ –6 in the ^{11}B NMR spectrum taken of the reaction mixture at the end of catalysis. In all cases, formation of polymer was supported by GPC chromatography.

Employing Ir(^{t}Bu-POCOP)HCl (**7**) resulted in an induction period of 2730 s before rapid hydrogen release (k_{obs} = 11.7(1) mM s^{-1}), Figure 5.6. The polymer formed by catalyst **7** was white in colour and M_n = 103,400 g mol^{-1}, and Đ = 1.4**.** The molecular weight of polymer formed with catalyst **7** is similar to that formed with dihydride catalyst **1**. It should be noted that use of catalyst **7** results in an increase in induction period compared to hydride catalyst **1** (2730 s and ~300 s, respectively).

Dehydropolymerisation of $H_3B{\cdot}NH_2Me$ using Ir(Ad-POCOP)HCl (**8**), resulted in the longest induction period (3900 s) of the three catalysts, before rapid hydrogen release (k_{obs} = 13.9(3) mM s^{-1}), Figure 5.6. The polymer formed with catalyst **8** was white in colour, M_n = 104,700 g mol^{-1}, and Đ = 1.4. The molecular weight of the polymer formed by catalyst **8** was similar to that formed with catalyst **7**, and the rates of reaction were also comparable. The main difference between the catalysts was that the induction period observed for catalyst **8** was longer than that for catalyst **7** by ~1000 s.

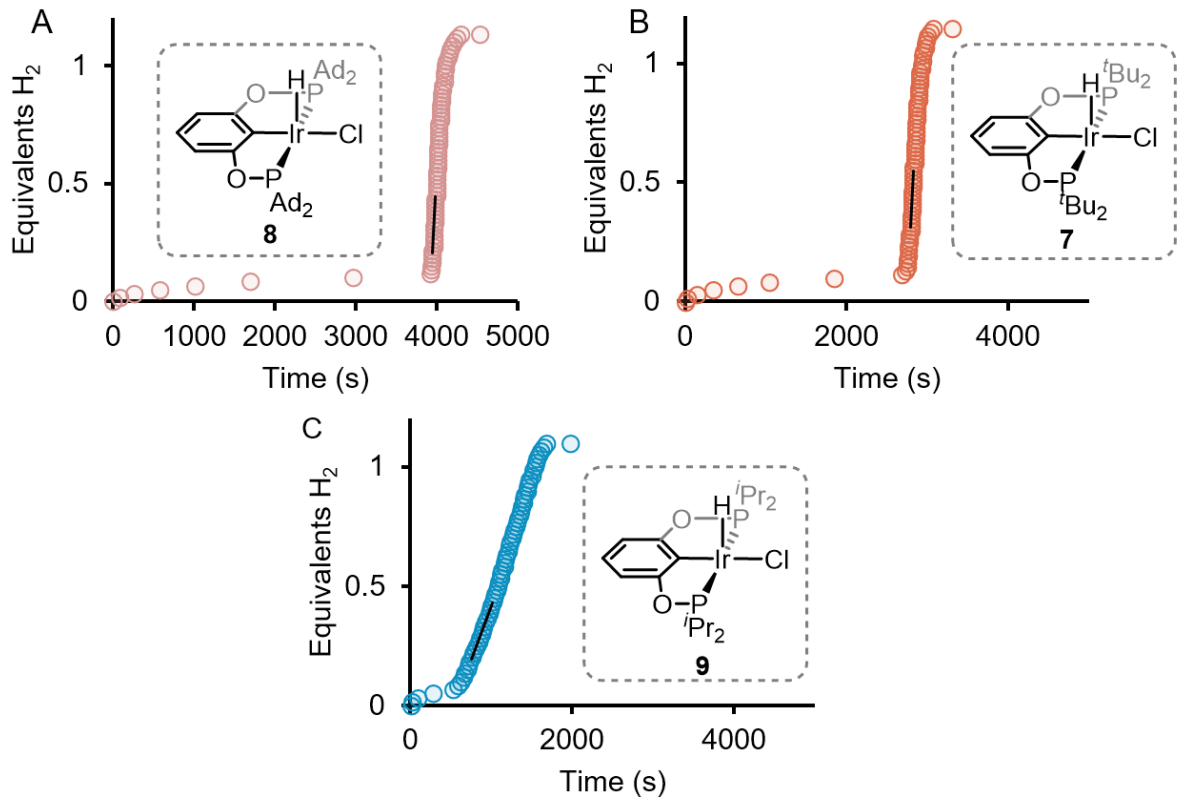

R-group (complex)	%V_{bur} (%)	k_{obs} (mM s^{-1})	Induction period (s)	M_n (g mol^{-1})	Đ	Yield (mg (%))
Ad (8)	64.3	13.9(3)	3900	104,700	1.387	63 (59)
^{t}Bu (7)	61.7	11.7(1)	2730	103,400	1.369	67 (63)
^{i}Pr (9)	53.9	1.83(2)	518	35,400	1.418	79 (74)

Figure 5.6. Kinetic profiles of the dehydropolymerisation of $H_3B{\cdot}NH_2Me$ with A) Ir(Ad-POCOP)HCl (**8**), B) Ir(^{t}Bu-POCOP)HCl (**7**), C) Ir(^{i}Pr-POCOP)HCl (**9**), and a table of kinetic data and polymer properties.

Reaction of $H_3B{\cdot}NH_2Me$ with Ir(^{i}Pr-POCOP)HCl (**9**), resulted in a much shorter induction period (518 s) than those observed for catalysts **7** and **8** (2730 s and 3900 s, respectively). In Chapters 2 and 3, the formation of the borohydride complex during the induction period was discussed. The shorter induction period with catalyst **9** over **7** and **8** may be caused by NH_2Me having better access once the borohydride complex forms due to the lesser steric demand of the *iso*-propyl groups. The rate of reaction of catalyst **9** was lower (k_{obs} = 1.83(2) mM s^{-1}) than those observed for catalysts **7** and **8** (k_{obs} = 11.7(1) mM s^{-1} and 13.9(3) mM s^{-1}, respectively).

This may be due to a change in the speciation of the catalyst during the reaction. The polymer formed with catalyst **9** was a white powder, M_n = 35,400 g mol^{-1}, and Đ = 1.4. The polymer formed with catalyst **9** is of lower molecular weight than that formed with catalysts **7** and **8**, but this would be expected based on the relationship discussed in Chapter 4 that under standard conditions k_{obs} has an effect on M_n.

Surprisingly, the *iso*-propyl derivative (**9**) was the least active catalyst. It is well reported in the literature for related PCP systems (PCP = κ^3-C_6H_3-2,6-$(CH_2PR_2)_2$, R = ^{i}Pr, ^{t}Bu, and Ad), that the isopropyl derivative of the catalyst is the most active for transfer and acceptorless dehydrogenation of alkenes,[7] presumably, due to it being the least sterically hindered.[7] For the same reaction, the adamantyl PCP catalyst was found to be the least active with the smallest number of turnovers reported after 1 hour, although at long reaction times of 96 hours the turnovers were greater for the adamantyl derivative than the others.[8] The authors attributed this to the adamantyl complex being more stable than the *tert*-butyl and *iso*-propyl catalysts due the bulkiness of the adamantyl group.[8]

The steric demands of each of the catalysts can be seen in their space fill models in Figure 5.7 A. In the adamantyl complex **8** the iridium centre is the least exposed due to the bulky adamantyl groups, the *tert*-butyl derivative (**7**) is more exposed than complex **8**, while the *iso*-propyl derivative (**9**) has the most exposed iridium centre. This relationship is also observed in the calculated buried volume of the ligand (%V_{Bur}), calculated using SambVca 2.1.[9] The adamantyl derivative complex **8** has the largest %V_{Bur} = 64.3%, then the *tert*-butyl derivative (**7**) %V_{Bur} = 61.7%, and the *iso*-propyl complex **9** has the smallest %V_{Bur} = 53.9%. %V_{Bur} calculations are often used to compare NHC or phosphine ligands, by calculating the percentage volume of a sphere which is occupied by a ligand, where the centre of the sphere is the metal centre (Ir in this case).[10] The buried volumes of the adamantyl and *tert*-butyl complexes are similar which may explain why the complexes have similar rates of reaction. The *iso*-propyl derivative has the smallest buried volume, and the rate of reaction

was considerably lower than the adamantyl and *tert*-butyl complexes. This does not explain why the reactivity of the catalysts with amine-borane gives a different correlation to the rate of reaction compared to similar reactions with alkanes.[7, 8]

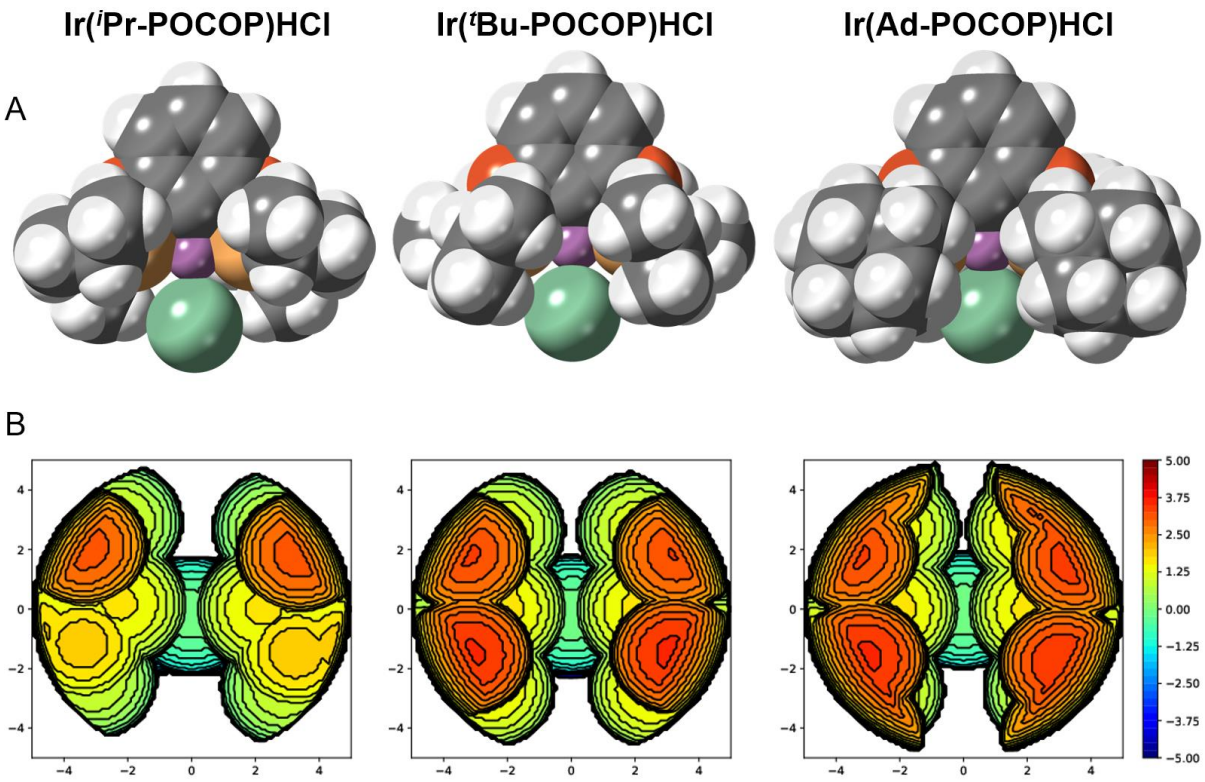

Figure 5.7. A) Space fill diagrams of catalysts **7**, **8** and **9** B) The percentage buried volume maps of catalysts **7**, **8** and **9** looking down the Ir–Cl bond.

Analysis by NMR spectroscopy showed that the speciation of the catalyst at the end of the reaction was different for each catalyst. The ^{1}H and ^{31}P{^{1}H} NMR spectra taken at the end of catalysis of the *tert*-butyl derivative complex **7** showed similar speciation to what has been observed with catalyst **1** (discussed in section 2.3). A broad singlet is observed at δ –8.26 in the ^{1}H NMR spectrum (Figure 5.8 A), assigned to Ir(^{t}Bu-POCOP)(H)$_4$ (**3**). In the ^{31}P{^{1}H} NMR spectrum two singlets are observed (Figure 5.8 B). One at δ 183 is assigned to the tetrahydride complex **3**, the other singlet at δ 170 may be assigned to Ir(^{t}Bu-POCOP)(H)$_2$(BH$_3$) (**2**), however there is no further evidence in the ^{1}H NMR spectrum to support this assignment, as it may be below the limit of detection.

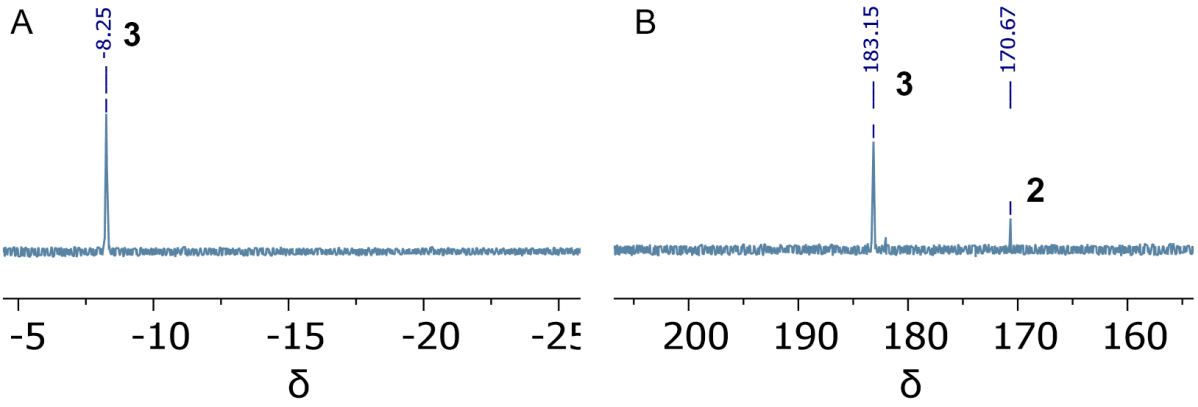

Figure 5.8. NMR spectra of the reaction mixture taken at the end of catalysis for the reaction of Ir(*t*Bu-POCOP)HCl (**7**) and $H_3B{\cdot}NH_2Me$. A) ^1H NMR spectrum (600 MHz, THF-H^8, 298 K), B) $^{31}P\{^1H\}$ NMR spectrum, (243 MHz, THF-H^8, 298 K).

The $^{31}P\{^1H\}$ NMR spectrum taken after catalysis for the dehydropolymerisation of $H_3B{\cdot}NH_2Me$ with Ir(*i*Pr-POCOP)HCl (**9**) showed two sets of signals (Figure 5.9), a singlet at δ 166 and a singlet at δ 173. The major resonance at δ 173 was identified as Ir(*i*Pr-POCOP)$(H)_2(BH_3)$ by the independent addition of $NaBH_4$ to complex **9** and analysis by NMR spectroscopy. The identity of the minor iridium species relating to the ^1H NMR δ –8.77 and $^{31}P\{^1H\}$ NMR δ 173 resonances is proposed to be Ir(*i*Pr-POCOP)$(H)_2(NH_2Me)$, as the shifts are similar to those established for complex **4** (Ir(*t*Bu-POCOP)$(H)_2(NH_2Me)$)**,** and do not match those previously reported for Ir(*i*Pr-POCOP)$(H)_4$ ^1H δ –11.0 and $^{31}P\{^1H\}$ δ 173.[4]

This may indicate that the equilibrium between the dihydride and the amine complex established for the *tert*-butyl derivative in section 2.7.1 may favour the dihydride-amine complex for the *iso*-propyl derivative. This equilibrium may have taken catalyst off-cycle and may be the cause of the slower rate of reaction when compared to complex **7** and **8**.

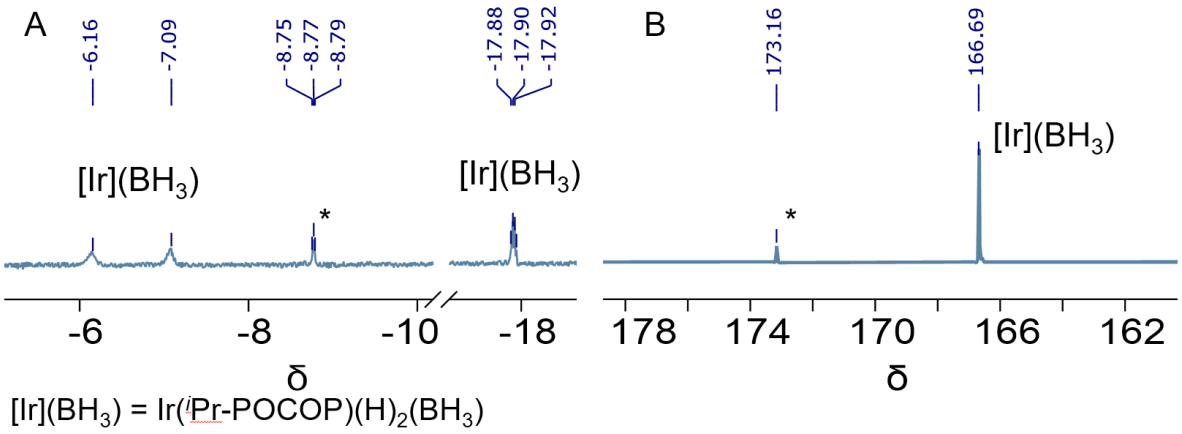

Figure 5.9. NMR spectra of the reaction mixture taken at the end of catalysis for the reaction of Ir(*i*Pr-POCOP)HCl (**9**) and $H_3B{\cdot}NH_2Me$. A) ^{1}H NMR spectrum (600 MHz, THF-H^8, 298 K), B) $^{31}P\{^{1}H\}$ NMR spectrum, (243 MHz, THF-H^8, 298 K).

The most complex speciation was observed by NMR spectroscopy at the end of catalysis from the reaction of $H_3B{\cdot}NH_2Me$ and Ir(Ad-POCOP)HCl (**8**). There are four singlets in the $^{31}P\{^{1}H\}$ NMR spectrum, δ 198, 187, 171, 167. The peak at δ 167 was identified as a borohydride complex Ir(Ad-POCOP)$(H)_2(BH_3)$ by analysis of an independent NMR-scale reaction of complex **8** and $NaBH_4$. The hydrides for Ir(Ad-POCOP)$(H)_2(BH_3)$ are not observed in the ^{1}H NMR spectrum of the catalysis mixture as they are below the limit of detection. The two signals in the $^{31}P\{^{1}H\}$ NMR spectrum at δ 198 and 187 are broad and likely undergoing an exchange process. These are proposed to be Ir(Ad-POCOP)$(H)_2$ and Ir(Ad-POCOP)$(H)_4$, respectively, supported by the similarity in chemical shifts to the *tert*-butyl dihydride catalyst **1** and tetrahydride catalyst **3**. In addition, there are two broad singlet resonances in the ^{1}H NMR spectrum at δ –8.53 and –17.70, for the tetrahydride and dihydride, respectively. The final hydride, a triplet at δ –8.02 ($J \sim 16$ Hz) with a $^{31}P\{^{1}H\}$ resonance at δ 170 is proposed to be Ir(Ad-POCOP)$(H)_2(NH_2Me)$, as the chemical shifts and the coupling constant observed are similar to that recorded for complex **4**.

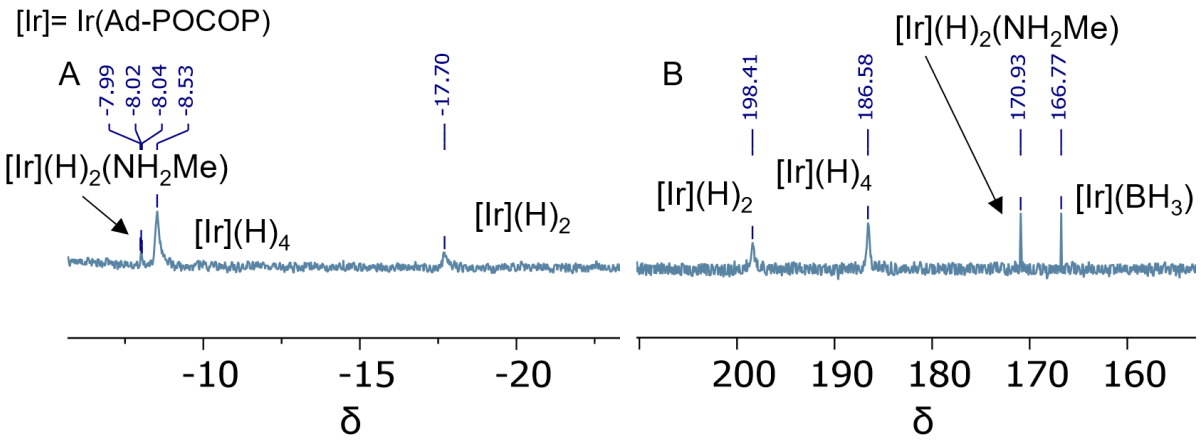

Figure 5.10. NMR spectra of the reaction mixture taken at the end of catalysis for the reaction of Ir(Ad-POCOP)HCl (**8**) and $H_3B{\cdot}NH_2Me$. A) ^{1}H NMR spectrum (600 MHz, THF-H^8, 298 K), B) $^{31}P\{^{1}H\}$ NMR spectrum, (243 MHz, THF-H^8, 298 K).

It is clear from the rates of reaction measured for catalysts **7**, **8**, and **9**, that changing the R-group on the phosphine of the pincer ligand has an effect on catalysis. The changes in speciation observed at the end of catalysis may show that the changing of the R-group effects some of the complex equilibria that have been discussed in the previous chapters. For example, Ir(^{i}Pr-POCOP)HCl (**9**) was the slowest of the catalysts, and was also the reaction that had the largest proportion of borohydride complex remaining at the end of catalysis (92% by NMR spectroscopy). This may explain the much lower rate as the equilibrium between the σ-complex and borohydride complex may favour the latter and so the catalyst is mostly sat in its dormant form, meaning there is less active catalyst available for catalysis resulting in a lower rate of reaction. The direction of this equilibrium may relate back to the steric properties and the bulk volume calculations: there simply may be more space for the 'BH_3' to bind, and so it binds more strongly.

5.3 Summary and conclusions

This chapter presented the synthesis and characterisation of the novel iridium POCOP complex Ir(Ad-POCOP)HCl. The kinetics and speciation were discussed and compared for Ir(^{t}Bu-POCOP)HCl (**7**), Ir(Ad-POCOP)HCl (**8**) and Ir(^{i}Pr-POCOP)HCl (**9**), to identify if changing the R-group on the phosphine of the pincer ligand could be used as another way to control the molecular weight of polymer. It was found that the *tert*-butyl and adamantyl complexes behaved very similarly, resulting in comparable rates and M_n of the polymer formed, which can be explained by their similar structure and steric demands, as shown by bulk volume calculations.

This chapter has contributed two new competent catalysts for amine-borane dehydropolymerisation. Ir(Ad-POCOP)HCl (**8**) can be used as an alternate catalyst to Ir(^{t}Bu-POCOP)HCl, although this is unlikely to be the case as (**7**) is commercially available. The use of Ir(^{i}Pr-POCOP)HCl (**9**) as a catalyst in the dehydropolymerisation of amine-boranes was identified as a way to obtain polymer of a low molecular weight (M_n ~35,000 g mol^{-1}) using the standard conditions described in Chapter 2. However, the multi-step synthesis makes use of **9** as a catalyst to achieve low molecular weight polyaminoborane unlikely, as alternate approaches such as higher temperatures can achieve a similar effect with catalysts **1** or commercially available **7**. Therefore, no further work was carried out to understand the changes in mechanism that may be occurring with these catalysts.

An alternate approach that may yield more interesting results is changing the transition metal in place of changing than the ligands steric demands. This has previously resulted in mechanistic pathways as was shown with the ^{i}Pr-PN^{H}P ligand with Ru, Fe, Co, Rh and Ir (see Chapter 1).[11-15]

5.4 References

1. I. Göttker-Schnetmann, P. White and M. Brookhart, *J. Am. Chem. Soc.*, 2004, **126**, 1804–1811.
2. B. Vabre, D. M. Spasyuk and D. Zargarian, *Organometallics*, 2012, **31**, 8561–8570.
3. A. Arunachalampillai, D. Olsson and O. F. Wendt, *Dalton Trans.*, 2009, 8626–8630.
4. D. Morales-Morales, R. Redón, C. Yung and C. M. Jensen, *Inorg. Chim. Acta*, 2004, **357**, 2953–2956.
5. N. T. Mucha and R. Waterman, *Organometallics*, 2015, **34**, 3865–3872.
6. L. P. Press, A. J. Kosanovich, B. J. McCulloch and O. V. Ozerov, *J. Am. Chem. Soc.*, 2016, **138**, 9487–9497.
7. F. Liu and A. S. Goldman, *Chem. Commun.*, 1999, 655–656.
8. B. Punji, T. J. Emge and A. S. Goldman, *Organometallics*, 2010, **29**, 2702–2709.
9. L. Falivene, Z. Cao, A. Petta, L. Serra, A. Poater, R. Oliva, V. Scarano and L. Cavallo, *Nat. Chem.*, 2019, **11**, 872–879.
10. L. Falivene, R. Credendino, A. Poater, A. Petta, L. Serra, R. Oliva, V. Scarano and L. Cavallo, *Organometallics*, 2016, **35**, 2286–2293.
11. C. N. Brodie, T. M. Boyd, L. Sotorríos, D. E. Ryan, E. Magee, S. Huband, J. S. Town, G. C. Lloyd-Jones, D. M. Haddleton, S. A. Macgregor and A. S. Weller, *J. Am. Chem. Soc.*, 2021, **143**, 21010–21023.
12. C. N. Brodie, L. Sotorrios, T. M. Boyd, S. A. Macgregor and A. S. Weller, *ACS Catal.*, 2022, **12**, 13050–13064.
13. T. M. Boyd, K. A. Andrea, K. Baston, A. Johnson, D. E. Ryan and A. S. Weller, *Chem. Commun.*, 2020, **56**, 482–485.
14. A. Glüer, M. Förster, V. R. Celinski, J. Schmedt auf der Günne, M. C. Holthausen and S. Schneider, *ACS Catal.*, 2015, **5**, 7214–7217.
15. M. Käß, A. Friedrich, M. Drees and S. Schneider, *Angew. Chem. Int. Ed.*, 2009, **48**, 905–907.

Chapter 6: Conclusions and Future Directions

6.1 Conclusions

This thesis presents the in-depth study of the dehydropolymerisation of $H_3B{\cdot}NH_2Me$ with Ir(POCOP) catalysts. The main focus of this thesis has been a mechanistic study on previously reported catalyst Ir(^{t}Bu-POCOP)$(H)_2$ (**1**). The catalyst had been reported for the dehydropolymerisation of amine-boranes but with limited details of the dehydrogenation mechanism.[1-4]

The combination of the speciation studies by flow NMR spectroscopy (Chapter 2) and analysis of the kinetic data (Chapter 3) have allowed for the proposal of two mechanisms that each fit the experimental data. One is an inner-sphere mechanism similar to that proposed by Paul and Musgrave,[5] the other is a proton rebound mechanism that involves an anionic iridium trihydride species. DFT calculations were used to investigate these mechanisms further, providing an energy span for both mechanisms in agreement with the experimentally determined values (Eyring), 16.1 kcal mol^{-1} and 16(2) kcal mol^{-1}, respectively and identifying both as plausible mechanisms. The rate-determining step in both was determined to be the reductive coupling of the tetrahydride complex **3** to a di-hydrogen dihydride complex **3'** prior to H_2 loss. This was also in agreement with the experimentally determined negative value for $\Delta S^{\ddagger}$ (–17(2) cal K^{-1} mol^{-1}), indicative of an associative mechanism towards the transition state. Kinetic modelling of the mechanisms using COPASI showed agreement between the experimental and the simulated data for both mechanisms, across eight holistically modelled data sets. Use of the models to simulate the speciation data for the reaction allowed for the B–H/N–H activation pathway (Mechanism A) to be determined as the more likely scenario.

Previously reported catalytically relevant intermediates, borohydride complex **2** and tetrahydride complex **3** were found to be competent pre-catalysts for the dehydrogenation of $H_3B{\cdot}NH_2Me$, albeit with a long induction period (~55 minutes) for the former. This is in contrast to what had been reported previously in the literature that found borohydride complex **2** to

show negligible catalytic activity.[1, 2] The identity of the pre-catalysts combined with the speciation data from the flow NMR spectroscopy revealed complex **2** as the predominant species present during the induction period with little to no monomer consumption during this time, and tetrahydride complex **3** as the resting state of the catalyst. To our knowledge this study is the first time that the speciation of an amine-borane dehydropolymerisation reaction has been studied in flow conditions, allowing for the conversion of the amine-borane monomer to be mapped onto the speciation data.

The observation of dihydride amine complex **4** during catalysis led to the independent synthesis and characterisation of the complex, as well as an investigation of the complex role of NH_2Me during catalysis. The role of NH_2Me during amine-borane dehydropolymerisation remains elusive with a number of proposed roles discussed in Chapter 3. Further work would be required to truly understand the role of this additive as it likely performs multiple roles in catalysis. The synthesis, characterisation and kinetic study of a novel anionic trihydride complex **[Na-18-crown-6][6]** was also reported as it was considered potentially to be a relevant catalytic intermediate (Chapter 3).

Chapter 4 presented different reaction conditions that could be used to control the molecular weight of polyaminoborane formed, with an unprecedented degree of control achieved with a single catalyst system leading to values of M_n ranging between 57,300-185,200 g mol^{-1}, achieved by varying reaction conditions. Prior to this the molecular weights of polyaminoborane with catalyst **1** varied widely from run-to-run under the same reaction conditions.[3, 4] The understanding gained from the experiments with varied reaction conditions allowed for optimisation of the reaction at scale and for catalyst loadings of 0.001 mol% to be deployed, reducing the amount of catalyst required for these large-scale reactions. This is important as it will assist with translation into an industrial setting, where cost and environmental impact are important.

A brief look at the applications of polyaminoboranes was addressed in Chapter 4, with discussion of the synthesis of boron nitride fibres using an easily accessible and air-stable precursor. Such fibres are industrially important as an inorganic analogue of carbon fibre but with superior chemical and thermal stability.[6] This study has provided an novel route to BN fibres using an easily accessible and air-stable precursor, namely polyaminoboranes. Building on this work, it was shown that a similar approach can be used to make boron nitride materials with residual iridium content and a proof-of-concept study used this iridium-doped material to hydrogenate propene in a heterogeneous reaction, opening a new avenue of investigation into these materials.

Finally, other variants of the iridium POCOP catalyst were prepared with varying R-groups on the phosphine, to determine if the steric demand of the R-group had an effect on catalysis and on the molecular weight of the polymer formed (Chapter 5). The adamantyl derivative was found to behave similarly to the *tert*-butyl derivative, in terms of rate and molecular weights. Meanwhile, the *iso*-propyl derivative resulted in shorter induction periods, lower rates of reaction and short polymer formed. This was rationalised in terms of the established kinetics and speciation observed with catalyst **1**, and how the steric demands of the R-group may affect equilibria within the catalytic cycle but also with off-cycle complexes. This chapter reported two new competent catalysts for the dehydropolymerisation of amine-boranes. However, there was no clear benefit to using these catalysts over the commercially available Ir(^{t}Bu-POCOP)HCl or Ir(^{t}Bu-POCOP)$(H)_2$.

In conclusion, the use of [Ir(^{t}Bu-POCOP)$(H)_2$] to catalyse the dehydropolymerisation of $H_3B{\cdot}NH_2Me$ remains a robust and simple system that selectively forms polyaminoborane with an unprecedented molecular weight range. This control of molecular weight and the scale up of the reaction to 20 g has allowed for initial investigation into the materials properties (*i.e.* BN ceramics).

6.2 Future Directions

6.2.1 Extension of range of molecular weights of polyaminoborane

In Chapter 3 the effect of Na^+ as an additive alongside catalyst **1** was discussed. The resulting molecular weight of polyaminoborane obtained from the reactions increased with the addition of [Na(18-crown-6)][BAr^F_4]. The reaction of **[Na-18-crown-6][6]** with $H_3B{\cdot}NH_2Me$ with one equivalent of [NH_3Me][BAr^F_4] resulted in the highest molecular weight observed with this catalyst under the standard conditions employed in this thesis (conditions: 0.1 mol% (2 mM [Ir]), 2 M $H_3B{\cdot}NH_2Me$, THF, 293 K).

While the promoting effects of alkali metals (Na^+ and K^+) and crown ethers in reactions catalysed by transition metals has been discussed in the literature,[7-10] their possible role has not been considered for amine-borane dehydropolymerisation. Understanding the role of the metal/crown addition with this catalyst system and probing its use with other known systems may provide a useful tool to further control the molecular weight of polyaminoborane. This matters as the synthesis of very high molecular weight polyaminoborane may unlock new materials properties and applications.

6.2.2 Optimisation and development of Ir@*h*-BN

Chapter 4 presented the synthesis and chatacterisation of polymer derived Ir@*h*-BN. The iridium from the catalyst used to synthesise the polyaminoborane was entrained within the polymer and remained through both curing and ammonolysis to form the Ir@*h*-BN. Initial experiments provided a proof-of-concept study showing that the material could be used to catalyse the hydrogenation of propene. With the precursor to Ir@*h*-BN being a polymer, the material can be spin coated to form thin films (Figure 6.1). However, this could not be further explored due to time constraints. Further work would be required to optimise this process, *e.g.* higher initial catalyst loadings of iridium to increase number of iridium nanoparticles in the final material. There would also be scope to investigate other reactions the material could be used to catalyse.

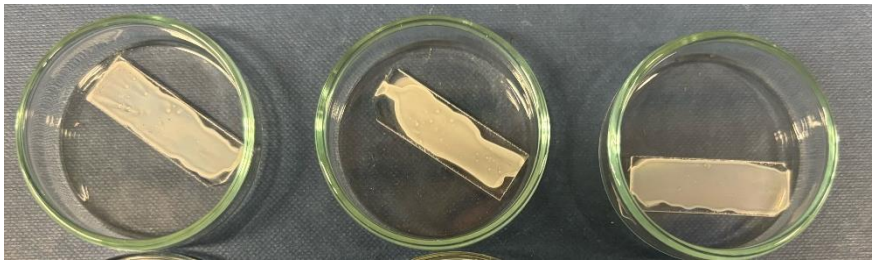

Figure 6.1. Samples of polyaminoborane that had been spin coated onto glass plates. Polyaminoborane was dissolved in THF (20 % w/w) to form the spin coating solution. The spin coating ramp programme that formed the most even thin film (right) was: 1000 rpm for 10 s with ramp up to 4000 rpm for 90 s.

6.2.3 Synthesis of polyaminoborane in flow

Moving the reaction from batch to flow would be an interesting avenue for future research with the benefits that come from a continuous process (*i.e*. control over reaction conditions, faster and more efficient production). This catalytic system would require optimisation to be used in flow. For example, reactions that have induction periods are not suitable for flow condition and modifications would be required to remove the induction period (*e.g.* addition of $[NH_3Me]Cl$ as discussed in Chapter 3 and 4). Likewise, the solubility of all reagents would need to be taken into account, meaning the reactions would have to be carried out at a lower concentration (*e.g.* 0.5 M instead of 2 M). Immobilisation of the catalyst may also be beneficial and presents another avenue of research; for example, there are literature reports of Ir(POCOP) catalysts being immobilised and used in the dehydrogenation of alkanes.[11] However, careful consideration would be required to apply this to amine-borane dehydropolymerisation as the supported catalyst would require compatibility with the reducing conditions caused by the substrate.

6.3 References

1. M. C. Denney, V. Pons, T. J. Hebden, D. M. Heinekey and K. I. Goldberg, *J. Am. Chem. Soc.*, 2006, **128**, 12048–12049.
2. B. L. Dietrich, K. I. Goldberg, D. M. Heinekey, T. Autrey and J. C. Linehan, *Inorg. Chem.*, 2008, **47**, 8583–8585.
3. A. Staubitz, M. E. Sloan, A. P. M. Robertson, A. Friedrich, S. Schneider, P. J. Gates, J. S. A. D. Günne and I. Manners, *J. Am. Chem. Soc.*, 2010, **132**, 13332–13345.
4. A. Staubitz, A. Presa Soto and I. Manners, *Angew. Chem. Int. Ed.*, 2008, **47**, 6212–6215.
5. A. Paul and C. B. Musgrave, *Angew. Chem. Int. Ed.*, 2007, **46**, 8153–8156.
6. P. Colombo, G. Mera, R. Riedel and G. D. Sorarù, *J. Am. Ceram. Soc.*, 2010, **93**, 1805–1837.
7. Y. Gao, C. Guan, M. Zhou, A. Kumar, T. J. Emge, A. M. Wright, K. I. Goldberg, K. Krogh-Jespersen and A. S. Goldman, *J. Am. Chem. Soc.*, 2017, **139**, 6338–6350.
8. S. Acosta-Calle and A. J. M. Miller, *Acc. Chem. Res.*, 2023, **56**, 971–981.
9. F. Fiorentini, W. T. Diment, A. C. Deacy, R. W. F. Kerr, S. Faulkner and C. K. Williams, *Nat. Commun.*, 2023, **14**, 4783.
10. Y. Ma and A. A. Hussein, *Phys. Chem. Chem. Phys.*, 2023, **25**, 3110–3120.
11. B. Sheludko, M. T. Cunningham, A. S. Goldman and F. E. Celik, *ACS Catal.*, 2018, **8**, 7828–7841.

Chapter 7 Experimental Methods

7.1 General Considerations

Unless otherwise stated all experiments were carried out under argon atmosphere using standard glovebox and Schlenk techniques. Glassware and cannulas were dried overnight at 140 °C. SPS THF, pentane and toluene were dried using a Grubbs' solvent purification system[1] and degassed by 3 freeze-pump-thaw cycles. THF (pretreated over AlO_3 then 3 Å molecular sieves) was distilled over sodium/benzophenone and degassed by 3 freeze-pump-thaw cycles. All solvents were stored over 3 Å molecular sieves. [Ir(^{t}Bu-POCOP)H_2] (**1**) (^{t}Bu-POCOP = k^3-2,6-(^{t}Bu$_2$PO)$_2$C$_6$H$_3$),[2, 3] [Ir(^{t}Bu-POCOP)H_4] (**2**),[3] [Ir(^{t}Bu-POCOP)(H)$_2$(BH_3)] (**3**)[4], Na[Ir(^{t}Bu-POCOP)H_3] [3], [Ir(^{t}Bu-POCOP)HCl)] (**7**),[2] and [Ir(^{i}Pr-POCOP)HCl] (**9**)[5] were prepared by literature methods. Commercially sourced $H_3B{\cdot}NH_2Me$ was recrystallised from minimum amount of OEt_2 at −20 °C and filtered prior to use and stored at −40 °C. All other reagents were obtained from commercial sources and used without further purification unless stated.

NMR spectra were collected using a Bruker Advance III 600 MHz spectrometer or Bruker Avance III 500 MHz spectrometer at 298 K unless otherwise stated. Chemical shifts are expressed in ppm, with coupling expressed in Hz. ^{1}H NMR spectra were referenced to residual protio solvent peaks. ^{31}P{^{1}H} NMR spectra were externally referenced to 85% H_3PO_4 in H_2O and ^{11}B NMR spectra were referenced to 15% BF_3OEt_2 in $CDCl_3$. ^{11}B NMR spectra were corrected for the boron content in the borosilicate glass NMR tubes by subtraction of a blank (recorded of an empty NMR tube). ^{11}B magic angle spinning − nuclear magnetic resonance (^{11}BMAS-NMR) measurements were carried out using a Varian VNMRS spectrometer (128.39 MHz and 4 mm (rotor o.d.) probe). Spectra were acquired at a spin rate of 12 kHz. Boron spectral referencing is relative to $BF_3{\cdot}OEt_2$.

All polymeric materials were analysed by **GPC** (Gel Permeation Chromatography) measured on a Malvern Viskotec GPC_{max} together with a Viskotec TDA 305 RI detector. Polymer M_n is referenced to polystyrene standards between M_n 474-476,500 g mol^{-1}. All samples were

passed through 3 columns consisting of a porous styrene divinylbenzene copolymer (column set: 2 × T5000 and 1 × T4000 Malvern columns). The eluent used was GPC grade THF containing $[NBu_4]Br$ (2.7 mmol dm^{-3}) and the flow rate was 1 cm^3 min^{-1}. All polymer samples were dissolved in GPC grade THF $[NBu_4]Br$ (2 g cm^{-3}) and filtered through a PTFE filter (pore size: 45 μm) prior to analysis.

The **IR** spectra were collected on a Bruker ALPHA FT-IR spectrometer.

ESI-MS was carried out in the absence of air on a Bruker Compact Time of Flight Mass spectrometer that was connected to a glovebox.

P-XRD was carried out on a Panalytical Aeris X-ray diffractometer.

STEM images were collected by Dr Leonardo Lari on an JEOL 200F NeoARM AC-STEM at the University of York Nanocentre.

ICP-OES analysis was carried out by Niall Donaldson on an Agilent ICP-OES 5800 VDV spectrometer. Plasma flow 12.0 L/min, RF power 1.20 kW, auxilliary flow 1.00 L/min, axial viewing mode. Working standards (0.01 - 10 ppm Ir) were prepared from commercial reference standard CCS-2 (100 ppm Ir) supplied by Inorganic Ventures, traceable to NIST certified reference materials. Analysis was completed at 224.268 nm with internal standard Y (371.029 nm). All standards were matrix matched to the digestion media.

Karl Fischer titrations were carried out on a Mettler Toledo C20S Coulometric KF Titrator.

DSC was carried out by Dr James Town at the University of Warwick on a TA Instruments DSC2500.

7.2 Catalytic procedures

7.2.1 Typical eudiometric dehydropolymerisation procedure

Eudiometric measurements of hydrogen gas production were performed using an upturned burette filled with water that was displaced as hydrogen gas was produced.

Method A - under standard conditions: $H_3B{\cdot}NH_2Me$ (112mg, 2.5 mmol) was placed in a two-neck jacketed Schlenk flask with temperature maintained by a circulating cooler (20 °C). The catalyst (1.5 mg, 0.1 mol%) was dissolved in a known volume of THF (1.25 mL) separately. The flask was connected to the water filled upturned burette *via* PTFE tubing. The catalyst solution was added to the jacketed flask and the solution stirred at 400 rpm. The volume and time were recorded at 1 cm^3 increments of gas collected, aided by video recording when required. After completion of gas evolution, an *in-situ* NMR sample (0.5 mL) was taken and analysed. Pentane (50 mL) was added, and the solution stirred rapidly to induce polymer precipitation. The off-white solid was isolated by filtration and remaining volatiles were removed *in vacuo*. The polymer was analysed by ^{1}H, $^{31}P\{^{1}H\}$ and ^{11}B NMR spectroscopies and gel permeation chromatography (GPC).

Method B - solid additives: Solid additives (*e.g.* $[NH_3Me]^+$ and Na^+ salts) were added to the two-neck jacketed Schlenk flask alongside the $H_3B{\cdot}NH_2Me$. This method then followed the steps detailed in Method A.

Method C - liquid additives: Method A was followed but with liquid additives (*e.g.* NH_2Me 2 M solution in THF) added to $H_3B{\cdot}NH_2Me$ in the two-neck jacketed Schlenk flask directly after the addition of the catalyst solution by Hamilton syringe.

In the cases where the order in catalyst and substrate were determined Method A was used with varied concentrations of catalyst and $H_3B{\cdot}NH_2Me$, respectively.

7.2.2 Kinetic experimental considerations

The reactions were carried out in THF, as $H_3B{\cdot}NH_2Me$ has good solubility in THF when compared to other commonly used solvents such as 1,2-$F_2C_6H_4$ or toluene.[6, 7] The [Ir] was chosen (2 mM, 0.1 mol%) due to it being of sufficient concentration to observe hydride signals in the ^{1}H NMR spectrum. The reactions were carried out at 2 M [$H_3B{\cdot}NH_2Me$] to remain consistent with the conditions used by Manners.[8, 9] In this thesis the following will be referred to as standard conditions: THF, 20 °C, 2 M [$H_3B{\cdot}NH_2Me$], 0.1 mol% [Ir] (2 mM). The iridium catalyst was added to the substrate as a THF solution to avoid unwanted interactions between the catalyst and the substrate in the solid state. The iridium/THF solution was made individually for each run rather than as a stock-solution due to degradation of the iridium catalyst over time in THF, as observed by NMR spectroscopies. The $H_3B{\cdot}NH_2Me$ was recrystallised from dry OEt_2 at −20 °C prior to use and dried *in vacuo* (10^{-3} mbar), to remove any impurities. Recrystalised $H_3B{\cdot}NH_2Me$ was used for all experiments unless otherwise stated. In the case where NH_2Me was added to experiments, this was added as a 2 M solution in THF after addition of the catalyst solution to the amine-borane.

In order to measure the kinetics of the reaction, the volume of hydrogen gas produced was measured eudiometrically, see Figure 7.1 for experimental set up. The amount of hydrogen produced is proportional to the amount of aminoborane that is formed from the dehydrogenation of amine-borane. This assumption can be made as the only by-product is hydrogen, as long as the reaction goes to completion and is selective. The selectivity of the reaction was determined by ^{11}B NMR spectroscopy upon catalysis completion.

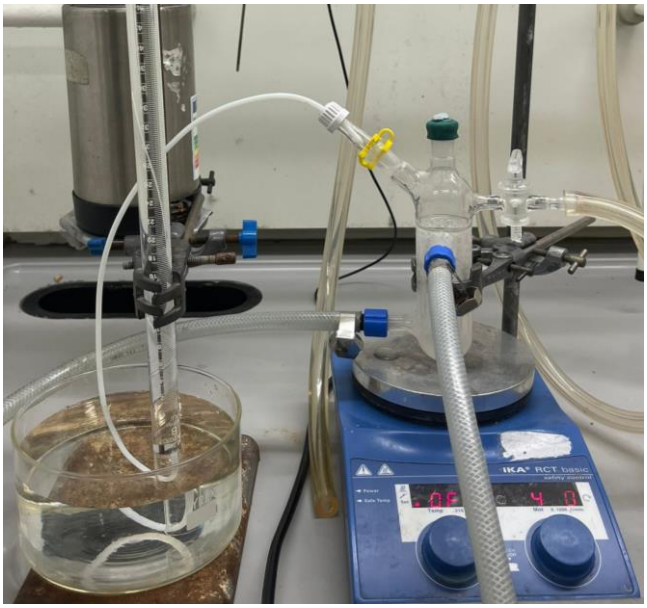

Figure 7.1. Eudiometric setup consisting of a jacketed Schlenk flask, upturned water-filled burette and magnetic stirring plate set at 400 rpm. A recirculating cooler controls the temperature with a 1:1 water:polyethylene glycol mixture.

As mentioned in section 1.3.1 the release of more than one equivalent of hydrogen gas in the dehydropolymerisation reaction can result in the formation of other dehydrocoupled products such as borazine (2 equivalents) and polyborazylene (>2 equivalents). If there is more than one equivalent of hydrogen released but no evidence in the ^{11}B NMR spectrum of formation of these products, then THF evaporation is the probable cause. An independent eudiometric experiment where only THF was left stirring over time resulted in 0.14 equivalents of gas released over 67 minutes, see Figure 7.2. The effect of this is expected to be exacerbated by vigorous effervescence. As a result of this THF evaporation all of the kinetic plots are presented in equivalents of hydrogen evolved rather than [aminoborane]. Due to the THF evaporation the [aminoborane] would be higher than the [amine-borane] starting material. Therefore, graphs of equivalents of hydrogen evolved against time are presented to show the kinetic profile and the relationships between different conditions. In all cases the raw data was presented without normalisation of the data. Graphs of [aminoborane] against time were used to determine the rate of reaction from the pseudo-zero order regime of the linear region of the

kinetic profile. Error for the rates were calculated in Microsoft Excel using the linear regression function (LINEST).

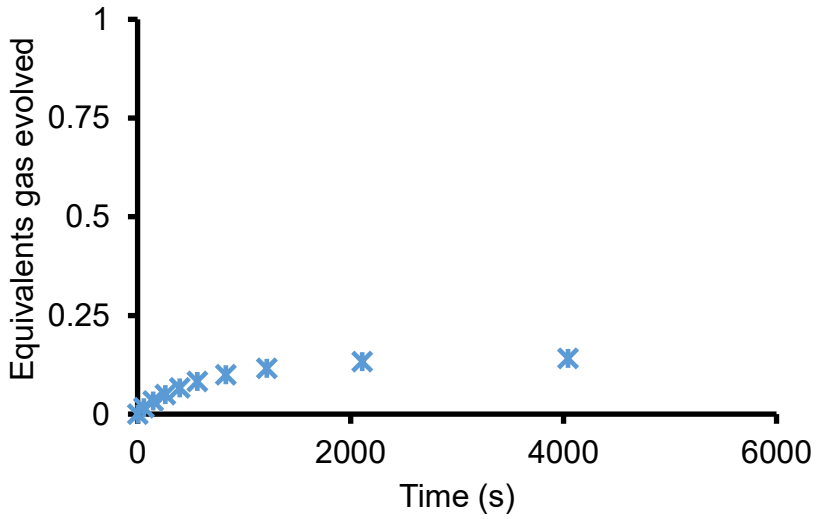

Figure 7.2. Plot showing the 'equivalents' of gas evolved when THF is stirred over time under eudiometric conditions, showing the effect that THF evaporation can have on the apparent equivalents of H_2 produced over the course of a reaction.

Upon completion of catalysis the reaction mixture was analysed by ^{1}H, $^{31}P\{^{1}H\}$ and ^{11}B NMR spectroscopies. ^{1}H and $^{31}P\{^{1}H\}$ NMR spectroscopies provide valuable information into the speciation of the catalyst. The selectivity and the conversion of the reaction was measured from the ^{11}B NMR spectrum.

7.3 Chapter 2 Experimental

7.3.1 General procedure for *in situ* NMR speciation experiments

In a typical experiment, mono-methyl amine-borane ($H_3B{\cdot}NH_2Me$) (112 mg, 2.5 mmol) was placed in a two-neck jacketed Schlenk flask with temperature (283 K) maintained by a circulating cooler. The Ir(^{t}Bu-POCOP)$(H)_2$ (0.1 mol%) was dissolved in a known volume of THF separately. The flask was connected to the water filled burette *via* PTFE tubing. The catalyst solution was added to the jacketed flask and the solution stirred at 400 rpm. The reactions were allowed to run to the desired point and were transferred into NMR tubes that were cooled to −94 °C to thermally quench the reaction and stop hydrogen production. The NMR tubes were then stored in liquid nitrogen until thawed in liquid nitrogen/ethyl acetate and put into a pre-cooled spectrometer at 198 K for analysis by NMR spectroscopies.

In the case of Figure 2.6 in Chapter 2, NMR spectra were recorded at 198 K (Figure 2.6 A), the spectrometry was then warmed to 258 K and reaction progress was monitored by NMR spectroscopy every 5 minutes for 20 minutes (Figure 2.6 B).

CAUTION: H_2 production at room temperature is fast. To limit the risk of explosion, NMR experiments were carried out in high pressure NMR tubes rated up to 12 bar pressure, the taps were fitted with HPLC tubing that was connected to a 5 bar pressure release valve as a safety precaution. The NMR tube, HPLC tubing and pressure release valve were all under argon atmosphere.

7.3.2 Procedure for flow NMR experiments

FlowNMR experiments at the DReaM Facility were carried out with a Bruker AVIIIHD 500 MHz spectrometer equipped with a Prodigy cryoprobe using a modified InsightMR flow tube with a fused silica injection capillary as described earlier.[10] All manipulations were carried out under a dry argon atmosphere using a combination of glovebox and Schlenk techniques, and reactions were carried out with 10 mM [$Cr(tmhd)_3$] added as chemically inert paramagnetic relaxation agent.[11] All spectra were acquired under flow conditions, using InsightMR to acquire ^{1}H, ^{1}H with selective excitation (to just excite the hydride signals), ^{31}P and ^{11}B spectra, either individually or interleaved as appropriate. ^{1}H experiments were typically carried out with WET solvent suppression (both THF resonances suppressed), 8 scans per experiment, a flip angle of 90°, a spectral width of 60 ppm centred at -17 ppm, and a repetition time of 4.1 s. Selective excitation ^{1}H experiments were carried out using a double pulsed field gradient spin echo, typically centred at -15 ppm and with an excitation bandwidth of ~20 ppm, 8 scans per experiment and a repetition time of 3 s. $^{31}P\{^{1}H\}$ experiments were carried out with inverse gated decoupling, 32 scans per experiment, a flip angle of 60°, a spectral width of 400 ppm centred at 200 ppm, and a repetition time of 0.9 s. ^{11}B spectra were carried out with 16 scans per experiment, a flip angle of 90°, a spectral width of 200 ppm centred at 0 ppm, and a repetition time of 2 s. In all cases the flow rate was set to 4 mL/min, with active temperature regulation of the sample, transfer lines and NMR probe to achieve the required reaction temperature. At the start of end of flow reactions, ^{1}H and inverse-gated $^{31}P\{^{1}H\}$ spectra were also acquired under static, fully quantitative conditions (0 mL/min flow, repetition times $>5T_1$) to allow for the determination of flow correction factors for the integrals of the main peaks of interest; these were subsequently applied to the integrals obtained from flow data to ensure accurate quantitation.[12] The flow set-up can be seen in Figure 7.3.

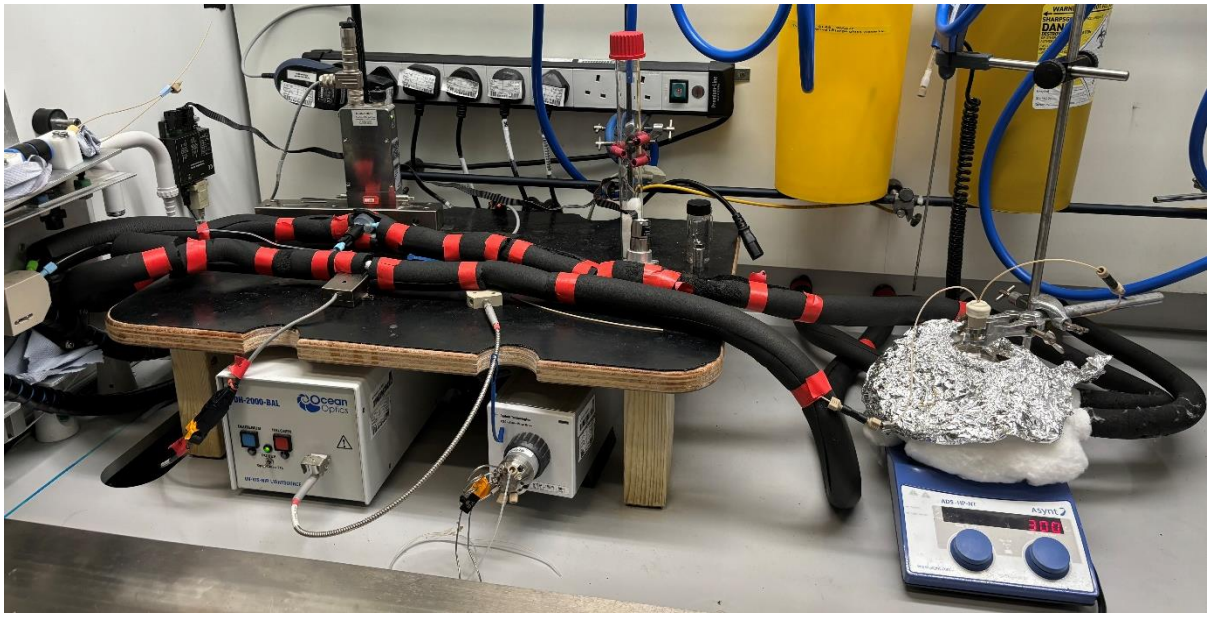

Figure 7.3. The flow set-up at the DReaM Facility, University of Bath.

Ir(ᵗBu-POCOP)$(H)_2$ (4.44 mg, 7.5 μmol), [Cr(tmhd)$_3$] (4.5 mg, 7.5 μmol) and 1,3,5-trimethoxybenzene (2.5 mg, 15 μmol) were dissolved in dry THF (15 mL). This solution was stirred to ensure thorough mixing, then filtered through a syringe filter (0.2 μm) into the reaction vessel. $H_3B{\cdot}NH_2Me$ (336.5 mg, 7.5 mmol) was weighed out separately. The reaction vessel was cooled to −7 °C. The iridium solution was allowed to flow through the system and pre-catalysis spectra taken. The pump was stopped and a portion of the THF solution (~5 mL) was transferred onto the $H_3B{\cdot}NH_2Me$, this was agitated, taken up and filtered through a syringe filter (*0.2 μm)* into the reaction vessel (QUICKLY). The pump was restarted, and data collection was started immediately and continued until bubble formation had stopped and catalysis was complete (^{11}B NMR). Optimised catalysis conditions: 0.5 M $H_3B{\cdot}NH_2Me$, 0.1 mol% catalyst, −7 °C.

Conditions for the study of this reaction were developed over multiple days. The first set of conditions used were 0.5 M $H_3B{\cdot}NH_2Me$, 0.5 mol% catalyst and −7 °C, they were chosen to avoid polymer precipitation in the flow set-up, to give good signal to noise, and to slow the reaction down, respectively. These conditions resulted in the reaction progressing quickly, so that *in-situ* monitoring of the induction period was impossible. Over the next two days the

reaction conditions were optimised to allow for the *in-situ* monitoring of the induction period as well as throughout the duration of catalysis. These conditions were: 0.5 M $H_3B{\cdot}NH_2Me$, 0.1 mol% catalyst, −7 °C. Pre-catalysis spectra were taken prior to all runs, for the first three runs (days 1-2) only **1** Ir(*t*Bu-POCOP)$(H)_2$ was present during these baseline spectra. For runs 4-7 (days 2-4) the presence of **4** Ir(*t*Bu-POCOP)$(H)_2(NH_2Me)$ as well as **1** was persistent in the baseline spectra.

7.3.3 Synthesis of Ir(ᵗBu-POCOP)(H)₂(NH₂Me) – Complex 4

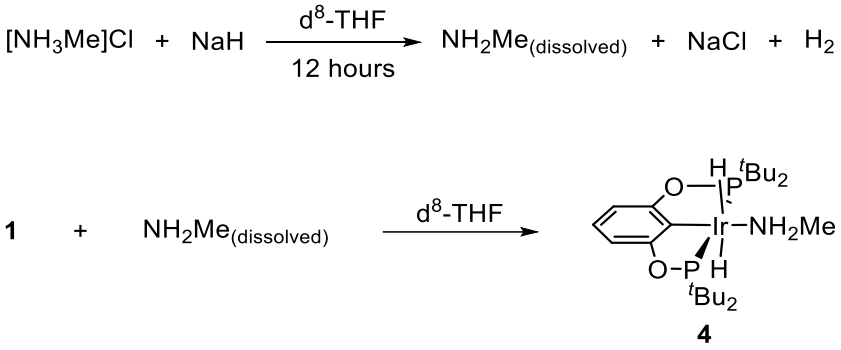

4 can be formed *in-situ* by two methods. The addition of NH_2Me (2 M in THF, 5 equiv.) to **1** (Ir(ᵗBu-POCOP)$(H)_2$) to form a yellow solution or by synthesis of $NH_2Me_{(g)}$ in d^8-THF then vacuum transferring this mixture onto **1**. To form **4** cleanly excess NH_2Me is required as **4** is unstable and is in equilibrium with **1** and 'free' NH_2Me.

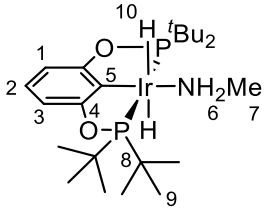

4

A mixture of $[NH_3Me]Cl$ (5.7 mg, 84.5 µmol) and NaH (4 mg, 169 µmol) we dissolved in THF-d^8 in a J-Youngs NMR tube, sonicated for 20 minutes and then inverted for 12 hours with intermittent mixing (until bubbling ceased). The NMR tube was cooled to 77 K and the hydrogen gas removed under vacuum. The THF-d^8 and $NH_2Me_{(g)}$ were vacuum transferred onto solid Ir(ᵗBu-POCOP)$(H)_2$ **1** (5 mg, 8.4 µmol) and the solution thawed and agitated. The colour of the solution was pale yellow and formed **4** cleanly, determined by NMR spectroscopy.

^{1}H NMR (600 MHz; THF-d^8) δ_H: 6.31 (1H, vt, $^3J_{HH}$ = 7.7 Hz, Ar-H2), 6.07 (2H, d, $^3J_{HH}$ = 7.7 Hz, Ar-H1), 3.23 (2H, s (br), N-H_2(6)), 2.88 (3H, t, $^4J_{HP}$ = 6.6 Hz, N-CH_3(7)), 1.42 (36 H, t, $^3J_{HP}$ = 6.6 Hz, ^{t}Bu-H9), −9.19 (2H, t, $^2J_{HP}$ = 16.1 Hz, Ir-H10).

^{31}P{^{1}H} NMR (243 MHz; THF-d^8) δ_P: 170.13.

$^{13}C\{^1H\}$ NMR (151 MHz; THF-d^8) δ_C: 163.6 (t, *J* = 6.6 Hz, C4), 129.2 (s, C5), 120.6 (s, C2), 103.4 (t, *J* = 6.5 Hz, C1/3), 44.38 (s, C7), 40.44 (t, *J* = 12.5 Hz, C8), 29.05 (t, *J* = 3.44 Hz, C9).

A small number of crystals were obtained by removal of THF (flow of argon at RT), then recrystallisation from pentane at −80 °C.

Compositional purity was determined to the detection limit of ^1H NMR spectroscopy. Elemental analysis was not collected for this complex as it is only stable in the presence of excess NH_2Me.

To study the complex using EXSY ^1H NMR spectroscopy a solution of Ir(*t*Bu-POCOP)$(H)_2$ **1** (10 mg, 16.9 μmol) and NH_2Me 2 M in THF (42.2 μL, 84.4 μmol) in THF (0.5 mL) was stirred for 12 hours. Analysis by ^1H and $^{31}P\{^1H\}$ NMR spectroscopies showed complete conversion to **4**. The solvent was removed (flow of argon), and d^8-THF was vacuum transferred onto the yellow residue. Analysis by ^1H and $^{31}P\{^1H\}$ NMR spectroscopies showed a mixture of **4** and **1**.

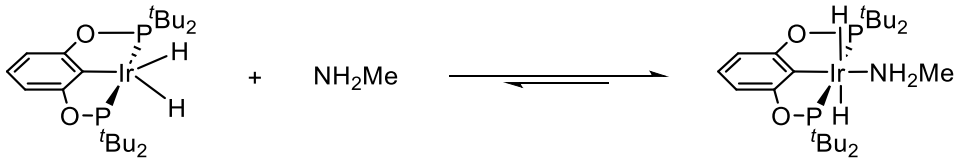

1 **4**

The exchange constant for the forward reaction = 0.33 M^{-1} s^{-1}

The exchange constant for the backward reaction = 0.0666 s^{-1}

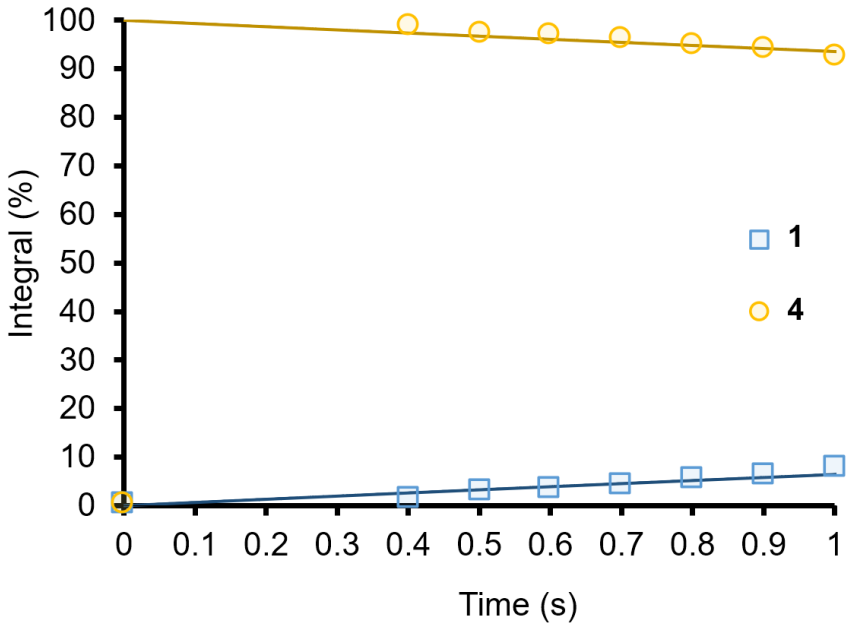

d_8 (s)	∫**1**	∫**4**
0.4	1.4	98.6
0.5	2.8	97.2
0.6	3.3	96.7
0.7	4.1	95.9
0.8	5.2	94.8
0.9	6.1	93.9
1.0	7.7	92.3

Figure 7.4. Plot of ^{1}H NMR integrals of the hydrides of **1** and **4** from the ^{1}H EXSY NMR data at different mixing times (d_8).

7.4 Chapter 3 Experimental

7.4.1 Synthesis of [Na-18-crown-6-(THF)$_2$][Ir(^{t}Bu-POCOP)H$_3$] [Na-18-crown-6][6]

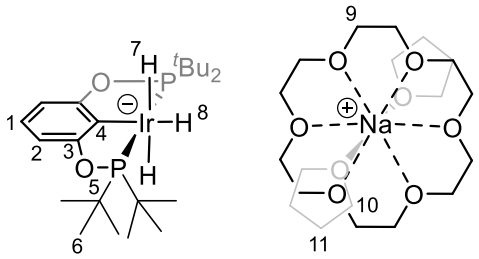

A solution of Ir(^{t}Bu-POCOP)H$_2$ (50 mg, 84.5 µmol), NaH (4 mg, 177 µmol) and 18-crown-6 (46.8 mg, 177 µmol) in THF (3 mL) were stirred at 298 K for 24 hours. The reaction was filtered by cannula filtration and layered with hexane to afford colourless crystals (46 mg, 52.3 mmol, 62 % yield).

^{1}H NMR (600 MHz; THF-d^8) δ_H: 6.16 (1H, t, $^3J_{HH}$ = 7.5 Hz, Ar-H1), 6.03 (2H, d, $^3J_{HH}$ = 7.5 Hz, Ar-H2), 3.61 (5H, m, crown-bound THF (10)), 3.56 (24H, s, C-H$_2$(9)), 1.77 (5H, m, crown-bound THF (11)), 1.33 (36H, t, $^3J_{HP}$ = 6.3 Hz, ^{t}Bu-H6), −11.58 (1H, septet app, $^2J_{HH}$ = 5.5 Hz, Ir-H(8)), −13.22 (2H, td, $^2J_{HP}$ = 16.7 Hz, $^2J_{HH}$ 5.5 Hz, Ir-H7,).

^{31}P{^{1}H} NMR (243 MHz; THF-d^8) δ_P: 192.31.

^{13}C{^{1}H} NMR (151 MHz; THF-d^8) δ_C: 165.0 (t, *J* = 7.5 Hz, C3), 140.0 (s, C4), 117.6 (s, C1), 101.3 (t, *J* = 5.5 Hz, C2), 70.9 (s, C9), 68.4 (s, C10), 39.6 (t, *J* = 11.5 Hz, C5), 30.3 (t, *J* = 3.5 Hz, C6), 26.6 (s, C11).

ESI-MS (−) [M]$^-$ 593.2 m/z (calc. [IrC$_{22}$H$_{42}$O$_2$P$_2$]$^-$ *m/z* 593.23)

Compositional purity was determined to the detection limit of ^{1}H NMR spectroscopy. Elemental analysis was attempted on this complex but due to the air sensitive nature the results were inconclusive.

Crystals suitable for single crystal X-ray diffraction were obtained by recrystallisation from THF/hexane.

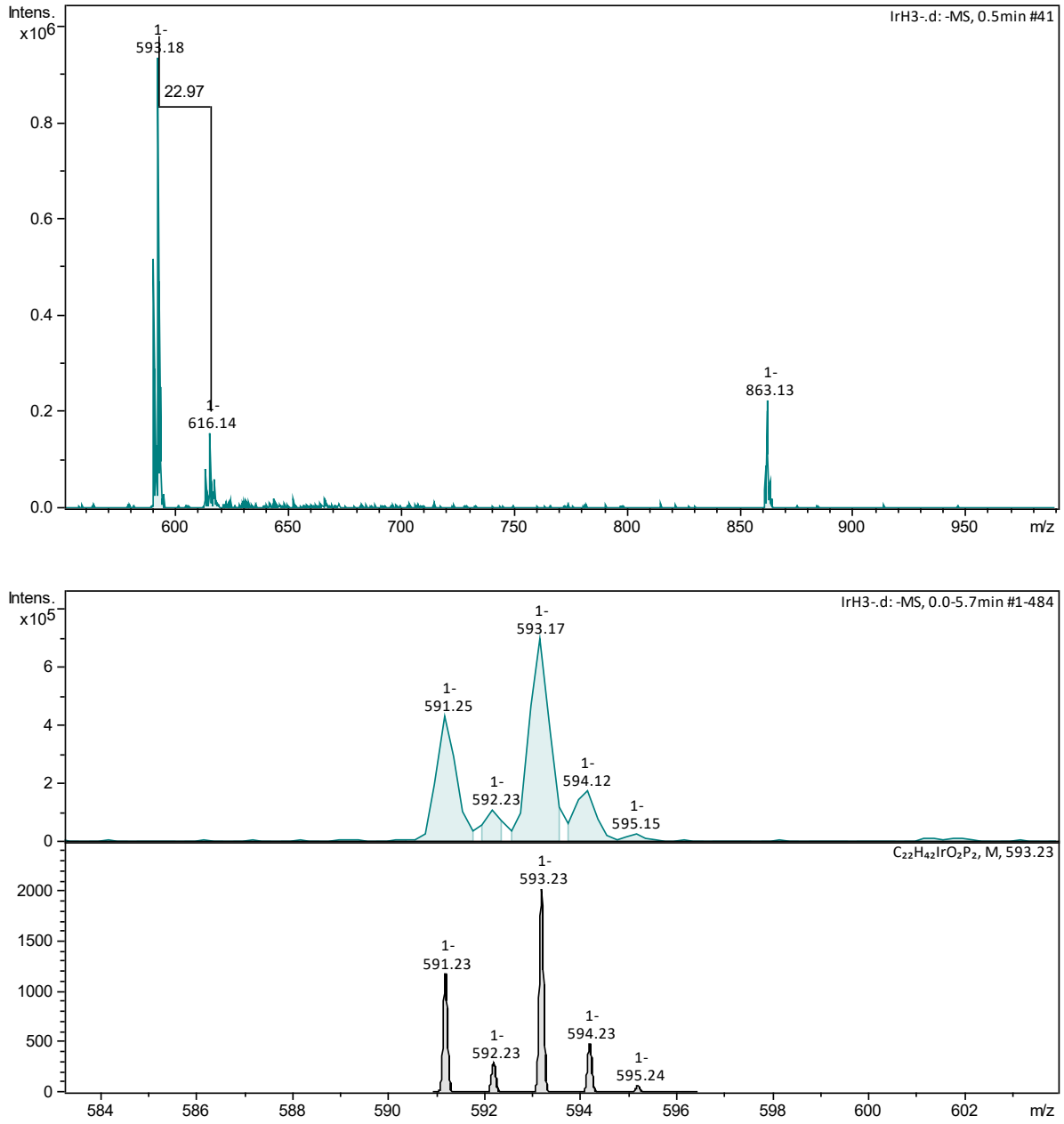

Figure 7.5. TOP: ESI negative mode mass spectrum of [Na-18-crown-6][Ir(^{t}Bu-POCOP)H_3] (**6**) recorded in THF, $[M]^-$ 593.2 m/z $[M+Na]^-$ 616.1 m/z. BOTTOM: shows an expanded view of the observed molecular ion and the simulated isotope pattern showing a good fit. The peak at m/z 863 is a persistent contaminate in the mass spectrometer which we attribute to $[BAr^F{}_4]^-$ (tetrakis[3,5-bis(trifluoromethyl)phenyl]borate).

7.4.2 Effect of [Na(18-crown-6)]$^+$ on [Ir(^{t}Bu-POCOP)H$_3$]$^-$ hydride region

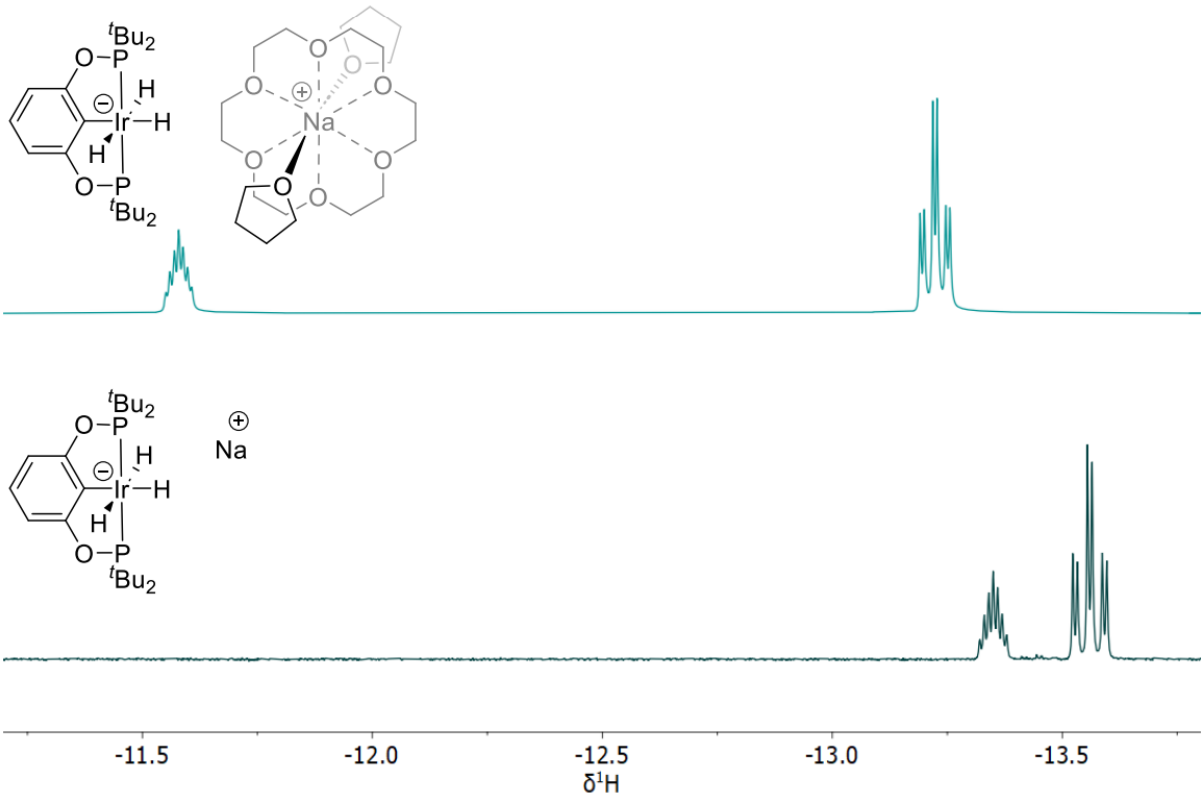

Figure 7.6. Stacked ^{1}H NMR spectra (THF-d^8, 600 MHz, 298 K) (hydride region) showing the downfield shift of [Ir(^{t}Bu-POCOP)H$_3$]$^-$ hydride signals with the [Na(18-crown-6)]$^+$ cation compared with the Na$^+$ cation.

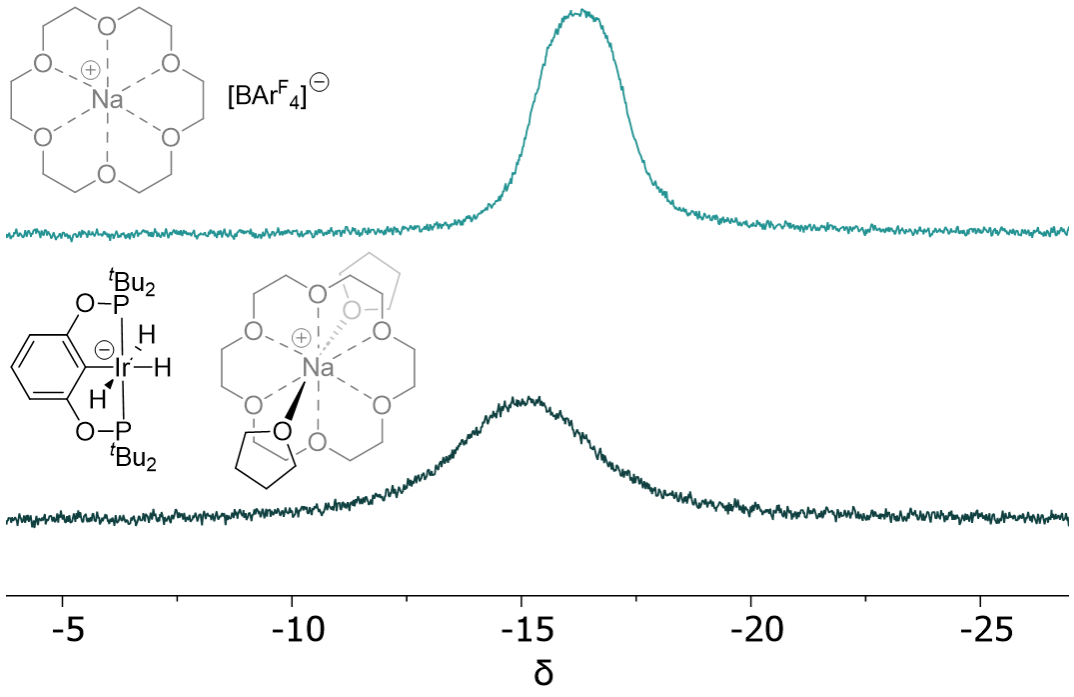

Figure 7.7. ^{23}Na NMR spectra (THF-d^8, 159 MHz, 298 K) of [Na(18-crown-6)(THF)$_2$][Ir(^{t}Bu-POCOP)H$_3$] compared with [Na(18-crown-6)(THF)$_2$][BAr$^F{}_4$].

7.4.3 Computational details.

DFT calculations were run with Gaussian 16 (Revision C.01).[13] Ir and P centers were described with Stuttgart RECPs and associated basis sets,[14] while 6-31G** basis sets[15, 16] were used for all other atoms. An additional set of *d*-orbital polarization functions was added to P (ζ^d=0.387).[17] This basis set is denoted BS1. Structures were optimized using the BP86 functional[18, 19] using BS1 and included the effect of THF solvent through the PCM model.[20] All stationary points were fully characterized *via* analytical frequency calculations as minima (all positive eigenvalues) or transition states (one negative eigenvalue). The final reported free energies are computed considering electronic energies obtained with the def2-TZVP basis set (denoted as BS2),[21, 22] together with the corresponding D3(BJ) dispersion correction.[23-25]

7.5 Chapter 4 Experimental

7.5.1 Scale up procedure

For scale up of reactions on a 1 g scale.:

$H_3B{\cdot}NH_2Me$ (112 mg, 2.5 mmol) and $[NH_3Me]Cl$ (0.1 mg, 1.25 μmol) was dissolved in THF (1.25 mL) in a jacketed Schleck flask fitted with a circulating cooler set to 0 °C. Ir(^{t}Bu-POCOP)H_2 (0.15 mg) was dissolved and added to the solution and stirred mechanically. Once catalysis had initiated, identified by observed effervescence, the remaining (90%) of $H_3B{\cdot}NH_2Me$ (1.008 mg, 22.5 mmol) was dissolved in THF (11.25 mL) and added dropwise by syringe pump at a flow rate of 0.1 mL/min. NH_2Me (10 μL) was also added. The reaction was left to stir at 0 °C over-night with the progress checked by ^{11}B NMR spectroscopy. Once full conversion of pre-monomer to polymer was observed by ^{11}B NMR spectroscopy the polymer was precipitated in pentane (200 mL), filtered and dried *in vacuo*. White free-flowing polymer (865 mg, 81 %) was isolated and analysed by GPC to give a M_n = 122,300 g mol−1, Đ = 1.5.

For scale up to 20 g:

The reactions took place in a 500 mL reaction vessel with a mechanical overhead stirrer (see Chapter 4), that was purged with N_2 for 1 hour prior to use.

$H_3B{\cdot}NH_2Me$ (as supplied, 2.1 g) and $[NH_3Me]Cl$ (1.6 mg) was added to the reaction vessel and dissolved in THF (22 ML) at room temperature (~20 °C). The remaining $H_3B{\cdot}NH_2Me$ (18.9 g) was dissolved in THF (211 mL) and connected to the rection vessel *via* dropping funnel. Ir(^{t}Bu-POCOP)H_2 (2.8 mg) was dissolved in THF (1 mL) and added to the reaction vessel. Once catalysis had initiated, identified by observed effervescence, NH_2Me (120 μL) was added and the remaining (90%) of $H_3B{\cdot}NH_2Me$ was added dropwise using the dropping funnel. The reaction was left over night with a slow constant flow of N_2 throughout. Overnight the reaction had reached 70% completion and effervescence had ceased, addition of further NH_2Me (120 μL) resulted in further gas evolution, the addition of NH_2Me was repeated 2 further times

at ~ 6 hour time intervals. After 48 hours total reaction time the polymer was precipitated in pentane (1 L), filtered and dried *in vacuo*. White free-flowing polymer (16 g, 80%) was isolated and analysed by GPC to give a M_n = 35,300 g mol−1, Đ = 1.9.

7.5.2 Synthesis of Ir@*h*-BN

Vacuum curing step: N-methyl-polyaminoborane (300 mg) was added to a large glass beaker and spread to make a thin layer of polymer. The polymer was heated in a vacuum oven (100°C, 10^{-1} bar) for 48 hours. There was no visible change to the polymer, but it had a reduced solubility in chloroform. This cured polymeric material also had a melting point over 370°C. Yield: 177 mg, 59 % yield by mass.

Ammonolysis: The vacuum cured polymeric material (176.5 mg) was put into the furnace and heated to 1200°C under ammonia (ramp rate 10°C per minute, held at 1200°C for 2 hours and then cooled. This process gave a grey coloured material assigned as boron nitride with iridium oxide embedded (Ir@*h*-BN, 84 mg, 48% yield by mass).

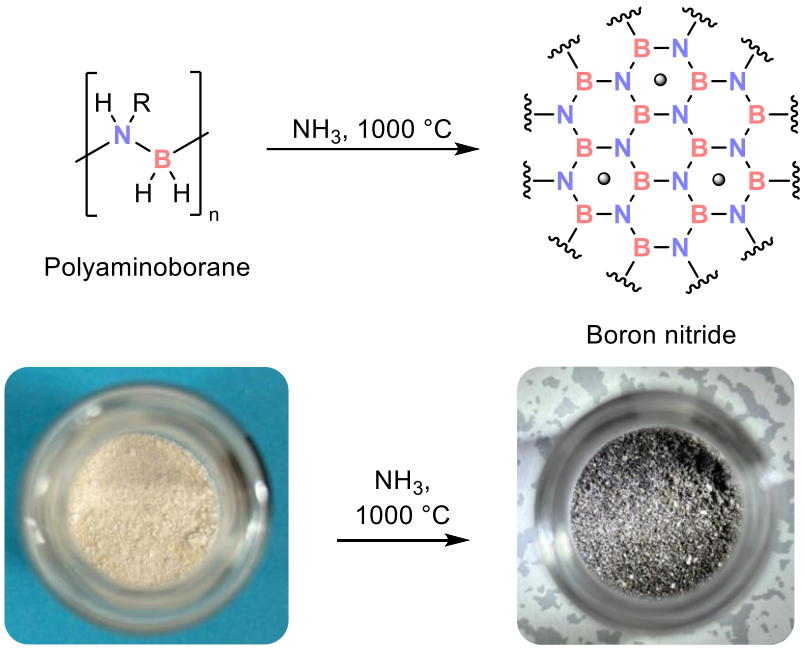

Figure 7.8. Images of the visible change to the polymeric material after the ammonolysis to form boron nitride.

7.5.3 Characterisation of Ir@*h*-BN

7.5.3.1 IR data

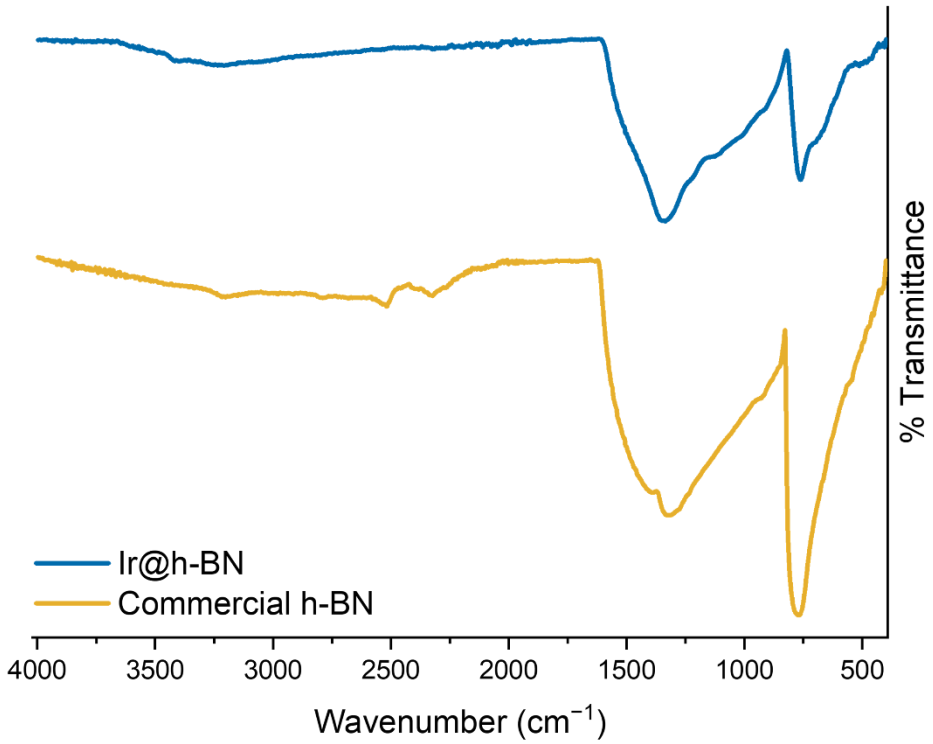

Figure 7.9. FT-IR spectrum of as synthesised Ir@*h*-BN, and commercially available hexagonal boron nitride.

7.5.3.2 pXRD data

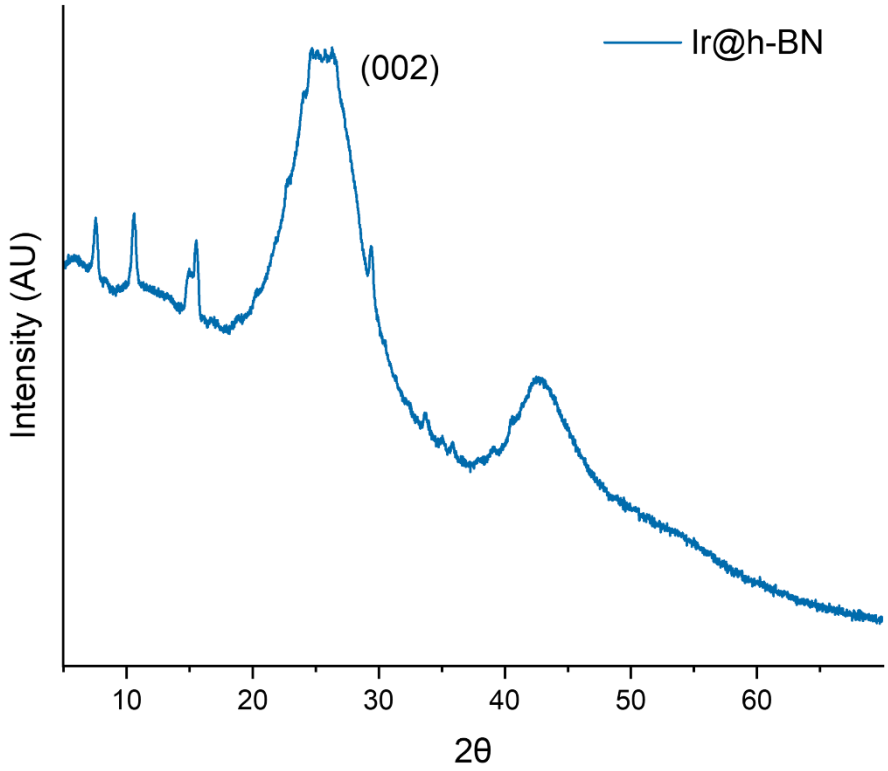

Figure 7.10. pXRD of Ir@*h*-BN before catalysis.

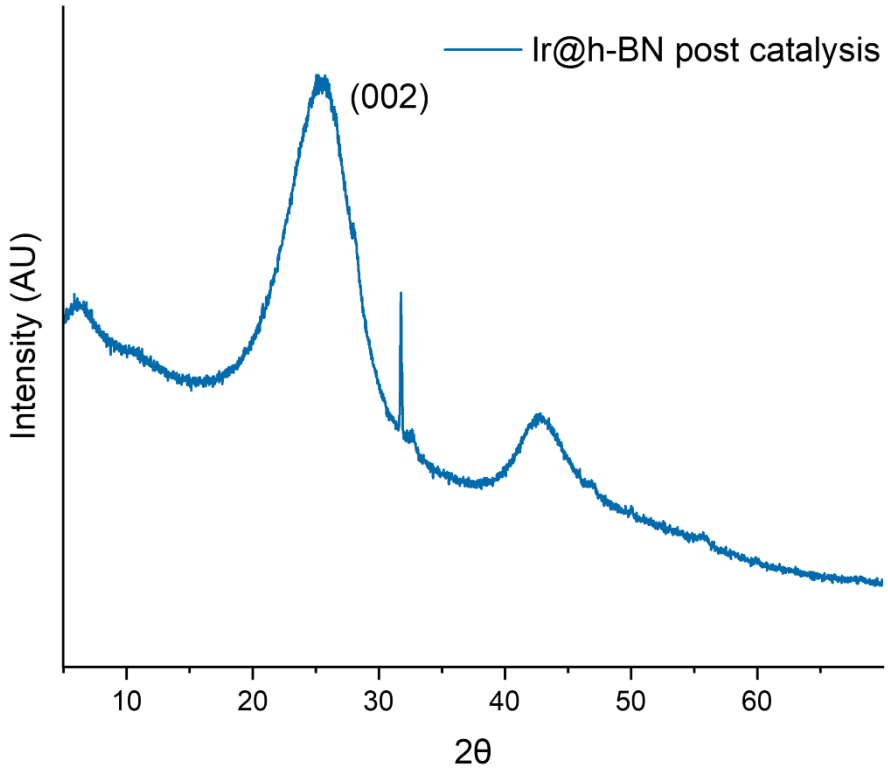

Figure 7.11. pXRD of Ir@*h*-BN post propene hydrogenation catalysis.

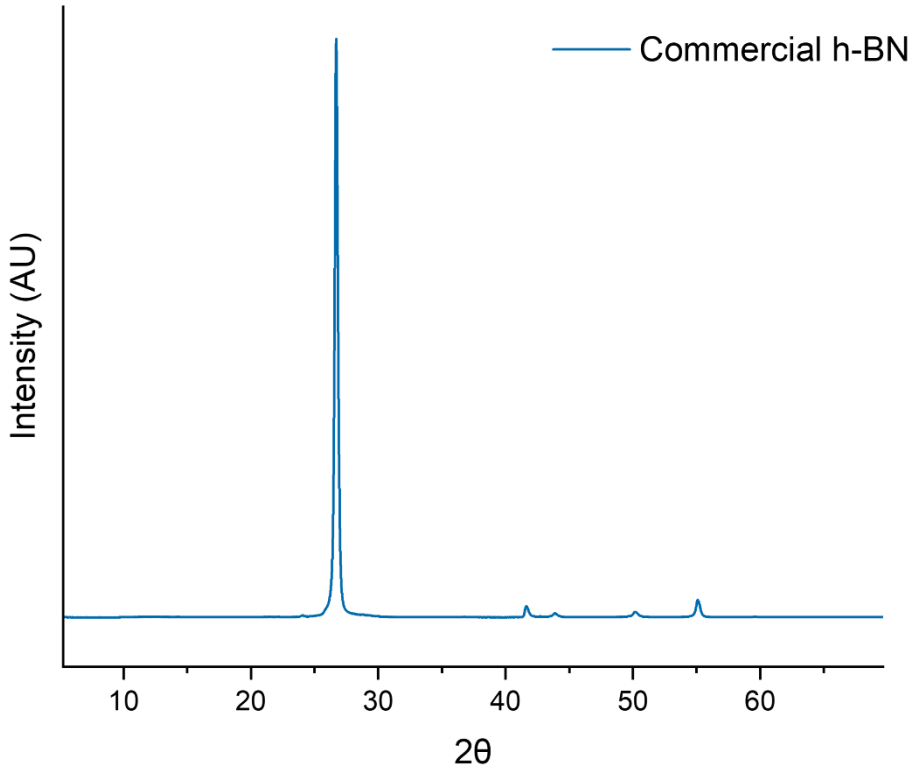

Figure 7.12. pXRD of commercial *h*-BN sample.

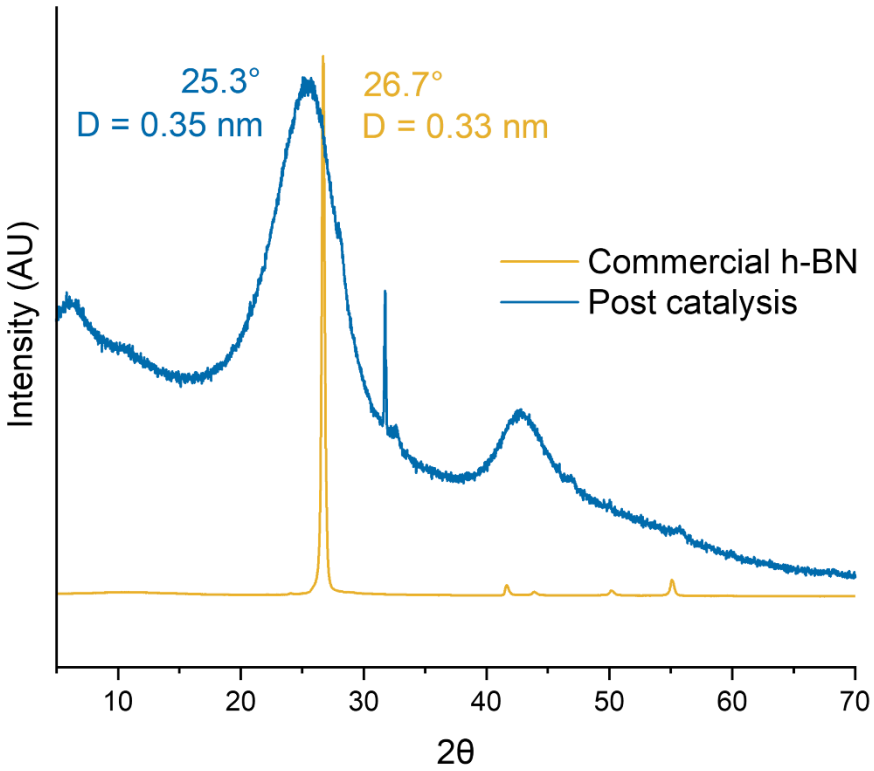

Figure 7.13. Enlarged (002) peak from the powder XRD of the commercial and post catalysis, including the calculated d-spacings.

7.5.3.3 XPS data

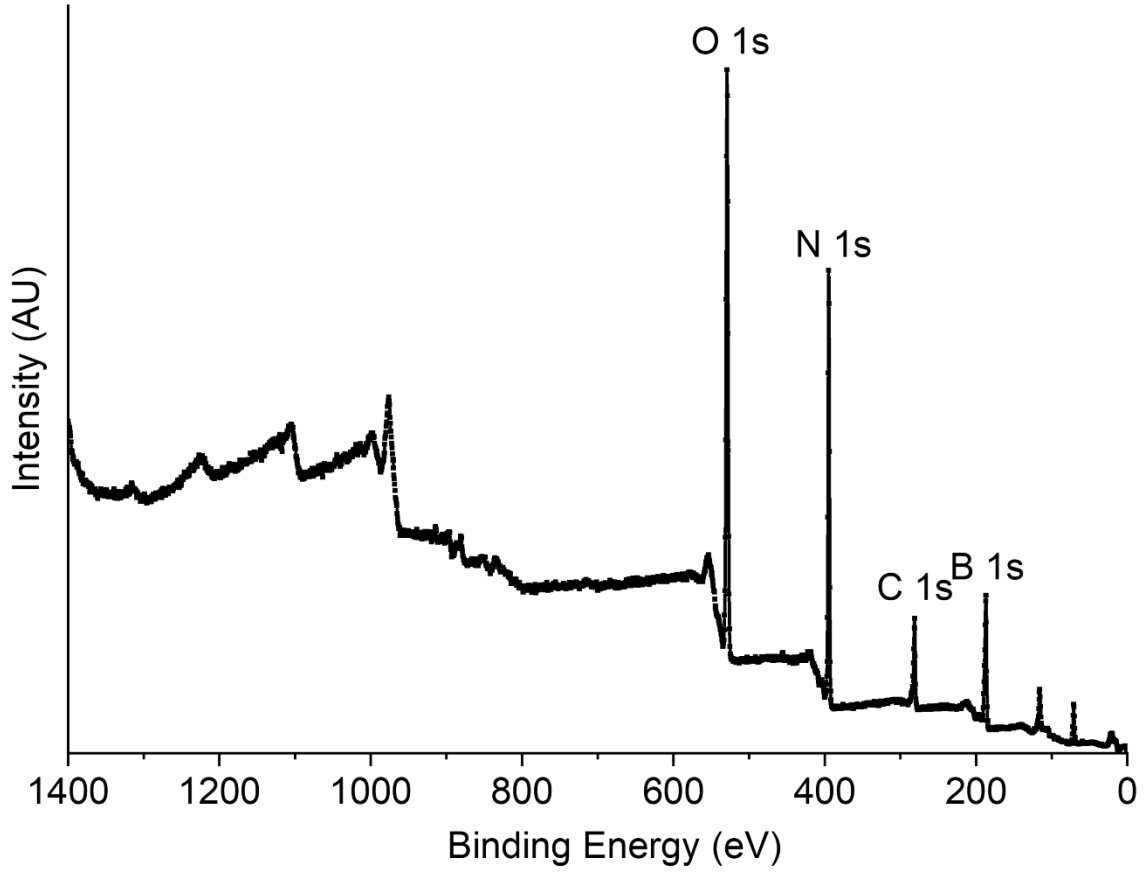

Figure 7.14. XPS survey spectrum, and high-resolution spectrum of Ir 4f, N 1s and B 1s.

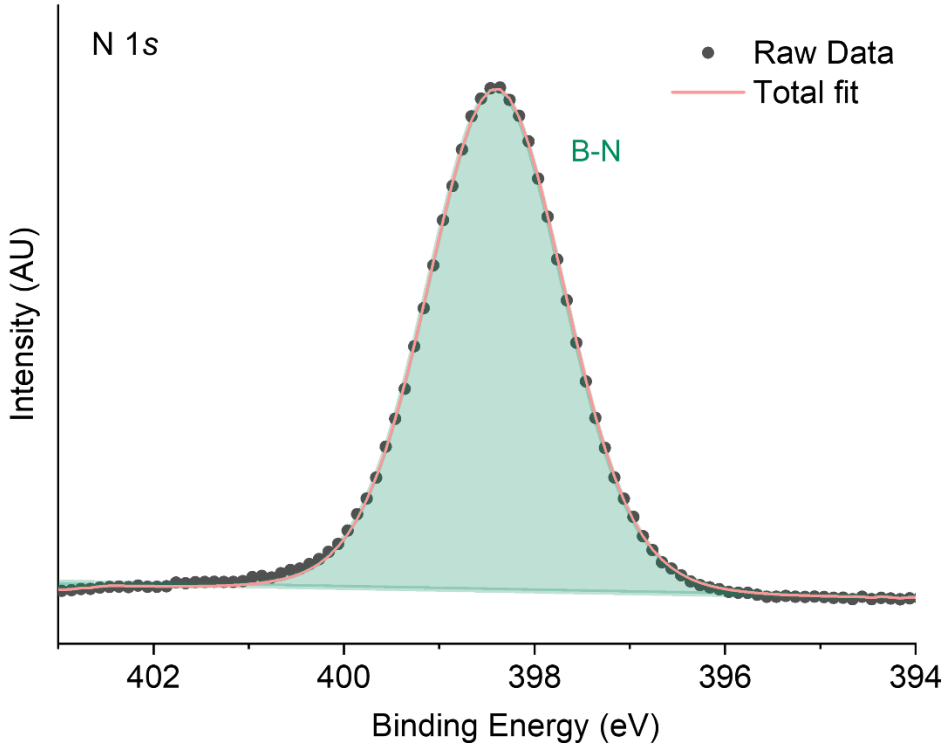

Figure 7.15. High resolution spectrum of N 1s.

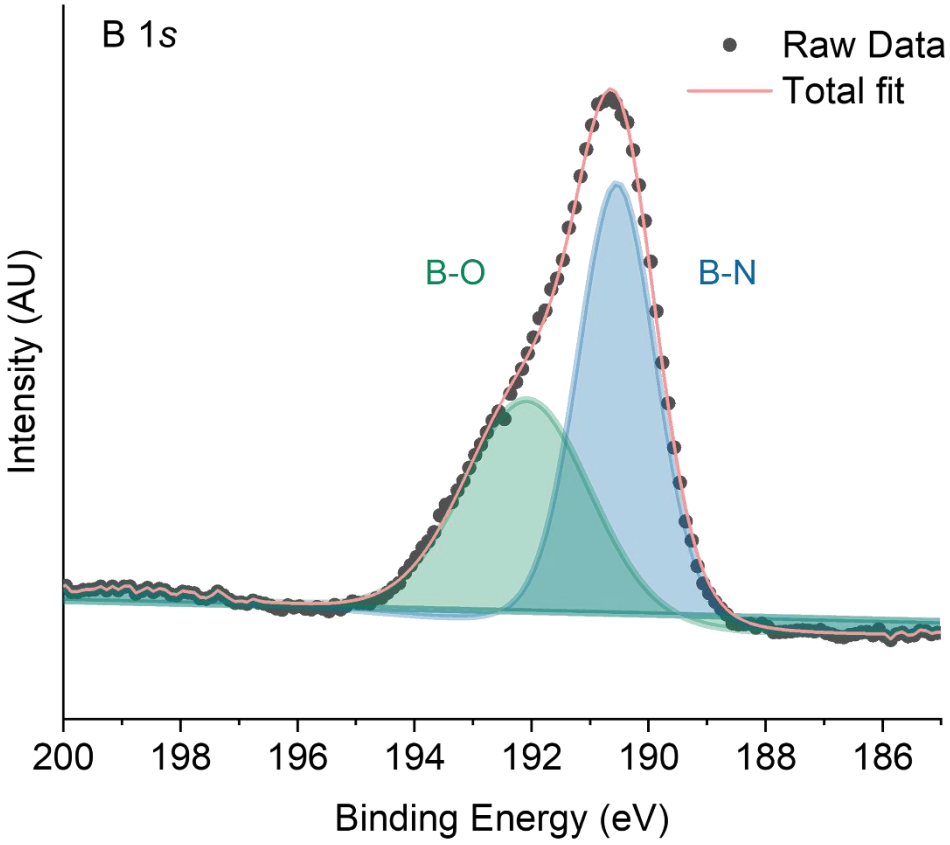

Figure 7.16. High resolution spectrum of B 1s.

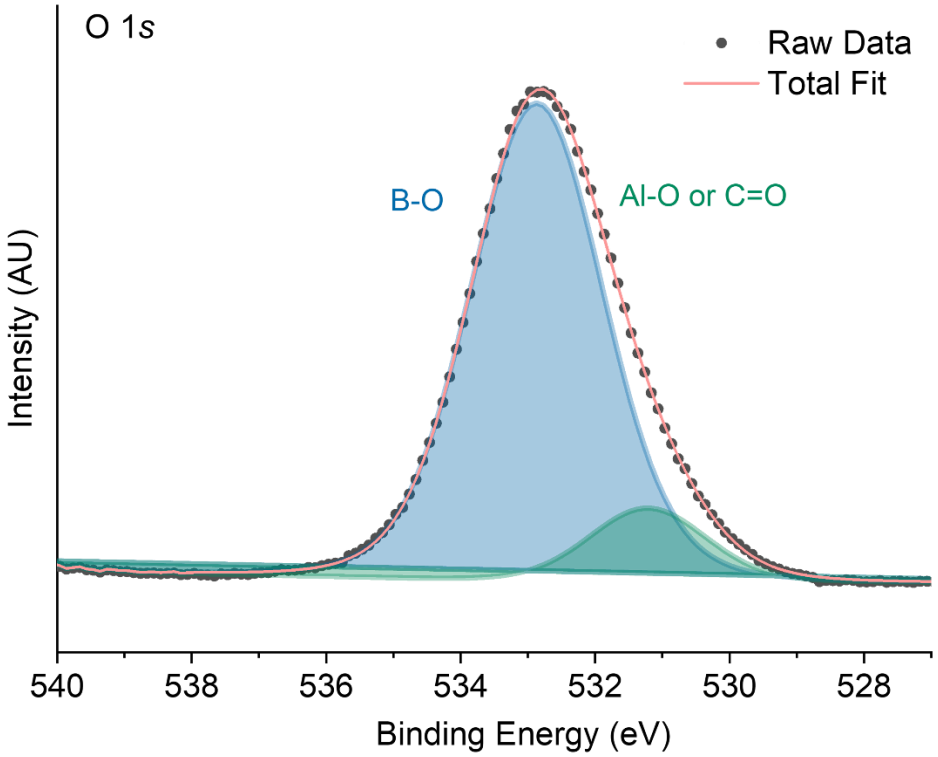

Figure 7.17. High resolution spectrum of O 1s.

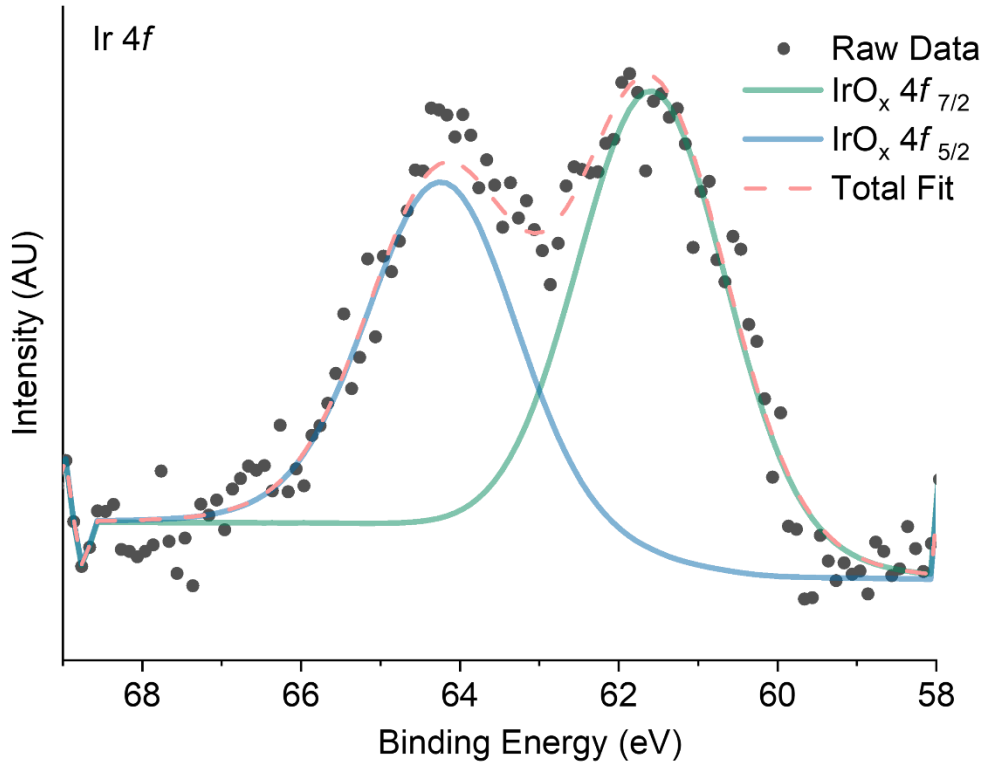

Figure 7.18. High resolution spectrum of Ir 4f.

Table 7.1. Calculated elemental content of Ir@*h*-BN from XPS.

Element	Calculated element content (%)
O 1s	27.48
C 1s	11.4
N 1s	23.72
B 1s	37.37
Ir 4f	0.02
Al 2p	7.86

7.5.3.4 SEM images

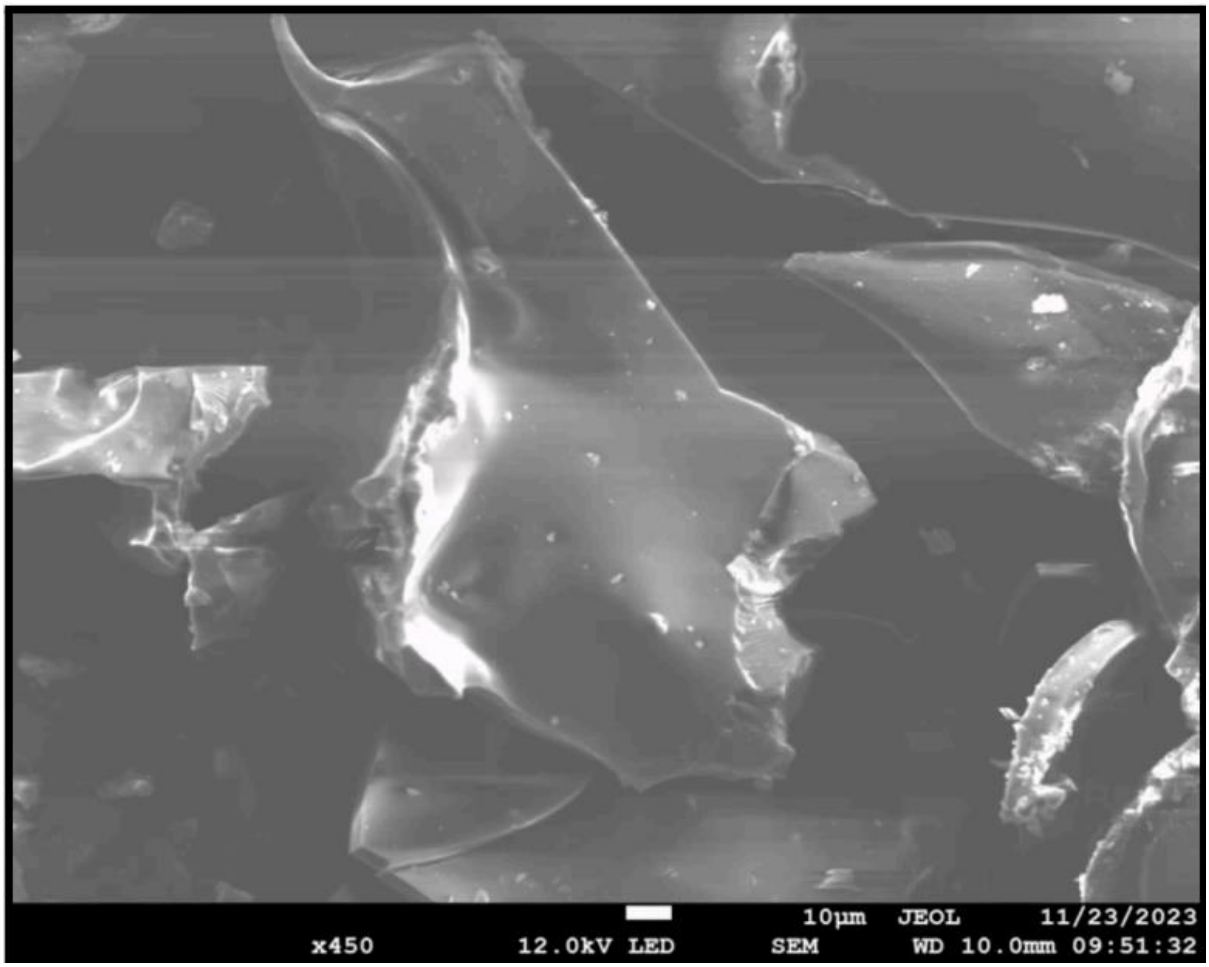

Figure 7.19. SEM image of Ir@*h*-BN flakes.

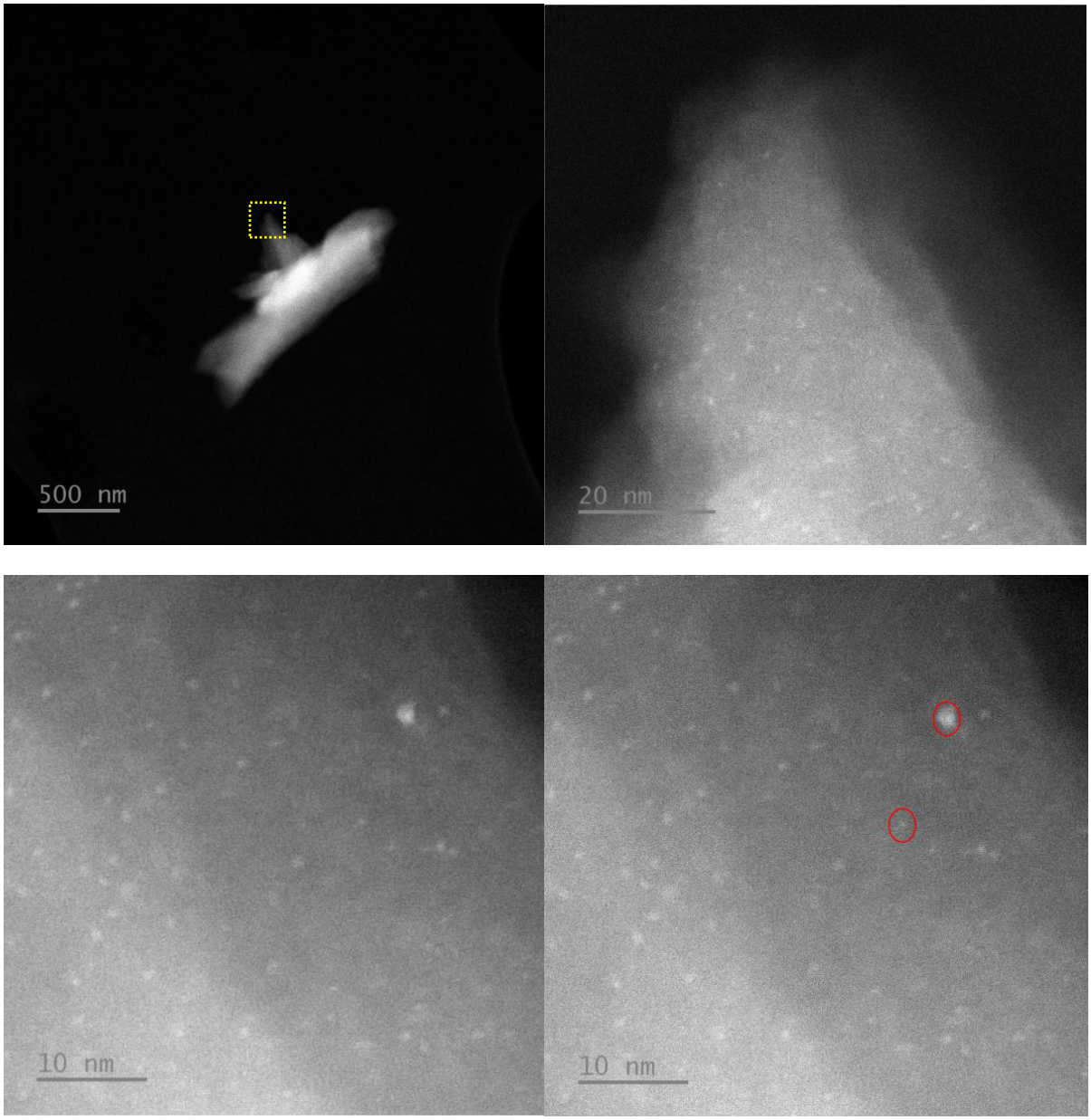

Figure 7.20. HAADF images of Ir@*h*-BN flakes at different magnifications.

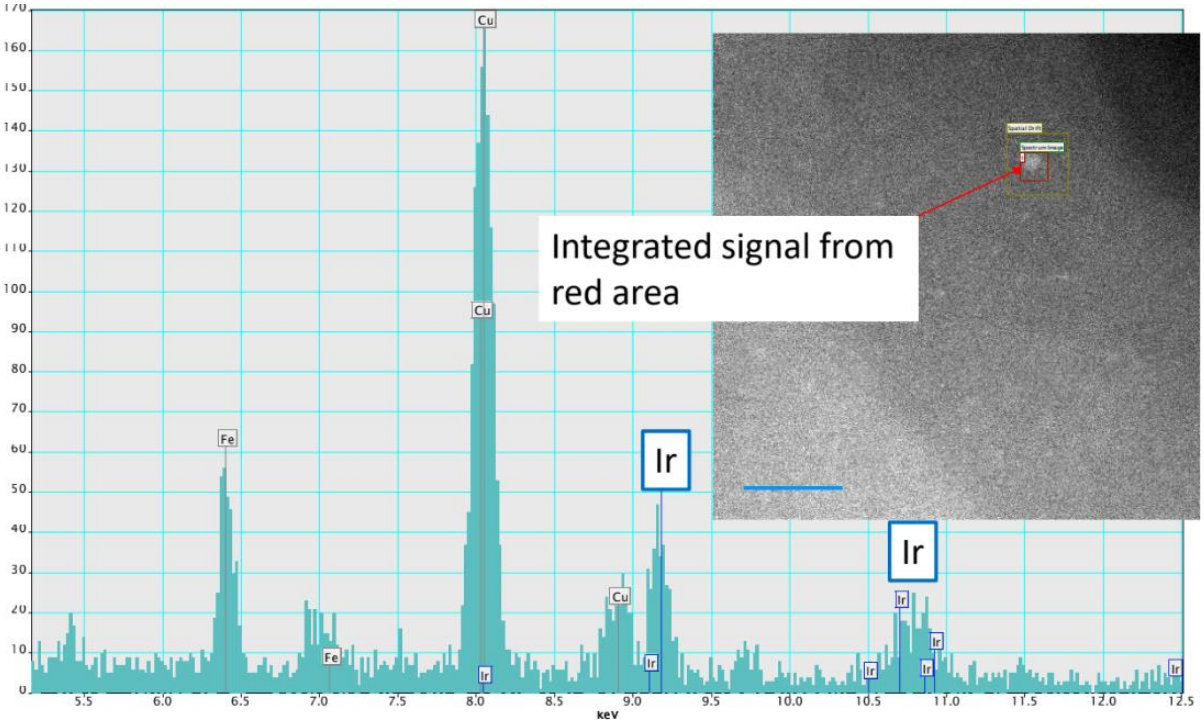

Figure 7.21. EDS analysis of Ir@*h*-BN flakes.

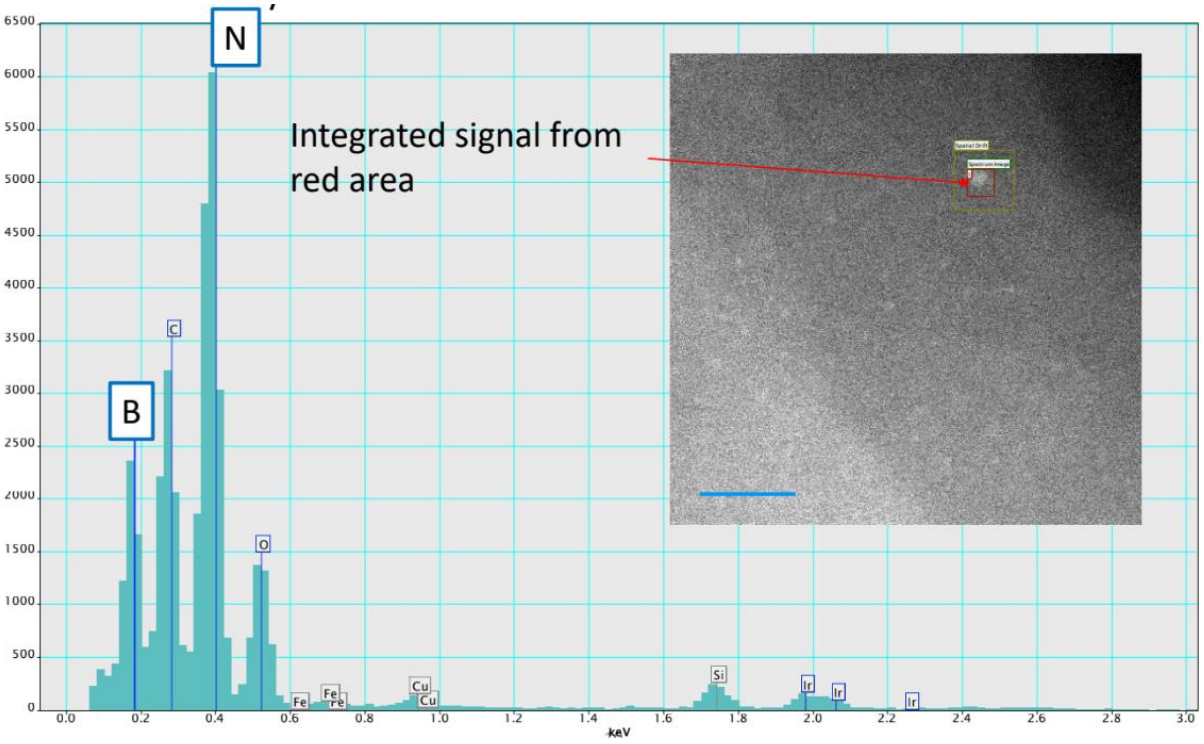

Figure 7.22. EDS analysis of Ir@*h*-BN flakes.

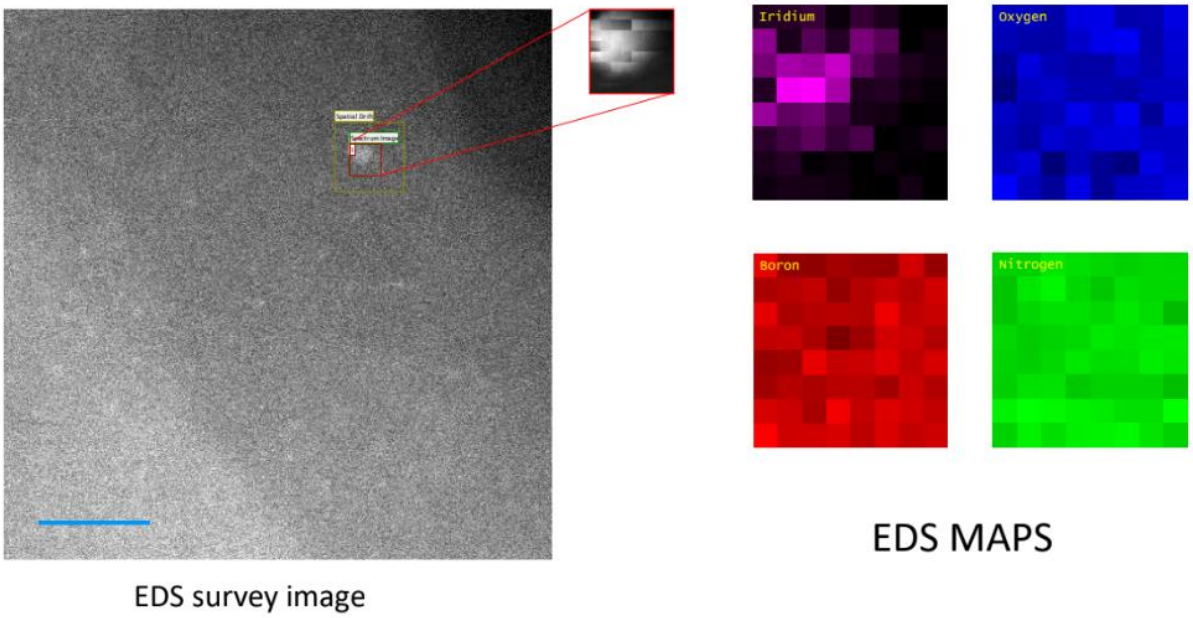

Figure 7.23. EDS survey image (left), EDS Maps (right) of Ir@*h*-BN flakes.

7.5.4 Catalysis with Ir@*h*-BN

General procedure

A J-Youngs NMR tube was charged with Ir@*h*-BN (5 mg). The NMR tube was evacuated and backfilled with 1 bar of propene. The propene was cooled to 77 K and 2 bar of hydrogen was added to the NMR tube (without evacuating the tube beforehand). The NMR tube was brought to room temperature and then heated at 100°C for 24 hours. The reaction progress was monitored by gas phase ^{1}H NMR spectroscopy.

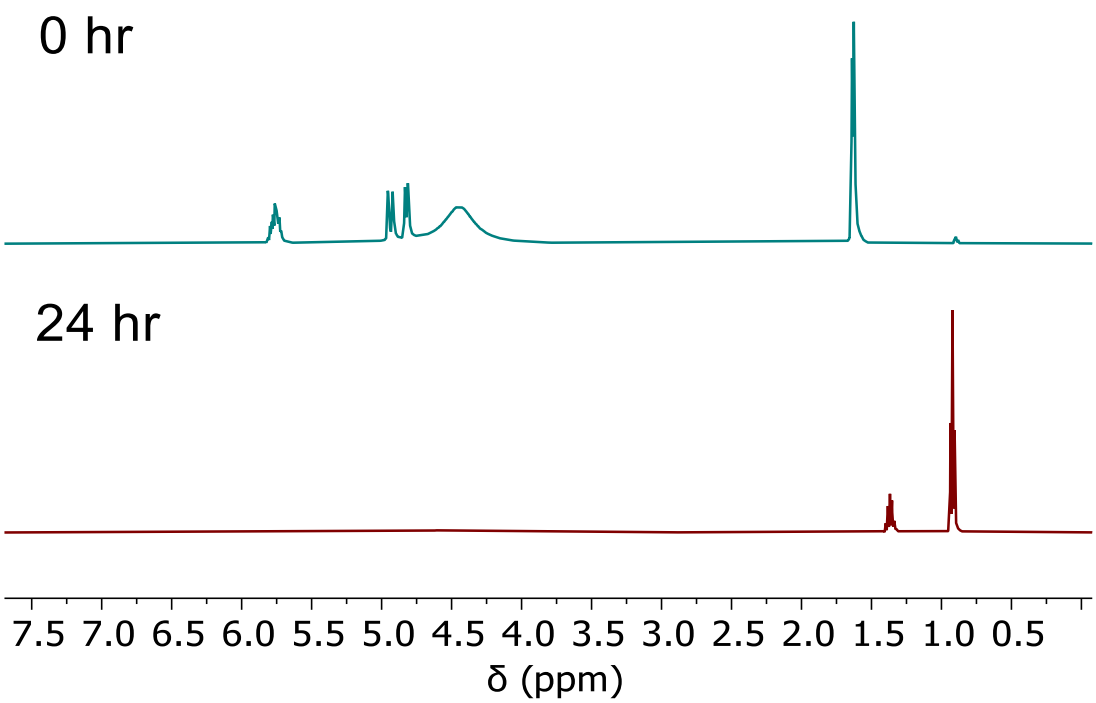

Figure 7.24. Gas phase ^{1}H NMR spectra showing full conversion to propane over 24 hours.

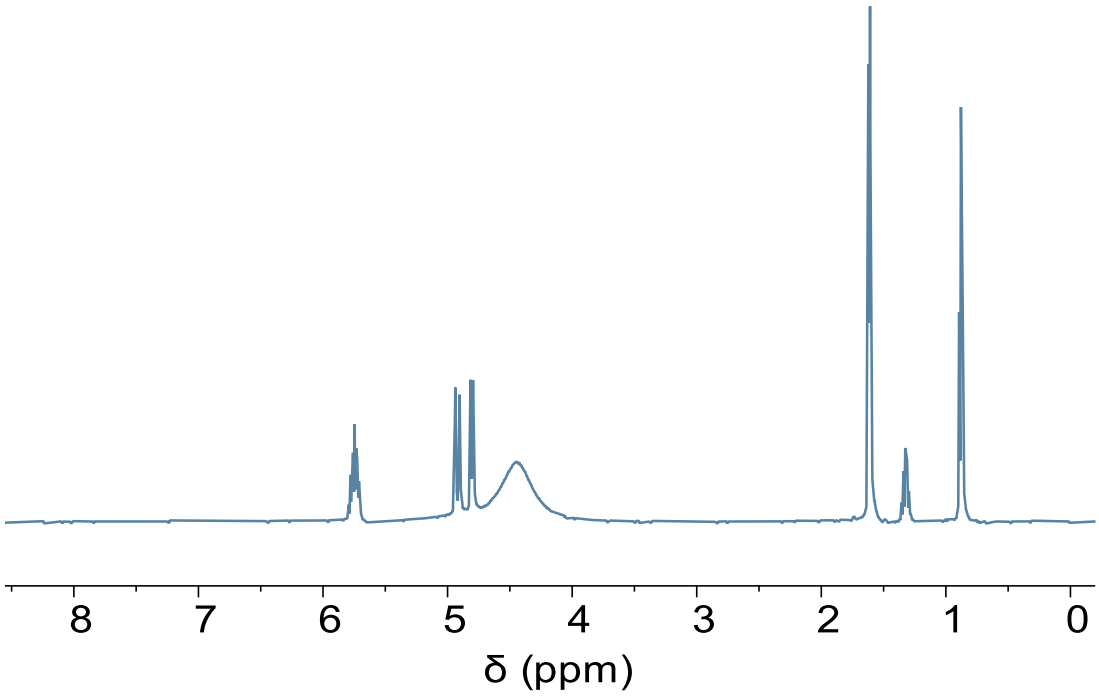

Figure 7.25. Hydrogenation of propene with commercial h-BN at 100°C, showing ~22% conversion to propane over 24 hours.

7.6 Chapter 5 Experimental

7.6.1 Synthesis of Ad-POCOP ligand

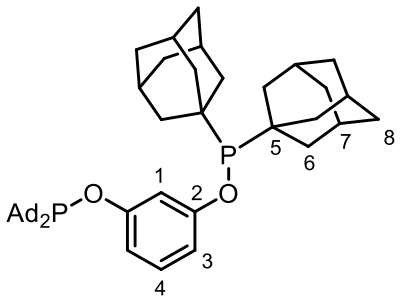

NaH (27 mg, 1.05 mmol) was suspended in THF (15 mL), and resorcinol (55 mg, 0.5 mmol) was dissolved in THF (5 mL) separately. The resorcinol solution was added to the NaH solution dropwise while stirring. This solution was heated to reflux for 1 hour, the solution was cooled and PAd_2Cl (353.5 mg, 1.05 mmol) dissolved in THF (5 mL) was added dropwise. The solution was heated to reflux for a further hour and bubbling was observed. The THF was removed *in vacuo*, pentane (10 mL) was added and the pentane solution cooled with an ice bath then filtered (twice). The remaining solid was extracted with toluene (5 mL) and the solvent removed *in vacuo*. Pentane (5 mL) was added and the solvent removed *in vacuo* to yield a white powder (151 mg, 43 % yield).

^{1}H NMR (500 MHz; C_6D_6) δ_H: 7.65 (1H, apparent pentet, *J* = 2.3 Hz, Ar-H1), 7.15-7.07 (2H, m, Ar-H3/4), 2.07 (24H, s (br), C-H6), 1.85 (12H, s (br), C-H7), 1.65 (24 H, s (br), C-H8).

^{31}P{^{1}H} NMR (243 MHz; C_6D_6) δ_P: 149.15.

^{13}C{^{1}H} NMR (75 MHz; C_6D_6) δ_C: 161.9 (d, *J* = 10.1 Hz, C2), 129.7 (s, C4), 111.4 (d, *J* = 11.3 Hz, C3), 109.0 (t, *J* = 11.3 Hz, C1), 40.0 (d, *J* = 27.2 Hz, C5), 38.8 (d, *J* = 13.2 Hz, C6), 37.0 (s, C8), 28.4 (d, *J* = 8.2 Hz, C7)

ESI-MS (+) $[M+H]^+$ *m/z* 711.47 (calc. $[C_{46}H_{64}O_2P_2+H]^+$ *m/z* 711.45)

Crystals suitable for X-ray diffraction were obtained from a cooled (4 °C) pentane solution.

7.6.2 Synthesis of [Ir(Ad-POCOP)HCl] – complex 8

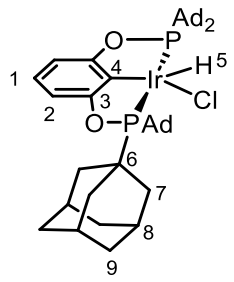

$[Ir(COD)Cl_2]$ (39 mg, 58 μmol) and Ad-POCOP (91 mg, 0.18 mmol) were added to an ampoule and toluene (15 mL) was added. The solution was heated at 150 °C for 12 hours. The solvent was removed *in vacuo*, pentane added and sonicated for 20 minutes. The mixture was cooled in an ice bath and filtered and the red/brown powder dried *in vacuo*. A red/brown solid was isolated (41.5 mg, 76% yield).

^{1}H NMR (600 MHz; C_6D_6) δ_H: 6.97-6.90 (3H, m, Ar-H1/2), 2.42 (12H, dd, *J* = 174.1 Hz, J_{HH} = 11.8 Hz, C-H7), 2.35 (12H, dd, *J* = 69.4 Hz, J_{HH} = 12.2 Hz, C-H7), 1.94 (6 H, s (br), C-H8), 1.87 (6 H, s (br), C-H8), 1.59 (24H, two overlapping doublet of doublets, J_{HH} = 50.1, 11.8 Hz C-H9), −40.17 (1H, s (br), H5).

^{31}P{^{1}H} NMR (243 MHz; C_6D_6) δ_P: 165.91

^{13}C{1H} NMR (151 MHz; C_6D_6) δ_C: 168.1 (s, C3), 125.9 (s, C1), 119.9 (s, C4), 105.2 (s, C2), 38.9 (d, *J* = 37.4 Hz, C7), 36.9 (s, C9), 28.6 (d, *J* = 28.4 Hz, C8).

ESI-MS (−) $[M-H]^-$ *m/z* 937.32 (calc. $[IrC_{46}H_{64}O_2P_2Cl-H]^-$ *m/z* 937.36)

Crystals suitable of single crystal X-ray diffraction were obtained from slow evaporation of pentane.

7.7 NMR spectra

7.7.1 Ir(ᵗBu-POCOP)H$_2$(NH$_2$Me)

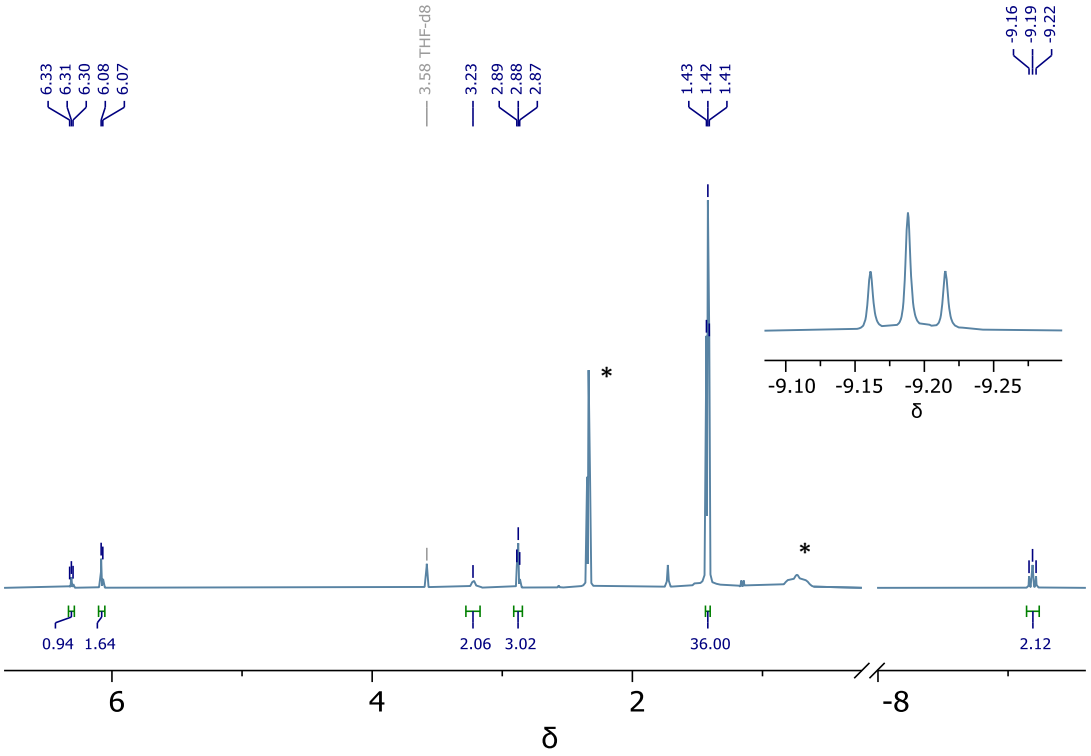

Figure 7.26. ^{1}H NMR spectrum (THF-d^{8}, 600 MHz, 298 K) of Ir(ᵗBu-POCOP)H$_2$(NH$_2$Me) – NH$_2$Me gas dissolved in THF indicated by *.

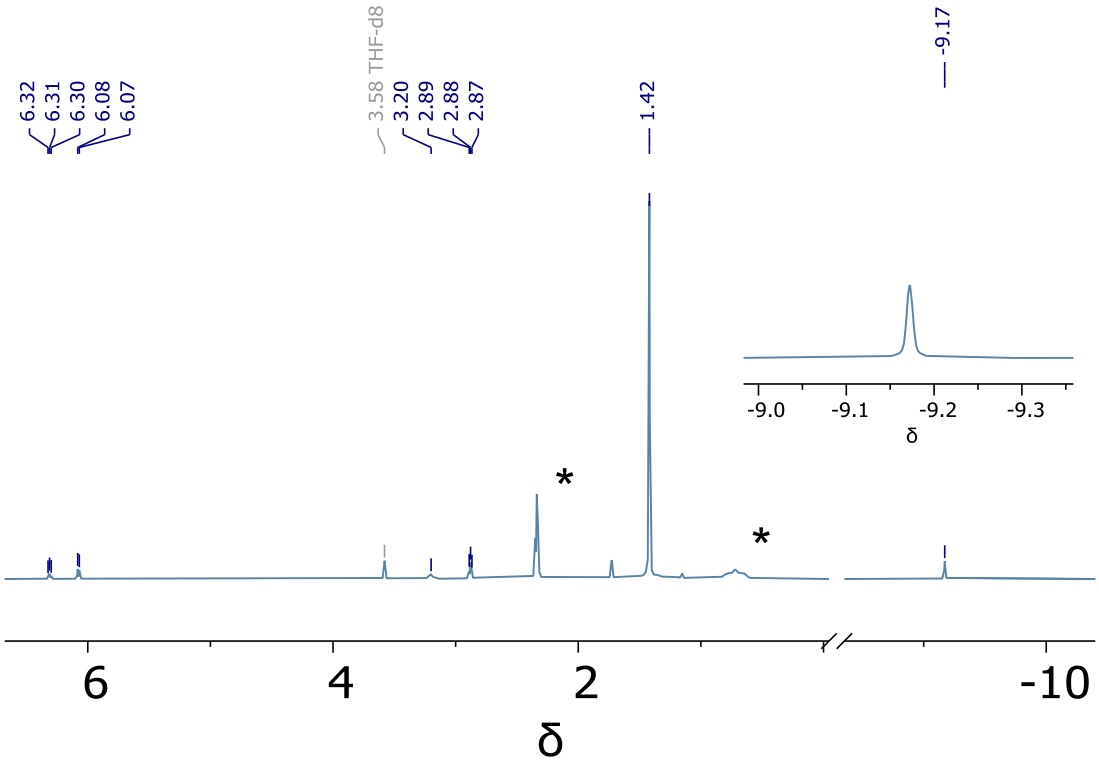

Figure 7.27. ^{1}H{^{31}P} NMR spectrum (THF-d^{8}, 600 MHz, 298 K) of Ir(ᵗBu-POCOP)H$_2$(NH$_2$Me) –NH$_2$Me gas dissolved in THF indicated by *.

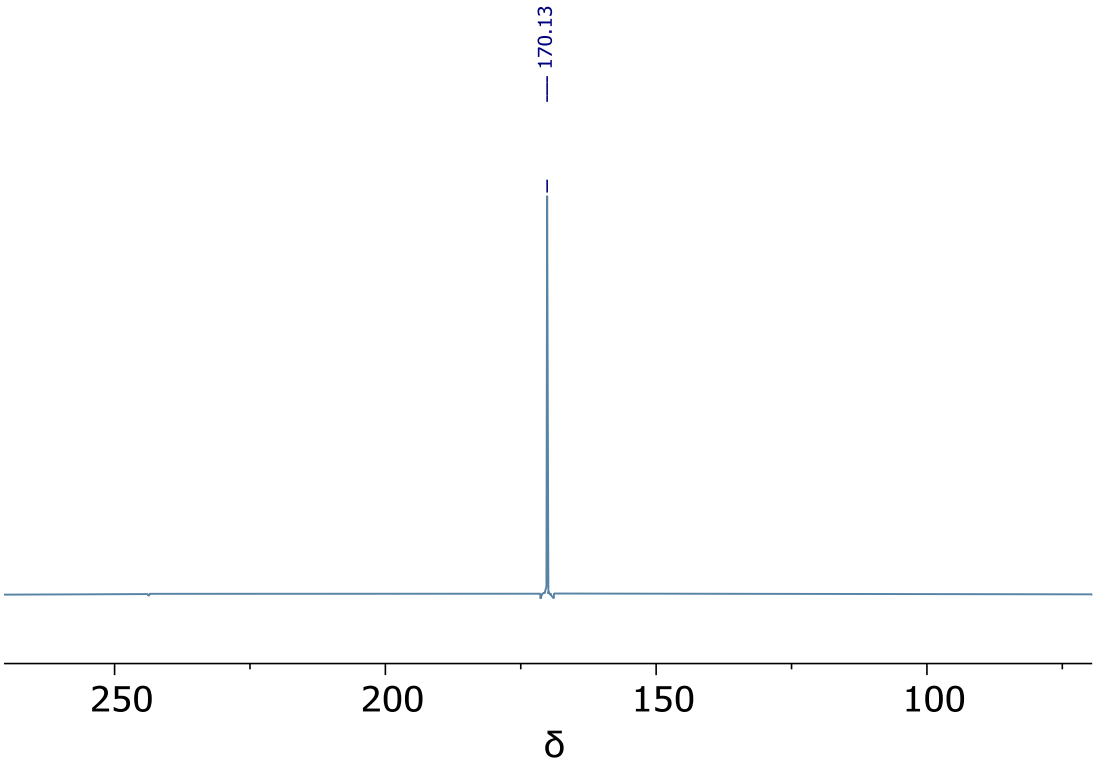

Figure 7.28. $^{31}P\{^{1}H\}$ NMR spectrum (THF-d^8, 243 MHz, 298 K) of Ir(^{t}Bu-POCOP)H_2(NH_2Me).

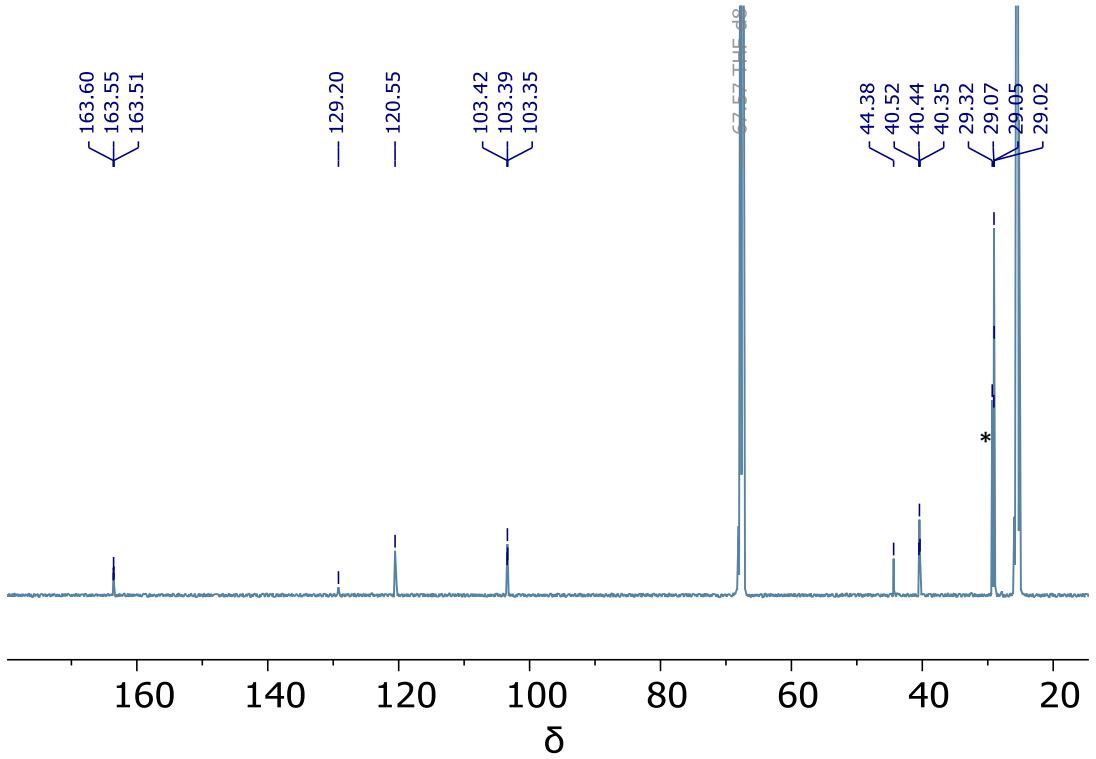

Figure 7.29. $^{13}C\{^{1}H\}$ NMR spectrum (THF-d^8, 151 MHz, 298 K) of Ir(^{t}Bu-POCOP)H_2(NH_2Me) –NH_2Me gas dissolved in THF indicated by *.

7.7.2 [Na(18-crown-6)(THF)$_2$][Ir(^{t}Bu-POCOP)H$_3$]

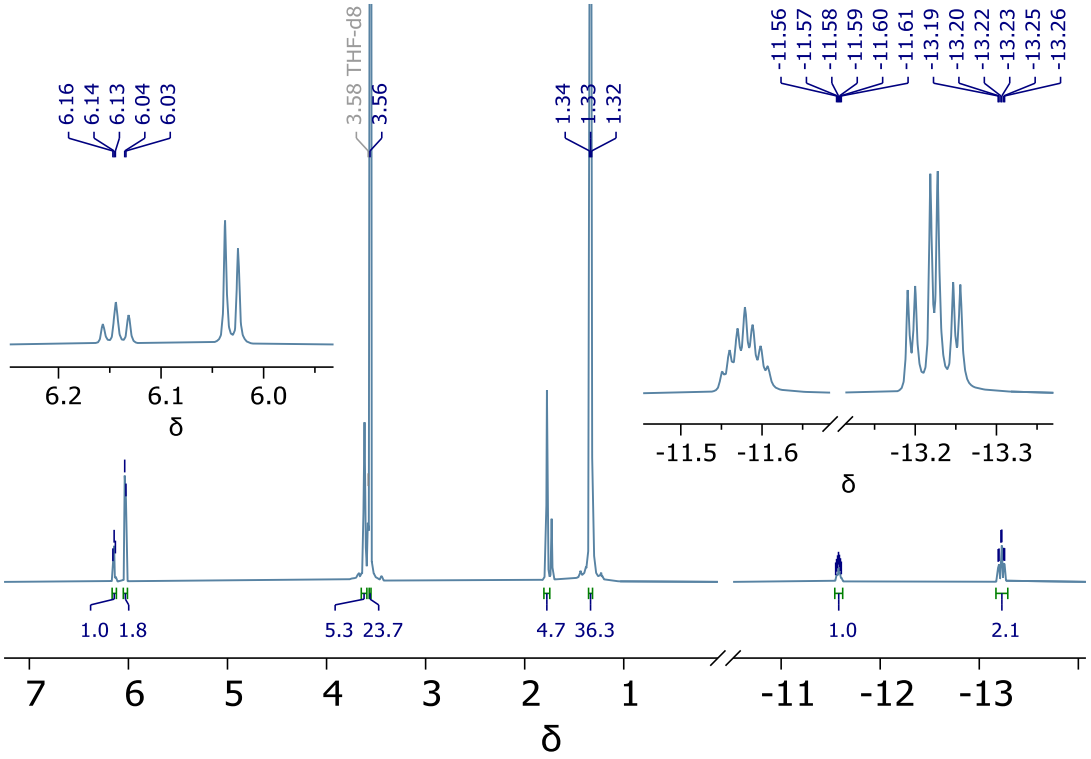

Figure 7.30. ^{1}H NMR spectrum (THF-d^8, 600 MHz, 298 K) of [Na(18-crown-6)(THF)$_2$][Ir(^{t}Bu-POCOP)H$_3$].

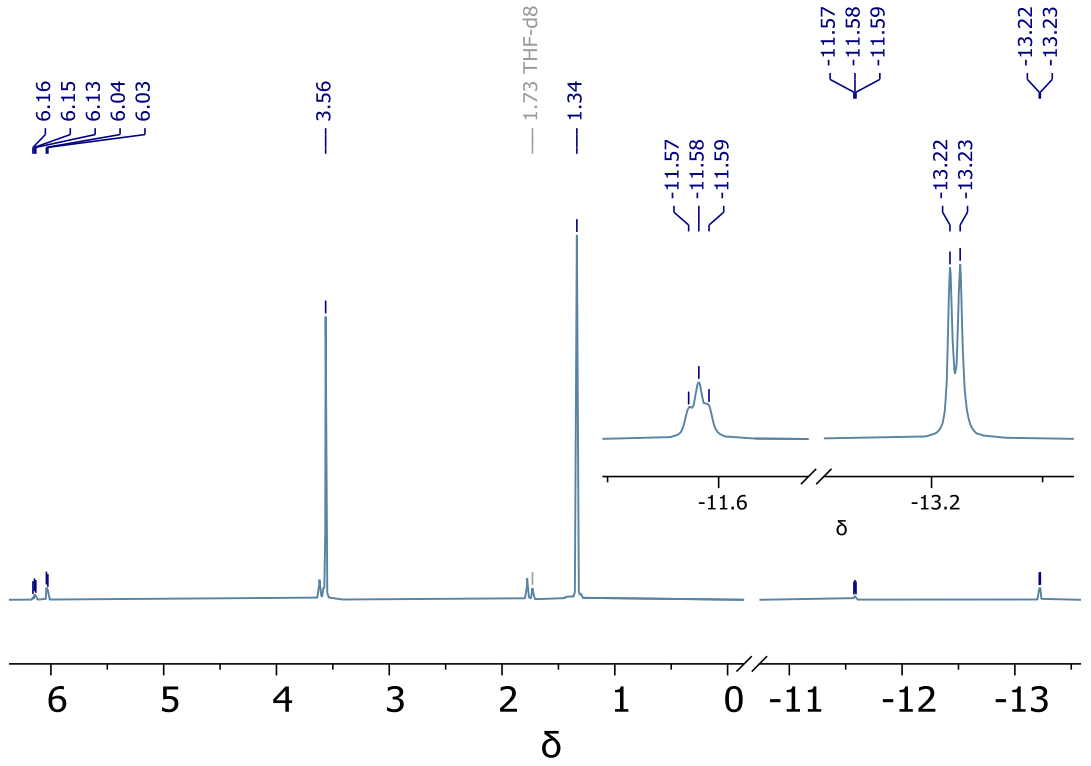

Figure 7.31. ^{1}H{^{31}P} NMR spectrum (THF-d^8, 600 MHz, 298 K) of [Na(18-crown-6)(THF)$_2$][Ir(^{t}Bu-POCOP)H$_3$].

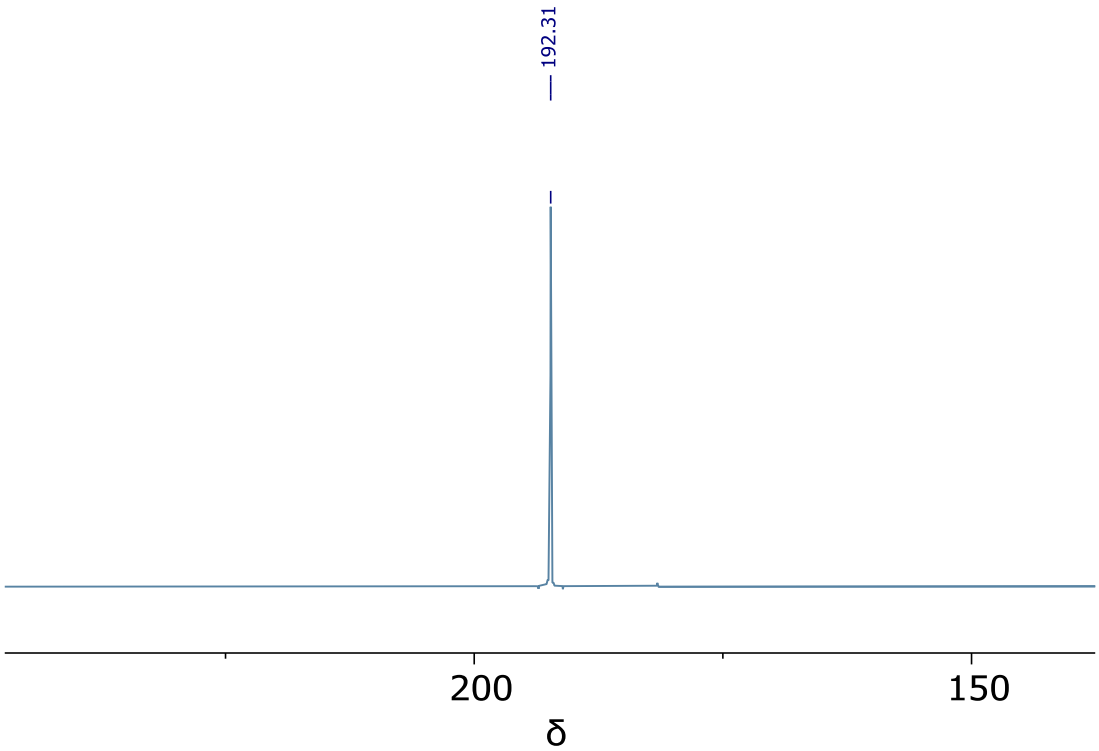

Figure 7.32. $^{31}P\{^{1}H\}$ NMR spectrum (THF-d^8, 243 MHz, 298 K) of [Na(18-crown-6)$(THF)_2$][Ir(^{t}Bu-POCOP)H_3].

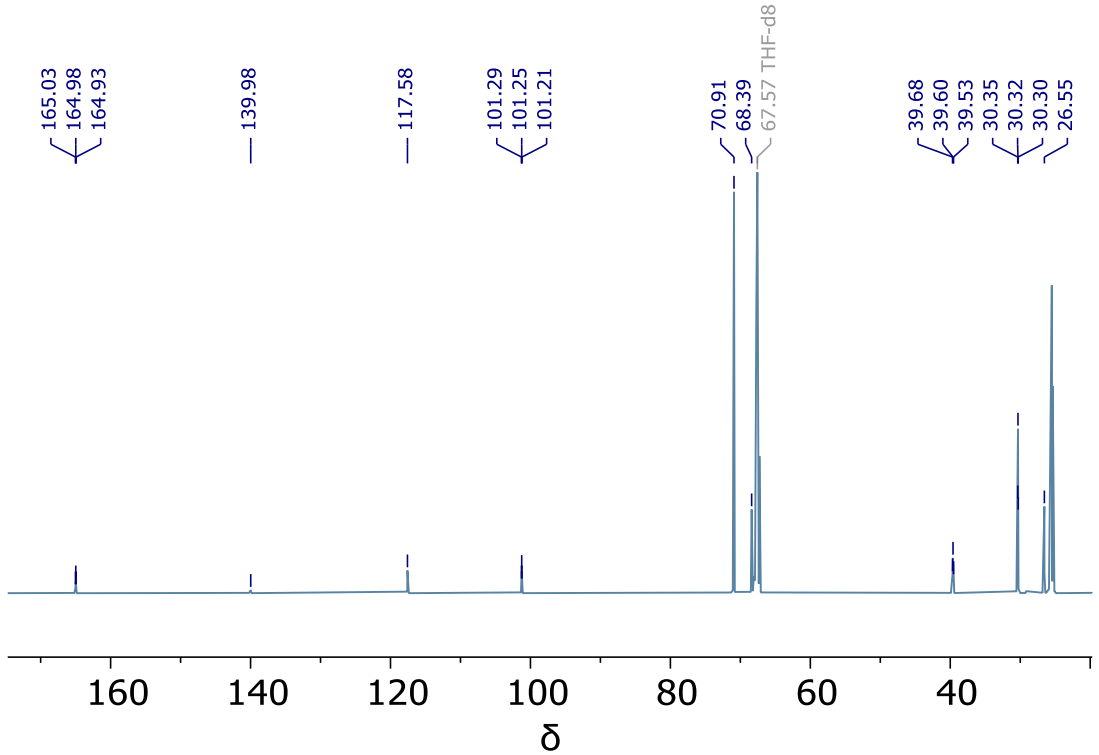

Figure 7.33. $^{13}C\{^{1}H\}$ NMR spectrum (THF-d^8, 151 MHz, 298 K) of [Na(18-crown-6)$(THF)_2$][Ir(^{t}Bu-POCOP)H_3].

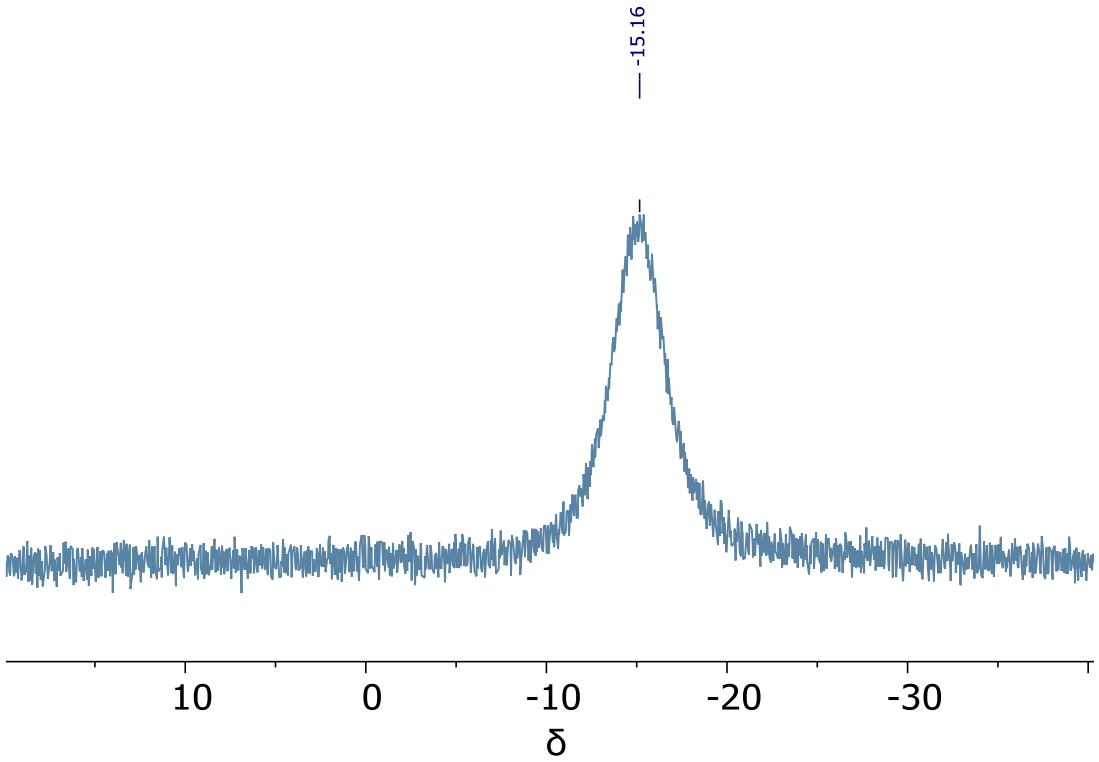

Figure 7.34. ^{23}Na NMR spectrum (THF-d^8, 159 MHz, 298 K) of [Na(18-crown-6)(THF)$_2$][Ir(^{t}Bu-POCOP)H$_3$].

7.7.3 *In situ* Na[Ir(ᵗBu-POCOP)H$_3$]

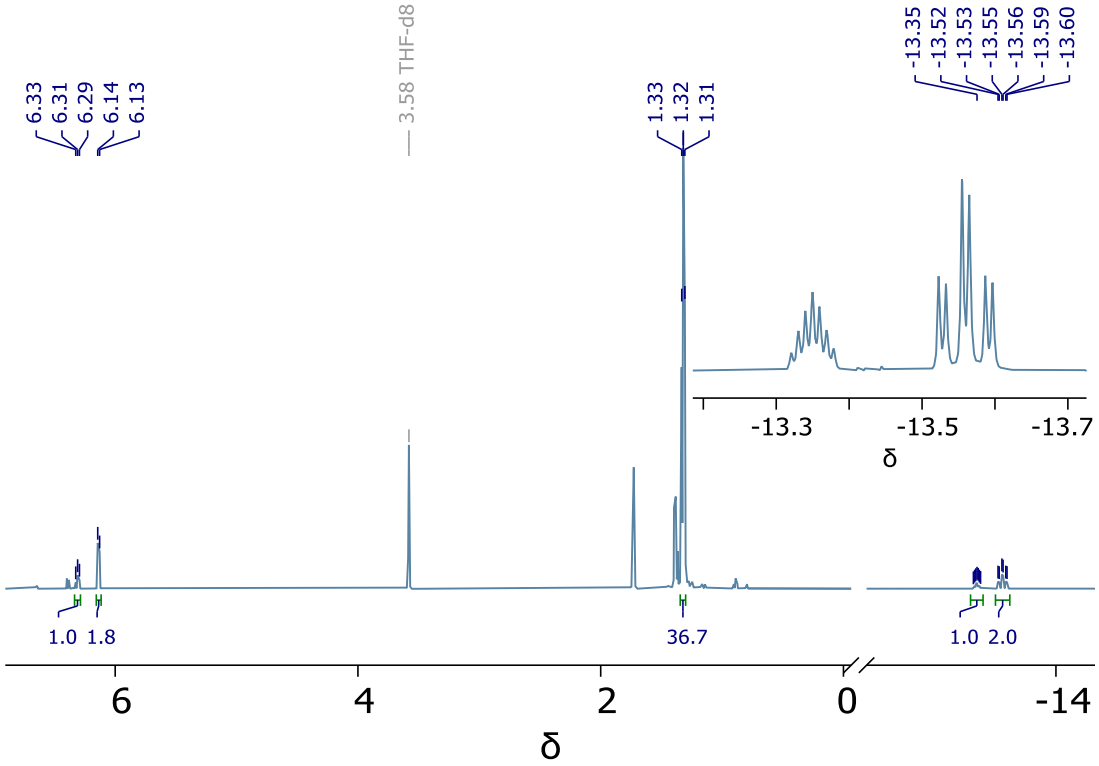

Figure 7.35. ^{1}H NMR spectrum (THF-d^{8}, 500 MHz, 298 K) of Na[Ir(ᵗBu-POCOP)H$_3$] made *in-situ*.

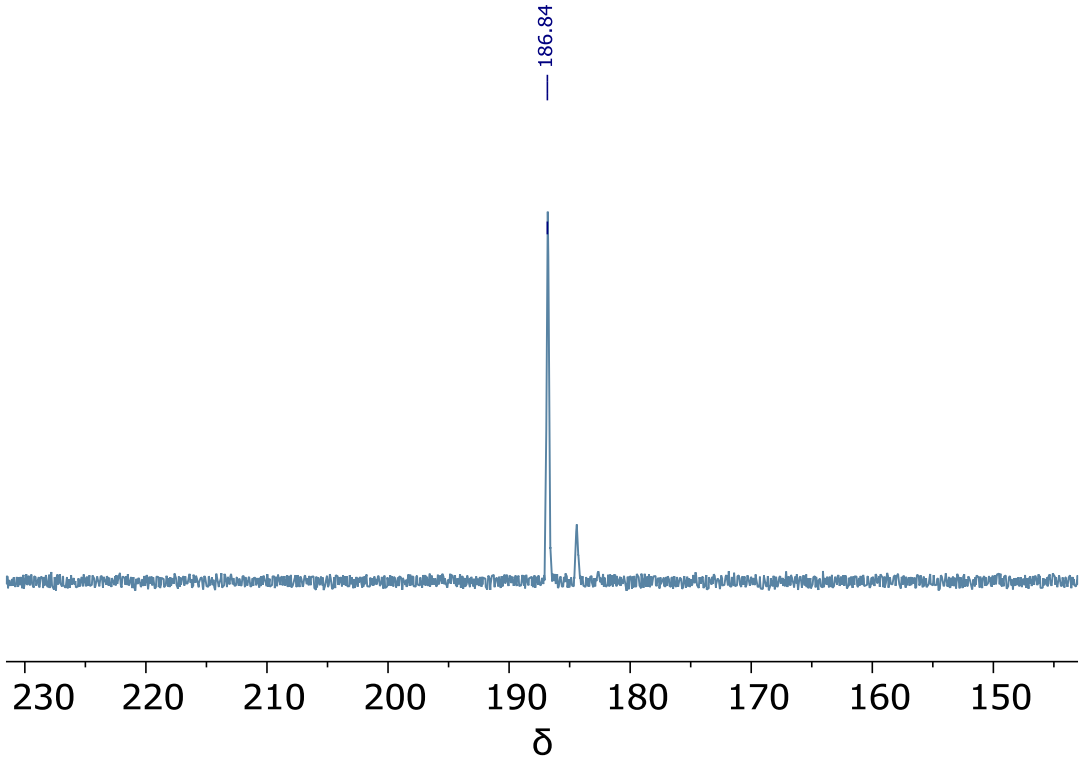

Figure 7.36. ^{31}P{^{1}H} NMR spectrum (THF-d^{8}, 203 MHz, 298 K) of Na[Ir(ᵗBu-POCOP)H$_3$] made *in-situ*.

7.7.4 Ad-POCOP

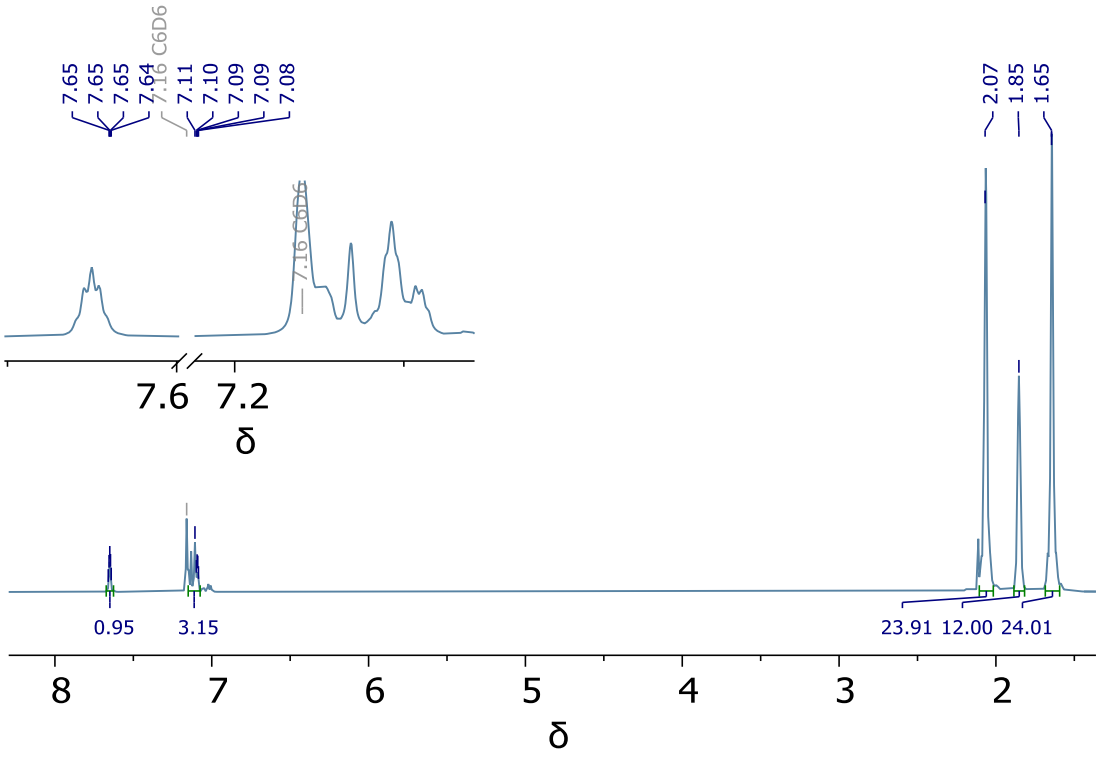

Figure 7.37. ^{1}H NMR NMR spectrum (C_6D_6, 500 MHz, 298 K) of Ad-POCOP.

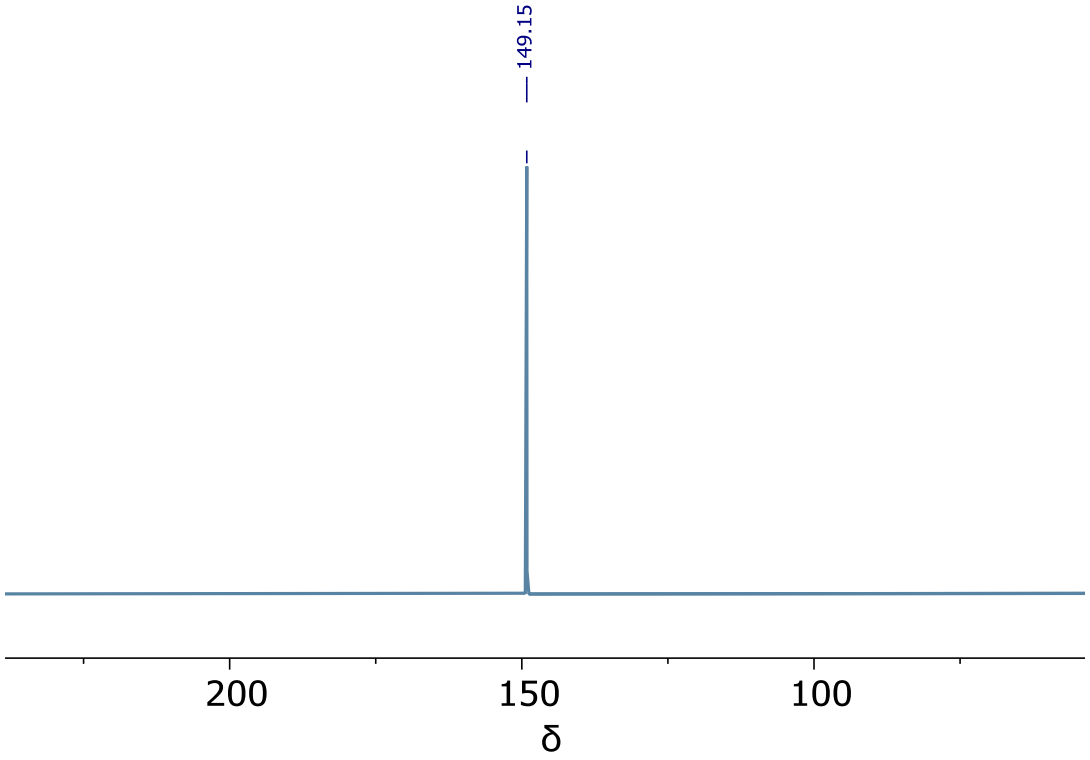

Figure 7.38. $^{31}P\{^{1}H\}$ NMR spectrum (C_6D_6, 203 MHz, 298 K) of Ad-POCOP.

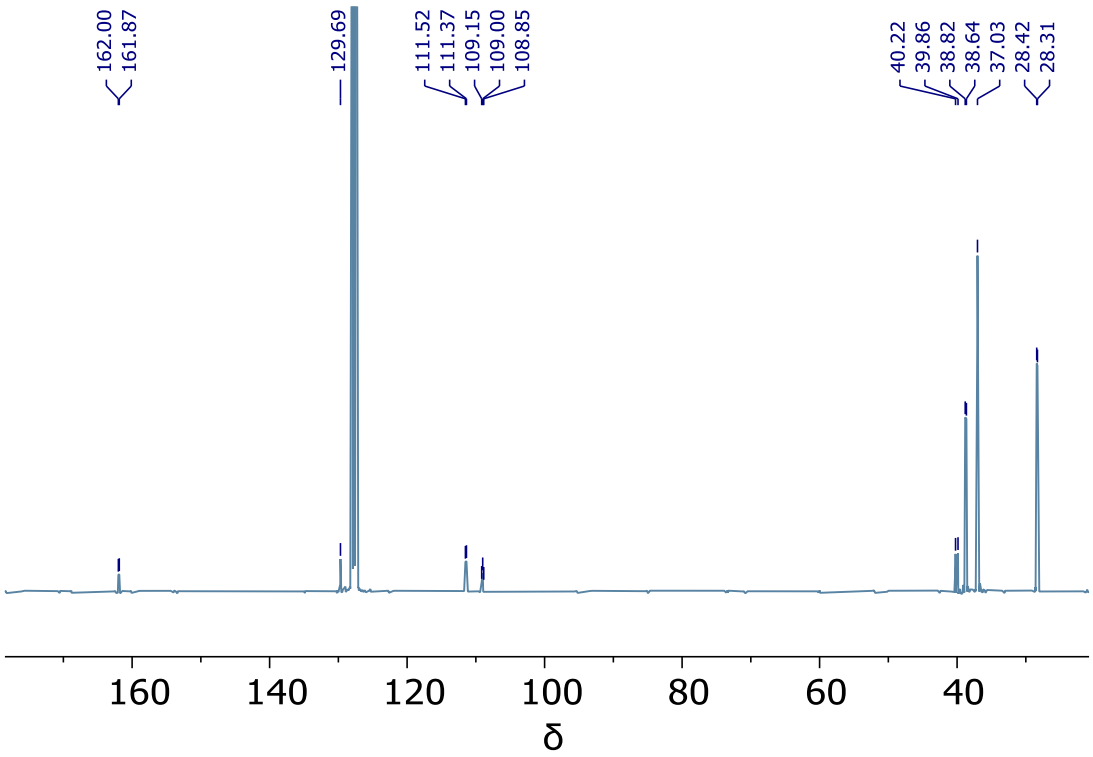

Figure 7.39. $^{13}C\{^{1}H\}$ NMR spectrum (C_6D_6, 75 MHz, 298 K) of Ad-POCOP.

7.7.5 Ir(Ad-POCOP)HCl

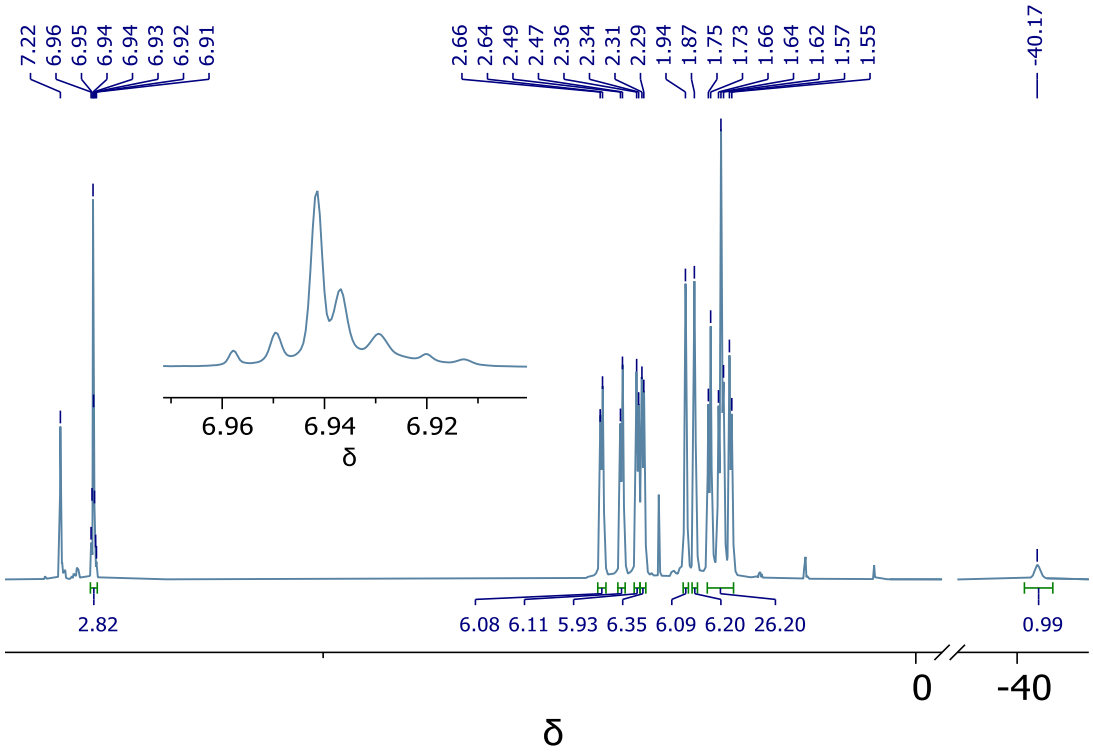

Figure 7.40. ^{1}H NMR spectrum (C_6D_6, 600 MHz, 298 K) of Ir(Ad-POCOP)HCl.

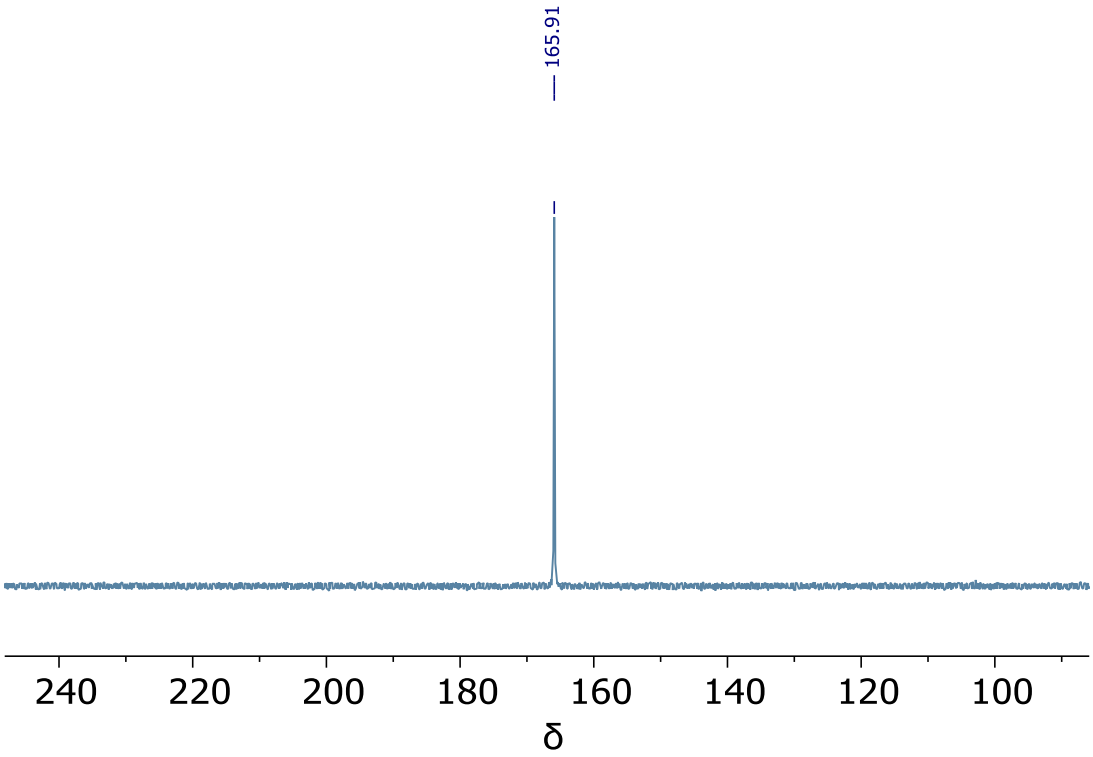

Figure 7.41. $^{31}P\{^{1}H\}$ NMR spectrum (C_6D_6, 243 MHz, 298 K) of Ir(Ad-POCOP)HCl.

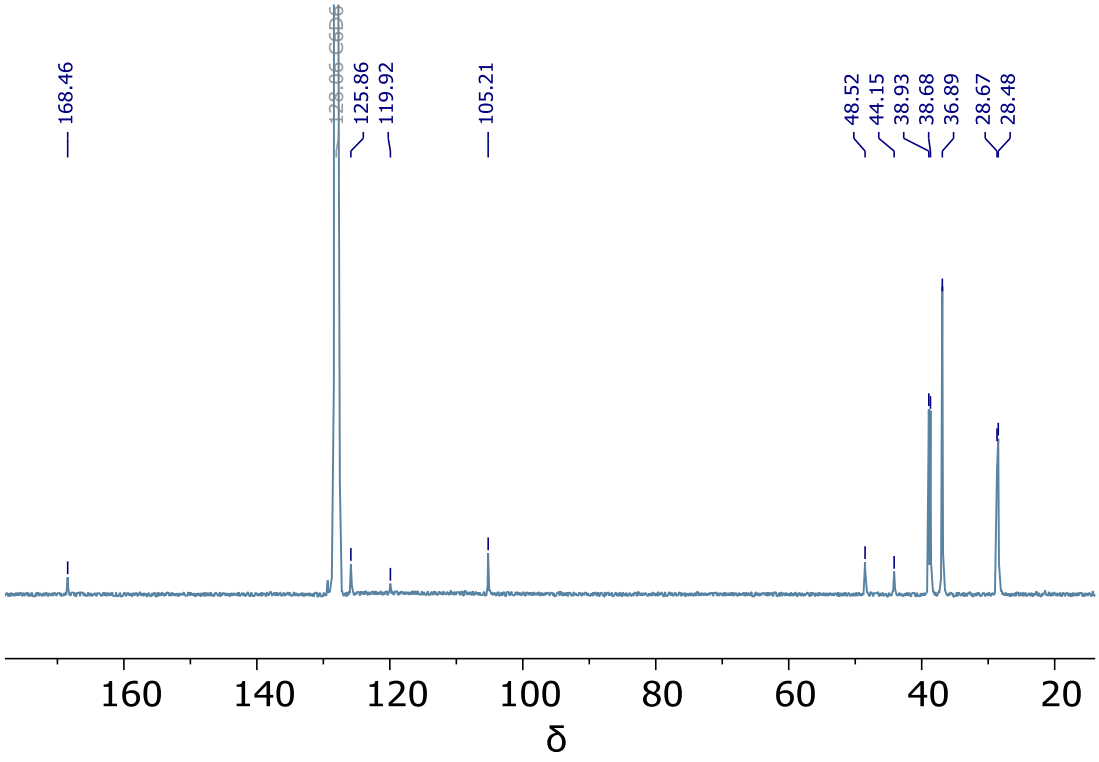

Figure 7.42. $^{13}C\{^{1}H\}$ NMR spectrum (C_6D_6, 151 MHz, 298 K) of Ir(Ad-POCOP)HCl.

7.7.6 Ir(Ad-POCOP)(H)$_2$(BH$_3$) – *in situ*

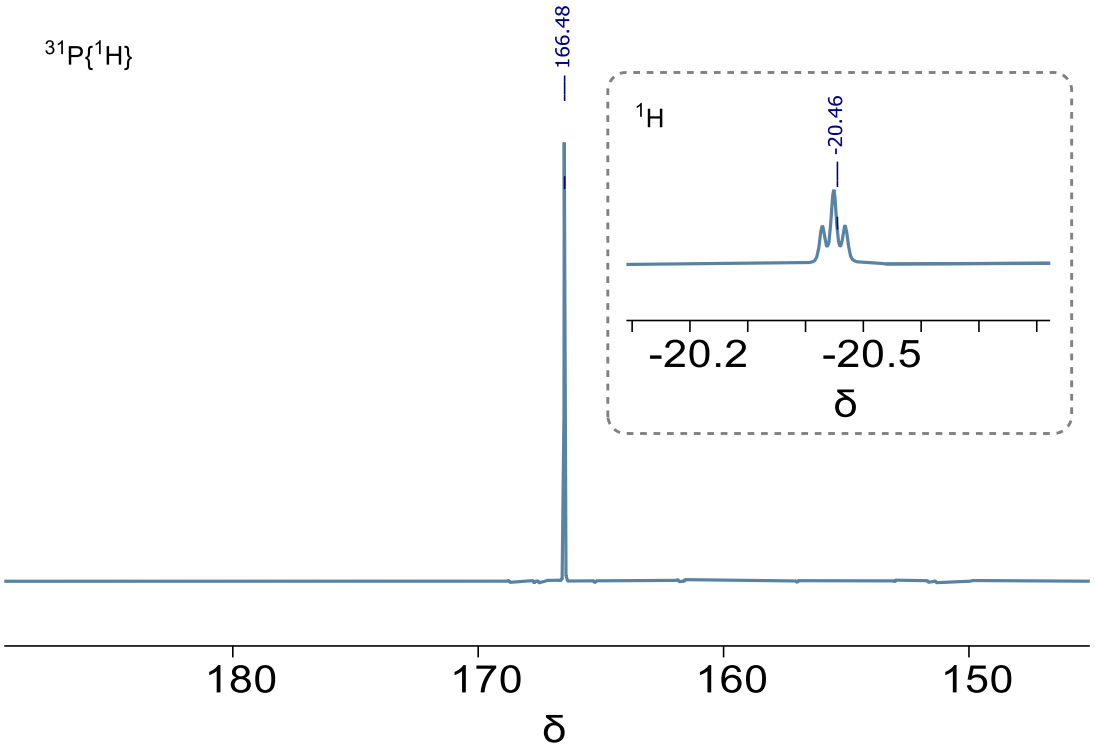

Figure 7.43. $^{31}P\{^{1}H\}$ NMR spectrum (C_6D_6, 243 MHz, 298 K) of Ir(Ad-POCOP)(H)$_2$(BH$_3$). Inset: ^{1}H NMR spectrum of hydride (C_6D_6, 600 MHz, 298 K).

7.7.7 Ir(^{i}Pr-POCOP)(H)$_2$(BH$_3$) – *in situ*

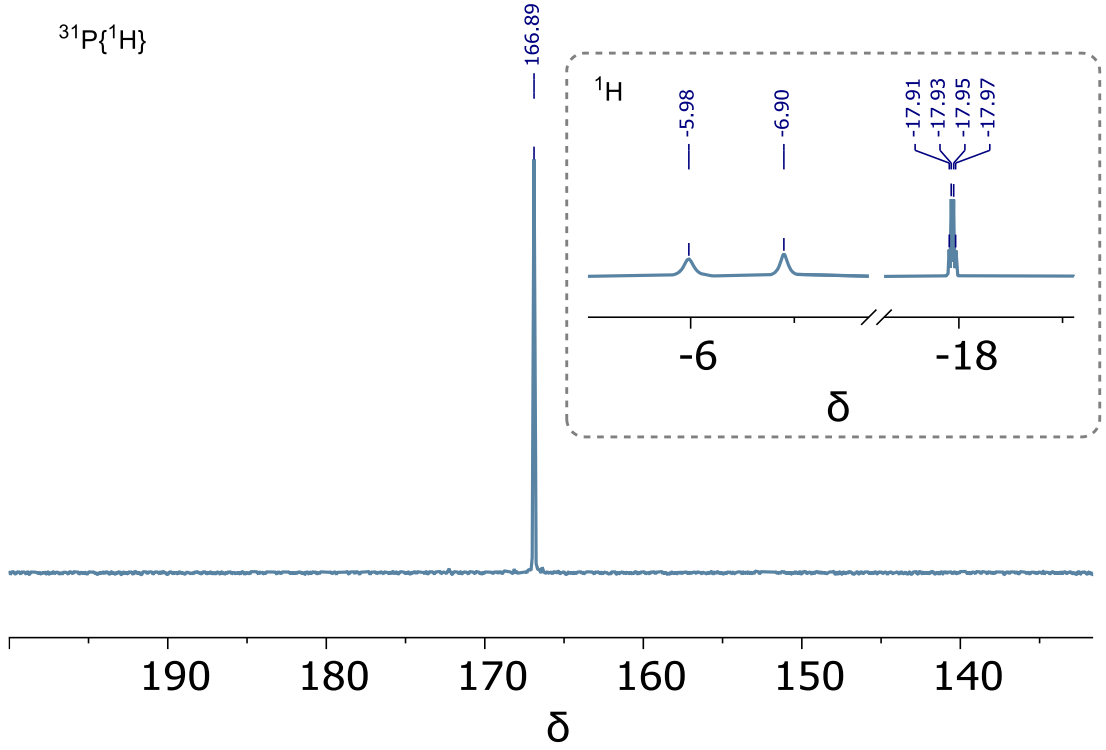

Figure 7.44. $^{31}P\{^{1}H\}$ NMR spectrum (C_6D_6, 243 MHz, 298 K) of Ir(^{i}Pr-POCOP)(H)$_2$(BH$_3$). Inset: ^{1}H NMR spectrum of hydrides (C_6D_6, 600 MHz, 298 K).

7.7.8 Ir(^{t}Bu-POCOP)(H)$_2$ (1)

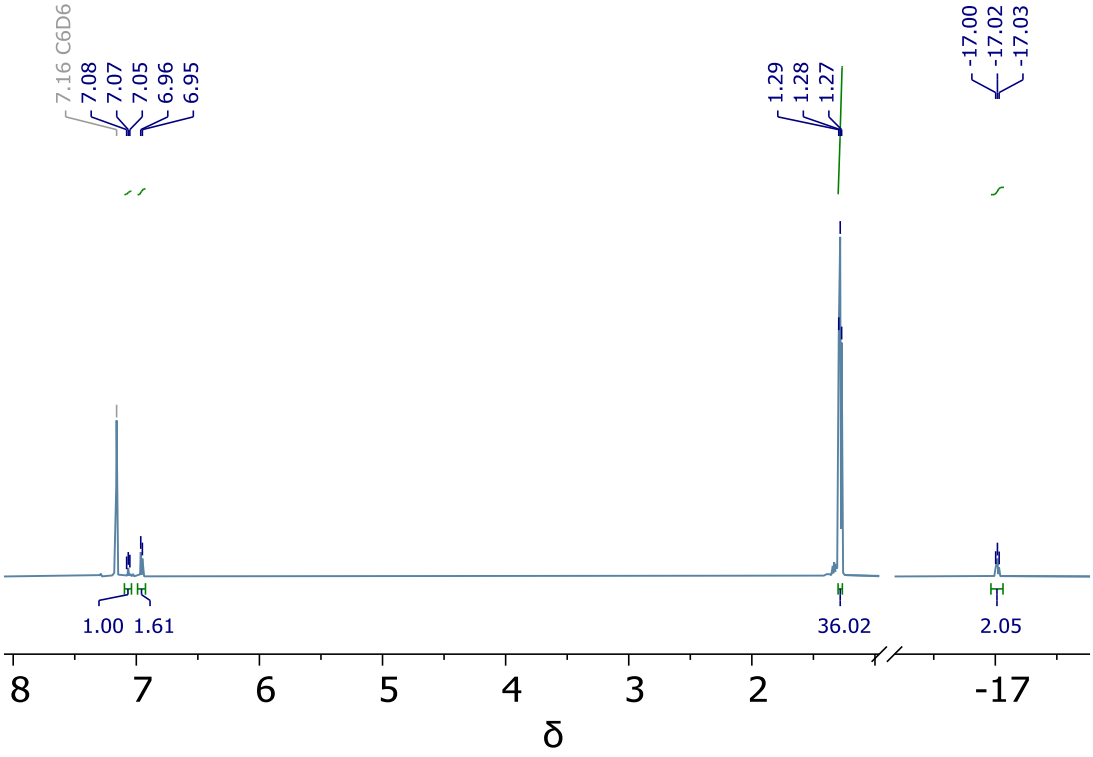

Figure 7.45. ^{1}H NMR spectrum (C_6D_6, 600 MHz, 298 K) of Ir(^{t}Bu-POCOP)(H)$_2$.

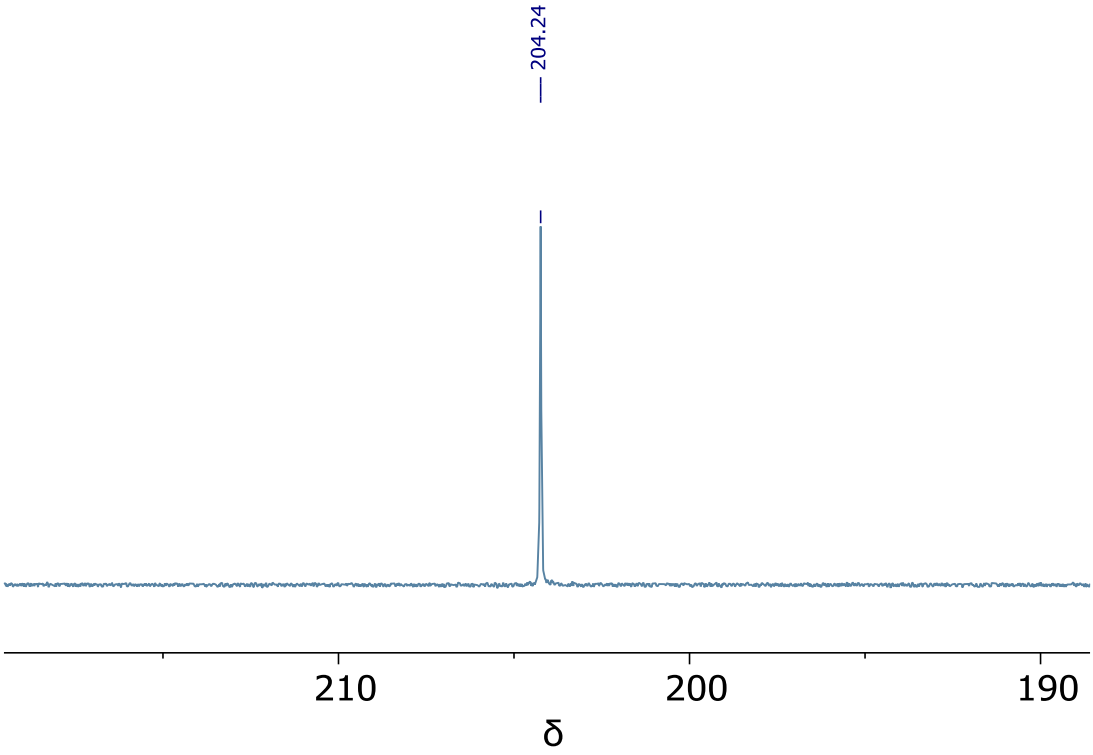

Figure 7.46. ^{31}P{^{1}H} NMR spectrum (C_6D_6, 243 MHz, 298 K) of Ir(^{t}Bu -POCOP)(H)$_2$.

7.7.9 Ir(^{t}Bu-POCOP)(H)$_2$(BH$_3$) (2)

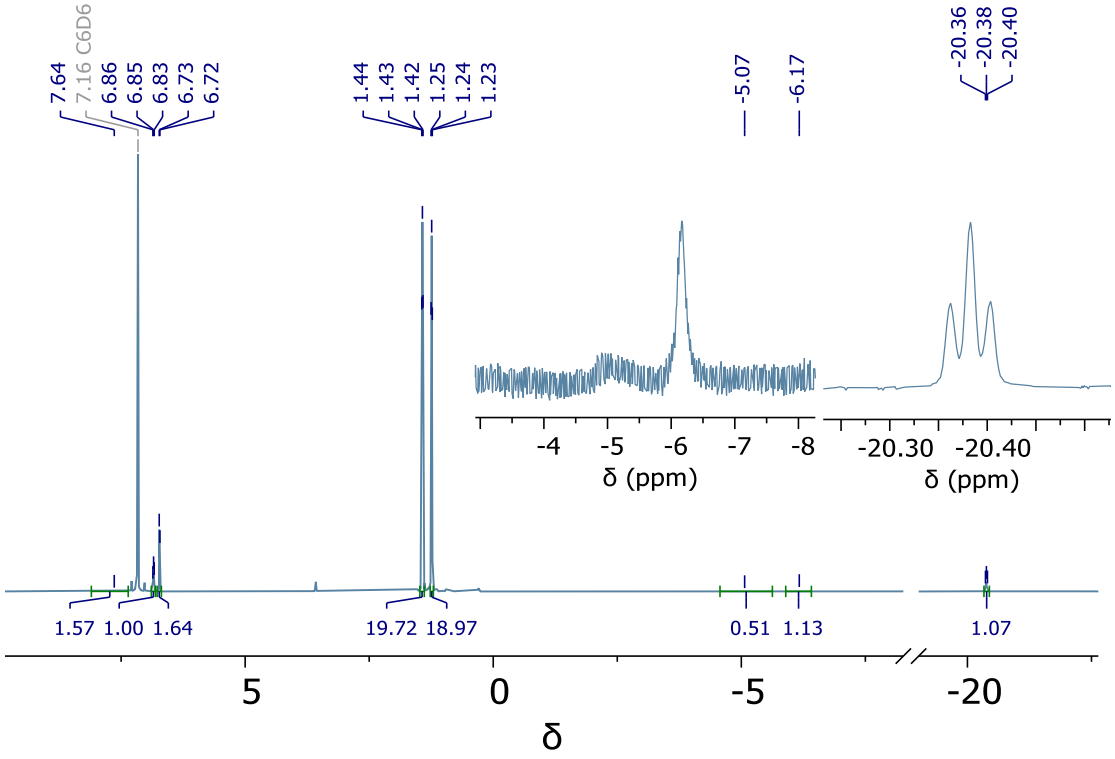

Figure 7.47. ^{1}H NMR spectrum (C_6D_6, 600 MHz, 298 K) of Ir(^{t}Bu-POCOP)(H)$_2$(BH$_3$).

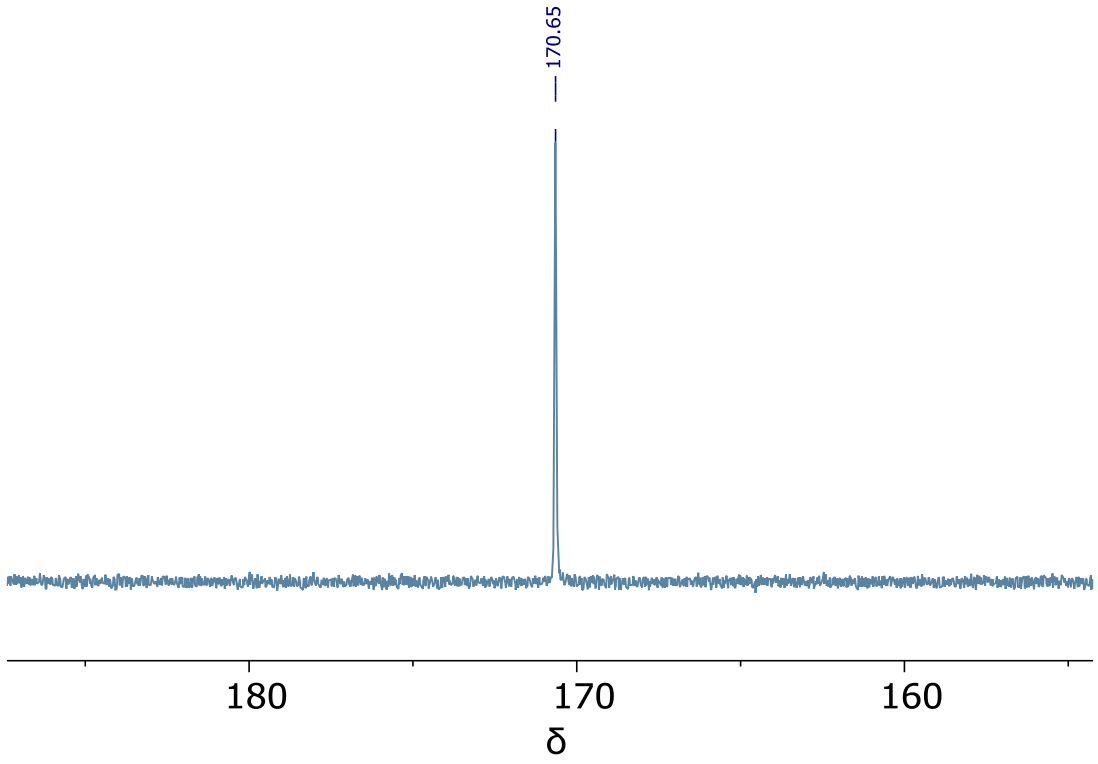

Figure 7.48. ^{31}P{^{1}H} NMR spectrum (C_6D_6, 243 MHz, 298 K) of Ir(^{t}Bu -POCOP)(H)$_2$(BH$_3$).

7.7.10 Ir(ᵗBu-POCOP)HCl (7)

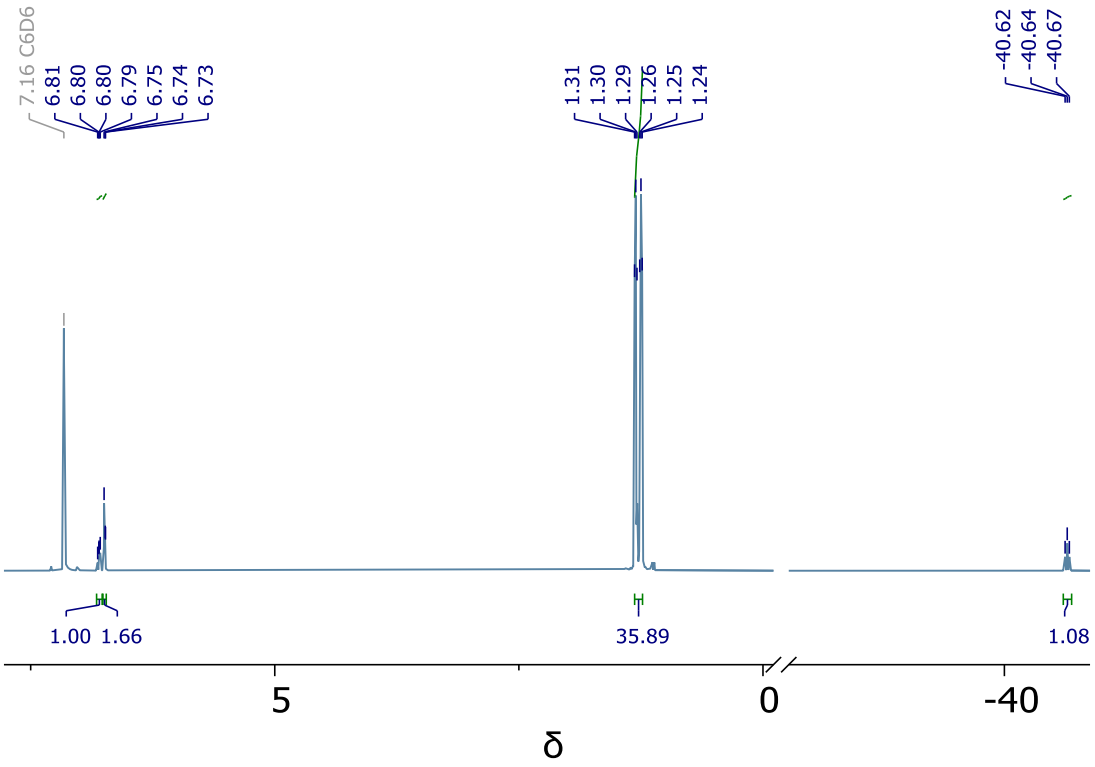

Figure 7.49. ^{1}H NMR spectrum (C_6D_6, 600 MHz, 298 K) of Ir(ᵗBu-POCOP)HCl.

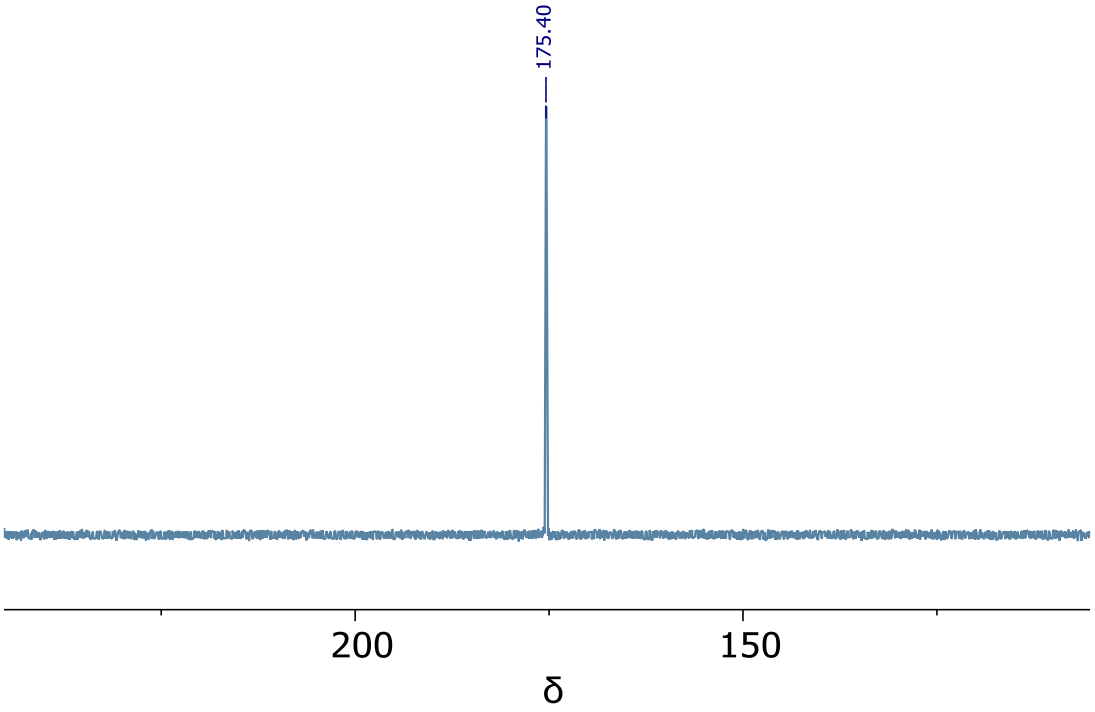

Figure 7.50. $^{31}P\{^{1}H\}$ NMR spectrum (C_6D_6, 243 MHz, 298 K) of Ir(ᵗBu -POCOP)HCl.

7.8 Single-Crystal X-ray Diffraction

Single crystal X-ray diffraction data were collected on a Rigaku SuperNova diffractometer with Cu Kα (λ = 1.54184 Å) radiation, equipped with a nitrogen gas Oxford Cryosystems Cryostream unit[26] and a Hybrid pixel (Hypix) array detector. Diffraction images from raw frame data were reduced using CrysAlisPro suite of programmes. The structures were solved using SHELXT,[27] and refined to convergence on F^2 against all independent reflections by full-matrix least-squares using SHELXL[28] (version 2018/3) through the Olex2 GUI.[29] All non-hydrogen atoms were refined anisotropically and non-hydride hydrogen atoms were geometrically placed and allowed to ride on their parent atoms. The hydride ligands in [Na(18-crown-6)$(THF)_2$][**6**] were located in the difference map and confirmed by altering the resolution of the data. Distances and angles were calculated using the full covariance matrix. Low data completeness in the dataset of [Na(18-crown-6)$(THF)_2$][**6**] (96.2%; full to 135.4 °, 92% to 153.7 °) was caused by weak diffraction at high angles, causing an absence of expected high angle reflections. The structure for Ad-POCOP contains half a molecule of pentane in the lattice. Crystallographic data are available free of charge *via* the Cambridge Crystallographic Data Centre, under deposition numbers 2486059 and 248060.

7.8.1 Crystallographic Tables

Table 7.2. Selected crystallographic data for complexes **4** and **[Na-18-crown-6][6]**.

	[Ir(^{t}Bu-POCOP)H_2(NH_2Me) (**4**)	[Na-18-crown-6-($THF)_2$] [Ir(^{t}Bu-POCOP)H_3] **[Na-18-crown-6][6]**
CCDC Deposition Number	2486059	2486060
Empirical formula	$C_{23}H_{44}IrNO_2P_2$	$C_{42}H_{82}O_{10}NaP_2Ir$
Formula weight	620.73	1024.20
Temperature/K	110.05(10)	110.00(10)
Crystal system	monoclinic	monoclinic
Space group	*P* 2_1	*C* 2/c
a/Å	7.9232(1)	30.2040(2)
b/Å	21.2029(3)	10.61750(10)
c/Å	15.4615(2)	30.3569(2)
α/°	90	90
β/°	91.090(1)	90.0680(10)
γ/°	90	90
Volume/Å^3	2596.98(6)	9735.18(13)
Z	4	8
ρ_{calc} g/cm^3	1.588	1.398
μ/mm^{-1}	11.250	6.424
F(000)	1248.0	4256.0
Crystal size/mm^3	0.186 × 0.083 × 0.047	0.153 × 0.082 × 0.073
Radiation	Cu Kα (λ = 1.54184)	Cu Kα (λ = 1.54184)
2Θ range/°	7.076 to 154.11	8.254 to 153.708
Index ranges	-10 ≤ h ≤ 9, -26 ≤ k ≤ 26, -19 ≤ l ≤ 19	-34 ≤ h ≤ 38, -11 ≤ k ≤ 13, -38 ≤ l ≤ 37
Reflections collected	17246	33891
Independent reflections	17246 [R_{int} = –, R_{sigma} = 0.0319]	9452 [R_{int} = 0.0339, R_{sigma} = 0.0298]
Data/restraints/parameters	17246/1/550	9452/18/548
Goodness-of-fit on F^2	1.033	1.261
Completeness	100	96.2
Final R indexes [I>=2σ (I)]	R_1 = 0.0392, wR_2 = 0.1029	R_1 = 0.0419, wR_2 = 0.1039
Final R indexes [all data]	R_1 = 0.0403, wR_2 = 0.1042	R_1 = 0.0431, wR_2 = 0.1044
Largest diff. peak/hole/ e Å^{-3}	2.47 / -1.60	1.17 / -1.64
Flack parameter	-0.031(7)	–

Table 7.3. Selected crystallographic data for Ad-POCOP and complex **8**.

	Ad-POCOP	[Ir(Ad-POCOP)(H)Cl] (**8**)
Empirical formula	$C_{48.5}H_{70}O_2P_2$	$C_{51}H_{75}ClIrO_2P_2$
Formula weight	746.98	1009.70
Temperature/K	110.02(10)	110.0(4)
Crystal system	triclinic	triclinic
Space group	P-1	P-1
a/Å	6.51580(10)	9.7358(2)
b/Å	16.1388(3)	10.3879(2)
c/Å	20.2370(4)	24.8721(6)
α/°	71.564(2)	86.670(2)
β/°	87.5610(10)	78.999(2)
γ/°	87.8940(10)	64.245(2)
Volume/Å^3	2016.41(7)	2223.04(9)
Z	2	2
ρ_{calc} g/cm^3	1.230	1.508
μ/mm^{-1}	1.267	7.345
F(000)	814.0	1042.0
Crystal size/mm^3	0.15 × 0.05 × 0.03	0.089 × 0.043 × 0.035
Radiation	Cu Kα (λ = 1.54184)	Cu Kα (λ = 1.54184)
2Θ range/°	5.774 to 160.262	7.244 to 160.836
Index ranges	-7 ≤ h ≤ 8, -20 ≤ k ≤ 20, -25 ≤ l ≤ 24	-12 ≤ h ≤ 12, -13 ≤ k ≤ 11, -29 ≤ l ≤ 31
Reflections collected	22614	42479
Independent reflections	8090 [R_{int} = 0.0344, R_{sigma} = 0.0367]	9089 [R_{int} = 0.0566, R_{sigma} = 0.0374]
Data/restraints/parameters	8090/61/498	9089/0/470
Goodness-of-fit on F^2	1.037	1.086
Completeness	99.9	100
Final R indexes [I>=2σ (I)]	R_1 = 0.0528, wR_2 = 0.1458	R_1 = 0.0461, wR_2 = 0.1130
Final R indexes [all data]	R_1 = 0.0613, wR_2 = 0.1517	R_1 = 0.0508, wR_2 = 0.1152
Largest diff. peak/hole/ e Å^{-3}	0.83/-0.31	2.29/-3.29
Flack parameter	-	-

7.9 References

1. A. B. Pangborn, M. A. Giardello, R. H. Grubbs, R. K. Rosen and F. J. Timmers, *Organometallics*, 1996, **15**, 1518–1520.
2. I. Göttker-Schnetmann, P. White and M. Brookhart, *J. Am. Chem. Soc.*, 2004, **126**, 1804–1811.
3. I. Göttker-Schnetmann, P. S. White and M. Brookhart, *Organometallics*, 2004, **23**, 1766–1776.
4. M. C. Denney, V. Pons, T. J. Hebden, D. M. Heinekey and K. I. Goldberg, *J. Am. Chem. Soc.*, 2006, **128**, 12048–12049.
5. L. P. Press, A. J. Kosanovich, B. J. McCulloch and O. V. Ozerov, *J. Am. Chem. Soc.*, 2016, **138**, 9487–9497.
6. G. M. Adams, A. L. Colebatch, J. T. Skornia, A. I. McKay, H. C. Johnson, G. C. Lloyd-Jones, S. A. Macgregor, N. A. Beattie and A. S. Weller, *J. Am. Chem. Soc.*, 2018, **140**, 1481–1495.
7. F. Anke, S. Boye, A. Spannenberg, A. Lederer, D. Heller and T. Beweries, *Chem. Eur. J.*, 2020, **26**, 7889–7899.
8. V. Pons and R. T. Baker, *Angew. Chem. Int. Ed.*, 2008, **47**, 9600–9602.
9. A. Staubitz, M. E. Sloan, A. P. M. Robertson, A. Friedrich, S. Schneider, P. J. Gates, J. S. A. D. Günne and I. Manners, *J. Am. Chem. Soc.*, 2010, **132**, 13332–13345.
10. A. Saib, A. Bara-Estaún, O. J. Harper, D. B. G. Berry, I. A. Thomlinson, R. Broomfield-Tagg, J. P. Lowe, C. L. Lyall and U. Hintermair, *React. Chem. Eng.*, 2021, **6**, 1548–1573.
11. A. Bara-Estaun, M. C. Harder, C. L. Lyall, J. P. Lowe, E. Suturina and U. Hintermair, *Chem. Eur. J.*, 2023, **29**, e202300215.
12. A. M. R. Hall, J. C. Chouler, A. Codina, P. T. Gierth, J. P. Lowe and U. Hintermair, *Cat. Sci. Technol.*, 2016, **6**, 8406–8417.
13. M. J. Frisch, G. W. Trucks, H. B. Schlegel, G. E. Scuseria, M. A. Robb, J. R. Cheeseman, G. Scalmani, V. Barone, G. A. Petersson, H. Nakatsuji, X. Li, M. Caricato, A. V. Marenich, J. Bloino, B. G. Janesko, R. Gomperts, B. Mennucci, H. P. Hratchian, J. V. Ortiz, A. F. Izmaylov, J. L. Sonnenberg, D. Williams-Young, F. Ding, F. Lipparini, F. Egidi, J. Goings, B. Peng, A. Petrone, T. Henderson, D. Ranasinghe, V. G. Zakrzewski, J. Gao, N. Rega, G. Zheng, W. Liang, M. Hada, M. Ehara, K. Toyota, R. Fukuda, J. Hasegawa, M. Ishida, T. Nakajima, Y. Honda, O. Kitao, H. Nakai, T. Vreven, K. Throssell, J. J. A. Montgomery, J. E. Peralta, F. Ogliaro, M. J. Bearpark, J. J. Heyd, E. N. Brothers, K. N. Kudin, V. N. Staroverov, T. A. Keith, R. Kobayashi, J. Normand, K. Raghavachari, A. P. Rendell, J. C. Burant, S. S. Iyengar, J. Tomasi, M. Cossi, J. M. Millam, M. Klene, C. Adamo, R. Cammi, J. W. Ochterski, R. L. Martin, K. Morokuma, O. Farkas, J. B. Foresman and D. J. Fox, Gaussian, Inc., Wallingford CT, 2016.
14. D. Andrae, U. Häußermann, M. Dolg, H. Stoll and H. Preuß, *Theor. Chim. Acta*, 1990, **77**, 123–141.
15. P. C. Hariharan and J. A. Pople, *Theor. Chim. Acta*, 1973, **28**, 213–222.
16. W. J. Hehre, R. Ditchfield and J. A. Pople, *J. Chem. Phys.*, 1972, **56**, 2257–2261.
17. A. Höllwarth, M. Böhme, S. Dapprich, A. W. Ehlers, A. Gobbi, V. Jonas, K. F. Köhler, R. Stegmann, A. Veldkamp and G. Frenking, *Chem. Phys. Lett.*, 1993, **208**, 237–240.
18. A. D. Becke, *Phys. Rev. A*, 1988, **38**, 3098–3100.
19. J. P. Perdew, *Phys. Rev. B*, 1986, **33**, 8822–8824.

20. J. Tomasi, B. Mennucci and R. Cammi, *Chem. Rev.*, 2005, **105**, 2999–3094.
21. F. Weigend, *Phys. Chem. Chem. Phys.*, 2006, **8**, 1057–1065.
22. F. Weigend and R. Ahlrichs, *Phys. Chem. Chem. Phys.*, 2005, **7**, 3297–3305.
23. S. Grimme, J. Antony, S. Ehrlich and H. Krieg, *J. Chem. Phys.*, 2010, **132**, 154104.
24. S. Grimme, S. Ehrlich and L. Goerigk, *J.Comput. Chem.*, 2011, **32**, 1456–1465.
25. A. D. Becke and E. R. Johnson, *J. Chem. Phys.*, 2005, **123**, 154101.
26. J. Cosier and A. M. Glazer, *J. Appl. Crystallogr.*, 1986, **19**, 105–107.
27. G. M. Sheldrick, *Acta Crystallogr. A*, 2015, **71**, 3–8.
28. G. M. Sheldrick, *Acta Crystallogr. A*, 2008, **64**, 112–122.
29. O. V. Dolomanov, L. J. Bourhis, R. J. Gildea, J. A. K. Howard and H. Puschmann, *J. Appl. Crystallogr.*, 2009, **42**, 339–34

Appendix

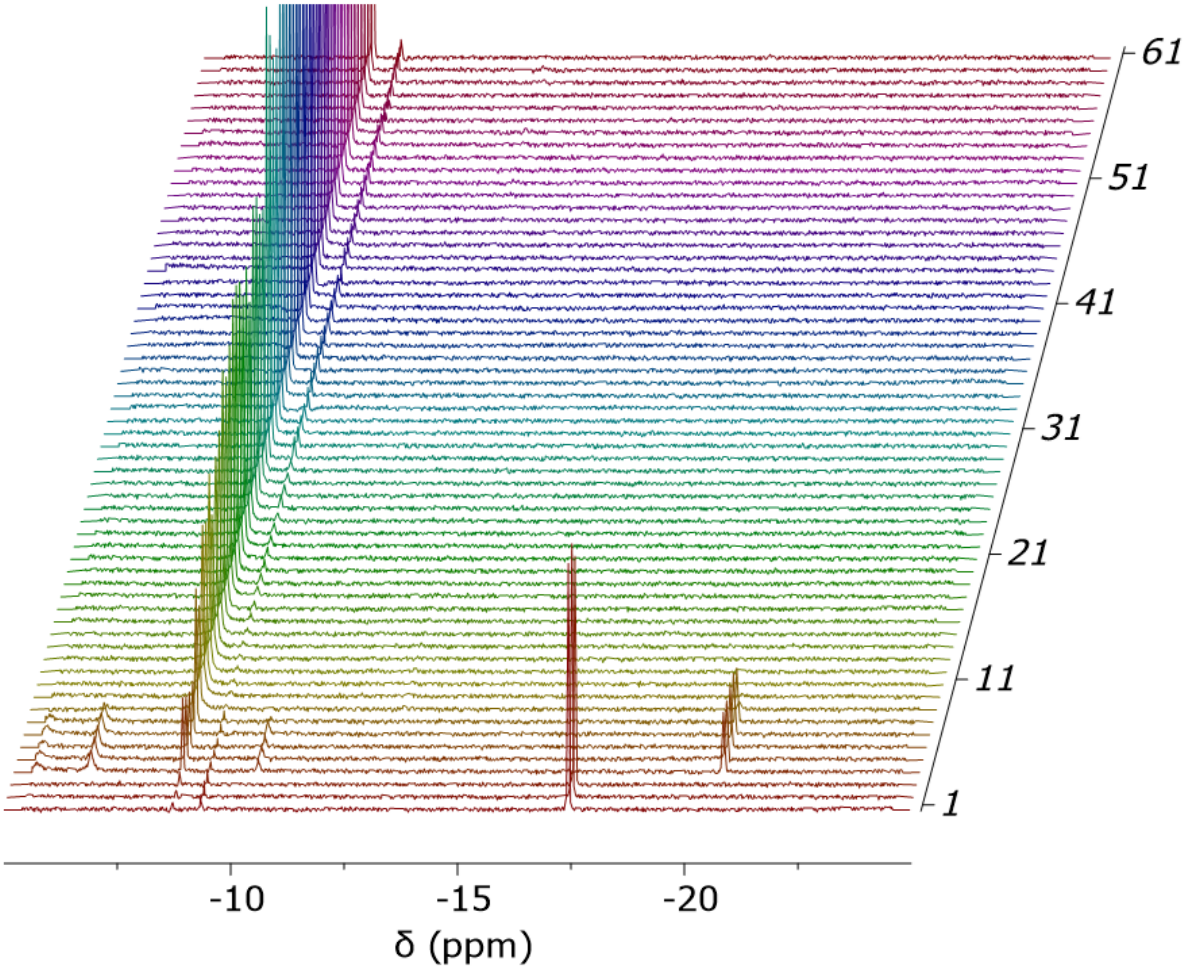

Figure A.51. ^{1}H NMR spectra (THF-H^{8}, 500 MHz, 266 K) throughout catalysis starting at spectrum 1 (hydride region only) – selective excitation experiment. Peak at δ −17.5 corresponds to Ir(^{t}Bu-POCOP)H_2, peaks at δ −5.6, −6.8 and −20.6 correspond to Ir(^{t}Bu-POCOP)$(H)_2(BH_3)$, peak at δ −8.7 corresponds to Ir(^{t}Bu-POCOP)H_4, peak at δ −9.4 corresponds to Ir(^{t}Bu-POCOP)$H_2(NH_2Me)$, peak at δ −10.4 corresponds to an unknown Ir-hydride species.

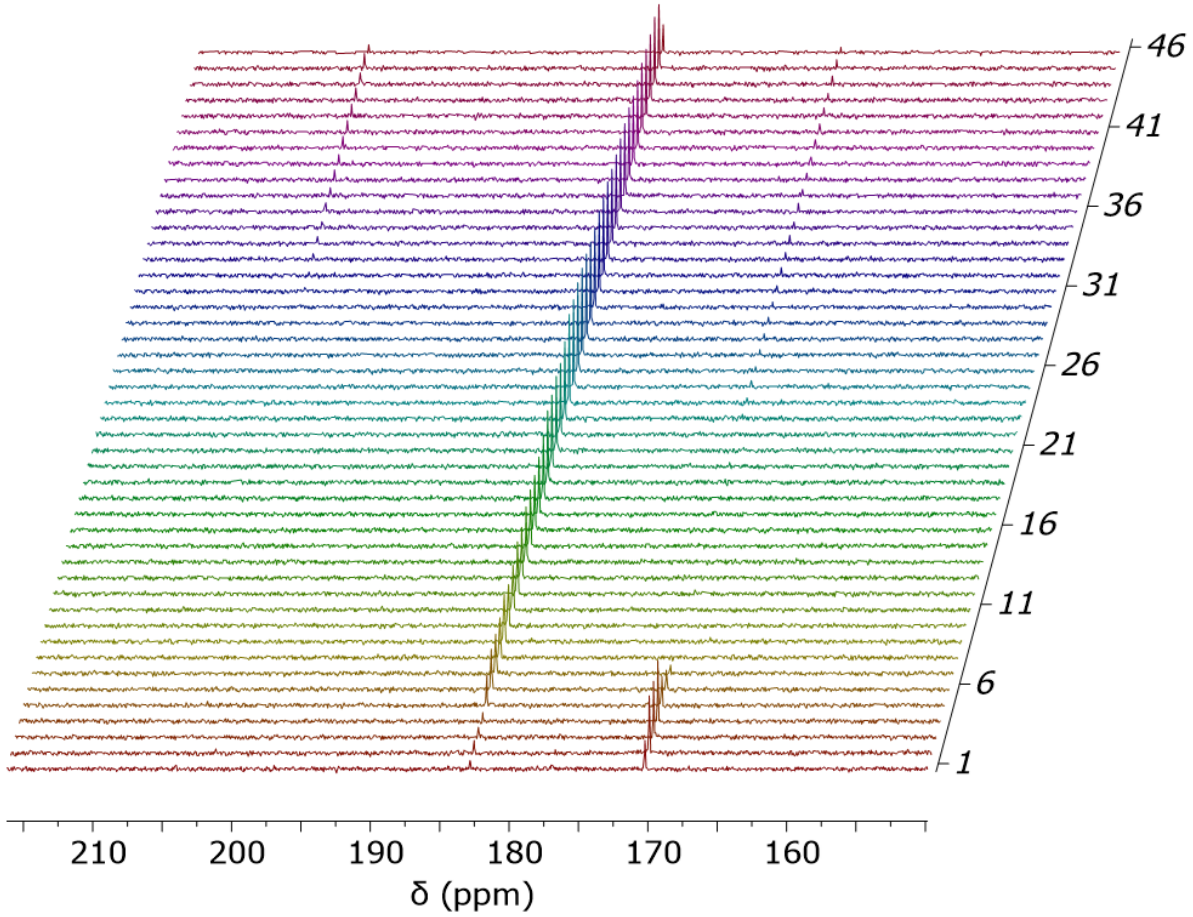

Figure A.52. $^{31}P\{^{1}H\}$ NMR spectra (THF-H^8, 203 MHz, 266 K) tracking speciation throughout catalysis, once $H_3B{\cdot}NH_2Me$ had been added to **1** starting at spectrum 1. Peak at δ 203 corresponds to Ir(^{t}Bu-POCOP)H_2, δ 183 corresponds to Ir(^{t}Bu-POCOP)H_4, δ 170 corresponds to Ir(^{t}Bu-POCOP)$(H)_2(BH_3)$, δ 169 corresponds to Ir(^{t}Bu-POCOP)$H_2(NH_2Me)$ (spectrum 23 onwards)

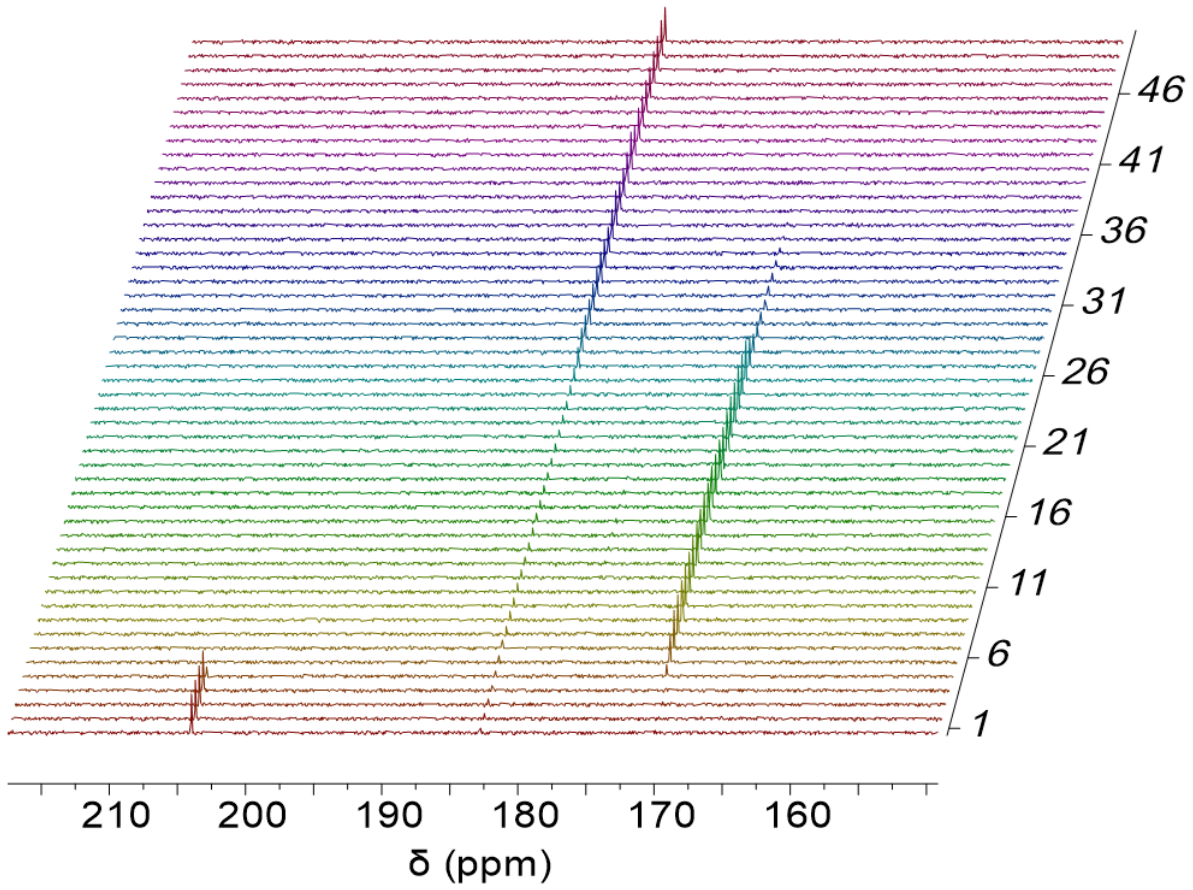

Figure A.53. $^{31}P\{^{1}H\}$ NMR spectra (THF-H^8, 203 MHz, 266 K) recorded during induction period. Peak at δ 203 corresponds to Ir(^{t}Bu-POCOP)H_2, δ 183 corresponds to Ir(^{t}Bu-POCOP)H_4, δ 170 corresponds to Ir(^{t}Bu-POCOP)$(H)_2(BH_3)$.

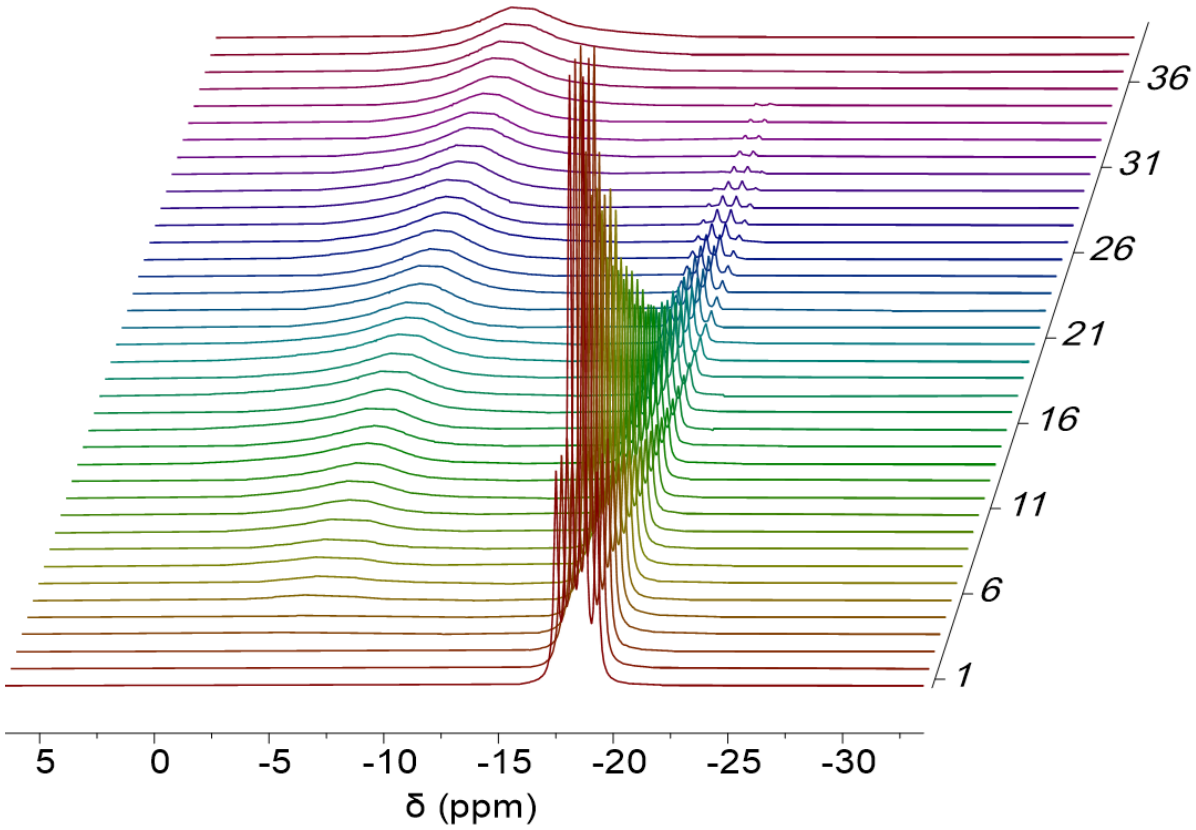

Figure A.54. Stacked ^{11}B NMR spectra (THF-H^8, 160 MHz, 266 K) showing reaction progression from $H_3B{\cdot}NH_2Me$ (δ −18, quartet) to polyaminoborane (δ −6, broad singlet).

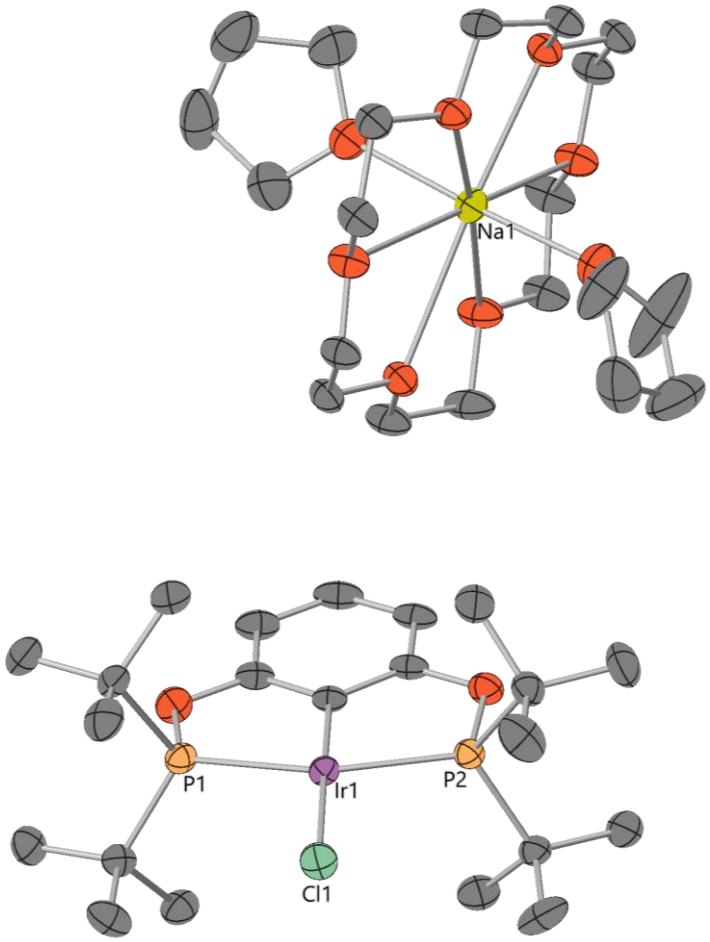

Figure A.55. The molecular structure of [Na-18-crown-6-$(THF)_2$][Ir(^{t}Bu-POCOP)Cl], displacement ellipsoids are set at 50% probability, only one complex from the asymmetric unit is shown and selected hydrogen atoms have been omitted for clarity. Selected bond lengths (Å): Ir1–Cl1 2.4403(7), Ir1–P1 2.2376(6), Ir1–P2 2.2316(6), Ir1–C10 2.048(9). Selected bond angles (°): P1–Ir1–P2 159.02(3).